COMPUTATIONAL MODELING OF ASTHMATIC AIRWAY COLLAPSE

by

CONSTANTINE ATHANASIOS HROUSIS

Bachelor of Science in Civil & Environmental Engineering
and Mechanical & Aerospace Engineering,
Cornell University, Ithaca, New York, 1992

Submitted to the Department of Mechanical Engineering
in partial fulfillment of the requirements for the degree of

Doctor of Philosophy in Mechanical Engineering

at the

MASSACHUSETTS INSTITUTE OF TECHNOLOGY

June 1998

Author.....
.....
Constantine A. Hrousis
Department of Mechanical Engineering
June 1998

Certified by.....
Roger D. Kamm
Professor of Mechanical Engineering
Thesis Supervisor

Accepted by.....
Ain A. Sonin
Professor of Mechanical Engineering
Chairman, Departmental Committee on Graduate Studies

Computational Modeling of Asthmatic Airway Collapse

by

Constantine Athanasios Hrousis

Submitted to the Department of Mechanical Engineering
on May 8, 1998 in Partial Fulfillment of the
Requirements for the degree of Doctor of Philosophy in
Mechanical Engineering

ABSTRACT

Pulmonary airways and a variety of other biological vessels are observed to buckle with multiple folds as they collapse under the action of smooth muscle constriction. Recent work in the study of airway collapse has concentrated on the significance of a thin but relatively stiff sub-epithelial collagen layer near the inner aspect of the bronchial wall. A thickening of this layer has been found to correlate strongly with the severity of airway obstruction in asthma. When the airway smooth muscle constricts, this sub-epithelial layer buckles into many folds. In asthmatics the entire airway is thickened due to remodeling, but the sub-epithelial collagen layer in particular is about twice as thick as in normals. Similarly, there are conditions of fibrosis in other biological vessels, such as arteries, the colon, the intestines, the stomach, the esophagus, etc., for which it would be helpful to better understand the mechanics behind the folding of their sub-epithelial collagen, basement membrane and/or other mucosal components.

This work focuses on a two-layer mathematical model for an airway subjected to smooth muscle constriction, analyzed using finite-element methods (via ABAQUS software), and verified with large-scale physical model experiments. Though simple, the two-layer model provides insight into how an airway wall's resistance to occlusion would change due to hypothetical changes in the geometry and intrinsic material stiffnesses of the wall components. Specifically, it predicts that the number of mucosal folds is reduced most by increased thickness of the inner sub-epithelial collagen layer and only marginally reduced by increased thickness of the outer submucosal layer. Increasing the inner-to-outer material stiffness ratio causes an intermediate reduction in the number of folds. "Remeshing" of the finite-element domain has been performed to better understand the postbuckling collapse. For a particular regime of airway geometry and material properties, a significant reduction in the number of mucosal folds will reduce the airway's resistance to luminal occlusion upon maximal smooth muscle constriction. Additional analyses using poroelastic material descriptions confirm that compressibility would not alter the airway model's behavior significantly.

Thesis Supervisor: Roger D. Kamm
Professor of Mechanical Engineering
Massachusetts Institute of Technology

ACKNOWLEDGMENTS

The research presented in this thesis was made possible by funding from the National Institutes of Health, the American Lung Association and the Freeman Foundation.

Many people have generously given me their support, advice and guidance throughout the production of this thesis and helped to make this piece of work possible.

Naturally, I would first like to thank Prof. Roger D. Kamm for being my thesis advisor, for offering me the opportunity to work with him on this project and for his kind guidance throughout my study as a graduate student. It has indeed been an honor to work with him and the many other fine researchers of the M.I.T. Fluid Mechanics Laboratory.

I appreciate the input and guidance given by Prof. Barry R. Wiggs of the University of British Columbia Pulmonary Research Laboratory in Vancouver, British Columbia, who originated this work and has provided me with opportunities to work with him at St. Paul's Hospital in Vancouver. I also thank Dr. James Hogg and Dr. Peter Paré for their guidance and support during my 1994 visit to the UBC PRL and for making it possible.

I thank Prof. Rohan Abeyaratne and Prof. Jeffrey M. Drazen for serving on my thesis committee, taking the time to come to committee meetings and my thesis defense, reading my thesis and offering their helpful input.

I thank Prof. Stephanie Shore of the Harvard School of Public Health for her guidance during the herein mentioned "split-lung" experiments which I performed in her laboratory.

Over the past five years, I have benefited from the advice offered by Dr. Mark Johnson and the other faculty of the M.I.T. Fluid Mechanics Laboratory. Thank you for your input.

I thank Dr. James Shin, Dr. Edwin Ozawa, Dr. Naomi Chesler and other alumni of the M.I.T. Fluid Mechanics Laboratory for their wise words of advice through the years.

Many thanks to Barbara Ressler, Hayden Huang, Gregg Duthaler, Hugo Ayala and the other students of the M.I.T. Fluid Mechanics Laboratory for their continuing support and friendship.

I also want to thank Claire Sasahara for her administrative support during these years.

For offering their advice when I sought it, I thank Prof. Klauss-Jurgen Bathe, Prof. Mohammad Durali, Dr. Marc Levenston, Leslie Regan and many other members of the faculty and staff of the M.I.T. Department of Mechanical Engineering.

Thanks to Ashish Verma and Shizuka Sugawara for their help with the herein mentioned indentation experiments. It was a pleasure to work with you, and I wish you good luck in your careers.

I thank Dr. Joan L. Bolker for her personal support, and wish her many happy writings in return.

Thank you to Dr. Terrance N. Horner, Jr., Claudia R. Johnson, and many other dear friends who have shown their support and been there to comfort me during my time at M.I.T. Thanks to those who have gone though this process of dissertation writing and given their advice. Some wisdom a la Horner: "I'm so sick of counting ones and zeroes! You know, once you've seen one zero, you've seen them all!"

A very special thank you to Dr. James F. McCarrick, who has always lent a friendly ear, allowed me to vent my various frustrations, and shared his keen insight on all sorts of engineering problems, particularly the ones discussed herein. One... two-hoo... tha-ree cheers for the ideal world of homogeneous, semi-infinite, moldy yet half-eaten donuts; may it merrily turbule along, or whatever the heck it is that it does!

Robert H. Garmezy, Alice E. Garmezy and Lorena M. Garmezy, thank you for taking such a thorough interest in my work, and my personal success and happiness. I am so very honored to be joining your family.

For sending me to college and supporting my interests since I was born, for always lending their eager ears and wise advice, for making me the center of their lives, no statement of my thanks is great enough for me to offer my parents, Athanasios C. Hrousis and Ruth M. Hrousis. Thank you for making me someone you can be proud of.

It is a well known fact that graduate students often find themselves in damaged and failing relationships because of their choice to pursue a Ph.D. Yet the thought of this has never worried me. That's because I am so lucky to be sharing a love so strong that nothing can threaten it. Carrie H. Garmezy, soon to be Mrs. Carrie G. Hrousis, thank you for your patience. Our real life together starts now.

This work,

like all the work that I shall ever do,

is dedicated to my family:

to my parents,

to my future wife

and to the children that we hope to have.

TABLE OF CONTENTS

1. Introduction

1.1 Asthma

1.1.1 General Characteristics of Asthma

Asthma is the most common respiratory disease, affecting one in seven children and one in 11 adults. About 15 million Americans currently suffer from asthma, twice as many as 15 years ago. Asthma is characterized by intermittent shortness of breath, related to triggers. The trigger is usually an allergic response, often to common allergens (such as waste products from dust mites and cats), or to cold air, a viral infection, a particularly strong emotional response, etc. Asthma is episodic and completely reversible, unlike chronic obstructive pulmonary diseases such as chronic bronchitis and emphysema, where the shortness of breath is persistent. It tends to run in families, suggesting a genetic predisposition, affecting men and women equally, although occurring in blacks and Hispanics with greater frequency. It is a common pattern for most cases to present themselves in childhood before age 25, often remitting during puberty and adolescence while the lungs are growing, then resurfacing sometime during adulthood and then persisting indefinitely.[12]

By an incompletely understood biochemical mechanism, the response to the trigger causes the smooth (involuntary) muscle lining the airway walls to contract, thus constricting the airways and lessening the cross-sectional airway lumen area available for airflow, markedly increasing the resistance to airflow. Both the time and effort required for simple breathing are markedly increased in an attack of asthma. The common symptom of wheezing is a direct result of difficult exhalation due to increased resistance to airflow. If the oxygen supply to the organs is disrupted for too long, organ death occurs. About 5000 Americans die yearly from fatal attacks of asthma.

Since this hallmark increase in resistance to airflow is a mechanical phenomenon, it must result from mechanical changes in the structure of the airways and/or an increase in the load capacity of the constricting airway smooth muscle. The goal of this work is to develop a more clear understanding of the physical mechanisms behind the increase in airway resistance due to asthma. Computational structural models (via finite element methods) will be essential in testing our intuition, supporting our hypotheses and further developing our understanding of the physical mechanisms of asthma.

1.1.2 Methods of Asthma Treatment

For mild cases of asthma (fewer than 2-3 attacks per week), multiple puffs of inhaled muscle relaxants such as albuterol are prescribed The response within 15 minutes of administering the relaxant is getting the airway smooth muscle to cease constriction, allowing the airways to reopen. For moderate asthma patients (from 3 to 5 attacks per week if untreated), a daily regimen of inhaled corticosteroids and/or anti-inflammatory agents is prescribed, decreasing the smooth muscle's sensitivity and making it less likely for the patient to have an attack. For severely asthmatic patients (greater than 5 attacks per week if untreated), a daily controller regimen including multiple medications is required to deaden the smooth muscle's sensitivity. For both moderate and severe cases, the inhaled muscle relaxant remains an emergency quick-response treatment for the patient.

1.1.3 Chronic Obstructive Pulmonary Diseases

There are other respiratory diseases which fall under the description "chronic obstructive pulmonary disease" or COPD. This term is used because patients often exhibit symptoms from more than one of these obstructive diseases. Each of these diseases has its special characteristics which might occur in combination with asthma. In the United States, tobacco smoking accounts for 80-90% of the risk for COPD. The prognosis for COPD is favorable for those with mild symptoms. For those with severe airway obstruction the risk of death is much greater, but usually due to complications that arise in the course of COPD progression, such as infection, pneumothorax, arrythmia and right heart enlargement due to pulmonary hypertension.

Emphysema is characterized by abnormal permanent enlargement of the air spaces beyond the terminal bronchioles where gas exchange occurs, accompanied by destruction of the airway walls, but without fibrotic growth of those that remain. Normally, there are parenchymal attachments to the exterior of small airways (described some more in Section 1.2.2) which help to keep them open during expiration. Emphysematous lungs have fewer of these attachments, and so the smaller airways often collapse prematurely during expiration, making it markedly difficult to exhale. Sufferers also experience a dry cough (unless combined with chronic bronchitis).

Chronic bronchitis is distinguished by "chronic productive cough for 3 months in each of 2 successive years." Sufferers are plagued with excessive airway mucous production and different degrees of inflammation and/or infection. Chronic bronchitis often accompanies the other forms of COPD. Bronchiectasis is abnormal dilation of the bronchi and larger bronchioles due to destruction of the muscular and elastic components of the bronchial wall. The condition is commonly a response to injury or a chronic bacterial infection. Small airways disease is the presence of lesions in airways smaller than 2 mm in diameter (generations 8 and greater), also often in response to infection and/or injury.

The characteristic which most sets asthma apart from COPD is the fact that it comes in attacks and is completely "reversible," meaning that the patient is only temporarily symptomatic. However, the duration of attacks does vary, and in chronic asthma, there are indeed seemingly irreversible changes in airway structure and function.

1.2 Airways

1.2.1 The Tracheobronchial Tree

The full tracheobronchial tree has approximately 23 generations of airway bifurcations where each larger airway splits into (usually) two slightly smaller daughter airways. The first 5 or 6 generations are "cartilaginous," but all smaller airways containing very little or no cartilage and are termed "membranous" airways. The only apparent difference in airway structure between the cartilaginous and membranous airways is the presence or absence of the cartilaginous bands.

Generations 0 through 16 are referred to as the "conducting airways," and 17 through 23 are the "acinar airways." The conducting airways merely convey air to the acinar airways where respiration begins to occur at alveoli (air sacs) that line them (see Figure 1-1). The airways are commonly thought to bifurcate into pairs such that there are 2^Z airways per generation Z (where generation 0 is the trachea, generation 1 is the main stem bronchi, etc.), although this is only approximately true. This is merely a model, so there may be different airway lengths at different locations in the lungs, as well as more than two daughter airways at a bifurcation, and possibly greater or fewer than 23 bifurcations from the trachea to a particular alveolus.

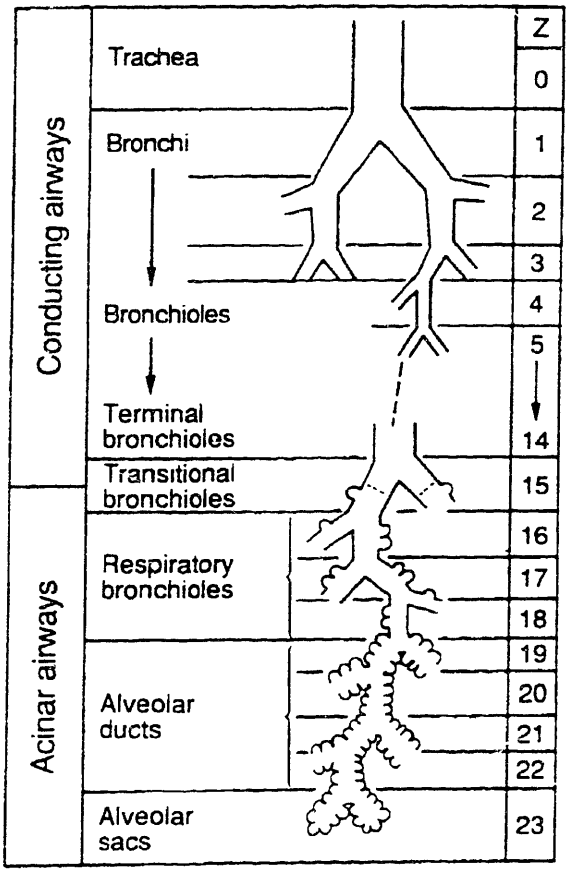

FIGURE 1-1: The symmetric typical path model of the tracheobronchial tree, showing the organization of airways in the human lung. Dichotomous branching occurs from one generation (Z) to the next. (from Weibel[47])

Figure 1-2 shows how the total cross-sectional area available for airflow (over all the airways of a particular generation) grows with generation number and length down the tree. Decreasing diameter of the airways with increasing generation number tends to increase resistance to airflow in a single airway, but the decreasing length of each generation tends to decrease resistance. The total resistance for a generation, then, is a balance of all these competing tendencies. The total resistance for a generation attains a maximum at generation 4 or 5, and becomes significantly smaller at higher generation numbers. The following table gives a brief overview of how the total resistance of a generation varies between normal and asthmatic airways. Note that the smaller the airway, the more of an effect asthma has on increasing the resistance.[50,51]

Z generation	R_{gen} (cm H_20 L^{-1} s^{-1})		PERCENT INCREASE
	NORMAL	ASTHMATIC	
0	1.10E–01	2.68E–01	144%
5	2.85E–01	2.51E+00	781%
10	6.33E–02	6.15E–01	872%
15	9.81E–03	1.36E–01	1286%

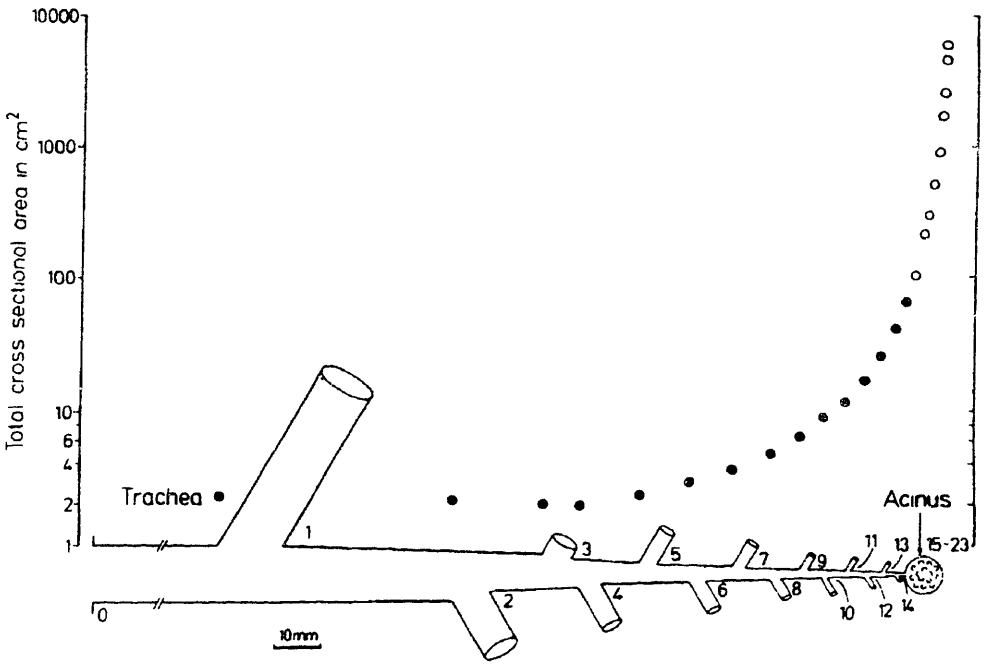

FIGURE 1-2: Symmetric typical path model drawn to scale along abscissa, with increase of total airway cross-sectional area shown on logarithmic ordinate. Filled circles represent conducting airways, and unfilled circles represent acinar airways. (from Weibel[47])

1.2.2 General Structure of an Airway

A sketch of the cross-section of a typical membranous airway is shown in Figure 1-3. Some of the components have been exaggerated in size for emphasis. The nomenclature used throughout this work is based on previously proposed standards,[2] but is mentioned here for completeness and clarity. In the center is the conducting airspace of the lumen. Bordering the lumen is the epithelial cell layer. Underneath the epithelium is a collagen

layer, to which this work will always refer as the "sub-epithelial collagen layer." Technically, the single thin layer of type IV collagen directly beneath the epithelium is the basement membrane, and the larger band of types III and V collagen (with a small amount of type I) is often called the lamina propria, although these definitions tend to vary from author to author. The two will be collectively known here as the sub-epithelial collagen layer to avoid this confusion. Sometimes the epithelium and sub-epithelial collagen layer are referred to collectively as the bronchial "mucosa."

Immediately external to the sub-epithelial collagen layer is a significantly thicker layer of loose connective tissue, mostly versican and other proteoglycans, often referred to as the "internal submucosa". External to this layer is the intermittent smooth muscle layer which actively contracts in an asthma attack. External to the smooth muscle is the adventitial submucosal layer and sparse collagenous parenchymal attachments between the airway and the surrounding alveoli.

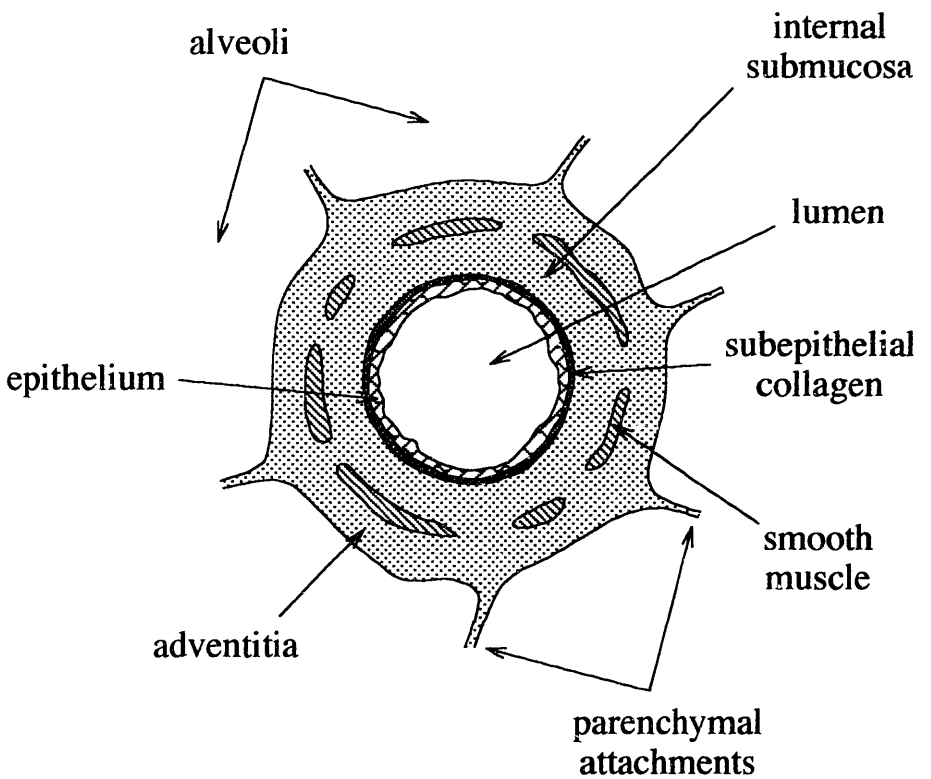

FIGURE 1-3: Sketch depicting key structures of a membranous (non-cartilaginous) bronchiole. Not to scale.

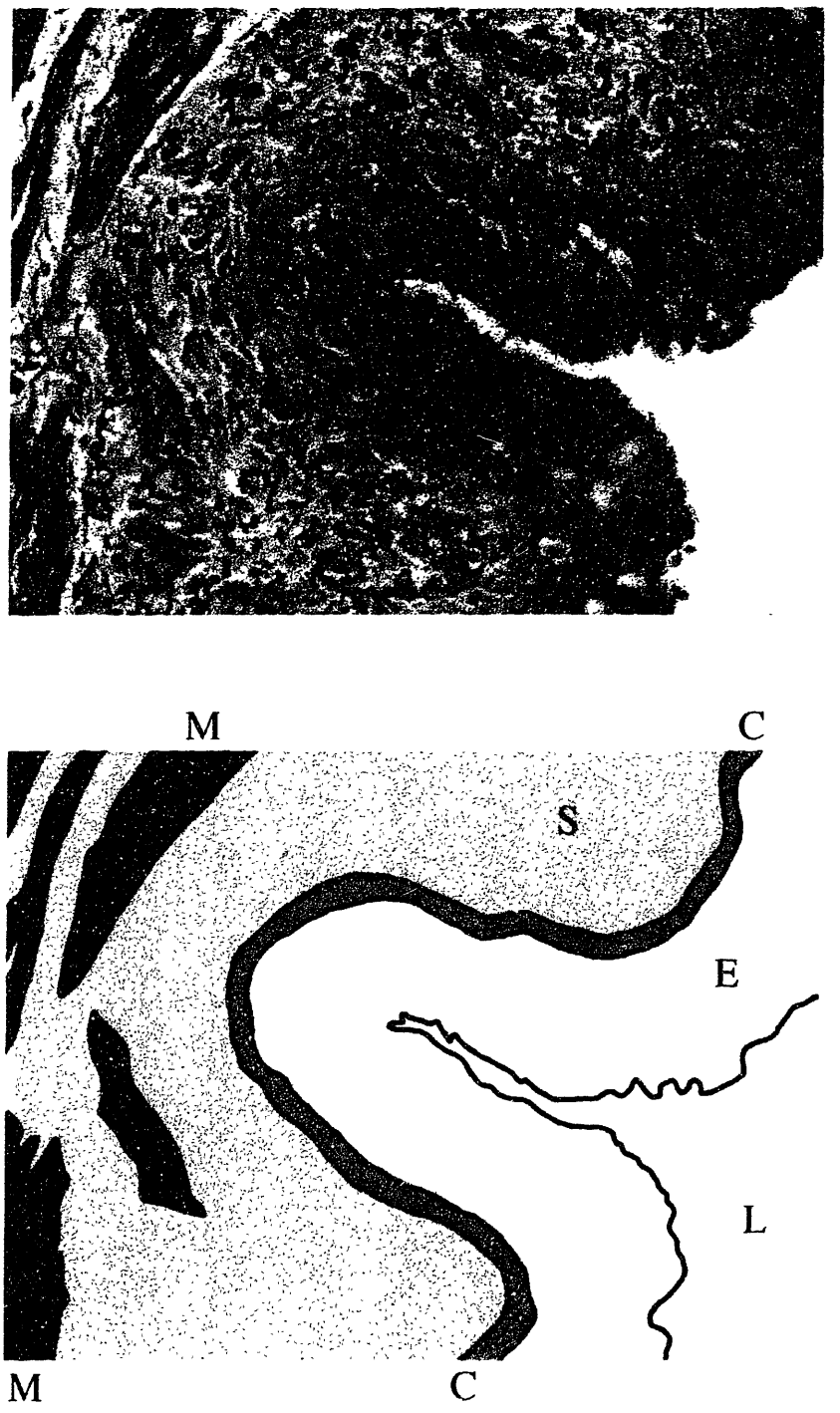

FIGURE 1-4: (top) Histology of a single fold of a constricted membranous bronchial airway. (from the University of British Columbia Pulmonary Research Laboratory) (bottom) Map indicating key components of the inner airway wall: lumen (L), epithelial cell layer (E), sub-epithelial collagen layer (C), internal submucosa (S), smooth muscle bundles (M). The thin "basement membrane" exists at the border between the sub-epithelial collagen layer and the epithelium.

Figure 1-4 shows a view of a single mucosal fold of a normal airway, from a slide prepared with a Gomori trichrome stain. This stain makes the sub-epithelial collagen layer show up as a bright blue band, making it easier to distinguish it from the submucosal layer, where collagen is present but not as dense. Also, the epithelial layer, submucosal layer and intermittent smooth muscle layer are easily identified in Figure 1-4.

1.2.3 Airway Hyperresponsiveness

Asthmatic bronchioles demonstrate "hyperresponsiveness." An airway is considered hyperresponsive when it constricts significantly more than a normal one would for a specified dose of smooth muscle agonist. Figure 1-5 is from paper by Wiggs et al.,[50] showing the difference in response to smooth muscle agonist between airways under normal ("control"), non-asthmatic COPD ("obstructed"), and asthmatic conditions. The abscissa is the concentration of a dose of agonist (for example acetylcholine or methacholine) which causes the airway smooth muscle to contract, constricting the airway. The ordinate is a measure of resistance to airflow through the airway, normalized by the

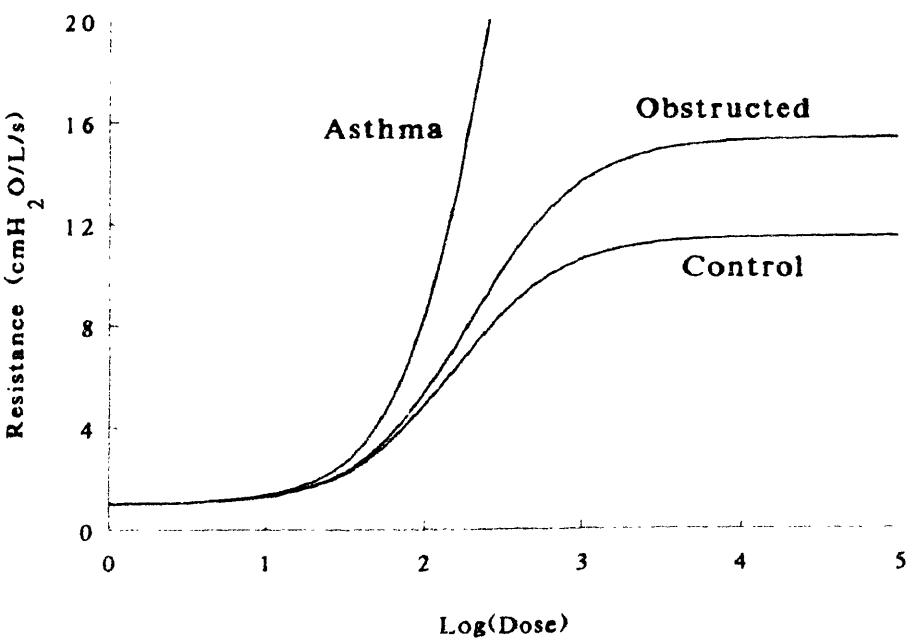

FIGURE 1-5: Theoretical dose response curves showing the marked increase in airflow resistance in asthma compared to normals and other chronic obstructive pulmonary diseases. (from Wiggs et al.[50])

amount of resistance that would be exhibited by an airway that is completely open (and has not collapsed at all).

The plot shows the simulated response for typical normal, COPD and asthmatic airways. The plateau in the response of normal and obstructed airways indicates some type of mechanism for resisting high levels of constriction. During the plateau, the airway's stiffness to occlusion increases dramatically, so much so that the smooth muscle reaches its load-generating capacity and is unable to collapse the airway beyond a certain point. Asthmatic airways do exhibit the same plateau in their response, but it is so markedly delayed to higher levels of constriction that it falls far off the axes of this plot. The smooth muscle is easily able to collapse such an asthmatic airway to very high airflow resistance levels under a comparable dose of agonist. Non-asthmatic COPD airways display a similar trend as asthmatic ones but to a far lesser degree.

1.2.4 Structural Differences Between Normal and Asthmatic Airways

The two cross-sections of human airways shown in Figure 1-6 are examples of typical normal (A) and asthmatic (B) bronchioles. Two more example airways are shown in Figure 1-7. They are not necessarily of exactly the same size, and are certainly not stained in the same way, but are presented here to show general trends in normal and asthmatic airway structure. In both cases the smooth muscle has contracted, and there is a resulting epithelial folding pattern. The change in airway structure from A to B in the course of chronic asthma is a type of "remodeling." Remodeling is the process of maintenance or turnover through which extracellular matrix is continually replaced.[58] Certain mechanisms of remodeling exhibit enhanced synthesis and reduced degradation of matrix materials, resulting in larger and/or stiffer tissues. Others are oppositely more catabolic, resulting in smaller and/or more compliant tissues. Asthmatic airway wall remodeling is an example of the former.

Following are some of the notable structural-mechanical differences between normal and asthmatic airways, not all of which can be discerned from Figures 1-6 and 1-7:

- All layers of the asthmatic airway are thickened: the epithelial cell layer, the sub-epithelial collagen layer, the proteoglycan submucosal layer, the smooth muscle layer, etc.[13,20,22,23,27,31] The sub-epithelial collagen layer is about twice its normal thickness.[4,7,44] It is pretty well established at this point that the increased sub-epithelial

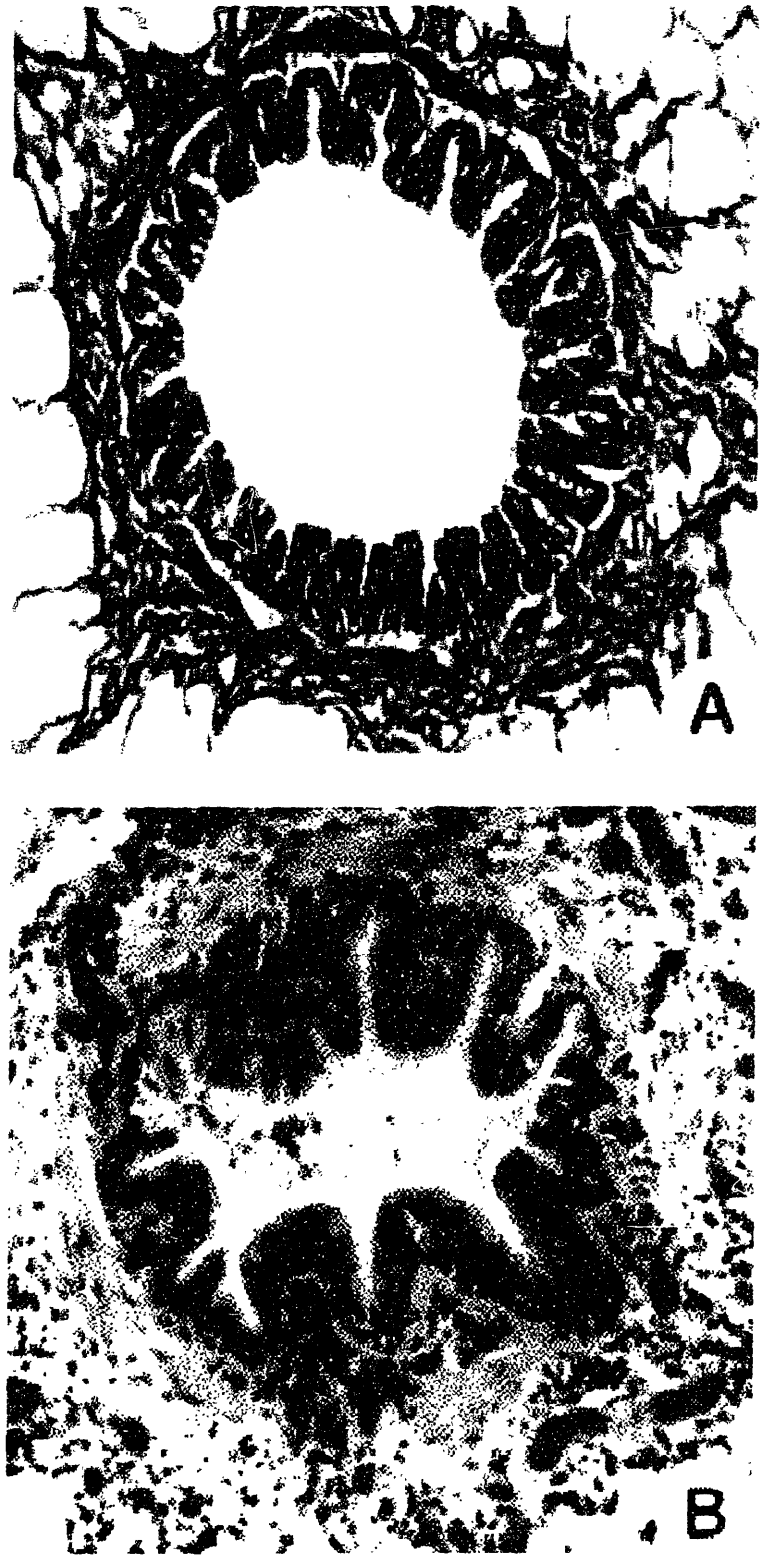

FIGURE 1-6: Two cross-sections of airways from normal (A) and asthmatic (B) human subjects. (from the University of British Columbia Pulmonary Research Laboratory)

collagen is deposited by fibroblasts as opposed to epithelial cells,[7] although current studies from our research group (Ressler and Kamm) are investigating the biochemical messages that epithelial cells are sending out under the stress that results from excessive bronchoconstriction. Preliminary results suggest that indeed epithelial cells do send out biochemical messages that would enhance synthesis. While the growth of the submucosal tissues requires ample time to reach its full extent, the growth of the sub-epithelial collagen has been known to occur within two weeks of asthmatic symptoms, and this thickening appears irreversible.[26]

- One might suspect that in asthma the smooth muscle layer, because it has thickened due to cell hyperplasia,[18] can generate greater stress. Bramley et al. have measured maximum stress capacities in asthmatic smooth muscle to be about 3 times as large as in normal smooth muscle.[6] Other researchers, however, have indicated that there is no evidence to suggest greater smooth muscle stress capacity in asthma.

- The lumen is far more occluded upon smooth muscle contraction in the asthmatic airway, not only from further constriction of the airway itself, but by interstitial fluid which had been squeezed out of the various airway layers, into the lumen.[8,19,56,57]

- Though there has been no systematic study which has demonstrated it, there is some anecdotal evidence to suggest that the number of mucosal folds upon smooth muscle contraction is fewer in an asthmatic airway than in a normal one of comparable size (and location down the tracheobronchial tree). There has long existed evidence that the folds are deeper in asthmatic airways.[22] It is in these large folds where fluid which has been squeezed out of the airway wall collects. Airways that collapse with fewer folds also tend to have an irregularly shaped lumen which appears to have collapsed greatly, while normal airways in general have more folds and a more circular, less obstructed lumen, as seen in Figures 1-6 and 1-7.

- Blood vessels which line the airway and run parallel to it through the submucosa tend to be fully open if they are located between two mucosal folds, but are shut closed if they are located at the tip of a fold.[46]

- Asthmatic airways contain a much larger number of inflammatory cells, particularly throughout the submucosa, including TH2 lymphocytes, eosinophils and mast cells.[12]

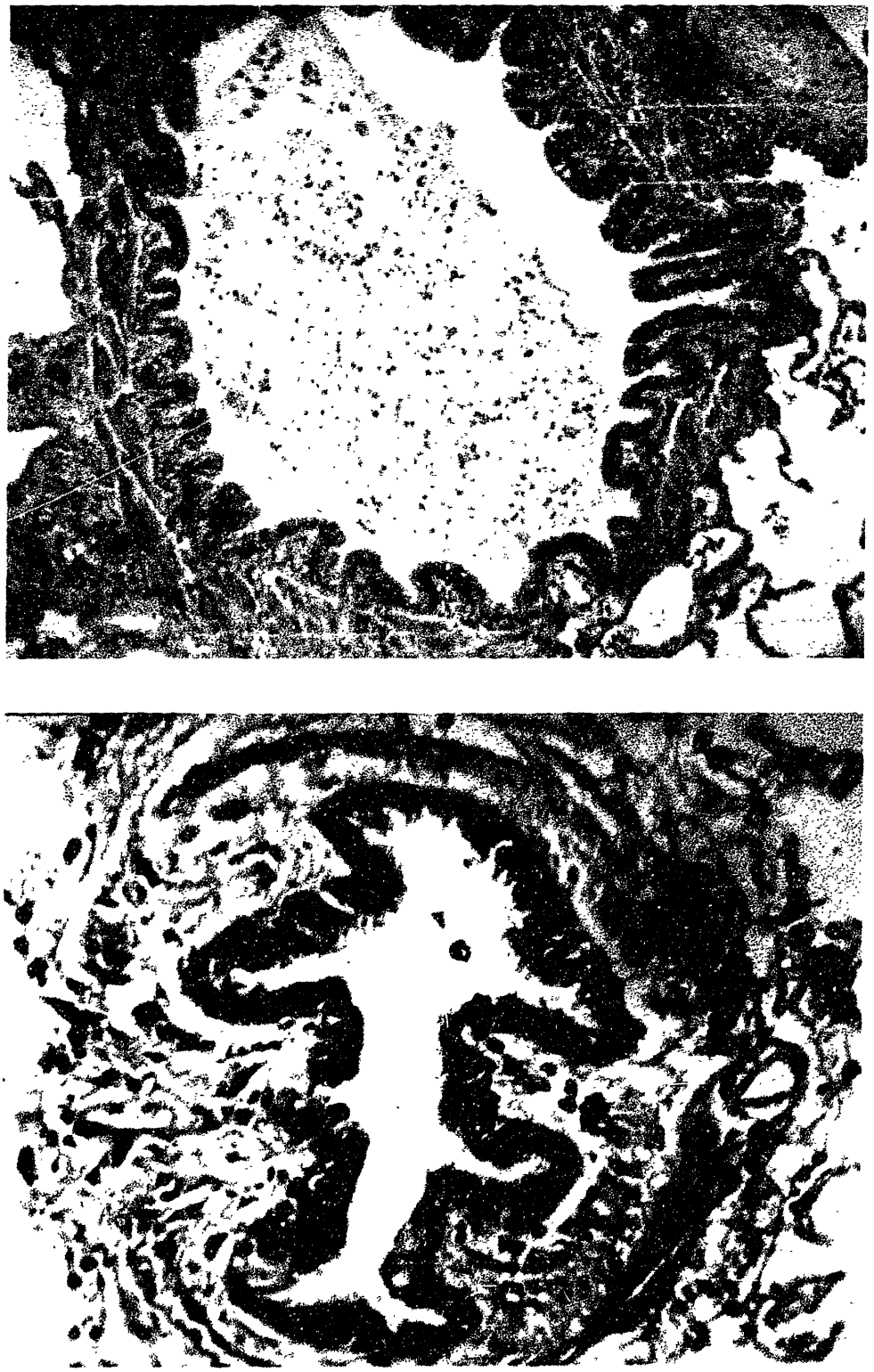

FIGURE 1-7: Another two cross-sections of airways from relatively normal (top) and highly asthmatic (bottom) human subjects. (from the University of British Columbia Pulmonary Research Laboratory)

- Epithelial desquamation is often observed in asthmatic airways. Those epithelial cells that have not been sloughed off are usually thicker and inflamed.[33]

All these changes occur in patches throughout the lungs in mild asthma, becoming more widespread in severe asthma.[12]

1.3 Previous Work

One feature that makes this work distinctive in the multitude of studies which attempt to elucidate airway wall mechanics is the special attention to the sub-epithelial collagen layer: how it folds and what possible ramifications its folding pattern has for an airway's load-resisting capacity. Most previous studies have considered only axisymmetric deformations of airway components, thus neglecting mucosal folding.[3,6,24,32,34,39,50,51] Such models would not consider buckling, and thus would grossly overestimate the stiffness of the airway to occlusion, perhaps dismissing the importance of the mode of collapse altogether.

Some recent studies, mostly by Lambert et al. focus on the sub-epithelial collagen layer and demonstrate its significance with regard to resistance to smooth muscle shortening and to intraluminal liquid-filling of the mucosal folds.[19,35,36] Our work is similar in that we also attempt to further understand mucosal folding, but our approach (which primarily uses finite element methods) is designed to better capture the interaction between the various layers internal to the constricting smooth muscle.

The simplest model which demonstrates this interaction is the planar sandwich panel, frequently used in structural design.[1] While incorporating circular geometries, earlier theoretical work by Lambert et al. obtains results based mostly on geometrical arguments, thus neglecting the full effect of material laws and force balance between the various airway layers.[35,36] Lambert's models are indeed bi-layered, but the outer (submucosal) layer is assumed to be a fluid, and thus to have a negligible shear modulus. Our criticism of these models is that such a solid-on-fluid configuration should most likely only buckle in a peanut-shaped two-lobe collapse, as the solid is a single-layered ring responding to a uniform pressure with no shear. Higher frequency modes of collapse require significantly greater strain energy and thus are highly unlikely to be observed under simple pressure.

Our work is in effect somewhat of a hybrid between planar sandwich panels and Lambert's bi-layered circular models, obtaining results through numerical methods with some analytical basis and experimental verification. The results that our models produce are significantly different from these previous modeling attempts.

1.4 Hypotheses

The implications of various hypothetical kinds of airway wall remodeling can be examined by varying the parameters of our two-layer model.

Firstly, one might hypothesize that growth of the proteoglycan-rich submucosal layer primarily stiffens the airway against luminal compromise. This thicker outer layer of loose connective tissue is likely to be the dominant source of resistance to smooth muscle contraction (because it is so much thicker than the mucosal components). Without the presence of some type of confining stiffer inner layer, there would be only one possible mode of airway deformation upon smooth muscle constriction, a simple axisymmetrc contraction, which (if the assumptions of incompressibility and plane-strain are valid) would preserve the cross-sectional area of the airway wall tissue. At a given airway size (specified by its inner diameter when relaxed[25]), having more outer layer tissue implies that more tissue has to be deformed to achieve the same amount of luminal compromise, resulting in greater resistance to deformation, and consequently, a stiffer airway. If this hypothesis is true, submucosal thickening cannot be the *only* mechanism of importance in asthmatic airway wall remodeling.

Another major hypothesis that we wish to justify is the idea that any type of thickening or stiffening of the thin mucosal layer is detrimental to the stiffness of the airway at large deformations, thus predisposing the lumen to greater compromise upon maximal smooth muscle constriction. At first glance, this hypothesis may seem counter-intuitive and contrary to some previous reports. To quote Roberts, "Thickening of the collagen-rich matrix beneath the basal lamina would be expected to increase both the tensile stiffness and resistance to deformation of the airway wall, thus tending to oppose the effect of smooth muscle shortening on airway narrowing."[43]

The argument is not really counter-intuitive after some examination of the mechanics governing the structure. It is inspired by thinking of the inner mucosal layer as a beam (on

an elastic foundation, the submucosa). Thickening or stiffening of the inner layer increases its intrinsic "beam stiffness" (EI, elastic modulus times moment of inertia). The inner layer's beam stiffness increases linearly with its elastic modulus, but with the cube of its thickness. Greater beam stiffness implies greater resistance to bending, but less curvature and larger wavelengths in the bending deformation. For a given airway size (same internal diameter & perimeter), this means fewer folds. We hypothesize that buckling in fewer folds requires a marginally larger buckling pressure, but once this pressure is met, collapse of the lumen can be more catastrophic than if the mucosa buckled into a greater number of smaller folds.

Furthermore, buckling in fewer folds implies that there is more constriction possible before the folds bend so much that they touch and eventually close up on themselves, providing more confinement of the surrounding submucosal tissue and markedly increasing the airway's stiffness. As a result, an airway with an increased mucosal layer thickness (or stiffness) under the same pressure generated by the surrounding smooth muscle would exhibit more luminal compromise in its postbuckling response than one with a normal mucosal layer.

Figure 1-8 depicts the contraction of two hypothetical two-layer tubes (or airways), abbreviated to show only a mechanically stiffer mucosal layer and a thicker, more compliant proteoglycan layer (representing the internal submucosa). The smooth muscle and adventitia are not shown but are assumed to move in a simple axisymmetric, radially inward deformation as the smooth muscle contracts. Suppose that the intrinsic stiffness of the material that the mucosal layers are made of is the same. The only way in which these two hypothetical airways differ is that airway B has a thicker mucosal layer than airway A. Because the mucosal layer is thin but relatively stiff, at larger deformations it becomes energy-efficient to bend (or buckle) non-axisymmetrically instead of compressing circumferentially.

It has been suggested that the number of folds remains roughly constant throughout the constriction of *in vivo* airways. Therefore, assume for now that after buckling each of our hypothetical airways continues to contract with the same number of folds until the sides of their folds are flat against one another. At this point, the mucosal layer cannot fold much more so the airway becomes stiffer to continued luminal occlusion. A different type of buckling mechanism is necessary to compress the airway further (perhaps buckling of the

outer proteoglycan layer), and that event will probably not occur because the load necessary would be greater than the smooth muscle's capacity.

The sketched plots to the right in Figure 1-8 give an idea of the load-displacement behavior of these hypothetical airways. The amount of lumen area available for airflow is plotted against the constricting smooth muscle pressure. P_{max} is the maximum amount of pressure that the smooth muscle can provide, assumed for now to be the same for asthmatic as for normal airways. The prebuckling behavior of the two airways is such that the airway with the thickened mucosa is slightly stiffer to airway obstruction. However, *when buckling does occur, the consequence of buckling with fewer folds is a more catastrophic collapse, resulting in less luminal area under maximal shortening of the smooth muscle,* even if that maximum were not to increase despite muscle hyperplasia.

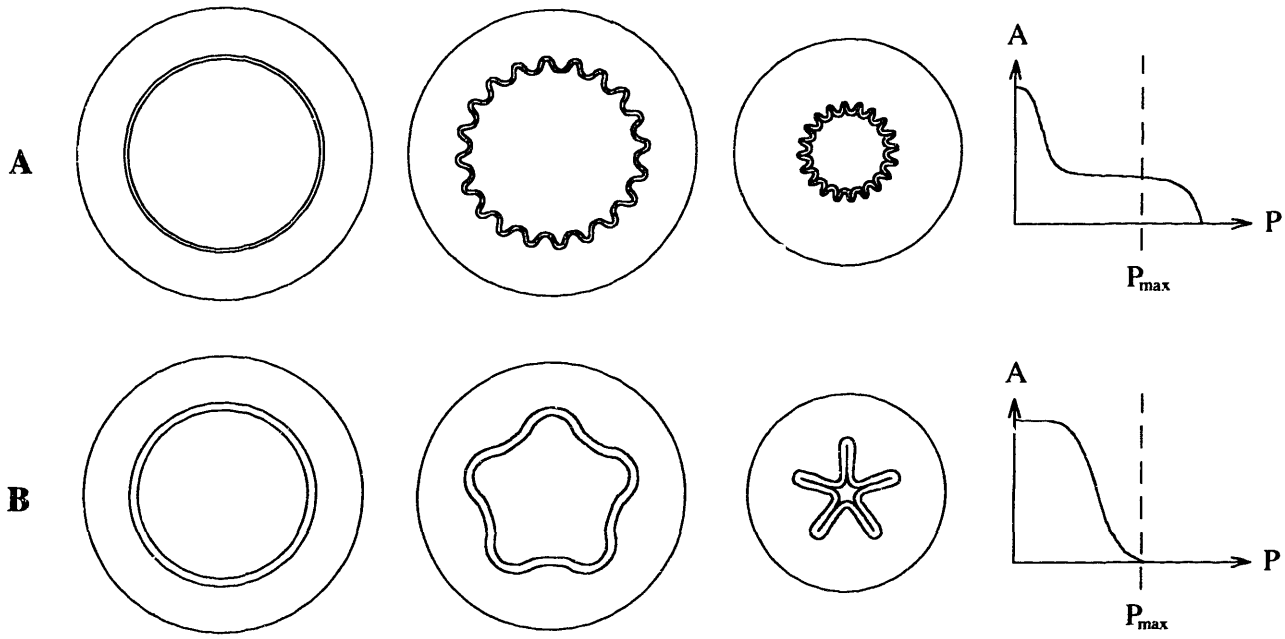

FIGURE 1-8: The major hypothesis of this work: having a relatively thin and/or compliant inner layer leads to buckling with relatively many folds (A), while having a thick and/or stiff inner layer causes buckling in relatively few folds (B). By the time the folds press up against one another, resisting further collapse, more cross-sectional lumen area is lost (in case B relative to A). The plots to the right show lumen area as a function of smooth muscle pressure applied throughout the contraction. P_{max} indicates a hypothetical maximal smooth muscle pressure.

Further hypotheses can be cast addressing why the asthmatic airway would remodel the way it does using mechanical arguments. In case A of Figure 1-8, the mucosal layer undergoes much deformation while most of the submucosal layer undergoes a simple compression. Most of the strain energy of deformation is put into the mucosal layer and the nearby portion of the surrounding submucosal layer. This suggests that under repeated airway contraction (due to an increasingly chronic asthmatic condition), cells in these regions (such as epithelial cells or fibroblasts in the nearby submucosa) might mediate the construction of more collagenous tissue to reduce stress levels locally. In case B, the increased thickness of the sub-epithelial collagen layer reduces stress on the epithelium and nearby cells by bending with less curvature, and more of the strain energy is devoted to larger deformations in the submucosa.

The purpose of the models to be presented in this work is not only to give credence to these hypotheses, but to attempt to quantify the effects of the possible structural changes considered. Though the second hypothesis offers an explanation for how the increased structure of an asthmatic airway may result in greater luminal compromise upon maximal smooth muscle activation, it is not necessarily the only mechanism which could cause such an effect.

1.5 Other Applications

There are several other biologic vessels of similar geometry and structure that also constrict, causing folds to appear at their luminal surfaces.

For instance, Lee and Chien have observed longitudinal ridges in the vascular endothelium and underlying internal elastic lamina of the canine carotid artery at reduced arterial pressures.[37] Razakamiadana et al. have studied the buckling instability of coronary microvessels, modeling them as thin extensible tubes embedded in a multi-phasic elastic medium. Their purpose was to study the reduction of coronary blood flow during cardiac contraction.[42] It has also been suggested that fibrosis of the vascular basement membrane may be associated with diabetic ischemia.[30,52,53]

Collagenous colitis, often characterized by inadequate absorption in the colon, involves thickening of the sub-epithelial collagen layer of the colon.[15,16,28,41] Lewis et al. observed some shortening and broadening of the villi accompanying the enhanced collagen

deposition.[38] Similar conditions of sub-epithelial fibrosis are known to exist in neighboring digestive organs such as the small intestine (collagenous sprue)[48] and the stomach (collagenous gastritis).[10] The walls of the esophagus and urethra also contain collagenous basement membranes which are known to fold and be prone to fibrosis.[11,29]

Because many biologic vessels share similar anatomical structure to airways, and because they exhibit various medical conditions associated with thickening and stiffening of the various vessel layers, the results of the simple models described here may have broader implications for many kinds of vessels and their corresponding pathologies.

CHAPTER 1 REFERENCES

1. Allen HG. *Analysis and Design of Structural Sandwich Panels.* Pergamon Press, London, 1969. pp. 156-163.

2. Bai A, Eidelman DH, Hogg JC, James AL, Lambert RK, Ludwig MS, Martin J, McDonald DM, Mitzner WA, Okazawa M, Pack RJ, Paré PD, Schellenberg RR, Tiddens HAWM, Wagner EM, Yager D. Proposed nomenclature for quantifying subdivisions of the bronchial wall. *J. Appl. Physiol.* 77(2): 1011-1014, 1994.

3. Bates JHT, Martin JG. A theoretical study of the effect of airway smooth muscle orientation on bronchoconstriction. *J. Appl. Physiol.* 69(3): 995-1001, 1990.

4. Boulet L-P, Laviolette M, Turcotte H, Cartier A, Dugas M, Malo J-L, Boutet M. Bronchial subepithelial fibrosis correlates with airway responsiveness to methacholine. *Chest.* 112(1): 45-52, 1997.

5. Bousquet J, Chanez P, Lacoste JY, White R, Vic P, Godard P, Michel FB. Asthma: a disease remodeling the airways. *Allergy.* 47: 3-11, 1992.

6. Bramley AM, Thomson RJ, Roberts CR, Schellenberg RR. Hypothesis: excessive bronchoconstriction in asthma is due to decreased airway elastance. *Eur. Respir. J.* 7: 337-341, 1994.

7. Brewster CEP, Howarth PH, Ratko D, Wilson J, Holgate ST, Roche WR. Myofibroblasts and subepithelial fibrosis in bronchial asthma. *Am. J. Respir. Cell Mol. Biol.* 3: 507-511, 1990.

8. Brown RH, Zerhouni EA, Mitzner W. Airway edema potentiates airway reactivity. *J. Appl. Physiol.* 79(4): 1242-1248, 1995.

9. Brown RE, Butler JP, Rogers RA, Leith DE. Mechanical connections between elastin and collagen. *Connective Tissue Research.* 30: 295-308, 1994.

10. Colletti RB, Trainer TD. Collagenous gastritis. *Gastroenterology.* 97(6): 1552-1555, 1989.

11. De Carvalho HF, Line SRP. Basement membrane associated changes in the rat ventral prostate following castration. *Biology International.* 20(12): 809-819, 1996.

12. Drazen JM. Asthma, in *Textbook of Medicine.* ed. Cecil. ch. 51.

13. Dunnill MS. The pathology of asthma, with special reference to changes in the bronchial mucosa. *J. Clin. Path.* 13: 27-33, 1960.

14. Ebina M, Yaegashi H, Takahashi T, Motomiya M, Tanemura M. Distribution of smooth muscles along the bronchial tree. *Am. Rev. Resp. Dis.* 141: 1322-1326, 1990.

15. Eckstein RP, Dowsett JF, Riley JW. Collagenous enterocolitis: a case of collagenous colitis with involvement of the small intestine. *The American Journal of Gastroenterology* . 83(7): 767-771, 1988.

16. Giardiello FM, Bayless TM, Jessurun J, Hamilton SR, Yardley JH. Collagenous colitis: physiologic and histopathologic studies in seven patients. *Ann. Intern. Med.* 106: 46-49, 1987.

17. Guyton AC. *Textbook of Medical Physiology,* 8th Ed. W.B. Saunders Co., Philadelphia, 1991. ch. 42.

18. Heard BE, Hossain S. Hyperplasia of bronchial muscle in asthma. *J. Pathol.* 110: 319-331, 1973.

19. Hill MJ, Wilson TA, Lambert RK. Effects of surface tension and intraluminal fluid on mechanics of small airways. *J. Appl. Physiol.* 82(1): 233-239, 1997.

20. Hogg JC. Bronchiolitis in asthma and chronic obstructive pulmonary disease. *Clinics in Chest Medicine.* 14(4): 733-740, 1993.

21. Hogg JC, Macklem PT, Thurlbeck WM. Site and nature of airway obstruction in chronic obstructive disease. *N. Engl. J. Med.* 278: 1355-1360, 1968.

22. Huber HL, Koessler KK. The pathology of bronchial asthma. *Arch. Int. Med.* 30(6): 689-760, 1922.

23. James AL. Relationship between airway wall thickness and airway hyperresponsiveness, in *Airway Wall Remodelling in Asthma.* ed. Stewart AG. CRC Press, Boca Raton, 1997. ch. 1.

24. James AL, Paré PD, Hogg JC. The mechanics of airway narrowing in asthma. *Am. Rev. Respir. Dis.* 139: 242-246, 1989.

25. James AL, Hogg JC, Dunn L, Paré PD. The use of internal perimeter to compare airway size and to calculate smooth muscle shortening. *Amer. Rev. Resp. Dis.* 138: 136-139, 1988.

26. Jeffrey PK, Godfrey RW, Ädelroth E, Nelson F, Rogers A, Johanson S-A. Effects of treatment on airway inflammation and thickening of basement membrane reticular collagen in asthma. *Am. Rev. Respir. Dis.* 145: 890-899, 1992.

27. Jeffery PK. Morphology of the airway wall in asthma and in chronic obstructive pulmonary disease. *Am. Rev. Respir. Dis.* 143: 1152-1158, 1991.

28. Jessurun J, Yardley JH, Gardiello FM, Hamilton SR, Bayless TM. Chronic colitis with thickening of the subepithelial collagen layer (collagenous colitis): histopathologc findings in 15 patients. *Human Pathology.* 18(8): 839-848, 1987.

29. Kalkay NM, Cordoba I, Plevy D. The nonreflux determinant of esophagitis. *The American Journal of Gastroenterology* . 63(2): 135-146, 1975.

30. Katz MA, McCuskey P, Beggs JL, Johnson PC, Gaines JA. Relationships between microvascular function and capillary structure in diabetic and nondiabetic human skin. *Diabetes.* 38(10): 1245-1250, 1989.

31. Kuwano K, Bosken CH, Paré PD, Bai TR, Wiggs BR, Hogg JC. Small airways dimensions in asthma and in chronic obstructive pulmonary disease. *Am. Rev. Respir. Dis.* 148(5): 1220-1225, 1993.

32. Lai-Fook SJ, Hyatt RE, Rodarte JR, Wilson TA. Behavior of artificially produced holes in lung parenchyma. *J. Appl. Physiol.* 43(4): 648-655, 1977.

33. Laitinen LA, Laitinen A. Modulation of bronchial inflammation: corticosteroids and other theraputic agents. *Am. Rev. Respir. Crit. Care. Med.* 150: S87-S90, 1994.

34. Lambert RK, Wiggs BR, Kuwano K, Hogg JC, Paré PD. Functional significance of increased airway smooth muscle in asthma and COPD. *J. Appl. Physiol.* 74(6): 2771-2781, 1993.

35. Lambert RK, Codd SL, Alley MR, Pack RJ. Physical determinants of bronchial mucosal folding. *J. Appl. Physiol.* 77(3): 1206-1216, 1994.

36. Lambert RK. Role of bronchial basement membrane in airway collapse. *J. Appl. Physiol.* 71(2): 666-673, 1991.

37. Lee MML, Chien S. Morphologic effects of pressure changes on canine carotid artery endothelium as observed by scanning electron microscopy. *The Anatomical Record.* 194(1): 1-14, 1979.

38. Lewis FW, Warren GH, Goff JS. Collagenous colitis with involvement of terminal ileum. *Dig. Dis. Sci.* 36(8): 1161-1163, 1991.

39. Moreno RH, Hogg JC, Paré PD. Mechanics of airway narrowing. *Am. Rev. Respir. Dis.* 133: 1171-1180, 1986.

40. Okazawa M, Paré PD, Hogg JC, Lambert RK. Mechanical consequences of remodelling of the airway wall, in *Airways and Vascular Remodelling.* eds. Page C, Black J. Academic Press, Toronto, 1994. ch. 8.

41. Rams H, Rogers AI, Ghandur-Mnaymneh L. Collagenous colitis. *Ann. Intern. Med.* 106: 108-113, 1987.

42. Razakamiadana A, Oddou C, Zidi M, Geiger D. Buckling instability of thin tube stressed by surrounding medium: application to coronary microvessels. Second World Congress of Biomechanics, Amsterdam, The Netherlands. July 10-15, 1994.

43. Roberts CR. Is asthma a fibrotic disease? *Chest.* 107(3): 111S-117S, 1995.

44. Roche WR, Beasley R, Williams JH, Holgate ST. Subepithelial fibrosis in the bronchi of asthmatics. *Lancet.* 1: 520-524, 1989.

45. Vincent NJ, Knudsen R, Leith DE, Macklem PT, Mead J. Factors influencing pulmonary resistance. *J. Appl. Physiol.* 29: 236-243, 1970.

46. Wagner EM, Mitzner W. Bronchial vascular engorgement and airway narrowing. *Amer. Rev. Resp. Dis.* 149(4): A585, 1994.

47. Weibel E. Design of airways and blood vessels considered as branching trees, in *The Lung: Scientific Foundations.* ed. Crystal R, et al. Vol. 1, pp. 711-720.

48. Weinstein WM, Saunders DR, Tytgat GN, Rubin CE. Collagenous sprue - an unrecognized type of malabsorption. *N. Engl. J. Med.* 283: 1297-1301, 1970.

49. Wiggs BR, Moreno R, James A, Hogg JC, Paré PD. A model of the mechanics of airway narrowing in asthma, in *Asthma: Its Pathology and Treatment.* eds. Kaliner MA, Barnes PJ, Persson CGA. Marcel Dekker, New York, 1991. ch. 3.

50. Wiggs BR, Bosken C, Paré PD, James A, Hogg JC. A model of airway narrowing in asthma and in chronic obstructive pulmonary disease. *Am. Rev. Respir. Dis.* 145: 1251-1258, 1992.

51. Wiggs BR, Moreno R, Hogg JC, Hilliam C, Paré PD. A model of the mechanics of airway narrowing. *J. Appl. Physiol.* 69(3): 849-860, 1990.

52. Williamson JR, Vogler NJ, Kilo C. Estimation of vascular basement membrane thickness: theoretical and practical considerations. *Diabetes.* 18: 567-578, 1969.

53. Williamson JR, Kilo C. Current studies of capillary basement-membrane disease in diabetes mellitus. *Diabetes.* 26: 65-73, 1977.

54. Wilson JW, Li X, Pain MCF. The lack of distensibility of asthmatic airways. *Am. Rev. Respir. Dis.* 148: 806-809, 1993.

55. Yager D, Cloutier T, Feldman H, Bastacky J, Drazen JM, Kamm RD. Airway surface liquid thickness as a function of lung volume in small airways of the guinea pig. *J. Appl. Physiol.* 77(5): 2333-2340, 1994.

56. Yager D, Kamm RD, Drazen JM. Airway wall liquid. *Chest.* 107(3): 105S-110S, 1995.

57. Yager D, Butler JP, Bastacky J, Israel E, Smith G, Drazen JM. Amplification of airway constriction due to liquid filling of airway intersticies. *J. Appl. Physiol.* 66(6): 2873-2884, 1989.

58. Yannas IV, Spector M. Lecture notes for M.I.T. course 2.785: Mechanical Forces in Organ Development and Remodeling. Spring 1993.

2. Development of the Two-Layer Model

2.1 Model Components

The simple two-layer structure of the models employed in these studies is based on the geometry of the passive vessel structure internal to the smooth muscle (Figure 2-1). The outer layer represents the loose connective tissue of the submucosa, mostly proteoglycans; the inner layer represents the mucosa, whose primary structural component is the sub-epithelial layer of relatively well-ordered collagen.[18] Thus while the outer layer may be an order of magnitude thicker than the inner layer, the inner layer is assumed to have at least an order of magnitude more material stiffness than the outer layer.

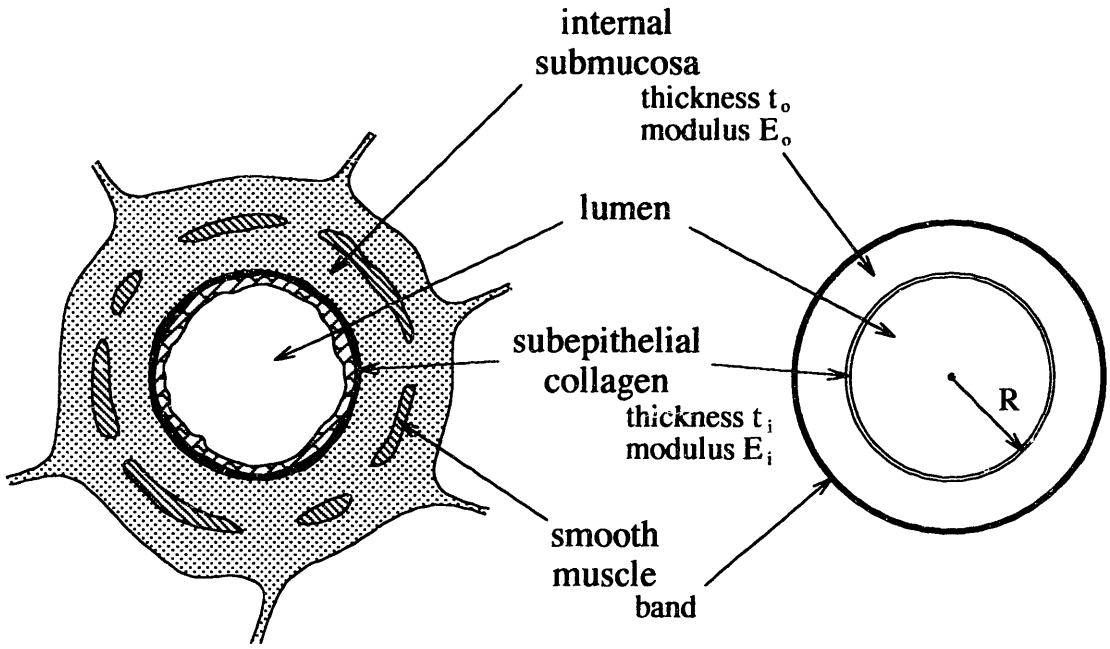

FIGURE 2-1: Sketch of a membranous bronchiole and the two-layer tube idealization, showing correspondence between airway components and tube layers.

For simplicity, only these two layers are included, thus the epithelial cell layer is considered a part of the stiffer inner layer. The epithelium in particular, while comparable in thickness to the collagen layer beneath it, is perhaps an order of magnitude less stiff than the submucosal layer, making it at least two orders of magnitude less stiff than the collagen

layer.[11] Therefore it is not included separately in the model because it cannot provide any significant resistance to collapse nor significantly affect the deformation behavior of the collapse. Similarly, airway fluids and gels which reside on and around the epithelium have a negligible elastic modulus and are therefore not included.

It is assumed that the smooth muscle layer and any other layers external to it move in a simple axisymmetric deformation, and therefore those layers do not need to be modeled in detail with continuum elements. The total effect of such external components is to impose a particular boundary condition on the internal submucosa (described in detail in the next section).

2.2 Mechanical Modeling Assumptions

2.2.1 Two-Dimensional Plane-Strain

All of the mechanical models presented here assume two-dimensional plane-strain deformation. When excised, split axially and examined from the side, constricted airways exhibit long ridges that run axially down the wall (Figure 2-2). In cross-section, these ridges are the mucosal folds. The number of these folds does not seem to vary with axial distance along an airway, assuming that the length of airway observed is far enough away from bifurcations between airway generations where in general, the overall airway dimensions change.

The smooth muscle in the airway wall is not a continuous band the way our simple model would suggest, but is intermittent around the cross-section of the airway. In fact, it is more like a randomly weaving mesh. It is assumed that the effect of the random wrapping is as if the muscle is continuous. Further examination of the airway cross-sections of Figures 1-6 and 1-7 reveals no appreciable difference in the deformation field in zones where the smooth muscle is present from where it is absent. This is because it is probable that a small distance axially up the airway there is muscle present where there wasn't previously, thus its effects tend to be averaged-out in the axial direction. Since there appears to be little variation with axial distance far enough away from bifurcations, our computations assume two-dimensional loading and deformation for simplicity and ease of computation.

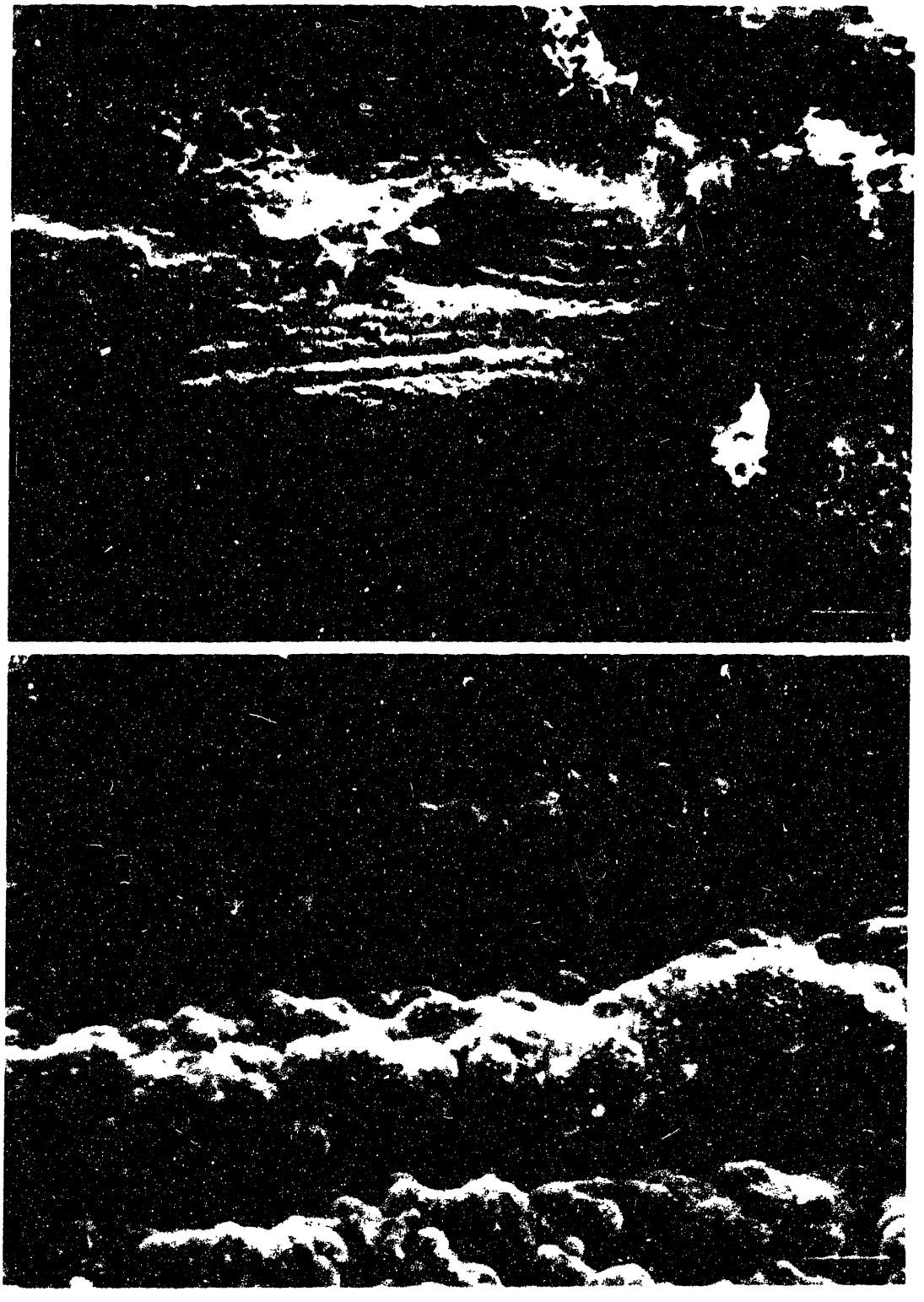

FIGURE 2-2: Micrograph showing ridges (folds) running axially up and down the airways.

Given that there is two-dimensional deformation, an assumption must be made regarding the displacements in the third (axial) direction. The two extremes possible are so-called "plane-stress" and "plane-strain," implying that all non-zero stresses or strains lie in a plane (which is to say that in plane-stress, there is no force in the axial direction and in plane-strain, there is no deformation in the axial direction). Of these two choices, plane-strain is more applicable to modeling airways because it is unlikely that they actually shorten or elongate axially during constriction. In such a case there would be motion of bifurcations toward and away from one another. The smooth muscle wraps around the airway at approximately a 13° angle to the plane of an airway cross-section (a relatively shallow angle), further supporting the idea that smooth muscle shortening should not produce any appreciable length change along the axis of the airway.[18] Bates et al. have shown that smooth muscle at angles of less than 30° has little effect on airway length during their constriction.[4] Simplification to two-dimensional plane-strain, poses certain computational difficulties when incompressible (or nearly incompressible) material laws are used. How such difficulties are circumvented is described in the next section.

2.2.2 Homogeneous Isotropic Layers

It is assumed that each of the two layers is a homogeneous isotropic continuum. The only difference between the two layers is the assigned elastic modulus (or roughly speaking, the intrinsic material "stiffness").

At a relatively macroscopic level, homogeneity of material properties in each layer is a good assumption. However, at sufficiently small scales it becomes apparent that there are collagen and elastin bundles which would correspond to regions of slightly higher or lower E in the submucosa. The sizes of these bundles are very small compared to the gross thickness of the submucosa, and so it is assumed that their effects average out to produce a roughly constant value of E over the layer. The boundary between the two layers is not nearly as clear in an actual airway as it is in our two-layer model. However, in human airways there is a jump in collagen content within a small thickness under the epithelium, and the location of that jump is taken to be the interface between the two discrete layers, as reported by various morphometric studies.

Another simplification is the assumption of isotropy (or rotational invariance of material properties). The submucosa, being a random array of loose connected tissue, is probably

best modeled as isotropic. The sub-epithelial collagen layer, however, does have significantly more order to it. The collagen fibers appear to align themselves at approximately 45° to the airway axis forming a loose helix.[18] The 45° angle orientation suggests that there is an equal tendency to be stretched longitudinally along the airway axis as well as to be expanded or contracted circumferentially. Perhaps this is the normal state of loading associated with lung expansion and contraction due to breathing.

Though some attempts to model the inner layer as anisotropic were attempted, mixed success with them has prohibited further research in that direction at present. Any material with more than a 2-to-1 parallel-to-perpendicular ratio of stiffnesses proved to be unstable under compression. All models discussed henceforth have homogeneous isotropic material properties within their respective layers.

2.2.3 Incompressible Hookean and Neohookean Materials

In creating structural models of biological tissues, knowing the appropriate constitutive law is probably the most elusive issue. This is because the microstructure of tissues is not nearly so simple as that of more traditional engineering materials such as steel or even concrete. This is further complicated by the fact that tissues are generally hydrated and can have varying properties depending on the degree of hydration and the degree of permeability, both of which may be affected by variations in the biochemical environment of the tissue. While it is more probable that the tissues modeled here demonstrate a nonlinear relationship between the strain they exhibit and the stress they develop, in the absence of proof to the contrary, they will be assumed linear. If not linear, are the materials strain-stiffening or strain-softening, and to what degree? Strain-stiffening and strain-softening material behaviors are contrasted pictorially with linear behavior in Figure 2-3. Under different conditions, tissues may exhibit either kind of nonlinear behavior. Some preliminary experiments on airway submucosa have yielded relatively linear results (see Section 6.2).

Even with the assumption of a linear material law, knowing the various moduli of these materials precisely is difficult. One could go to great lengths to develop sophisticated

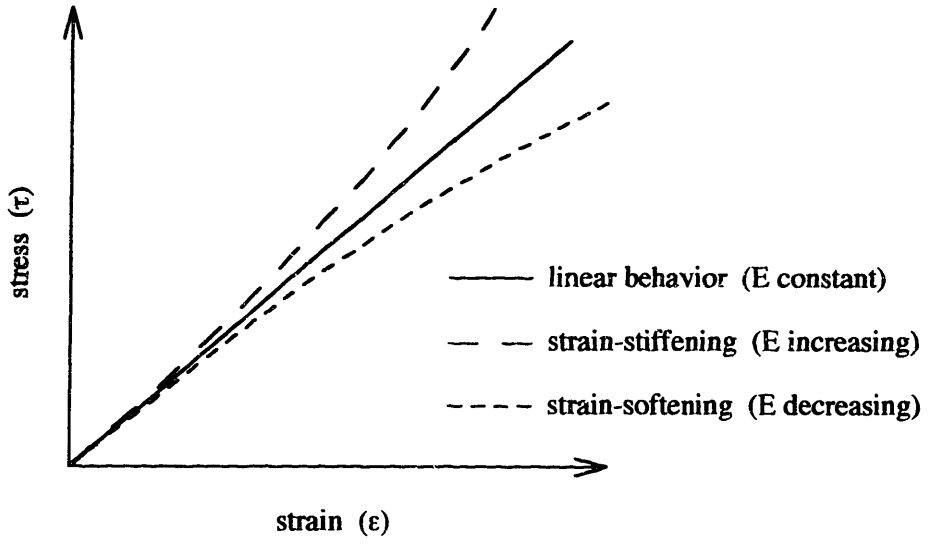

FIGURE 2-3: Typical assumptions of stress versus strain behavior. The sketch depicts linear, strain-stiffening and strain-softening material laws. E is defined as the slope of this curve.

material models with many parameters, only to find that the space of possible material behaviors that is spanned by the best estimate of the parameters – plus or minus the large error in those parameters – could just as easily have been spanned by a simple model with relatively few similarly uncertain parameters. That is why it is preferable in this case to model the materials involved with as few moduli as possible. Obtaining a reasonable guess at just two moduli has been difficult enough.

Our computational models assume the simplest material constitutive law possible, that of an incompressible linear-elastic (Hookean) material, characterized by a single parameter (E) for each layer. An isotropic, linear-elastic material is completely described by only two elastic moduli. For those two constants we will use Young's uniaxial elastic modulus (E) and the Poisson ratio (ν). One might also have chosen some combination using the shear modulus (G), the bulk modulus (K) or the Lamé constant (λ), but our choice is a common one. Aside from some of the details in this section, the modeled materials will be described using E and ν exclusively, though conversion to the other constants is entirely equivalent.

Young's uniaxial elastic modulus is so named because it is the ratio of stress to strain in a uniaxial unconfined tension or compression test. The Poisson ratio describes how the material will behave in the two unstressed directions during such a test. It ranges from 0 (when there is no displacement in the other two directions) to $^1/_2$ (when there is half as much opposite displacement in each of the other two directions).

As ν approaches $^1/_2$ the material becomes more volume-preserving or "incompressible." This is because in a compression test where the material is completely confined in the untested directions, there will be no deformation – i.e. the material is "incompressible." Such a material has an infinite bulk compression modulus (K). The constituents of tissues (mostly water and proteins) do indeed appear to be incompressible when each is taken separately. When examining the combination of these constituents in a bi-phasic material, however, there is the possibility of a gross "compressible" behavior when the water is allowed to squeeze out of the solid matrix.

Most of the simulations presented here will make the leap of assuming that the *gross* materials involved are nearly incompressible. That is to assume that the interval of time over which the smooth muscle contracts is sufficiently short that the water which is inside the tissue does not have enough time to move any significant distance. It is as if the water is bound to the solid protein matrix and the material has a single phase. Some simulations have also been performed at different values of ν, implying that water is squeezed out of the tissues, but this is a highly approximate way of incorporating water movement. Chapter 8 investigates loosening the incompressibility assumption in a more rigorous way using a bi-phasic poroelastic material formulation. Until then, however, the material models used in the simulations presented will be the single-phase ones discussed in this section.

Stress and Strain Measures:

In describing the constitutive laws that have been used to develop the two-layer computational models, there will be several references to stress and strain. The stress used here is the Cauchy or "true" stress, which is the force intensity per unit of current area in the deformed configuration. The stress is a full second-order tensor, which for two-dimensional computations is abbreviated as:

$$\tau \equiv \begin{bmatrix} \tau_{11} & \tau_{12} \\ \tau_{21} & \tau_{22} \end{bmatrix} = \begin{bmatrix} \tau_{11} & \tau_{12} \\ \tau_{12} & \tau_{22} \end{bmatrix}$$

Conservation of angular momentum dictates that the off-diagonal shear stresses (τ_{12} and τ_{21}) be equal, making the stress tensor symmetric. If plane-strain is assumed, τ_{33} is not necessarily zero, but it is typically not needed in computations and can be calculated afterward. For simplicity it is often preferable to express the three distinct stresses in a column matrix.

$$\begin{Bmatrix} \tau_{11} \\ \tau_{22} \\ \tau_{12} \end{Bmatrix}$$

The strain can be defined in many ways. Presented below is a derivation of the nonlinear (**B**) and linear (ε) strain measures which have been of use in this work. Note that in a plane-strain analysis, the deformation in the third direction is zero, and thus terms pertaining to that direction cancel out.

$$\text{identity matrix:} \quad \mathbf{1} \equiv \begin{bmatrix} 1 & 0 \\ 0 & 1 \end{bmatrix}$$

$$\text{current position as a function of reference position:} \quad \mathbf{y}(\mathbf{x})$$

$$\text{displacement as a function of reference position:} \quad \mathbf{u}(\mathbf{x}) = \mathbf{y}(\mathbf{x}) - \mathbf{x}$$

$$\text{deformation gradient:} \quad \mathbf{F} \equiv \nabla \mathbf{y} = \frac{\partial \mathbf{y}}{\partial \mathbf{x}} = \begin{bmatrix} \frac{\partial y_1}{\partial x_1} & \frac{\partial y_1}{\partial x_2} \\ \frac{\partial y_2}{\partial x_1} & \frac{\partial y_2}{\partial x_2} \end{bmatrix} = \begin{bmatrix} 1 + \frac{\partial u_1}{\partial x_1} & \frac{\partial u_1}{\partial x_2} \\ \frac{\partial u_2}{\partial x_1} & 1 + \frac{\partial u_2}{\partial x_2} \end{bmatrix}$$

$$\text{displacement gradient:} \quad \mathbf{H} \equiv \nabla \mathbf{u} = \frac{\partial \mathbf{u}}{\partial \mathbf{x}} = \begin{bmatrix} \frac{\partial u_1}{\partial x_1} & \frac{\partial u_1}{\partial x_2} \\ \frac{\partial u_2}{\partial x_1} & \frac{\partial u_2}{\partial x_2} \end{bmatrix} = \mathbf{F} - \mathbf{1}$$

$$\text{left Cauchy-Green strain tensor:} \quad \mathbf{B} \equiv \mathbf{F}\,\mathbf{F}^T$$

$$\mathbf{B} = \begin{bmatrix} \left(\frac{\partial y_1}{\partial x_1}\right)^2 + \left(\frac{\partial y_1}{\partial x_2}\right)^2 & \frac{\partial y_1}{\partial x_1}\frac{\partial y_2}{\partial x_1} + \frac{\partial y_1}{\partial x_2}\frac{\partial y_2}{\partial x_2} \\ \frac{\partial y_1}{\partial x_1}\frac{\partial y_2}{\partial x_1} + \frac{\partial y_1}{\partial x_2}\frac{\partial y_2}{\partial x_2} & \left(\frac{\partial y_2}{\partial x_1}\right)^2 + \left(\frac{\partial y_2}{\partial x_2}\right)^2 \end{bmatrix}$$

$$\mathbf{B} = \begin{bmatrix} 1 + 2\frac{\partial u_1}{\partial x_1} + \left(\frac{\partial u_1}{\partial x_1}\right)^2 + \left(\frac{\partial u_1}{\partial x_2}\right)^2 & \frac{\partial u_1}{\partial x_2} + \frac{\partial u_2}{\partial x_1} + \frac{\partial u_1}{\partial x_1}\frac{\partial u_2}{\partial x_1} + \frac{\partial u_1}{\partial x_2}\frac{\partial u_2}{\partial x_2} \\ \frac{\partial u_1}{\partial x_2} + \frac{\partial u_2}{\partial x_1} + \frac{\partial u_1}{\partial x_1}\frac{\partial u_2}{\partial x_1} + \frac{\partial u_1}{\partial x_2}\frac{\partial u_2}{\partial x_2} & 1 + 2\frac{\partial u_2}{\partial x_2} + \left(\frac{\partial u_2}{\partial x_2}\right)^2 + \left(\frac{\partial u_2}{\partial x_1}\right)^2 \end{bmatrix}$$

$$\mathbf{B} = \mathbf{F}\,\mathbf{F}^T = (\mathbf{1} + \mathbf{H})\,(\mathbf{1} + \mathbf{H})^T = \mathbf{1} + \mathbf{H} + \mathbf{H}^T + \mathbf{H}\,\mathbf{H}^T$$

By design, this strain measure is symmetric (caused by multiplying a tensor by its transpose). While the left Cauchy-Green strain tensor is good for measuring nonlinear strains, a simpler measure is desired for the small strains used in linear elasticity. The small strain tensor (ε) is defined as follows:

$$\varepsilon \equiv \frac{1}{2}\left(\mathbf{H} + \mathbf{H}^T\right) = \begin{bmatrix} \frac{\partial u_1}{\partial x_1} & \frac{1}{2}\left(\frac{\partial u_1}{\partial x_2} + \frac{\partial u_2}{\partial x_1}\right) \\ \frac{1}{2}\left(\frac{\partial u_1}{\partial x_2} + \frac{\partial u_2}{\partial x_1}\right) & \frac{\partial u_2}{\partial x_2} \end{bmatrix}$$

Note that $\mathbf{B} = \mathbf{1} + 2\,\varepsilon +$ quadratic strain terms.

As with the Cauchy stress, it is often convenient to write the three unique small strain terms in a column matrix:

$$\begin{Bmatrix} \varepsilon_{11} \\ \varepsilon_{22} \\ \varepsilon_{12} \end{Bmatrix} = \begin{Bmatrix} \frac{\partial u_1}{\partial x_1} \\ \frac{\partial u_2}{\partial x_2} \\ \frac{1}{2}\left(\frac{\partial u_1}{\partial x_2} + \frac{\partial u_2}{\partial x_1}\right) \end{Bmatrix}$$

Hookean (Linear-Elasticity) Constitutive Theory:

Using the linear-elastic material description, the stresses at any particular point are a linear transformation of the strains at that point. For instance, the isotropic linear-elastic constitutive behavior linking the stress components with the strain components in a two-dimensional plane-strain analysis can be expressed as follows:

$$\begin{Bmatrix} \tau_{11} \\ \tau_{22} \\ \tau_{12} \end{Bmatrix} = \begin{bmatrix} \frac{E(1-\nu)}{(1+\nu)(1-2\nu)} & \frac{E\nu}{(1+\nu)(1-2\nu)} & 0 \\ \frac{E\nu}{(1+\nu)(1-2\nu)} & \frac{E(1-\nu)}{(1+\nu)(1-2\nu)} & 0 \\ 0 & 0 & \frac{E}{1+\nu} \end{bmatrix} \begin{Bmatrix} \varepsilon_{11} \\ \varepsilon_{22} \\ \varepsilon_{12} \end{Bmatrix}$$

This is Hooke's law for two-dimensional plane-strain. Note that as ν approaches $^1/_2$, some of the constitutive terms give rise to singularities. This is because the average stress (or pressure) is becoming less dependent upon any of the strains taken independently. In finite element analyses, this problem manifests itself as non-physical mesh-dependent stress banding and element locking. To circumvent this problem, the so-called "u/p" or displacement-pressure formulation is introduced. Here is how the u/p formulation is derived for this situation:

For convenience, we can write Hooke's law for plane-strain in terms of the other elastic moduli, defined as follows:

$$\text{shear modulus:} \quad G \equiv \frac{E}{2(1+\nu)}$$

$$\text{bulk modulus:} \quad K \equiv \frac{E}{3(1-2\nu)}$$

$$\text{Lamé constant:} \quad \lambda \equiv \frac{E\nu}{(1+\nu)(1-2\nu)}$$

Thus the above expression of Hooke's law for plane-strain is more simply written:

$$\begin{Bmatrix} \tau_{11} \\ \tau_{22} \\ \tau_{12} \end{Bmatrix} = \begin{bmatrix} 2G+\lambda & \lambda & 0 \\ \lambda & 2G+\lambda & 0 \\ 0 & 0 & 2G \end{bmatrix} \begin{Bmatrix} \varepsilon_{11} \\ \varepsilon_{22} \\ \varepsilon_{12} \end{Bmatrix}$$

The pressure (p) and dilation (e) are defined as follows (note that tensile normal stresses contribute to a negative pressure):

$$p \equiv -\frac{\tau_{11} + \tau_{22} + \tau_{33}}{3}$$

$$e \equiv \varepsilon_{11} + \varepsilon_{22} + \varepsilon_{33}$$

In plane-strain, the third normal strain (ε_{33}) is assumed to be zero. Given the above definition of the dilation (e), another way to write the constitutive law is as follows using the Kronecker delta (if i = j, then $\delta = 1$; if $i \neq j$, then $\delta = 0$):

$$\tau_{ij} = 2\,G\,\varepsilon_{ij} + \lambda\,\delta_{ij}\,e$$

The deviatoric stress ($\tilde{\tau}$) and strain ($\tilde{\varepsilon}$) components are defined as follows (note that the deviatoric shear stresses and strains are equal to the total shear stresses and strains):

$$\tilde{\tau}_{11} \equiv \tau_{11} + p \qquad \tilde{\tau}_{22} \equiv \tau_{22} + p \qquad \tilde{\tau}_{12} \equiv \tau_{12}$$

$$\tilde{\varepsilon}_{11} \equiv \varepsilon_{11} - \frac{e}{3} \qquad \tilde{\varepsilon}_{22} \equiv \varepsilon_{22} - \frac{e}{3} \qquad \tilde{\varepsilon}_{12} \equiv \varepsilon_{12}$$

Now with some manipulation the constitutive law can be written:

$$\begin{Bmatrix} \tilde{\tau}_{11} \\ \tilde{\tau}_{22} \\ \tilde{\tau}_{12} \\ p \end{Bmatrix} = \begin{bmatrix} 2G & 0 & 0 & 0 \\ 0 & 2G & 0 & 0 \\ 0 & 0 & 2G & 0 \\ 0 & 0 & 0 & -K \end{bmatrix} \begin{Bmatrix} \tilde{\varepsilon}_{11} \\ \tilde{\varepsilon}_{22} \\ \tilde{\varepsilon}_{12} \\ e \end{Bmatrix}$$

Or more simply as:

$$\tilde{\tau}_{ij} = 2\,G\,\tilde{\varepsilon}_{ij}$$

$$p = -K e$$

What this decomposition does is separate dilational energy from distortional energy, but ultimately the finite element method still minimizes the sum of both of them over the set of admissible model deformations. As a material becomes more incompressible, more energy is devoted to distortion and less to dilation. In the u/p formulation the distortional strain energy is a function of the deviatoric stresses and strains, and the dilational energy is a function of the pressure and dilation only. As a material becomes more incompressible, the dilation approaches zero everywhere, making the pressure-dilation constitutive statement more of a constraint equation where the pressure is a Lagrange multiplier. For nearly incompressible materials ($\nu > 0.45$), the u/p formulation is helpful by making the stress-strain relationship better conditioned, and therefore more accurate.

Neohookean (Rubber Elasticity) Constitutive Theory:

Strictly speaking, the linear-elastic material description is not appropriate for large-deformation analyses because it is not completely invariant to rotation. Alternatively, we can use the so-called "neohookean" material description, which is a particular case of the hyperelastic material description frequently used for rubbers and other incompressible or nearly incompressible materials.

Many of the finite element analyses presented in this thesis have been computed twice, once with linear-elastic materials and again with hyperelastic materials. In all cases, both gave remarkably similar results, despite the inappropriateness of the linear-elastic description at large deformations. In general, it would seem preferable to use the linear-elastic description because it is somewhat more intuitive and direct. For certain analyses (poroelastic ones in particular), the finite element package used (ABAQUS) will not accept a hyperelastic material description (which is understandable given that the present formulation of poroelasticity in ABAQUS is a small-displacement, small-strain one). Most of the results presented here will be from analyses using linear-elastic materials, noting when hyperelastic ones are used.

Hyperelastic materials are isotropic by definition. Most rubbers are very loosely organized and thus are well described as isotropic. In a hyperelastic material description, the Cauchy stress at any point is related to the deformation there by means of a strain energy function

(W), which is defined based upon the three invariants of the left Cauchy-Green strain tensor (**B**). The invariants of a tensor are so named because they do not change regardless of how the reference coordinate system may be oriented. Therefore, it is convenient to define an isotropic material's behavior in terms of these strain invariants.

$$\text{first invariant of } \mathbf{B}: \quad I_1 \equiv \text{tr}(\mathbf{B}) = B_{11} + B_{22}$$

$$\text{second invariant of } \mathbf{B}: \quad I_2 \equiv \frac{1}{2}\left[\text{tr}(\mathbf{B})^2 - \text{tr}(\mathbf{B}^2)\right] = B_{11}B_{22} - B_{12}^2$$

$$\text{third invariant of } \mathbf{B}: \quad I_3 \equiv \det(\mathbf{B}) = B_{11}B_{22} - B_{12}^2$$

It is often useful to define material behavior in terms of the jacobian (J) instead of the third invariant (I_3). The jacobian is related to the third invariant as follows.

$$J = \sqrt{I_3}$$

The strain energy function can be defined in many ways, the very simplest of which is with a first-order polynomial description, also known as the Mooney-Rivlin description. Higher order polynomial descriptions and the common Ogden descriptions are often used, but the number of necessary parameters increases rapidly with the increased precision these models afford. For a general compressible Mooney-Rivlin material, the strain energy function is defined in terms of the invariants of the left Cauchy-Green strain and three parameters that characterize the material (C_{10}, C_{01} and D_1).[15]

$$W = C_{10}(I_1 - 3) + C_{01}(I_2 - 3) + \frac{1}{D_1}(J - 1)^2$$

In general, the Cauchy stress can be calculated from the strain tensor (B), its invariants (I_1, I_2, I_3 or J) and the derivatives of the constitutive strain energy function with respect to the invariants (W_1, W_2, W_3) using the following relationship.

$$\tau = 2J W_3 \mathbf{1} + \frac{2}{J}(W_1 + I_1 W_2)\mathbf{B} - \frac{2}{J} W_2 \mathbf{B}^2$$

The derivatives of the strain energy function with respect to each of the invariants are calculated as follows for a compressible Mooney-Rivlin material:

$$W_1 \equiv \frac{\partial W}{\partial I_1} = C_{10}$$

$$W_2 \equiv \frac{\partial W}{\partial I_2} = C_{01}$$

$$W_3 \equiv \frac{\partial W}{\partial I_3} = \frac{2}{D_1 J}$$

So that now the Cauchy stress can be calculated:

$$\tau = \frac{4}{D_1}\mathbf{1} + \frac{2(C_{10} + C_{01}I_1)}{J}\mathbf{B} - \frac{2\,C_{01}}{J}\mathbf{B}^2$$

The coefficients C_{10}, C_{01} and D_1 are the material constants which typically are found from curve fits of experimental data. In general, there is no broadly accepted physical meaning behind any of these three parameters taken independently. For instance, with linear-elasticity, E gives a measure of how stiff a material is while ν gives a rough measure of compressibility. To a certain degree, however, C_{10} is a "stiffness" parameter, C_{01} is a "strain-stiffening" or nonlinearity parameter and D_1 is a "compressibility" parameter, but not in the neat independent way that the linear-elastic constants are.

The subset of descriptions which have C_{01} set to zero are the so-called "neohookean" material descriptions. Of all the hyperelastic descriptions, they exhibit the most linear relationship between stress and strain. Given that $C_{01} = 0$, the following parallels exist between compressible neohookean (C_{10}, D_1) and Hookean (E, ν) material descriptions:

$$C_{10} = \frac{E}{4(1+\nu)} \qquad D_1 = \frac{6(1-2\nu)}{E}$$

$$E = \frac{18}{D_1 + \frac{3}{C_{10}}} \qquad \nu = \frac{3-2C_{10}D_1}{6+2C_{10}D_1}$$

The Cauchy stress for a compressible neohookean material is then:

$$\tau = \frac{4}{D_1}\mathbf{1} + \frac{2C_{10}}{J}\mathbf{B}$$

For an entirely incompressible neohookean material (where $J = 1$ and $W_3 = 0$), this reduces down to:

$$\tau = -p\,\mathbf{1} + 2C_{10}\,\mathbf{B}$$

and the pressure (defined as before) is independent of the strain. Note that for nearly incompressible materials (as D_1 approaches 0), the same problem that happened for nearly incompressible linear-elastic materials develops. In this case, the stresses and strains are divided into these average (pressure) and deviatoric parts to avoid ill-conditioning.

2.2.4 Smooth Muscle Shortening Boundary Conditions

The smooth muscle layer within the airway wall is not modeled in detail, but is assumed to exert a uniform circumferential strain on the exterior of the passive internal submucosa. This is implemented via an infinitesimally thin but extremely stiff band which surrounds the airway and uniformly shortens in the circumferential direction. From observing histological specimens, it seems reasonable to assume that though the smooth muscle is intermittent around a particular cross-section, the effect that it has is roughly uniform around the circumference since collapsed airways are almost always circular (if they are taken far enough away from any bifurcations), as if they were constricted by a uniform band of muscle (see Figures 1-6 and 1-7).

It appears from observation of histological cross-sections that the smooth muscle layer does not fold much as it constricts in its mostly axisymmetric and uniform fashion. In most airways, the mucosal folding appears to be of similar amplitude all around the airway. If there were more constriction on one side than another, we would expect much deeper folds on that side and perhaps an oblong shape to the cross-section. Axisymmetric deformation is also assumed in the passive airway structure external to the smooth muscle, including the adventitial layer and any parenchymal attachments. The assumption employed in these models is that the smooth muscle layer, once activated, decouples the inner airway's deformation from the outer airway's deformation. That is, a fraction of the total load that the smooth muscle layer exerts is devoted to axisymmetrically pulling the external airway inward, and the rest is devoted to buckling and collapsing the inner airway. Since the deformation of the outer airway is relatively predictable and well-modeled by existing

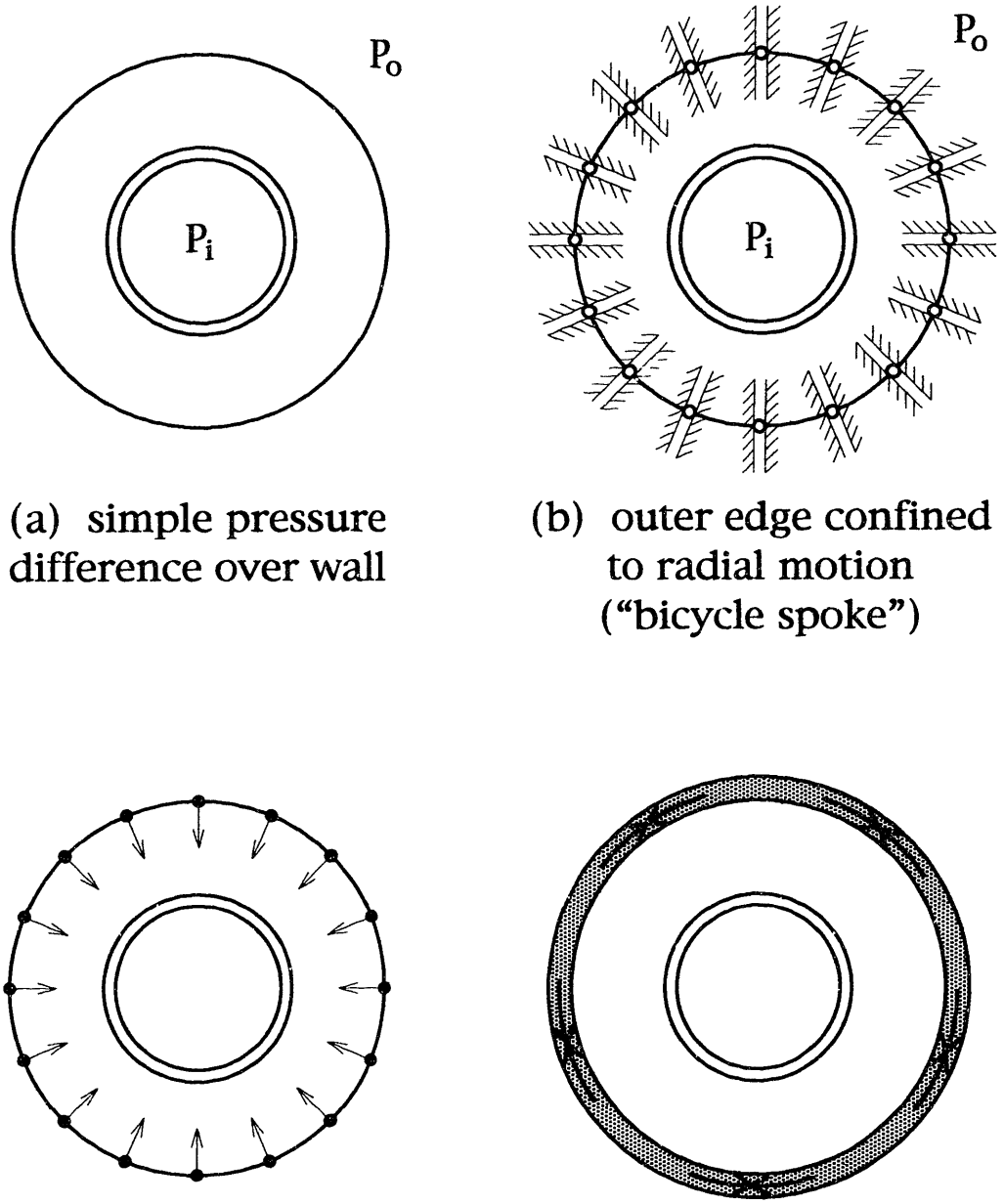

FIGURE 2-4: **Four different possible boundary conditions for modeling smooth muscle shortening: (a) external pressure only, (b) "bicycle-spoke" loading, (c) imposed outer edge displacement, (d) imposed hoop strain.**

analytical solutions, it is not in our interest to include it in our models and correspondingly increase model complexity and computation time.

Determining which set of boundary conditions would best simulate the action of the smooth muscle was a critical task. Four different possibilities were considered, as described below.

Pressure only: The first and seemingly most natural boundary condition to try is to simply impose a pressure (normal force only) along the outer edge of the submucosal layer to simulate the smooth muscle pressure (Figure 2-4a). The problem with this boundary condition is that the most common type of collapse is a two-lobed peanut-shaped buckling of the outer layer as shown in Figure 2-5a (with a small amount of wrinkling at the ends of the "peanut" due to the multi-fold higher modes shown in Figure 2-5b). This type of collapse turns out not to be physiological because there are regions on the outer perimeter of the submucosal layer (at the protruding ends moving outward) which are not contracting but extending, despite the inward normal pressure there. Such a buckling mode, if the only one present, cannot be due to uniform shortening around the outer perimeter.

"Bicycle spoke" loading: The next boundary condition tried was a normal pressure along the outer perimeter, combined with a displacement boundary condition which keeps all points along the perimeter moving radially inward or outward only, with no circumferential movement, as if the outer perimeter were lined up with a bicycle wheel and attached to sliders which only slide up and down the spokes (Figure 2-4b). Though this boundary condition inhibits the peanut-shaped mode, it still allows the possibility of localized extension of the outer perimeter.

Imposed displacement: This boundary condition does not impose a known load along the perimeter, but completely prescribes the displacement along it regardless of what load is necessary to produce it (Figure 2-4c). This boundary condition does have the desired effect of inhibiting the peanut-shaped buckling mode, so much that it completely precludes it. If there were evidence to say that the smooth muscle layer must stay completely circular throughout airway constriction, this boundary condition would seem appropriate. However, in real airways there does seem to be some ovalization of the smooth muscle layer at more extreme levels of collapse, suggesting buckling of the outer layer, and the presence of a small amount of the peanut-shaped mode, but only in combination with a large amount of the multi-fold modes.

Imposed hoop strain: The fourth and last boundary condition, which was decided to be the best approximation to smooth muscle shortening, is to surround the outer perimeter with a band which must shrink everywhere along it (Figure 2-4d). In the finite element model, this is accomplished by placing extremely stiff truss (or cable) elements along the outer perimeter, assigning them a thermal coefficient of expansion (α), and then lowering the ambient temperature. The temperature change causes a contractile thermal strain in the truss elements. Because they are so stiff, any force with which the inner airway might resist their deformation is negligible and the thermal strain predominates. The truss elements

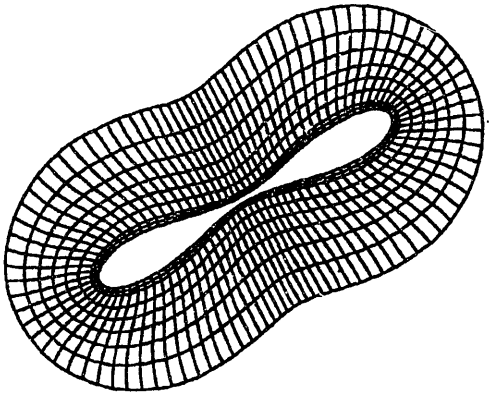

(a) peanut-shaped buckling resisted by the smooth muscle shortening boundary condition

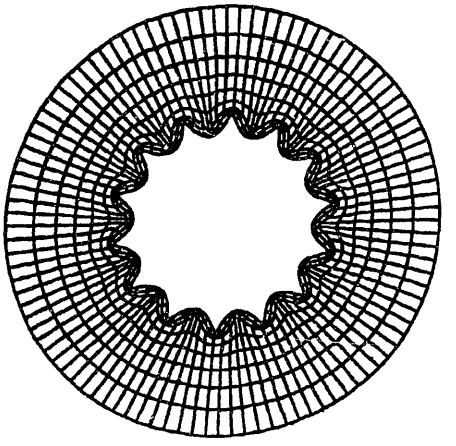

(b) typical multi-fold buckling pattern

FIGURE 2-5: Possible buckling modes due to the boundary conditions: (a) peanut-shaped buckling of the outer layer, (b) a typical multi-fold mode. These meshes are plots of possible displacement eigenvectors in a linearized buckling analysis (see Section 2.4.5).

have no bending stiffness, however, and so ovalization of the outer perimeter is possible (in a nonlinear static collapse analysis, but not in a linearized buckling analysis). Regardless of whether or not that happens, local shortening is guaranteed at all locations along the perimeter. In a nonlinear analysis, a small amount of the peanut-shaped "mode" is possible in combination with collapse in the multi-fold modes such that the net deformation at the protruding ends of the "peanut" is still a shortening one. (To speak of "modes" in a nonlinear analysis is imprecise; mode shapes are a consequence of linear analysis.)

Dr. Mic Okazawa of the University of British Columbia Pulmonary Research Laboratory observes that when he applies a suction to the trachea of rabbit lungs, then fixes them and sections them, he observes the peanut-shaped airway collapse. When he instead excises the lungs and applies a smooth muscle agonist, fixes them and sections them, he does not observe peanut-shaped collapse, but multi-lobed mucosal folding instead.[17] Okazawa's experiments demonstrate how the difference in applied boundary conditions on the airway completely change the collapse behavior observed. In the trachea suction experiment, he is applying boundary conditions similar to the pressure only condition (Figure 2-5a), where there is merely a pressure difference between the interior and the exterior of the wall and no necessity to have shortening of the perimeter everywhere along the outer circumference. If the airway wall material is indeed well-modeled as incompressible, the conditions of external pressure and internal suction are truly equivalent and produce the same collapse. In the experiment where Okazawa applies the contractile agonist, he is invoking smooth muscle shortening, and enforcing a boundary condition which is best described by imposed hoop strain along the outer perimeter (Figure 2-5d). This is a reasonable simulation of smooth muscle constriction *in vivo*.

2.2.5 Initial Stress State

It is assumed in this work that the initial state of a membranous airway (when it is circular and fully open) is stress-free. Some initial and as yet unpublished studies by Prof. Barry R. Wiggs et al. at the University of British Columbia Pulmonary Research Laboratory have suggested that this is true because newly excised membranous airways do not exhibit an opening angle when sliced open longitudinally. It may also be that an initial stress exists, but it is too small to be detected in this manner. Han and Fung indeed have observed opening angles in excised canine trachea indicating the presence of an initial stress,[14] but it

is probable that the cartilage is producing the stress in that case. In the absence of any significant proof of initial stress in fully membranous airways, there will be none assumed in the analyses presented here.

Sometimes a small amount of mucosal folding is present in unconstricted airways, suggesting that the fully-open and circular geometry would have a tensile initial stress state. Such a situation may be modeled (more approximately) using the tools developed by the author (see Section 2.6.3).

2.3 Simple Two-Layer Model Parameters

The mechanical model described in this section is frequently referred to as the "simple" two-layer model to distinguish it from the somewhat more complex model (the "poroelastic" two-layer model) described in Chapter 8. The simple model incorporates all of the constituents and assumptions described to this point. Such a physical system is independent of time and so termed "static." Because of the constitutive laws used, the response of the structure to any loading is immediate and completely elastic (that is, all strain energy stored in the structure can be recovered upon unloading).

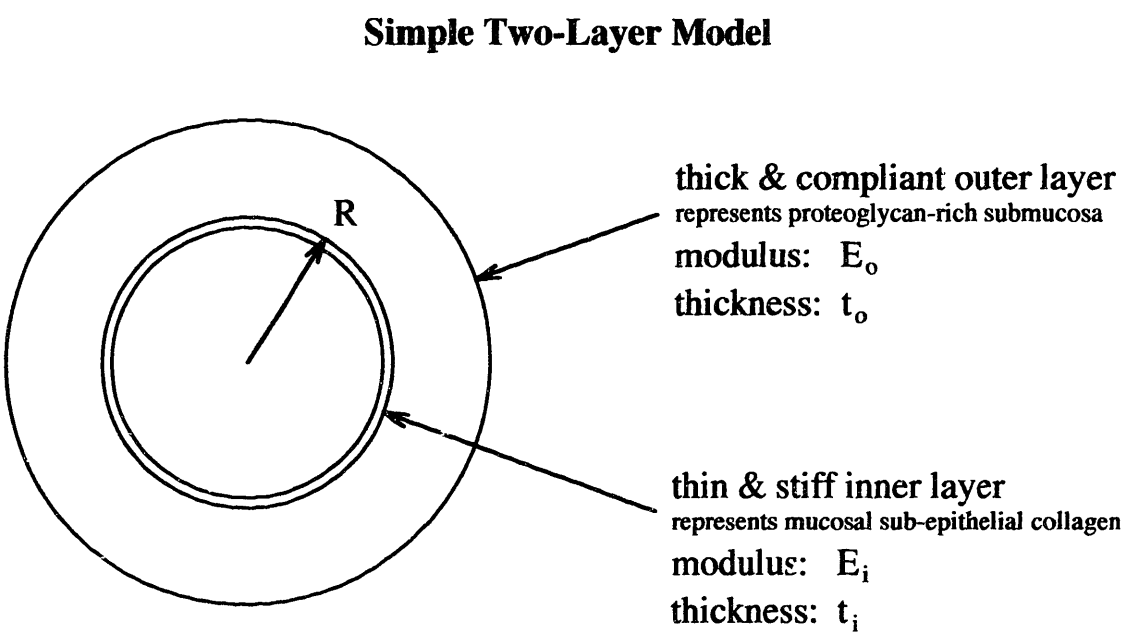

FIGURE 2-6: Sketch of the simple two-layer model with 5 varying dimensional parameters.

Figure 2-6 shows a sketch of the simple two-layer model. It is completely described by five varying parameters: the characteristic radius (R) measured from the airway axis to the interface between the two layers, the outer layer thickness (t_o), the inner layer thickness (t_i), the elastic modulus of the outer layer (E_o) and the elastic modulus of the inner layer (E_i). The materials of the simple model are assumed to be incompressible ($\nu = 1/2$) unless otherwise stated, thus keeping the number of varying parameters down to five.
We can nondimensionalize the problem to reduce the number of independent parameters to three. The general results from the simple model will be cast in terms of the following three dimensionless ratios.

$$\text{outer thickness ratio:} \quad t_o^* \equiv \frac{t_o}{R}$$

$$\text{inner thickness ratio:} \quad t_i^* \equiv \frac{t_i}{R}$$

$$\text{stiffness ratio:} \quad E^* \equiv \frac{E_i}{E_o}$$

Other variables are necessary for quantifying how much (equivalent) pressure is being applied to the exterior of the outer layer by the smooth muscle (P), how much inward radial displacement is observed at that location (Δ), how much smooth muscle shortening is necessary to produce that displacement (S) and how much lumen area results from the deformation (A). These input and output variables of interest are also nondimensionalized as follows:

$$\text{normalized equivalent external smooth muscle pressure:} \quad P^* \equiv \frac{P}{E_o}$$

$$\text{normalized outer edge inward radial displacement:} \quad \Delta^* \equiv \frac{\Delta}{R}$$

$$\text{percent of smooth muscle shortening:} \quad S \equiv \frac{2\pi(R+t_o) - 2\pi(R+t_o-\Delta)}{2\pi(R+t_o)} \cdot 100 = \frac{\Delta}{R+t_o} \cdot 100 = \frac{\Delta^*}{1+t_o^*} \cdot 100$$

$$\text{normalized lumen area:} \quad A^* \equiv \frac{A}{\pi(R-t_i)^2}$$

If the modeled materials are incompressible, then:

$$A^* = 1 - \frac{\Delta^*[2(1+t_o^*)-\Delta^*]}{(1-t_i^*)^2}$$

To a certain degree, knowing how much lumen area is available for airflow before and after the collapse tells how severely the collapse has reduced the airflow. However, an airway's performance is best quantified by its effort-to-flow resistance factor. Knowing that the airways we are studying are relatively small, the airflow through them is reasonably well described by laminar Poiseuille flow. However, the entry length is not long enough for the flow's velocity profile to be entirely parabolic. Therefore the following relationships slightly underestimate the flow and overestimate the resistance of the airways. For small circular tubes, the drop in pressure (Δp) over a length (L) is related to the flow rate (Q) through it by the following relationship:

$$\frac{\Delta p}{L} = \frac{8\mu}{\pi R^4} Q$$

Here, μ is the absolute dynamic viscosity of the conducted fluid (air). For such a tube, the effort-to-flow resistance factor is then $\frac{8\mu}{\pi R^4}$. In a non-circular tube, the above relationship can still be used approximately by replacing the radius (R) with the computed hydraulic radius (R_{hy}) as defined below. In a perfectly circular tube, $R_{hy} = R$.

$$\text{hydraulic radius:} \quad R_{hy} \equiv \frac{2\,A}{\text{lumen perimeter}}$$

$$\text{normalized airway hydraulic radius:} \quad R_{hy}^* \equiv \frac{R_{hy}\,R}{(R-t_i)^2}$$

$$\text{airway resistance to airflow} \propto \frac{1}{R_{hy}^4}$$

$$\mathcal{R} \equiv \frac{\text{collapsed airway resistance}}{\text{open airway resistance}} = \frac{1}{R_{hy}^{*4}}$$

The resistance ratio ($\mathcal{R}$) gives a lower bound for the factor of increase in airflow resistance caused by an airway's collapse. It is a lower bound because, particularly for more asthmatic airways, airway fluids collect in the folds and take up more of the cross-sectional

lumen area. If it is indeed true that the inner perimeter remains constant through the course of the deformation then:

$$\mathcal{R} = \frac{1}{R_{hy}{}^{*4}} = \frac{1}{A^{*4}}$$

This implies that slight changes in the amount of lumen area can result in much more significant changes in the amount of airflow resistance. The above relationship is perhaps a bit too non-conservative. If one were so entirely conservative as to neglect the effect of the undulation of the inner aspect of the airway wall, assuming that it remains circular and that the inner perimeter squared decreases linearly with the lumen area, then the resistance to airflow would be inversely related to the lumen area squared. So the correct relationship between the resistance ratio and the normalized lumen area is bounded as follows.

$$\frac{1}{A^{*2}} < \mathcal{R} < \frac{1}{A^{*4}}$$

Finally, it is often of interest to speak of the state of the model at the buckling point. The subscript 'b' is placed on the variable to distinguish it as the particular value that variable takes at buckling.

2.4 Numerical Solution Procedure

To this point we have developed a somewhat "black box" model of the mechanics of the airway. One puts into the box a desired amount of smooth muscle shortening, then the black box computes how much smooth muscle pressure, outer edge displacement, lumen area and airflow resistance corresponds to that amount of shortening. Aside from the above discussion of the assumed constitutive material behavior, not much has yet been said about how the black box goes about making these computations. The following discussions are intended to demystify the black box and bring its critical ingredients to light.

2.4.1 The Principle of Virtual Work

One important result from basic continuum mechanics is the balance of linear momentum. The local (or differential) expression of linear momentum conservation is the following equation of motion:

$$\mathrm{div}\,\boldsymbol{\tau} + \mathbf{b} = \rho\,\dot{\mathbf{v}}$$

In the absence of significant inertial forces and body forces, stress equilibrium reduces to simply:

$$\mathrm{div}\,\boldsymbol{\tau} = \mathbf{0}$$

Along any surface, there must also be equilibrium between the internal stresses in the material on the interior of the surface and the external surface tractions on the exterior of the surface. In the following statement, $\boldsymbol{\tau}$ is the Cauchy stress tensor at the point of interest, $\mathbf{n}$ is the normal vector at that point on the surface, and $\mathbf{f}$ is the surface traction vector at that point.

$$\boldsymbol{\tau}\,\mathbf{n} = \mathbf{f}$$

Now we introduce a virtual displacement field vector $\hat{\mathbf{u}}$ which applies at every point on the surface and within the volume it encloses. It is "virtual" in the sense that it is a small hypothetical perturbation upon an existing deformed structure. Note that this virtual displacement field must comply with any prescribed displacements that are dictated by the boundary conditions. Each side of the differential equilibrium statement is dotted with the virtual displacement vector and integrated over the entire structure volume.

$$\int_V (\mathrm{div}\,\boldsymbol{\tau}) \bullet \hat{\mathbf{u}}\; dV = 0$$

Similarly, both sides of the statement of stress-traction equilibrium is dotted with the virtual displacement vector and integrated over the entire bounding surface.

$$\int_S (\boldsymbol{\tau}\,\mathbf{n}) \bullet \hat{\mathbf{u}}\; dS = \int_S \mathbf{f} \bullet \hat{\mathbf{u}}\; dS$$

The product on the left can be rearranged as follows.

$$\int_S (\tau^T \hat{\mathbf{u}}) \bullet \mathbf{n} \, dS = \int_S \mathbf{f} \bullet \hat{\mathbf{u}} \, dS$$

Next, the divergence of a tensor-vector product is expanded as follows using the chain rule of differentiation.

$$\text{div}\,(\tau^T \hat{\mathbf{u}}) = (\text{div}\,\tau) \bullet \hat{\mathbf{u}} + \tau \bullet \nabla\hat{\mathbf{u}}$$

Rearrange to get:

$$(\text{div}\,\tau) \bullet \hat{\mathbf{u}} = \text{div}\,(\tau^T \hat{\mathbf{u}}) - \tau \bullet \nabla\hat{\mathbf{u}}$$

Substituting this in the integrated internal stress equilibrium statement yields:

$$\int_V \left[\text{div}\,(\tau^T \hat{\mathbf{u}}) - \tau \bullet \nabla\hat{\mathbf{u}}\right] dV = 0$$

Applying the divergence theorem to the first term above results in:

$$\int_S (\tau^T \hat{\mathbf{u}}) \bullet \mathbf{n} \, dS - \int_V \tau \bullet \nabla\hat{\mathbf{u}} \, dV = 0$$

Now the first term above is equal to a term which resulted from the traction-stress equilibrium. Substituting in the traction term and rearranging yields the theorem of virtual work.

$$\int_V \tau \bullet \nabla\hat{\mathbf{u}} \, dV = \int_S \mathbf{f}\,\hat{\mathbf{u}} \, dS$$

For small virtual displacements (or a variation in the displacement), it can be shown that $\nabla\hat{\mathbf{u}} = \hat{\mathbf{H}} = \hat{\varepsilon}$. Therefore, the theorem of virtual work is equivalently expressed:

$$\int_V \tau \bullet \hat{\varepsilon} \, dV = \int_S \mathbf{f}\,\hat{\mathbf{u}} \, dS$$

The left-hand side is an expression for the virtual strain energy stored in the structure (the internal virtual work) and the right-hand side is the virtual work done by the loads (the external virtual work).

2.4.2 Total Lagrangian Formulation

Now that the principle of virtual work has been established, it is desirable to modify it in such a way that can be applied to a nonlinear incremental analysis. The first step is to replace the Cauchy stress (τ), which is force per unit of (unknown) current area, with a stress that refers instead to the original (known) configuration. For this purpose, the second Piola-Kirchhoff stress ($\mathbf{S}$) is defined:

$$\mathbf{S} \equiv \frac{1}{J}\mathbf{F}^{-1}\tau\mathbf{F}^{-T} \qquad \text{or} \qquad \tau = J\,\mathbf{F}\,\mathbf{S}\,\mathbf{F}^{T}$$

$$\text{where} \quad J \equiv \det\mathbf{F} = \frac{\text{original density}}{\text{current density}}$$

It is important to define $\mathbf{S}$, because τ is not additive. We cannot simply add τ at time t to some increment of stress over an interval Δt, say $\Delta\tau$, and get τ at time $t+\Delta t$. That is:

$$^{t+\Delta t}\tau \neq {}^{t}\tau + \Delta\tau$$

This is because ${}^{t}\tau$ and ${}^{t+\Delta t}\tau$ refer to different areas. However, we *can* write:

$$^{t+\Delta t}\mathbf{S} = {}^{t}\mathbf{S} + \Delta\mathbf{S}$$

The second Piola-Kirchhoff stress always refers to the same area, the reference configuration area, which does not change with t. The strain measure which is energetically conjugate to $\mathbf{S}$ is the Green-Lagrange strain ($\mathbf{E}$). The Green-Lagrange strain is a nonlinear measure of strain which, like $\mathbf{S}$, is invariant under rigid-body rotation. $\mathbf{E}$ is derived from the deformation gradient, $\mathbf{F}$, as follows.

$$\text{right Cauchy-Green strain tensor:} \quad \mathbf{C} \equiv \mathbf{F}^{T}\mathbf{F} = (\mathbf{1} + \mathbf{H})^{T}(\mathbf{1} + \mathbf{H})$$

$$\text{Green-Lagrange strain:} \quad \mathbf{E} \equiv \frac{1}{2}(\mathbf{C} - \mathbf{1}) = \frac{1}{2}(\mathbf{H} + \mathbf{H}^{T} + \mathbf{H}^{T}\mathbf{H})$$

The Green-Lagrange strain is also additive, and can be subdivided into linear and nonlinear incremental strains.

$$ {}^{t+\Delta t}\mathbf{E} = {}^{t}\mathbf{E} + \Delta\mathbf{E} $$

$$ \Delta\mathbf{E} = \frac{1}{2}\left[\Delta\mathbf{H} + \Delta(\mathbf{H}^{T}) + \Delta(\mathbf{H}^{T}\,\mathbf{H})\right] = \frac{1}{2}(\Delta\mathbf{H} + \Delta\mathbf{H}^{T} + \Delta\mathbf{H}^{T}\mathbf{H} + \mathbf{H}^{T}\Delta\mathbf{H} + \Delta\mathbf{H}^{T}\Delta\mathbf{H}) $$

$$ \text{linear incremental strain:} \quad \Delta\varepsilon \equiv \frac{1}{2}(\Delta\mathbf{H} + \Delta\mathbf{H}^{T} + \Delta\mathbf{H}^{T}\mathbf{H} + \mathbf{H}^{T}\Delta\mathbf{H}) $$

$$ \text{nonlinear incremental strain:} \quad \Delta\eta \equiv \frac{1}{2}(\Delta\mathbf{H}^{T}\Delta\mathbf{H}) $$

$$ \Delta\mathbf{E} = \Delta\varepsilon + \Delta\eta $$

Suppose everything is known for a body at time t. (Note, time = t is later than the reference state, time = 0, to which **S** and **E** refer.) Now it is desired to determine stresses, strains, etc. at time t+Δt given the increments in loading and prescribed displacements over Δt. We apply the principle of virtual work at time t+Δt:

$$ \int_{{}^{t}V} {}^{t+\Delta t}\boldsymbol{\tau} \bullet {}^{t+\Delta t}\hat{\boldsymbol{\varepsilon}}\; d^{t}V = \int_{{}^{t}S} {}^{t+\Delta t}\mathbf{f}\; {}^{t+\Delta t}\hat{\mathbf{u}}\; d^{t}S $$

The fact that **S** is energetically conjugate to **E** means that **S** operating on **E** yields the strain energy. Therefore we can substitute in the internal virtual work (or strain energy) based on **S** and **E** as follows, noting that the integral is now over the reference configuration.

$$ \int_{{}^{0}V} {}^{t+\Delta t}\mathbf{S} \bullet {}^{t+\Delta t}\hat{\mathbf{E}}\; d^{0}V = \int_{{}^{t}S} {}^{t+\Delta t}\mathbf{f}\; {}^{t+\Delta t}\hat{\mathbf{u}}\; d^{t}S $$

Note that a perturbation on E at the time t+Δt is the same as a perturbation on merely the change in E over Δt. This allows us to write:

$$ \int_{{}^{0}V} {}^{t+\Delta t}\mathbf{S} \bullet \Delta\hat{\mathbf{E}}\; d^{0}V = \int_{{}^{t}S} {}^{t+\Delta t}\mathbf{f}\; {}^{t+\Delta t}\hat{\mathbf{u}}\; d^{t}S $$

Next we make use of the fact that S is additive by decomposing the strain energy at time t+Δt into the strain energy at time t and an increment in strain energy over the interval Δt.

$$\int_{{}^0V} \Delta \mathbf{S} \bullet \Delta \hat{\mathbf{E}} \, d^0V + \int_{{}^0V} {}^t\mathbf{S} \bullet \Delta \hat{\mathbf{E}} \, d^0V = \int_{{}^tS} {}^{t+\Delta t}\mathbf{f} \, {}^{t+\Delta t}\hat{\mathbf{u}} \, d^tS$$

By decomposing $\Delta \hat{\mathbf{E}}$ into its linear and nonlinear parts, we can write:

$$\int_{{}^0V} \Delta \mathbf{S} \bullet \Delta \hat{\mathbf{E}} \, d^0V + \int_{{}^0V} {}^t\mathbf{S} \bullet \Delta \hat{\boldsymbol{\eta}} \, d^0V = \int_{{}^tS} {}^{t+\Delta t}\mathbf{f} \, {}^{t+\Delta t}\hat{\mathbf{u}} \, d^tS - \int_{{}^0V} {}^t\mathbf{S} \bullet \Delta \hat{\boldsymbol{\varepsilon}} \, d^0V$$

To this point, we have made no approximations. However, now we must linearize this equation of motion to obtain a solution. The two approximations we will make are:

$$\Delta \mathbf{S} \approx \mathbb{C} \, \Delta \boldsymbol{\varepsilon}$$

$$\Delta \hat{\mathbf{E}} \approx \Delta \hat{\boldsymbol{\varepsilon}}$$

The first approximation is a linear constitutive law (a fourth order tensor) that relates each component of the change in strain to each component of the change in stress. The second approximation merely states that for the first term of the equation of motion, it is sufficient to throw out the nonlinear component of the change in strain. This leaves us with the following statement for the equation of motion.

$$\int_{{}^0V} (\mathbb{C} \, \Delta \boldsymbol{\varepsilon}) \bullet \Delta \hat{\boldsymbol{\varepsilon}} \, d^0V + \int_{{}^0V} {}^t\mathbf{S} \bullet \Delta \hat{\boldsymbol{\eta}} \, d^0V = \int_{{}^tS} {}^{t+\Delta t}\mathbf{f} \, {}^{t+\Delta t}\hat{\mathbf{u}} \, d^tS - \int_{{}^0V} {}^t\mathbf{S} \bullet \Delta \hat{\boldsymbol{\varepsilon}} \, d^0V$$

2.4.3 Finite Element Discretization and Solution

The next step in our solution scheme is to make the domain discrete and convert the above integral equation into a set of linear algebraic equations. Each of the terms in the equation of motion is evaluated as a product of matrices operating on the vector of nodal displacements as follows.

$$\int_{{}^0V} (\mathbb{C}\ \Delta\varepsilon) \bullet \hat{\Delta\varepsilon}\ d^0V \approx \{\hat{u}\}^T \sum_{{}^0V} \left([B_L]^T\ [C]\ [B_L]\right) \{\Delta u\} = \{\hat{u}\}^T\ [K_L]\ \{\Delta u\}$$

$$\int_{{}^0V} {}^tS \bullet \hat{\Delta\eta}\ d^0V \approx \{\hat{u}\}^T \sum_{{}^0V} \left([B_{NL}]^T\ [S]\ [B_{NL}]\right) \{\Delta u\} = \{\hat{u}\}^T\ [K_{NL}]\ \{\Delta u\}$$

$$\int_{{}^tS} {}^{t+\Delta t}\mathbf{f}\ {}^{t+\Delta t}\hat{\mathbf{u}}\ d{}^tS \approx \{\hat{u}\}^T \sum_{{}^tS} [H_S]^T\ \{f\} = \{\hat{u}\}^T\ \{R\}$$

$$\int_{{}^0V} {}^tS \bullet \hat{\Delta\varepsilon}\ d^0V \approx \{\hat{u}\}^T \sum_{{}^0V} [B_L]^T\ \{S\} = \{\hat{u}\}^T\ \{F\}$$

$[B_L]$ is the linear strain-displacement matrix which transforms a vector of nodal displacements into a column matrix containing the linear parts of the Green-Lagrange strain components. Similarly, $[B_{NL}]$ produces the nonlinear parts. [C] is a constitutive matrix which transforms this column matrix of strain components into one of stress components via a selected constitutive law. $\{\Delta u\}$ is the vector of change in nodal displacements over Δt, and $\{\hat{u}\}$ is a vector of virtual displacements (or perturbative displacements). [S] is a matrix of second Piola-Kirchhoff stresses (at time t). The components of [S] are rearranged and written in the column matrix, $\{S\}$. $[H_S]$ is a matrix which linearly interpolates between the components of its argument on the surface of the body. $\{f\}$ is a vector of surface tractions condensed to the nodes at time $t+\Delta t$. $[K_L]$ and $[K_{NL}]$ are the linear and nonlinear incremental stiffness matrices. $\{R\}$ is the vector of surface traction forces at time $t+\Delta t$, and $\{F\}$ is the vector of nodal point forces which is equivalent to the internal stresses at time t. Using all these constructs, our now discrete equation of motion becomes:

$$\{\hat{u}\}^T \left([K_L] + [K_{NL}]\right) \{\Delta u\} = \{\hat{u}\}^T \left(\{R\} + \{F\}\right)$$

The vector of perturbative virtual displacements is arbitrary and can be eliminated at this time, leaving us with the discrete FEM equations for a static analysis:

$$\left([K_L] + [K_{NL}]\right) \{\Delta u\} = \{R\} + \{F\}$$

The equations are solved iteratively until convergence is reached. Note that $[K_I]$ and $[K_{NL}]$ are global stiffness matrices. Usually, these matrices are determined for each element in the domain, transformed from that element reference frame to the global reference frame, then summed over the entire domain. The choice of element manifests itself in the number of nodes associated with each element, and how displacements are interpolated between those nodes.

Most of the results presented have been obtained from ABAQUS finite element models composed of quadrilateral elements with second-order polynomial interpolants. These so-called "serendipity" elements have only 8 nodes each, and because they lack the center node are prone to "hourglassing," a certain zero-energy spurious mode which can arise in the finite element solution and give misleading results. Fortunately, the conditions that the elements were used under in this work did not activate the hourglass mode.

Another complication, discussed in Section 2.2.3, is the necessity for the "u/p" formulation. In order to improve the conditioning of problems with nearly or completely incompressible materials, it is necessary to introduce another degree of freedom at each element's corner nodes for the pressure. The finite element matrix equations are reformulated in terms of the deviatoric stresses and strains. Then an equal number of compatibility constraint equations are introduced to make the complete set solvable. The pressure degrees of freedom exist only at the corner nodes for optimal element performance.

2.4.4 Nonlinear Static Analysis Procedure

To this point a framework has been developed for finding the structure's displacement, stresses and strains throughout the history of loading. This is accomplished by dividing up the modeled domain into small regions (elements) over which the displacement field is interpolated based on the displacements of a few important reference points (nodes) associated with the region. The element stiffness matrices are evaluated using numerical integration over the element domain, resulting in a set of constants which transform nodal displacements into nodal loads.

Some results from a sample analysis are shown in Figures 2-7 and 2-8. Figure 2-7 shows the pressure at the outer edge (P*) required to produce an inward displacement of the outer

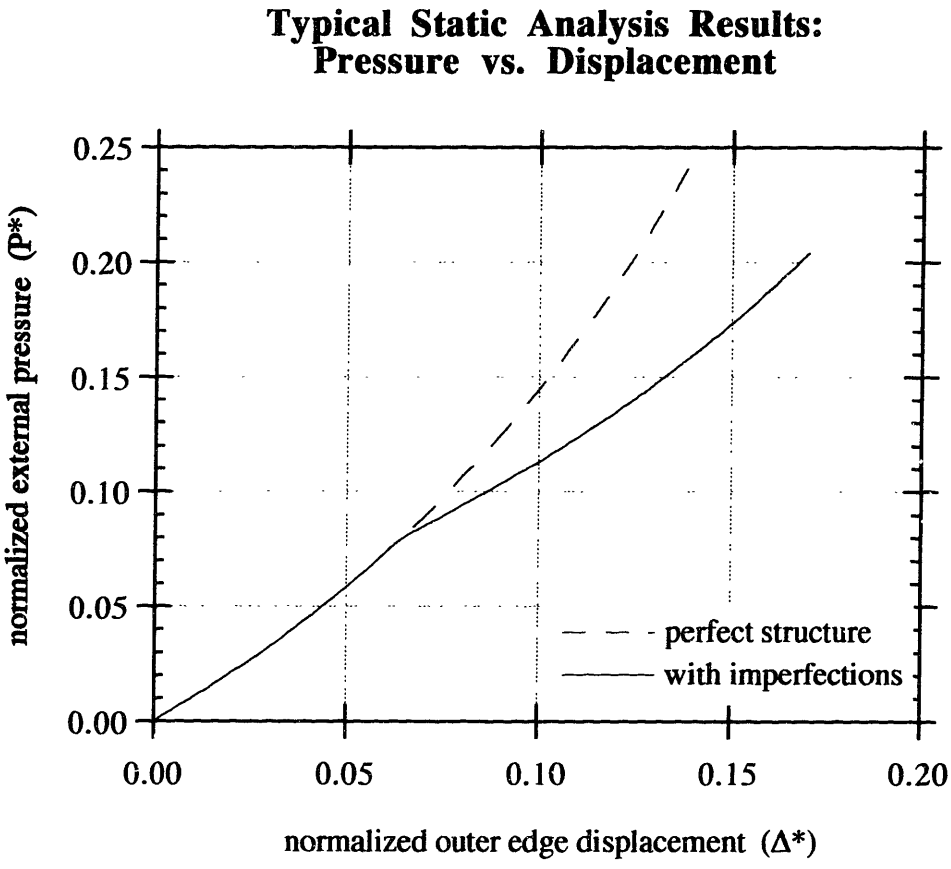

FIGURE 2-7: Typical pressure-displacement results from the static analysis of a two-layer tube simulation, with and without minute initial imperfections in the geometry.

edge (Δ*). Thus the area under this curve at any point is the amount of external work which has been put into the structure, which, because this is a completely conservative elastic system, is equal to the amount of strain energy stored in the structure, which could be recovered upon unloading. The dotted solution, showing no bifurcation or change in mode of deformation, is the non-buckling solution. It assumes only axisymmetric deformation of the structure. Note that the non-buckling solution lies everywhere above the solution which incorporates buckling (indicated by the solid line), indicating that the buckled state is a lower energy state, and is thus preferred.

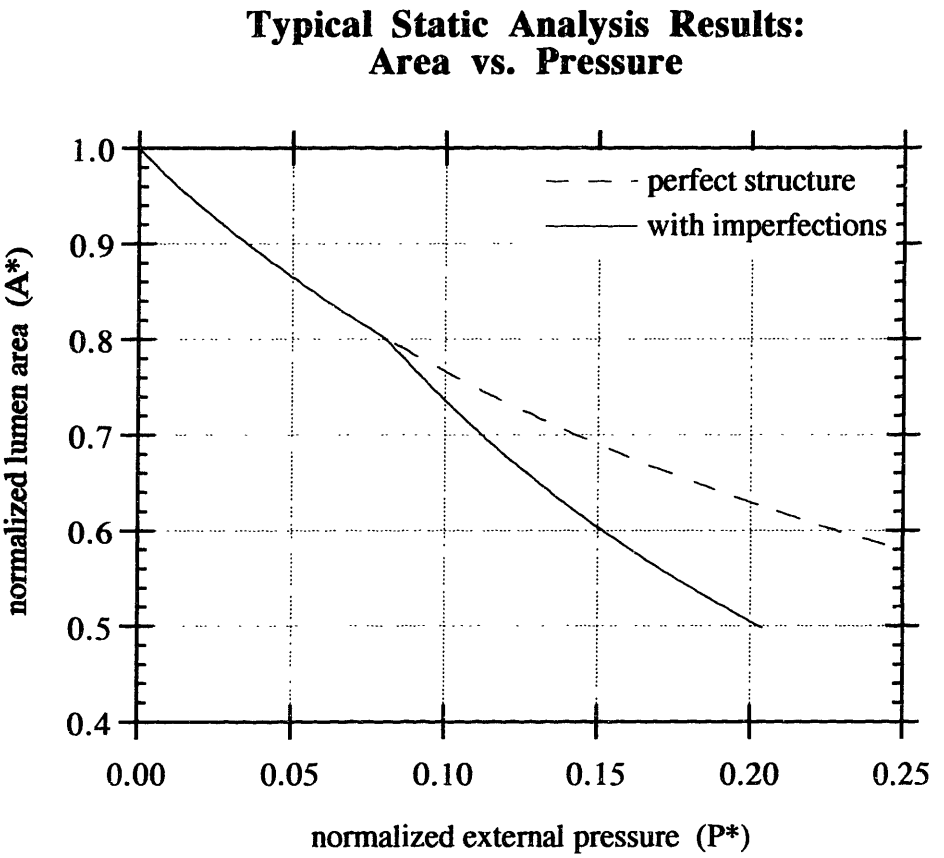

FIGURE 2-8: A more insightful way of reporting static analysis results: lumen area as a function of applied equivalent external pressure. Provides a quick assessment of resistance to airflow.

Similarly, Figure 2-8 shows lumen area (A*) versus pressure (P*) for the same analysis. Note that failing to incorporate buckling into one's solution would tend to overestimate the amount of luminal area remaining for airflow after buckling.

One problem that naturally exists when solving these problems is that the nonlinear equations of motion do have the non-buckling solution as a valid equilibrium. What the finite element method we use does not do is evaluate the stability of that solution, thus allowing it as a permissible solution, even though it is not a physical one. One way to test the stability of a solution is to perturb the nodal loads or locations by some small amount and see if equilibrium is still achieved. The non-buckling solution becomes more and more unstable as it progresses.

The way we ensure that the solution we generate is a physical one and incorporates buckling is by prescribing imperfections in the initial geometry of the structure. The notation "perfect structure" and "with imperfections" in Figures 2-7 and 2-8 reflects the idea that initial imperfections are one way of generating the correct (buckled) solution. (Perturbations of load on the nodes would be another.) Section 2.5 discusses in more detail the way initial imperfections are introduced. The state at which the buckling solution deviates from the non-buckling solution is frequently referred to as the "buckling point,"

Undeformed Wedge-Model Mesh:

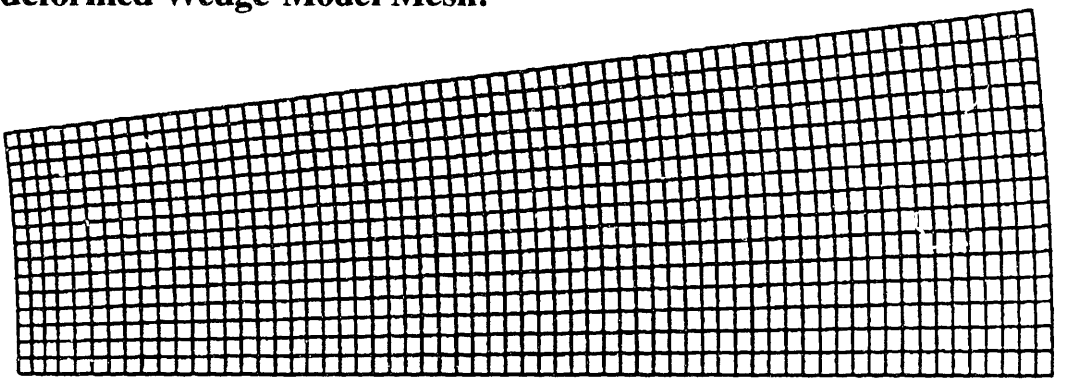

Deformed Wedge-Model Mesh:

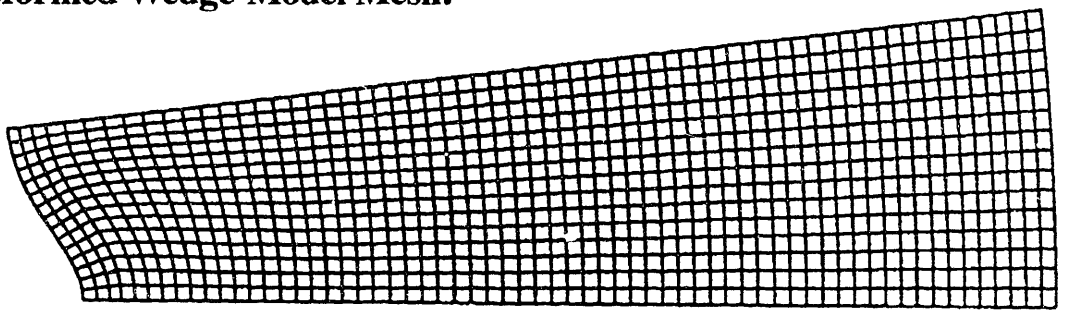

FIGURE 2-9: A half-wavelength "wedge-model" exploits the known symmetry in the preferred mode of collapse. These meshes show the wedge-model domain before and after an outer edge displacement or pressure is applied.

and is characterized by a buckling pressure (P_b or P_b*), buckling lumen area (A_b or A_b*), etc.

If the number of folds is known a priori, a mesh which exploits rotational symmetry in the buckled configuration can be constructed, modeling only a half-wavelength of one fold. Simulations using this half-wavelength domain are often called "wedge-models" in this work. The deforming mesh of a typical wedge-model using second-order quadrilateral elements is shown in Figure 2-9. After a certain amount of deformation, the elements become too distorted and their computed stresses no longer converge upon iterative solution. This usually happens between normalized lumen area values of about 55% and 65%. This is long before contact (much less closure) of the folds, indicating that the analysis must be stopped and a new mesh created which will better accommodate the larger deformations. This procedure of remeshing is described in detail in Section 2.6.

The preferred number of folds (N) to be used in the construction of a wedge-model is determined a priori for a set of input parameters (t_o*, t_i* and E*) using the linearized buckling analysis, described in the next section.

2.4.5 Linearized Buckling Analysis

The linearized buckling analysis (LBA) is a very useful way of determining which buckling mode is preferred by a structure. A perturbation of a preloaded structure is subjected to an eigenvalue analysis, ranking each of the possible buckling modes of collapse by how much energy is required to produce that mode. The buckling mode which requires the least amount of energy to produce it is the one that is preferred by nature, the "preferred buckling mode," with the optimal number of folds, N. Other modes may be present in small quantities if large-scale imperfections cause local parts of the structure to be biased toward them. These modes, however, will be close to the preferred buckling mode, since the further a non-preferred buckling mode is from N, the more energy is required to produce it.

The general technique of the linearized buckling analysis begins with a static analysis (of a perfectly circular structure) up to a particular preload. The preload may be larger or smaller than the buckling load corresponding to the preferred buckling mode of the structure. At that point, the stiffness matrix $[K_0]$, and load vector $\{R_0\}$, are recorded. Then a small

perturbation in the load $\{\Delta R\}$ is added. The resulting change in stiffness $[\Delta K]$ is used to estimate the buckling load of the structure, assumed to occur when the determinant of the stiffness matrix goes to zero. The reason this is called a "linearized" buckling analysis is because the structure stiffness is assumed to decrease in a linear fashion between the preloaded state and the extrapolated buckling point state.

$$\det\left([K_0] - \lambda [\Delta K] \right) = 0$$

This results in the following matrix eigenproblem.

$$[K_0] \{\psi\} = \lambda [\Delta K] \{\psi\}$$

The eigenvalue λ is the necessary amplification of the incremental stiffness (and load) to bring the structure to the extrapolated buckling point. The eigenvector $\{\psi\}$ is the vector of incremental nodal displacements which describe the new (buckling) modes of deformation, and ultimately tells us the number of folds, N.

$$\{R_b\} = \{R_0\} + \lambda \{\Delta R\}$$

The above statement shows how the vector of nodal external loads is similarly amplified to determine the external loads at the buckling point. As far as we are concerned, the only number of interest is the single scalar quantity representing the radially directed equivalent external pressure (P). P_b is calculated from the preloaded state P_0 and the load increment as follows.

$$P_b = P_0 + \lambda \Delta P$$

A pictorial representation of the linearized buckling analysis is presented in Figure 2-10. (Note that it may be misleading to plot the stiffness and load as a scalar on an axis versus displacement since none of these are simple scalar quantities. One could think of the plotted quantity as a norm of each of them perhaps. Also, the case shown is not representative of the buckling of a two-layer tube, but better illustrates the method of the linearized buckling analysis.)

Figure 2-10 shows how the calculated buckling load is merely an approximation of the true buckling load, and how as the preload gets closer and closer to the buckling load, a better

Linearized Buckling Analysis

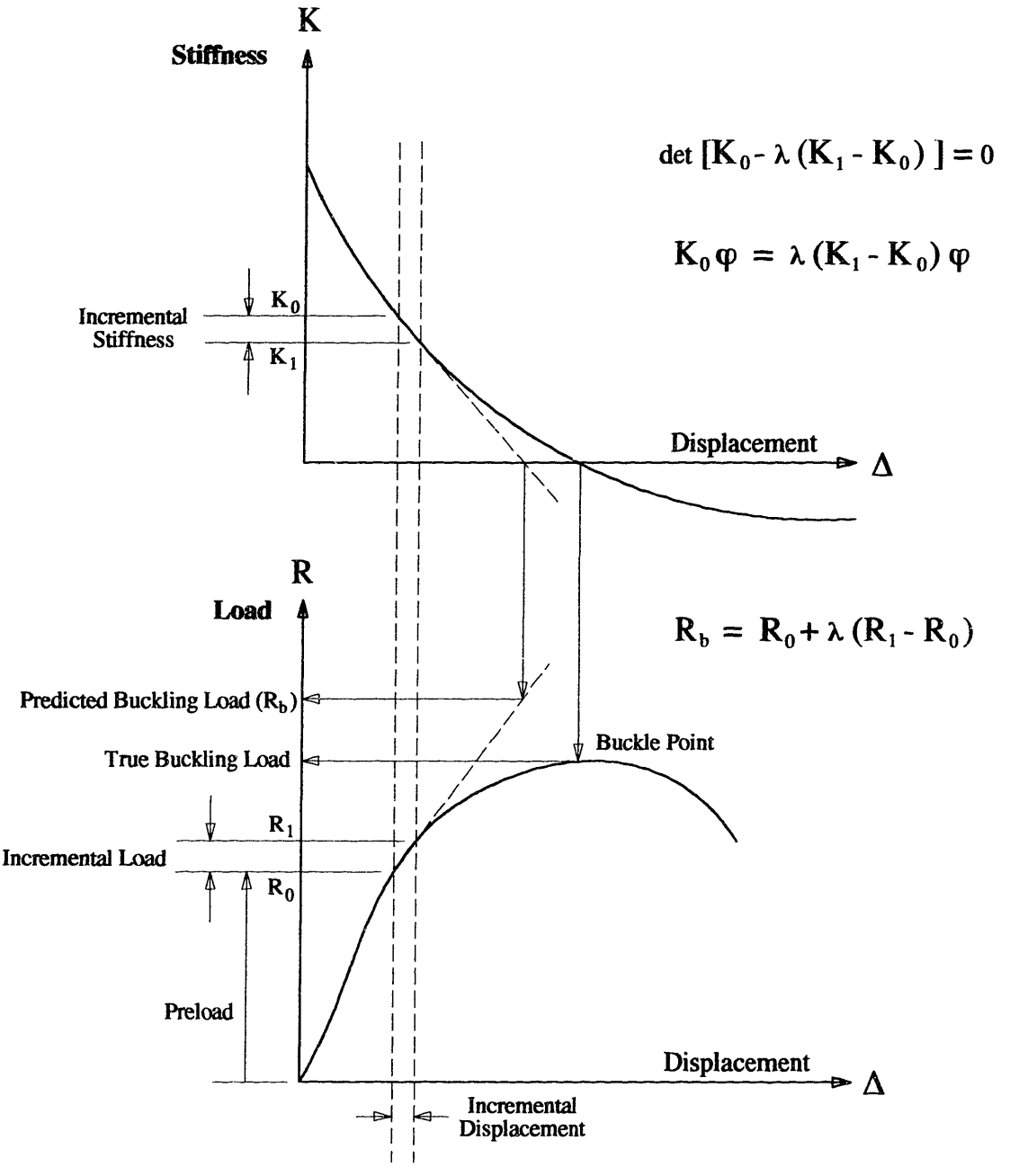

FIGURE 2-10: A graphical explanation of the linearized buckling analysis. A nonlinear analysis is performed to some user-defined preload. At that point, the structure stiffness is perturbed, and a linear extrapolation is performed to estimate the point of buckling.

guess at the true buckling load is obtained. Because our ultimate goal is to compare multiple analyses with one another, there has to be a consistent amount of this buckling approximation error among cases, preferably very close to zero. For this purpose, after the completion of a particular linearized buckling analysis, another is performed at a preload equal to the buckling load (of the lowest mode) predicted by the first analysis, resulting in a better estimation of the buckling load (and corresponding N). This procedure is repeated until the buckling load converges on the preload (thus the term "converged linearized buckling analysis").

All eigenvalue analyses result in a set of eigenvalues λ_i and their corresponding eigenvectors $\{\psi_i\}$. Each λ_i can be converted to a corresponding P_{b_i} as shown above, and

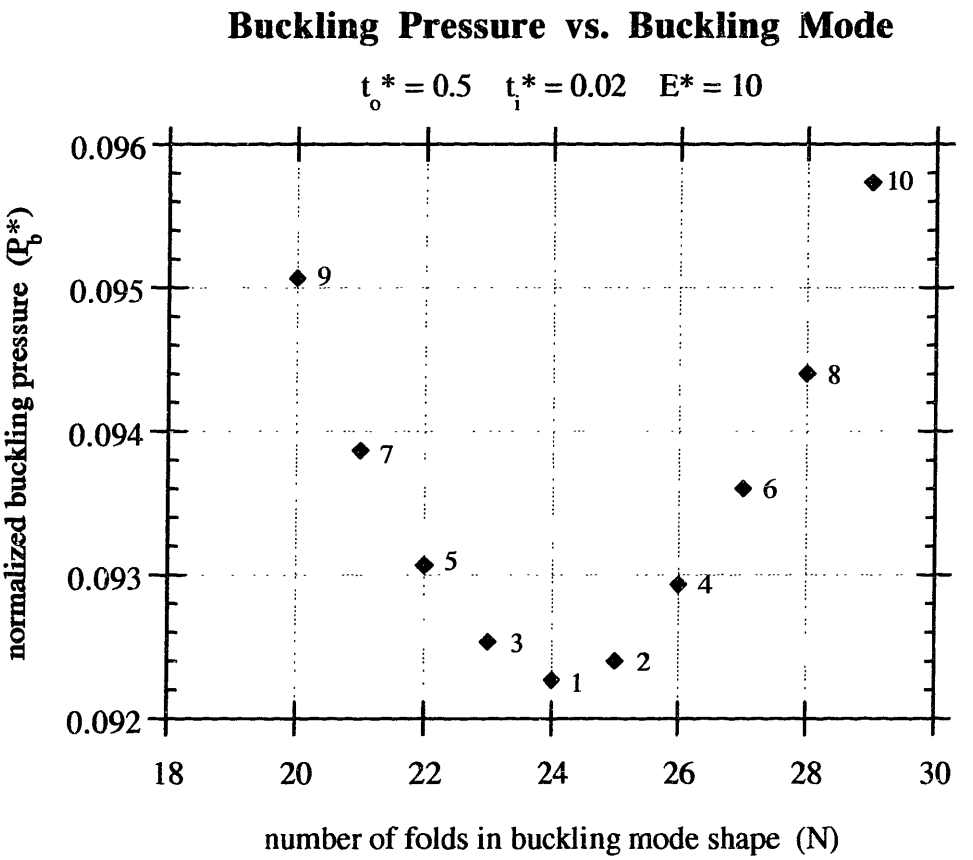

FIGURE 2-11: A plot of buckling loads (eigenvalues) vs. buckling mode shapes (eigenvectors). The lower the buckling load associated with a particular mode shape, the less energy is required to produce it and the more preferred it is.

each $\{\psi_i\}$ can be converted to an N_i either through visual observation of the buckling modes or some very simple discrete spectral analysis of them. The P_{b_i} versus N_i results from a particular converged linearized buckling analysis are shown in Figure 2-11. The ranking of the eigenmodes is such that P_{b_1} is the smallest P_b, then P_{b_2} is next smallest, etc. Note that for a two-layer tube, because P is an always increasing function of Δ (as shown in Figure 2-7) the amount of energy stored in the structure positively correlates with the load P. Thus the buckling mode with the minimum P_b (the "lowest mode") requires the least strain energy and is preferred by nature. However, the neighboring buckling modes do not require significantly more energy, so if the conditions are right in some localized portion of the tube, those modes may be observed to some smaller degree as well. That is why in a "real" structure which has many built-in imperfections, the activated buckling modes will be clustered around N with the maximum response in the "preferred" N which is dictated by the gross (or average) geometry and material properties of the structure.

Figure 2-11 shows the buckling modes falling into a parabola-like pattern. To achieve better accuracy with future curve fits and models (see Section 3.1.2), non-integral values of N are estimated by fitting the lowest three modes to a parabola and assuming that the "preferred" state of the structure is the one at the minimum of the parabola. From here onward, that minimum $(N_{min}, P_{b_{min}})$ will be referred to as simply (N, P_b).

2.5 Imperfection Issues

This section is a brief discussion of the concerns that arise regarding the necessity of imperfections in the initial structure geometry and the impact those imperfections have on the resulting number of folds in the structure's response. In most instances it is possible to examine the response from a two-layer tube that is known to buckle with a particular number of folds (N), using static analyses of wedge-models. However, with this method, progressing from the point of buckling onward assumes that there is no change in N throughout the course of the deformation. Section 2.5.2 addresses the validity of that assumption numerically. The assumption is also verified for actual airways in Section 5.2.

2.5.1 Imperfection Magnitude

In order to observe buckling in these numerical models of two-layer tubes, it is necessary that there be some component to them which is not perfectly axisymmetric. If there should be any type of symmetry to all of the geometry, material properties, confinement and loading of a structural model, then the response it exhibits will have that symmetry also. Therefore it is necessary to break those symmetries somehow, thus increasing the model's solution space to include all types of response with any type of symmetry, or none at all if that is the "best" (most energy-efficient) solution.

Once the number of folds preferred by a particular two-layer model is determined, say, by a linearized buckling analysis, that number of folds can be assumed constant throughout the rest of the deformation. Then by assuming that symmetry in the two-layer tube response, a

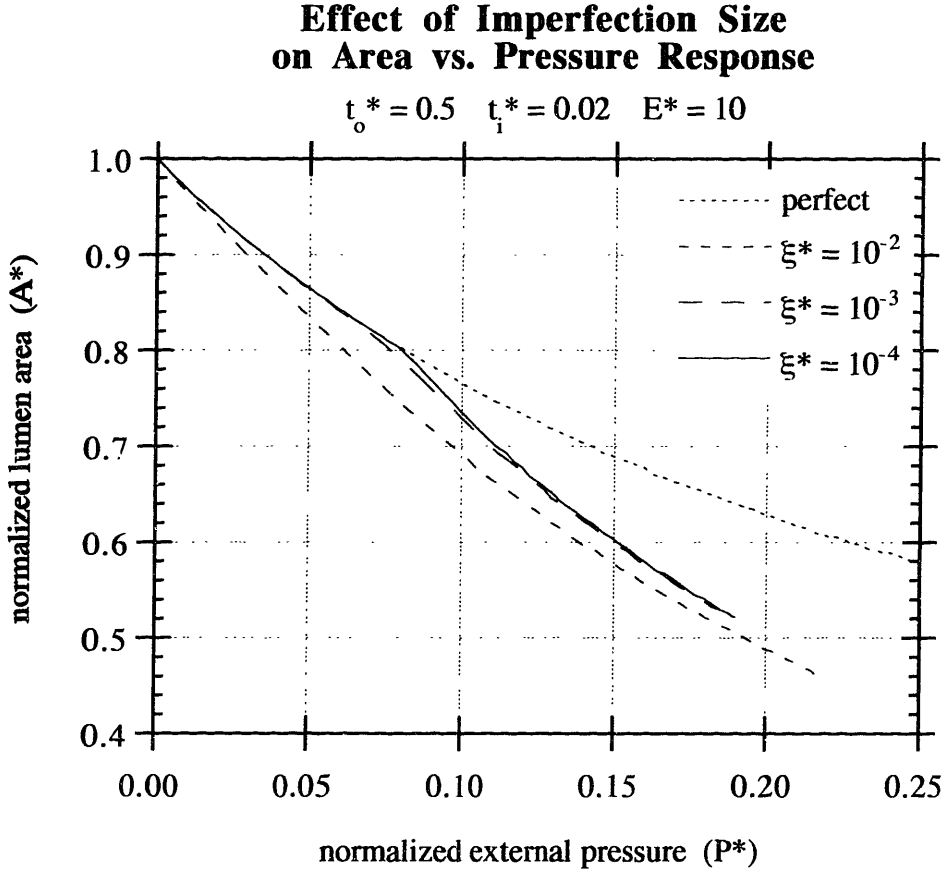

FIGURE 2-12: Effect of imperfection size (ξ^*) on the simulated A*(P*).

wedge-model of only one-half of a fold's wavelength need be modeled in the collapse analysis. Still, a non-axisymmetric perturbation in the geometry (or loading) must be imposed in the wedge-model to induce buckling of the inner layer. The technique used here will be to introduce minute imperfections in the geometry, so small that they cannot be seen unless the model is magnified greatly. However, if the imperfection is too small, the symmetry will not be broken and no buckling will be observed. The measure of imperfection size (and fold size) used in this work is defined as follows.

$$\text{imperfection or fold amplitude:} \quad \xi \equiv \frac{1}{2}(\text{largest inner radius} - \text{smallest inner radius})$$

$$\text{normalized imperfection or fold amplitude:} \quad \xi^* \equiv \frac{\xi}{R}$$

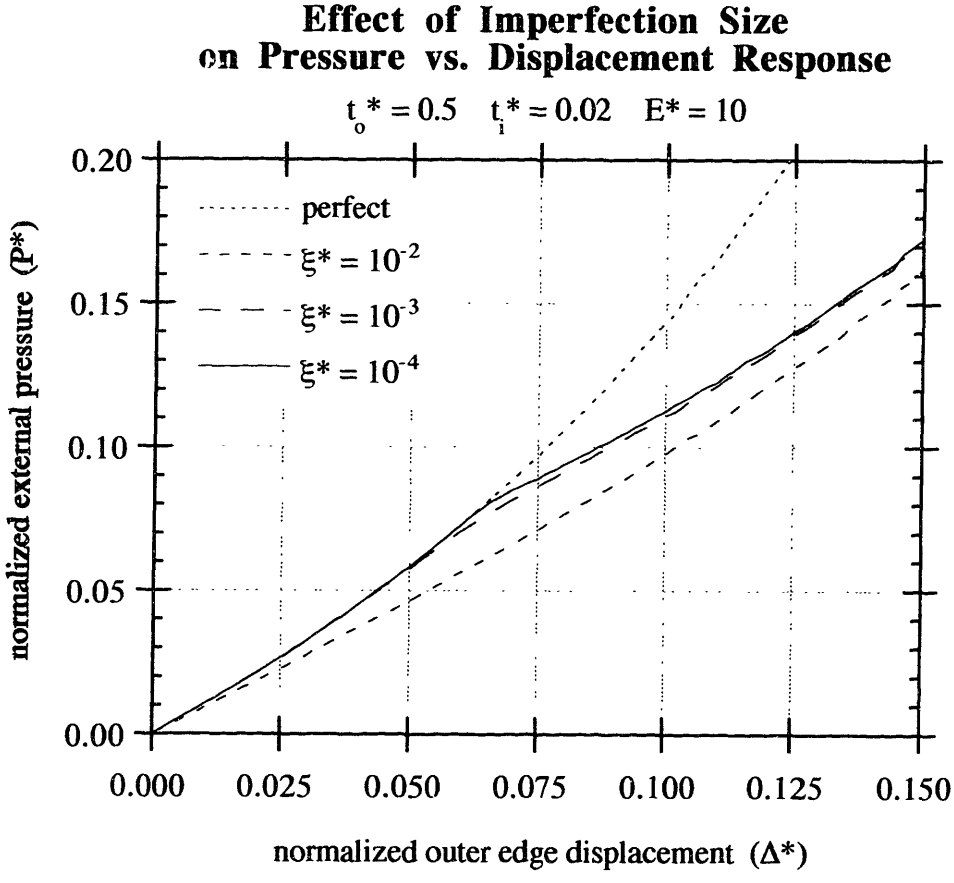

FIGURE 2-13: Effect of imperfection size (ξ^*) on the simulated $P^*(\Delta^*)$.

If ξ^* is less than the machine precision, the symmetry will not be broken. Figure 2-12 shows how the area-pressure curve is affected by increasing the imperfection amplitude. If ξ^* is less than 10^{-4}, sometimes buckling is not observed. Note that as the imperfection grows greater in size, the bifurcation is smoothed out, leaving a pressure-area response that would hardly indicate that a buckling event has occurred.

Figure 2-13 shows the same comparison, except between pressure-displacement curves. Differentiating this curve, that is, finding $dP^*/d\Delta^*$, yields a measure of "airway stiffness," shown in Figure 2-14. Note that at buckling, the airway stiffness drops significantly. If the imperfection is slight, the transition in airway stiffness is abrupt. If the imperfection is large, there is no abrupt transition – it is as if the two-layer tube has a stiffness between that

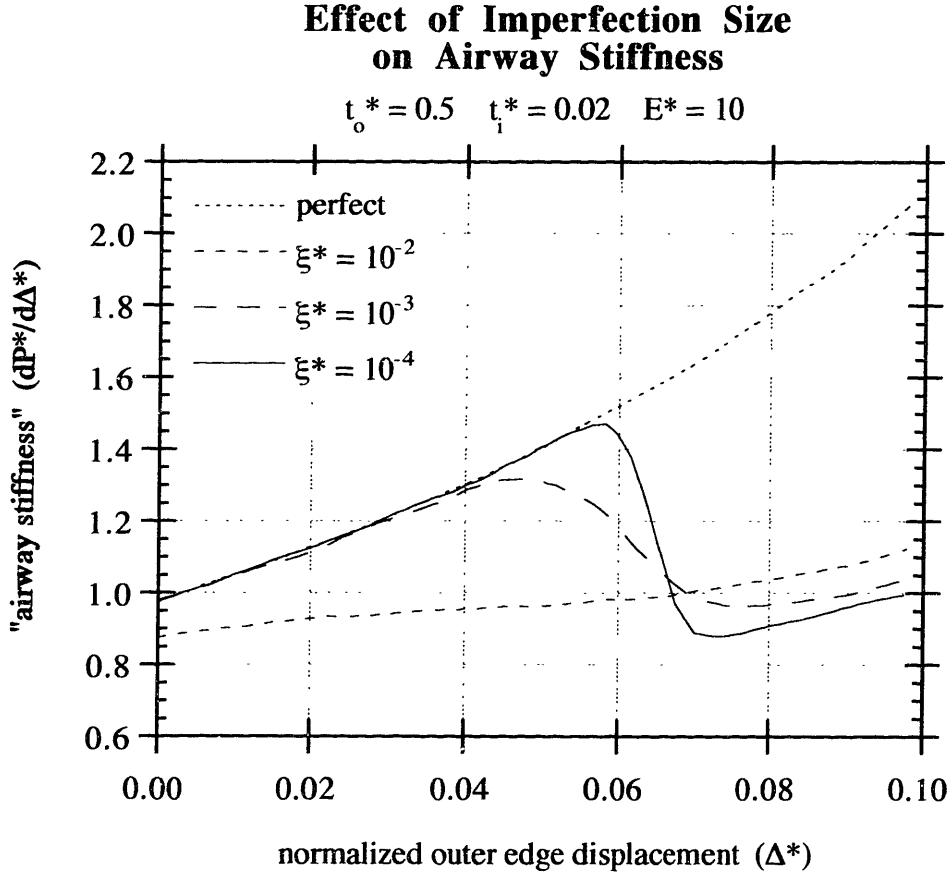

FIGURE 2-14: Effect of imperfection size (ξ^*) on the simulated $dP^*/d\Delta^*(\Delta^*)$. This measure gives an idea of the two-layer tube's stiffness. Small imperfections cause an abrupt buckling event; larger imperfections tend to smooth it out.

of the buckled and non-buckled solutions. Note, however, that regardless of what size the imperfection is, the late-response solutions all converge to the same curve, indicating that the choice of imperfection size is somewhat arbitrary and depends only upon whether or not one wants to see a sharp or gradual or virtually indistinguishable transition from pre-buckling to post-buckling behavior.

2.5.2 Spectral Analysis

All the methods of inducing buckling in a collapse analysis discussed so far require the predetermination of N from a previous analysis, followed by the assumption that N does not change during the entirety of the collapse. This section discusses another technique, which requires neither of these (but does turn out to be more "expensive" computationally,

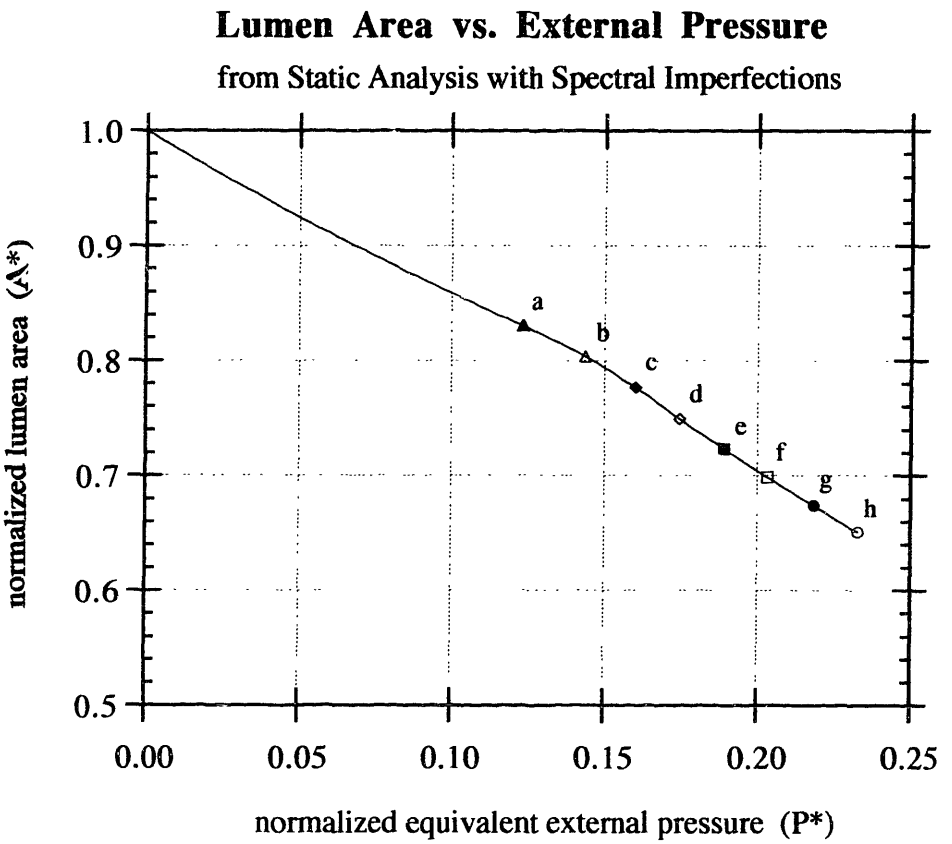

FIGURE 2-15: Pressure-area curve generated from a spectral analysis using a high-resolution mesh. The letters label area-pressure states that correspond to the folding profiles shown in Figure 2-16.

requiring many more degrees of freedom for the same accuracy of the solution). The basic technique is to perturb all of the possible modes of collapse and observe which modes are amplified in the response. A discrete fourier transform is applied to the nodal displacements along the inner boundary to go from the displacement domain to the frequency of folds (or mode number) domain. This way, the dominant mode number can be tracked throughout the course of the collapse. The graph of the discrete fourier transform versus mode number provides a "folding profile" at selected load levels, indicating how much energy is being put into each of the possible mode shapes.

Figure 2-15 shows an area-pressure curve generated by a simulation that makes use of these spectral imperfections. The lettered points along the curve indicate states at which

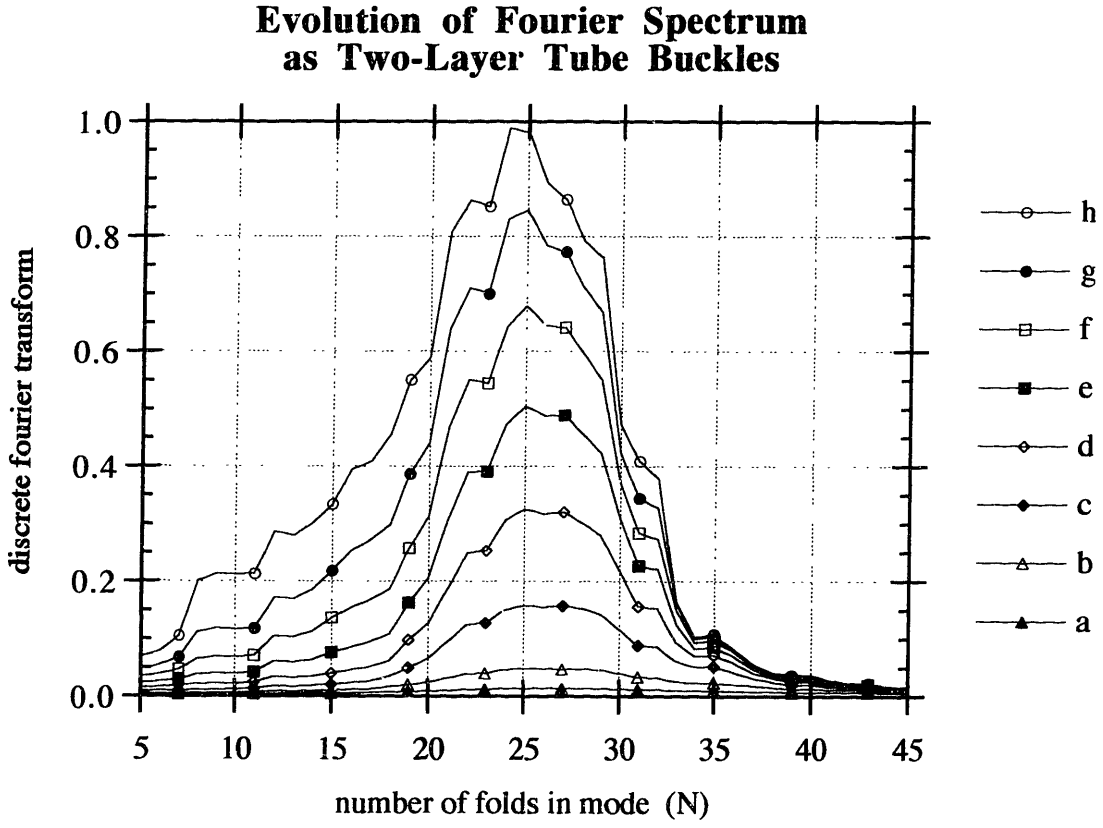

FIGURE 2-16: Folding profiles showing how imperfections evolve into folds during the process of buckling. Small flat profiles indicate imperfections; larger peaked profiles indicate folding. As collapse progresses, the preferred number of folds decreases slowly (but not significantly).

discrete fourier transforms were performed on the deformed geometry. Figure 2-16 shows the results of these transforms. Note that the early folding profile starts out with a very small amount of all modes. As collapse progresses, a peak forms about the preferred buckling mode, indicating that neighboring modes are present, but are not as prevalent as the preferred mode. With continued collapse, it can be seen that the preferred N is decreasing slightly.

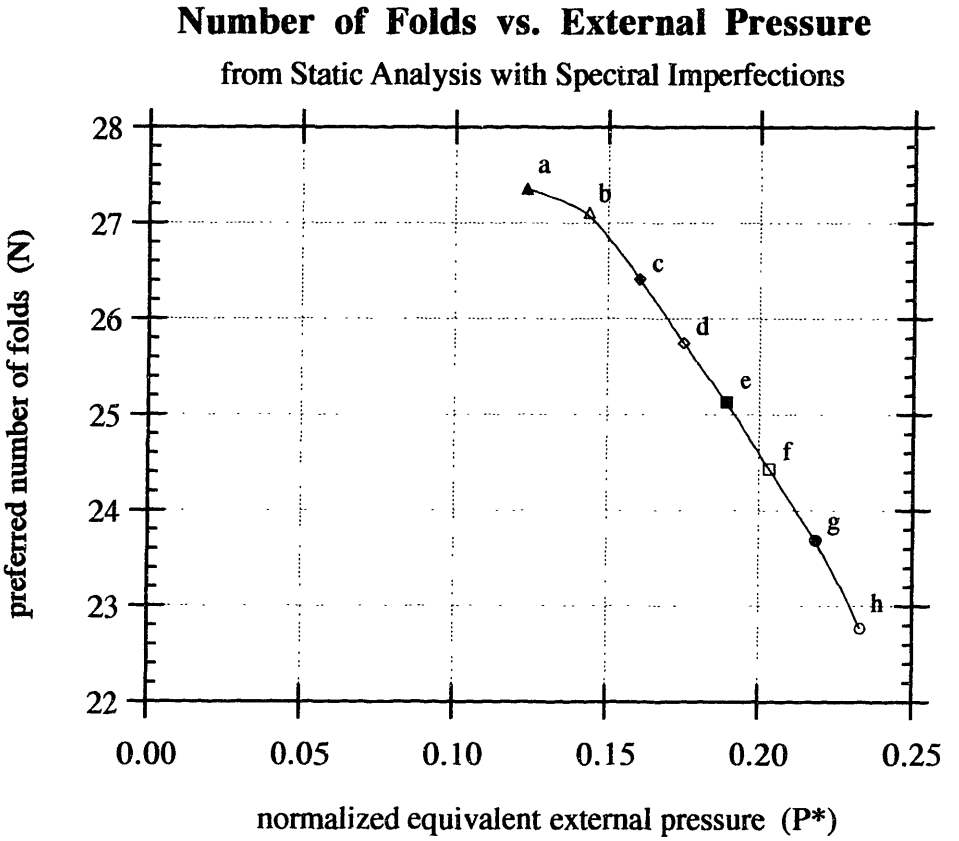

FIGURE 2-17: Preferred (median) N as a function of the normalized lumen area (A*) showing how N varies throughout the collapse.

The way that preferred number of folds (N) is defined in such analyses is the "median" mode number, or the mode number such that half of the area under the folding profile lies to the left of N and half lies to the right of N. The evolution of N through the course of the example analysis is shown in Figure 2-17. Note that before the buckling point, the calculated value of N is irrelevant because there are no such "folds" yet, only magnified

imperfections. Naturally, if one starts with a flat imperfection profile for a mesh that has 200 nodes around the internal boundary, the calculated value of N will be 100. It is better to view N versus the amplitude of the fluctuation in radial displacements at the internal periphery, to see if we would deem the undulations to be "imperfections" or true "folds." Figure 2-18 shows a typical plot of the dominant mode (N) versus the normalized imperfection/fold magnitude (ξ^*) defined in Section 2.5.1. When $\xi^* < 0.015$, the fluctuation is merely due to imperfections (the size of the undulations is very small). Once $\xi^* > 0.015$, the fluctuation is due to folding into a buckling pattern (the size of the undulations is appreciable). The boundary dividing these two regimes is the buckling point.

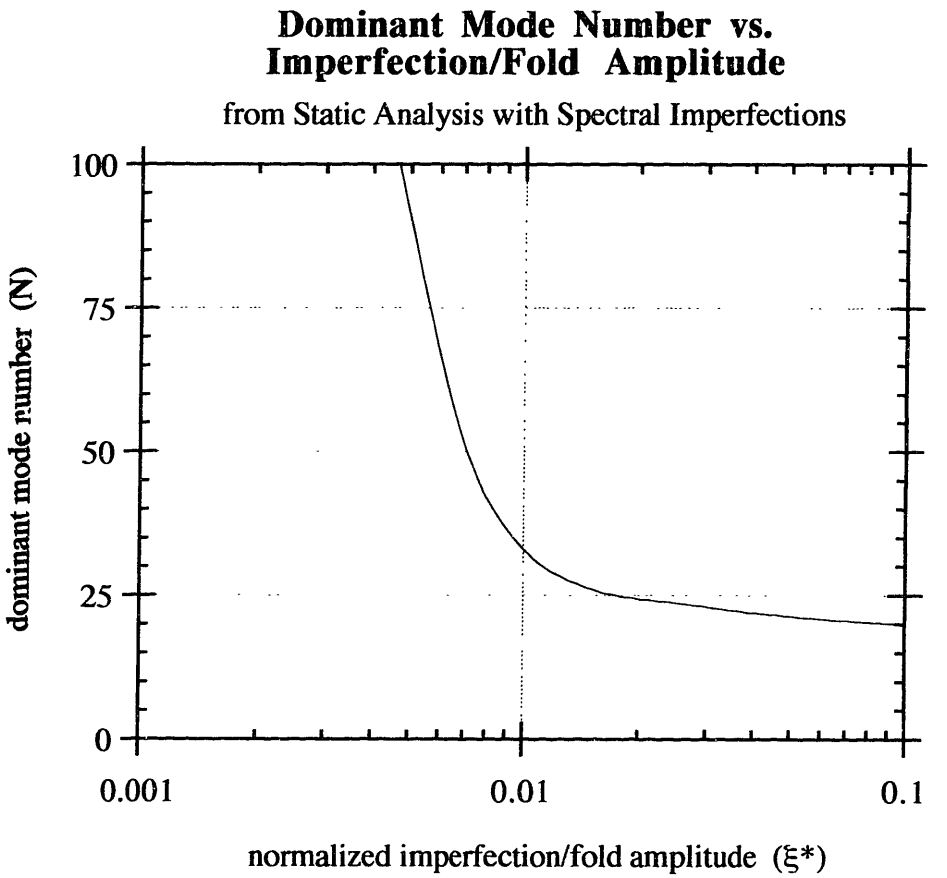

FIGURE 2-18: Preferred (median) N as a function of the normalized fold/imperfection amplitude (ξ^*). Large prebuckling values of N indicate that the imperfections started out uniformly. Once buckling occurs, the fold amplitude becomes significant and N decreases slowly.

This spectral analysis technique is used whenever it is impossible or not advisable to use a linearized buckling analysis, followed by a wedge-model collapse analysis, as in the poroelastic simulations of Chapter 8. Note that once buckling has occurred, the preferred number of folds (N) is decreasing, but at a very small rate. To some extent, this justifies the assumption that N remains constant throughout the collapse, supporting the use of wedge-models.

2.6 Remeshing Techniques

2.6.1 Implementation of Remeshing

At some point during the collapse of a half-wavelength wedge-model, the finite element simulation is unable to continue because the elements have distorted too much to provide an accurate representation of the material. What is necessary is a new simulation with a complete redefinition of the finite element domain, including what are now "initial" stresses that have been taken from the last reliable computed state of the previous analysis. Then the new simulation is begun, adding more and more load until the elements are again distorted to their limit. At the point where the elements stop deforming, the computed element stresses fail to converge within a reasonable number of iterations, and the simulation stops. A quadrilateral element, for example, performs best when it is rectangular. As it is distorted or "sheared" (into a parallelogram shape), its accuracy of interpolation lessens and the stresses are less likely to converge. The goal of remeshing is to replace highly distorted elements with more rectangular ones.

The remeshing routine begins by reading from the stopped simulation the nodal locations along (1) the inner surface of the inner layer, (2) the outer surface of the outer layer and (3) the interface between the two layers. The first step in creating the new mesh is to define new nodes along the interface, then to begin defining nodes outward toward the outer edge such that the sides of the new elements are as perpendicular as possible to the previous line of nodes. After the geometry of the outer layer is redefined, the inner layer is similarly generated. To relieve the bunching of elements that occurs along the top edge of the wedge domain and keep the elements along the bottom from getting too long, there is the ability for elements to be "created" along the bottom edge and "re-absorbed" along the top edge from one element layer to the next one external to it. From one mesh to the next, element stresses are extrapolated from the integration points to the nodes of the original mesh (using

the ABAQUS software), then interpolated to the new nodal locations in the replacement mesh (using routines developed by the author).

The progression of remeshing is illustrated in Figures 2-9, 2-19 and 2-20. This example shows a collapse analysis using rectangular elements, although sometimes it is beneficial to use meshes of triangular elements (created by chopping each quadrilateral into four triangles along its diagonals). Refer back to Figure 2-9 to see the original mesh and how it

Deformed Wedge-Model Mesh:

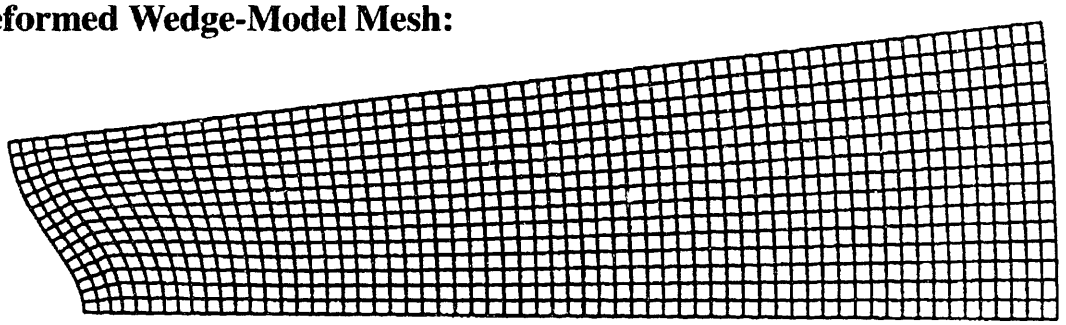

After Remeshing:

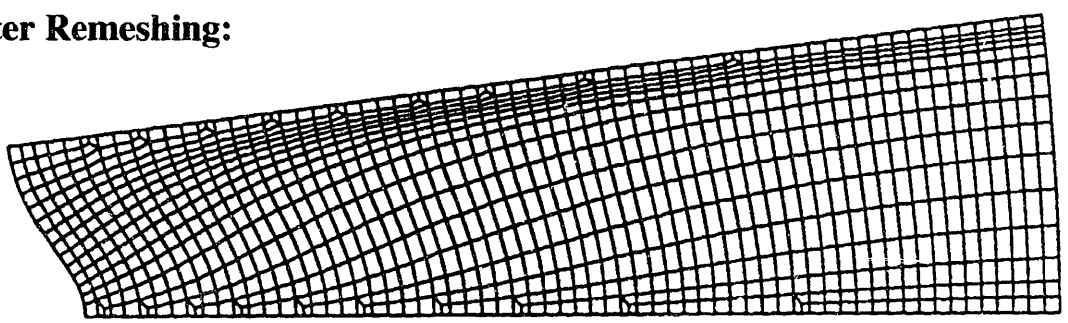

FIGURE 2-19: Deformed mesh plots before and after the remeshing algorithm is applied. Distorted elements are removed from the highly shearing region and introduced in areas they are less likely to cause numerical problems.

deforms into a buckled shape. The leftmost three layers of elements constitute the inner layer, and all others external to them constitute the outer layer. The only difference between the elements from one layer to the next is their E-value. Note that the elements which are being sheared most lie halfway up the length of the inner layer. It is there that new elements with more perpendicular corners are placed. Figure 2-19 shows the deformed mesh and the mesh that it is replaced with. The transition regions lining the top and bottom surfaces do not undergo much distortion in the model deformation; their original amounts of distortion are not amplified by continued collapse.

After Successive Remeshings:

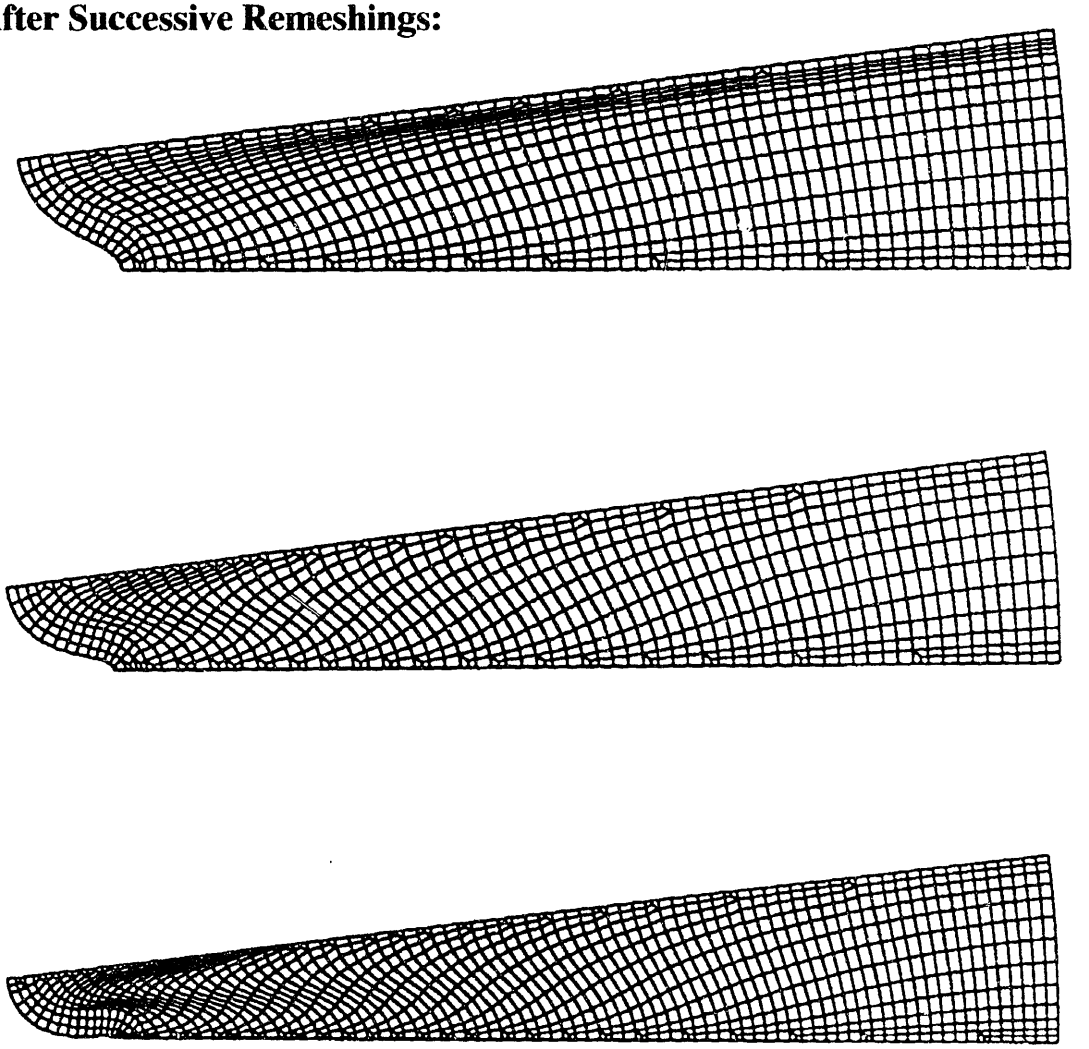

FIGURE 2-20: Successive remeshings can be done up to and past the point of fold closure.

Remeshing continues until eventually (and very gradually) the folds press up against one another (see Figure 2-20). The inner surface is constrained to not penetrate beneath the horizontal symmetry surface, thus modeling fold contact. There turns out to be no jump in the force generated when the folds touch since it happens very gradually and the large stress concentration at the point where the fold is closing is where the strain energy is increasing most rapidly.

2.6.2 Smoothing and Extrapolation

The pressure-area output from several successively remeshed simulations is shown in Figure 2-21. The data points from one mesh to the next alternate between "X" and "O"

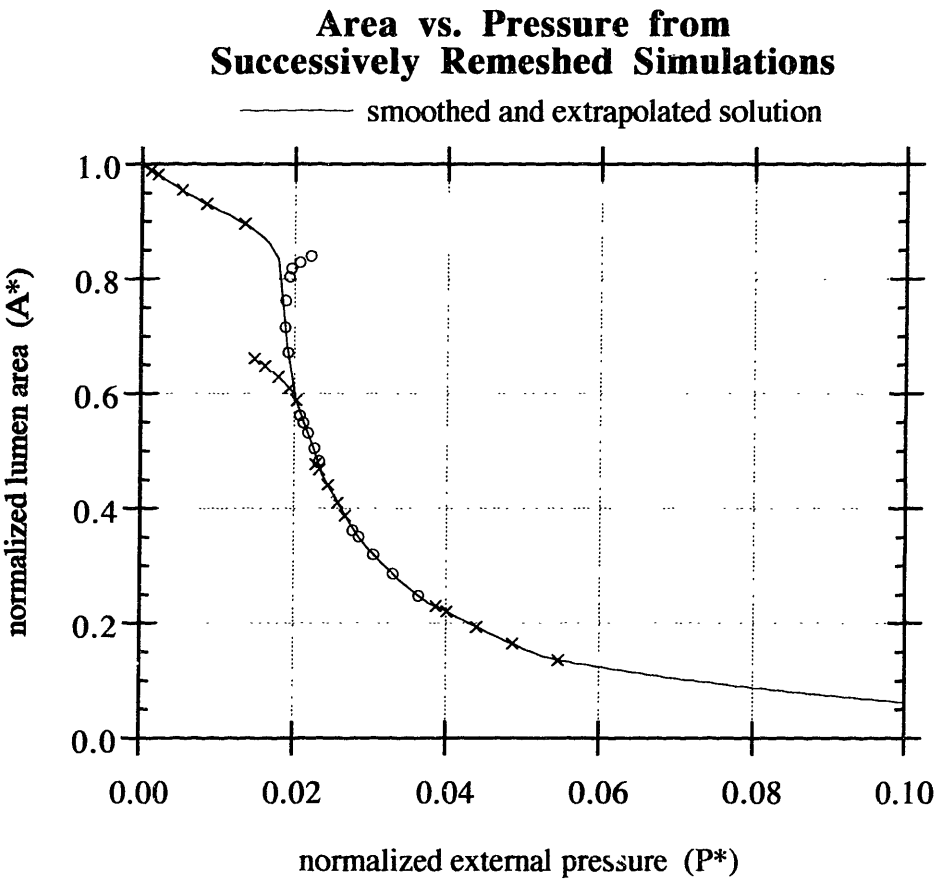

FIGURE 2-21: Area-pressure output from several succeeding remeshed simulations better models the late postbuckling response. The curve is drawn to smooth out the error introduced because of remeshing and to extrapolate to further collapse.

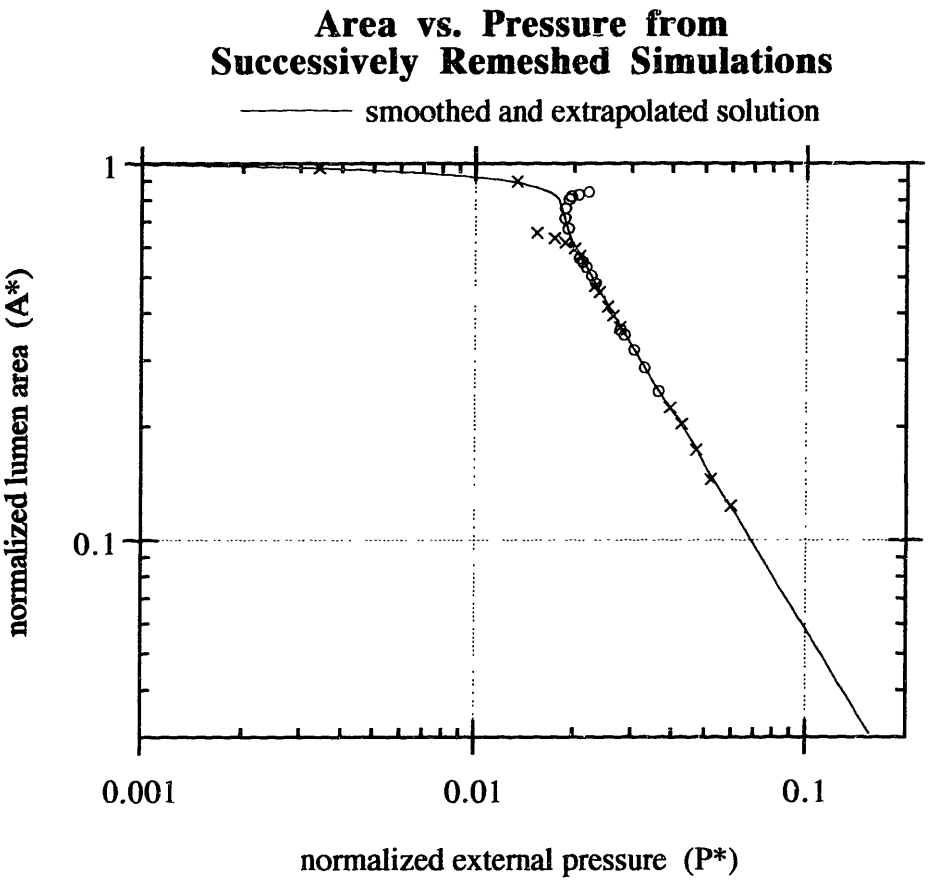

FIGURE 2-22: Log-log presentation of the data from Figure 2-21 better supports the fitting of a power law relationship to the remeshed two-layer tube collapse data.

markers. After each remeshing, error is introduced into the model, and this error dissipates within a few new load increments. Since the raw output from the simulations is somewhat confusing, it is smoothed by fitting to a power law curve. This is more readily acceptable upon viewing the raw data in a log-log format (as in Figure 2-22).

The remeshing scheme is really only partially successful. For many simulations, the scheme will allow collapse down to lumen areas less than 20%, while for others it barely passes 40%. For some simulations, quadrilateral elements are more successful, while for others triangles are. There is no pattern to whether or not a particular remeshing case will be successful; it seems to be the result of so-called "numerical accidents" where nonlinear element instability is insufficiently controlled.

For future remeshing schemes, the author recommends two things: (1) to use more of a "free" or random placement of remeshed nodes and elements, and (2) to use a finite element package which has a reputation for better implementation than ABAQUS. Navigating the pitfalls in ABAQUS' implementation (and the corresponding lack of documentation of them) was the greatest source of delay and frustration for the author. Another technique that the author would have liked to pursue had time permitted was the solution of this problem with boundary element techniques, where remeshing should be trivial.

2.6.3 Initially Folded Airway Simulations

Using the remeshing scheme described above, the situation where the airway is initially folded before the smooth muscle begins constricting can be modeled relatively easily. Some simulations were performed up until a point just past buckling (picked somewhat arbitrarily) then the analysis was continued after remeshing and relieving all stress. The result was a pressure-area curve which was virtually a translation of the unfolded case, so the initial folding did not seem to have an appreciable effect.

This complication brings up some difficult issues, however. For instance, the amount of pre-existing folding may vary around the inner perimeter of the airway, and that would necessitate a more elaborate meshing scheme. Exactly how much folding there is in general seems to vary also. If it is desired to truly understand the effect of initial folding, it would be more rigorous to construct a finite element mesh using morphometric image data, mapping the observed geometry to the nodes and elements directly. Simulations presented here are based on gross or average geometries which are uniform around the circumference of the model.

CHAPTER 2 REFERENCES

1. Abeyaratne R. Lecture notes from M.I.T. course 2.072, Mechanics of Continuous Media. Spring 1995.

2. Allen HG. *Analysis and Design of Structural Sandwich Panels*. Pergamon Press, London, 1969. pp. 156-163.

3. Anand L. Lecture notes from M.I.T. course 2.072, Mechanics of Continuous Media. Spring 1994.

4. Bates JHT, Martin JG. A theoretical study of the effect of airway smooth muscle orientation on bronchoconstriction. *J. Appl. Physiol.* 69(3): 995-1001, 1990.

5. Bathe K-J. *Finite Element Procedures in Engineering Analysis.* Prentice-Hall, Toronto, 1982.

6. Bathe K-J. Lecture notes from M.I.T. course 2.093, Computer Methods in Dynamics. Spring 1993.

7. Bathe K-J. Lecture notes from M.I.T. course 2.094, Theory and Practice of Continuum Mechanics. Fall 1993.

8. Cook RD, Malkus DS, Plesha ME. *Concepts and Applications of Finite Element Analysis,* 3rd Ed. John Wiley & Sons, New York, 1989.

9. Fay JA. *Introduction to Fluid Mechanics.* MIT Press, Cambridge MA, 1994. pp. 288-293.

10. Flaherty JE, Keller JB, Rubinow SI. Post buckling behavior of elastic tubes and rings with opposite sides in contact. SIAM J. Appl. Math. 23(4): 446-455, 1972.

11. Fung Y-C. *Biomechanics: Motion, Flow, Stress and Growth.* Springer-Verlag, New York, 1990.

12. Gunst SJ, Warner DO, Wilson TA, Hyatt RE. Parenchymal interdependence and airway response to methacholine in excised dog lobes. *J. Appl. Physiol.* 65(6): 2490-2497, 1988.

13. Gurtin ME. *An Introduction to Continuum Mechanics.* Academic Press, Boston, 1981.

14. Han HC, Fung YC. Residual strains in porcine and canine trachea. *J. Biomechanics.* 24(5): 307-315, 1991.

15. Hibbitt, Karlsson & Sorensen, Inc. *ABAQUS Theory Manual,* ver. 5.5. Pawtucket RI, 1995.

16. Lei M, Ghezzo H, Chen MF, Eidelman DH. Airway smooth muscle orientation in intraparenchymal airways. *J. Appl. Physiol.* 82(1): 70-77, 1997.

17. Okazawa M. Personal communication, Summer 1994.

18. Roberts CR. Is asthma a fibrotic disease? *Chest.* 107(3): 111S-117S, 1995.

3. General Results of the Two-Layer Model

3.1 Linearized Buckling Analysis Results

3.1.1 Perturbations of Parameters About a Base State

Using ABAQUS, linearized buckling analyses were performed (until convergence – see Section 2.4.5) on the simple two-layer model with a particular choice of parameters, somewhat arbitrary, although perhaps characteristic of a small and somewhat thickened airway. These "base state" values are as follows:

$$t_o^* = 0.5 \qquad t_i^* = 0.02 \qquad E^* = 10$$

Next buckling analyses were performed to investigate the effect of an increase or decrease in each of the parameters, independent of the other two. In all of the plots in this section, the analysis results show as data points, then these points are connected with a curve to indicate trends over the chosen ranges.

The three output variables reported from these analyses are the preferred number of folds in the buckling pattern (N), the normalized buckling smooth muscle equivalent external pressure or simply "buckling pressure" (P_b^*) and the normalized buckling lumen area or "buckling area" (A_b^*). The buckling pressure is normalized by the elastic modulus of the outer layer (E_o). The buckling area is normalized by the original lumen area ($\pi(R-t_i)^2$), so that 1 implies completely open and 0 is completely collapsed. P_b^* and A_b^* are the normalized pressure and area at the buckling point. The number of folds is hypothesized to be critical in determining how severe the airway collapse will be. This hypothesis is tested in Section 3.3, which reports the results from static analyses. The buckling pressure gives an idea of the effort that is required to buckle the tube, and the buckling area gives an idea of how much the tube has collapsed at the point of buckling.

It is important to note that the results presented in this section apply only to the phenomenon of multi-fold buckling of the stiff inner layer into multiple folds, and not the peanut-shaped buckling of the outer layer. For most of the hypothetical tubes analyzed here, multi-fold buckling is greatly preferred over peanut-shaped buckling, though the latter is indeed possible. If the buckling load for multi-fold buckling grows very large (as it does

in Figure 3-5 at high values of t_i*), it is possible that some peanut-shaped buckling will occur along with multi-fold buckling.

On each of the plots in this section, the x-axis scale for each plot with a particular input parameter (be it t_o*, t_i* or E*) is the same. Similarly, each y-axis has the same scale for all plots with the same ordinate (N, P_b* or A_b*). Note that the ranges of each input parameter shown span exactly one order of magnitude. After demonstrating the effects of each of the three input parameters on each of the three output parameters separately, some summary plots are shown with remarks regarding how strong an effect each of the input parameters has relative to the others over the respective parameter ranges.

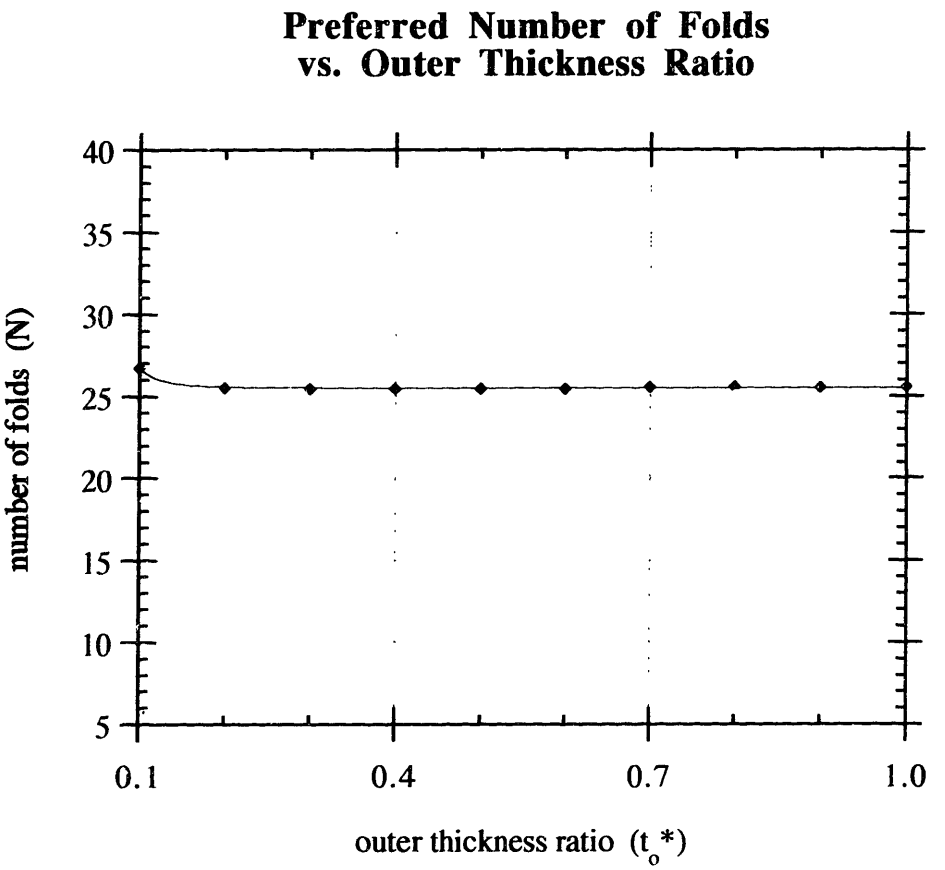

FIGURE 3-1: Linearized buckling analysis results: N vs. t_o* for perturbative cases.

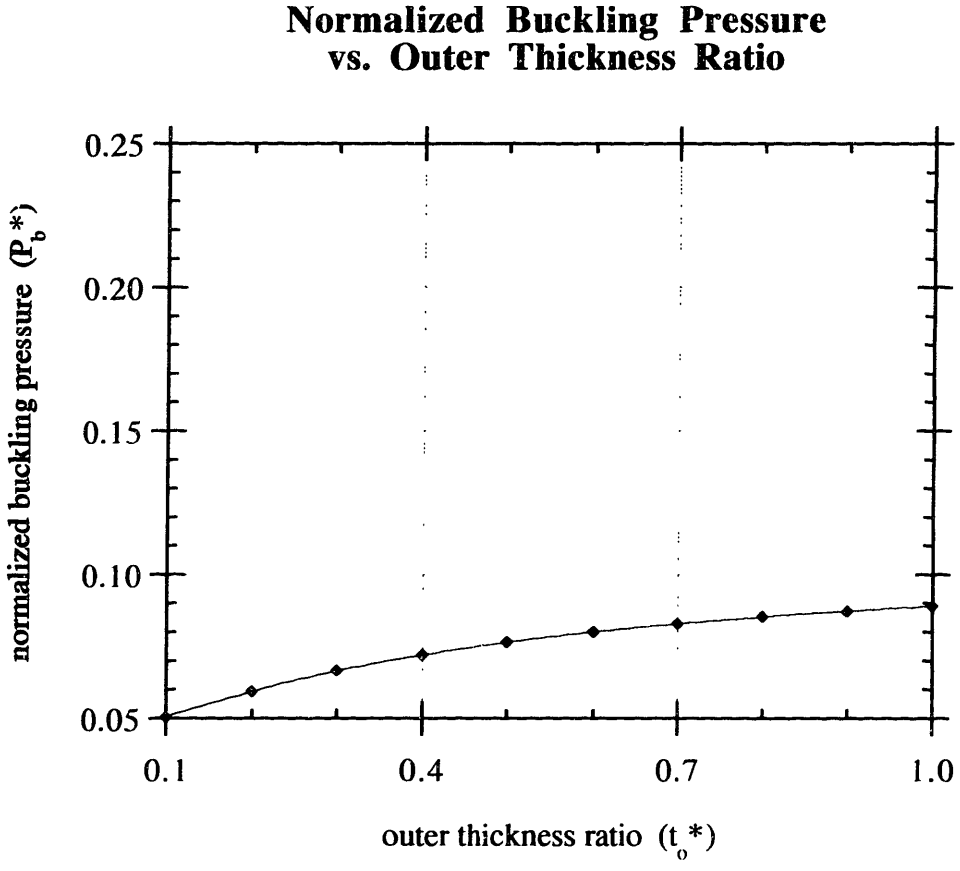

FIGURE 3-2: Linearized buckling analysis results: P_b* vs. t_o* for perturbative cases.

Effect of Outer Thickness Ratio (t_o):*

The outer thickness ratio appears to have little effect on the preferred number of folds in a multi-fold buckling pattern, particularly above a threshold value (which depends on t_i* and E*). The pressure required to buckle the tube appears to increase logarithmically with increased outer thickness. As with the preferred number of folds, the area at buckling is rather insensitive to increasing outer thickness, although buckling does appear to happen at a marginally earlier point in the collapse. All three of the outputs are becoming less and less sensitive to the outer thickness as it increases (their derivatives are tending toward zero). This makes sense physically since material is being added further and further away from the site of the buckling. After a point (determined more by t_i* and E*) one may as well add an infinite amount of outer thickness – the amount of occlusion at buckling, the

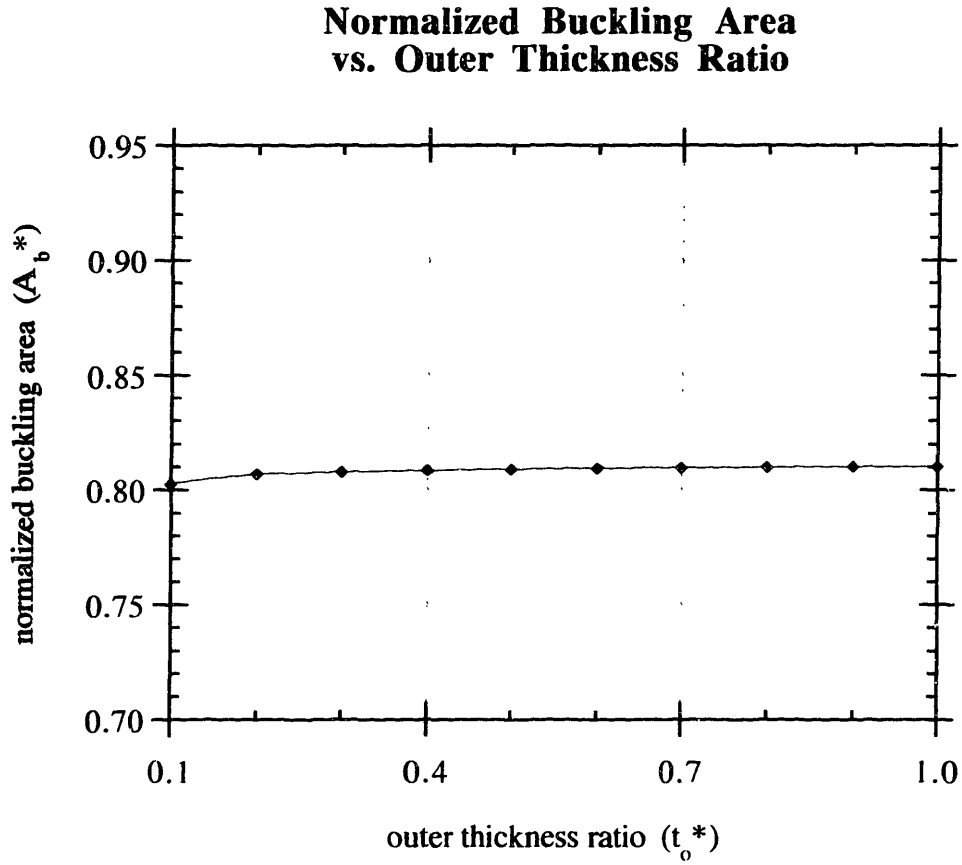

FIGURE 3-3: Linearized buckling analysis results: A_b* vs. t_o* for perturbative cases.

pattern of buckling and the amount of energy going into the inner layer area all unchanged. The only appreciable effect is an increase in P_b* since more energy has to be put into the outer layer before it is transferred into the inner layer. Increasing the outer layer thickness simply "adds padding" around the structure and does not alter the character of multi-fold buckling.

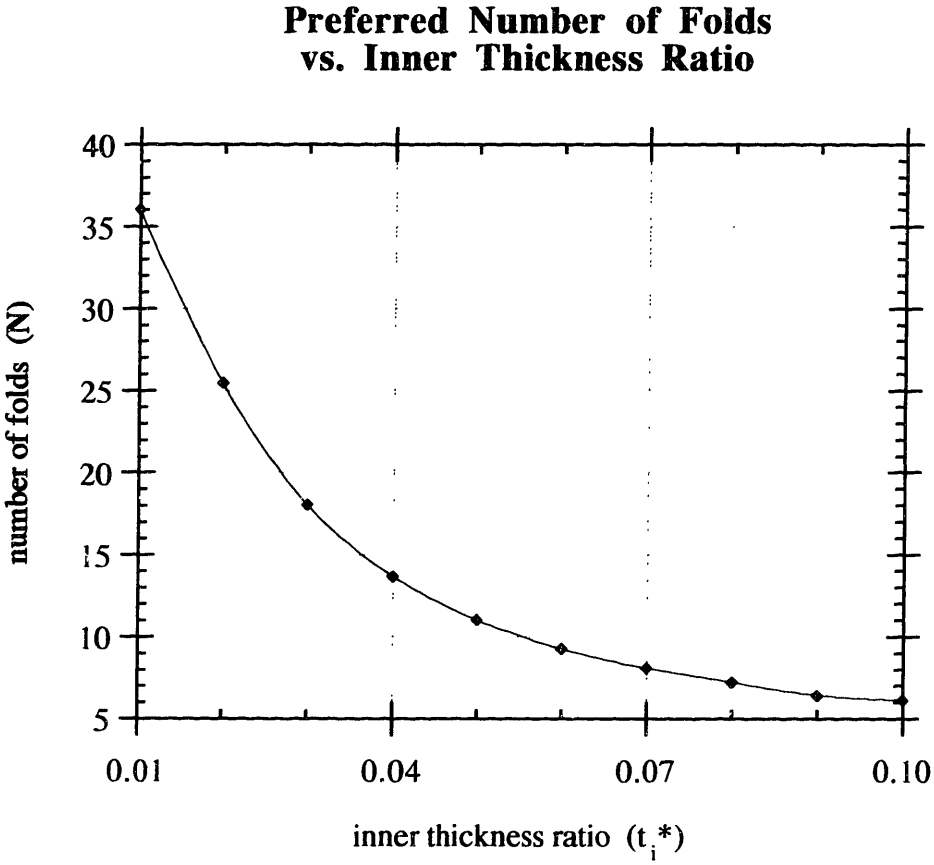

FIGURE 3-4: Linearized buckling analysis results: N vs. t_i* for perturbative cases.

Effect of Inner Thickness Ratio (t_i):*

The inner layer thickness appears to have a strong effect on the buckling pattern. As the inner thickness is increased, the preferred number of folds decreases. For this particular choice of t_o* and E*, doubling the inner layer thickness roughly halves the expected number of folds. An increase in the inner thickness also markedly increases the pressure required to buckle the structure. Unlike most of the other trends reported in this section, the speed of increase in P_b* with increasing t_i* does not seem to wane at larger values of t_i* – that is, the increase does not appear to taper off asymptotically or even logarithmically. In fact, it appears linear even at the larger t_i* values. The effect of the inner thickness on the amount of occlusion at buckling appears more complex, obtaining some optimum around t_i* = 0.03 and requiring marginally more collapse at other values. The inner

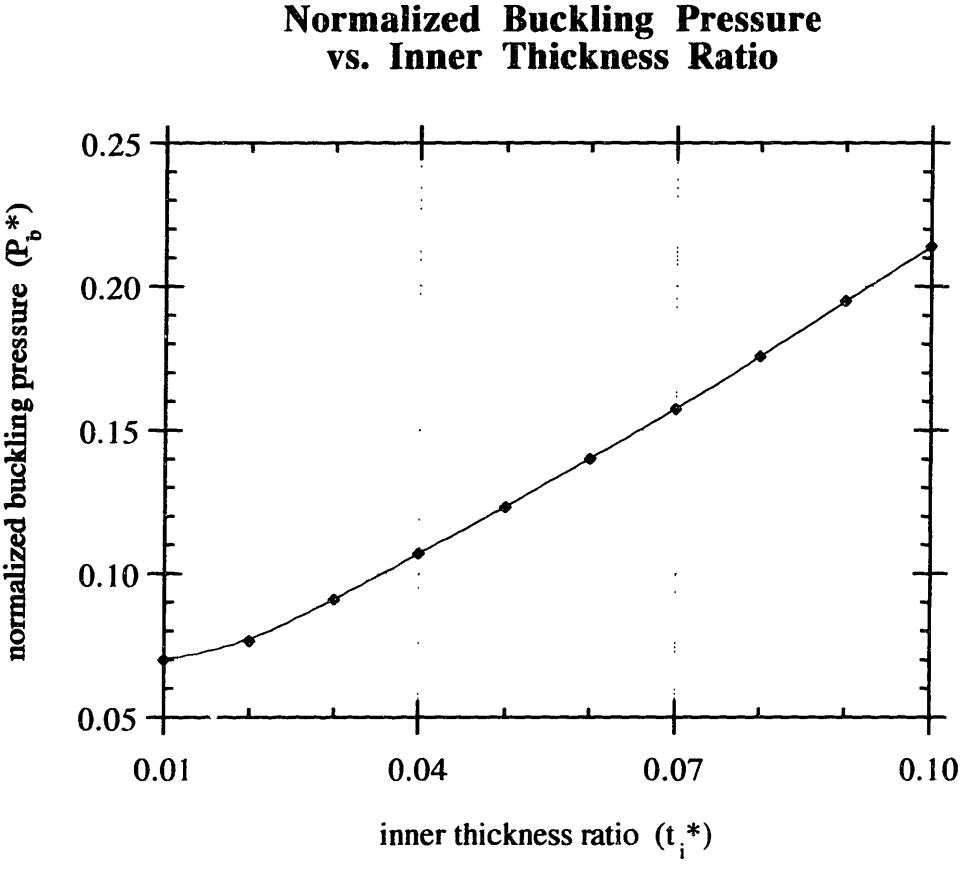

FIGURE 3-5: Linearized buckling analysis results: P_b* vs. t_i* for perturbative cases.

thickness has a profound effect on both the buckling pattern and the amount of energy required to buckle, but (like the outer thickness) little effect on what point in the collapse the buckling occurs.

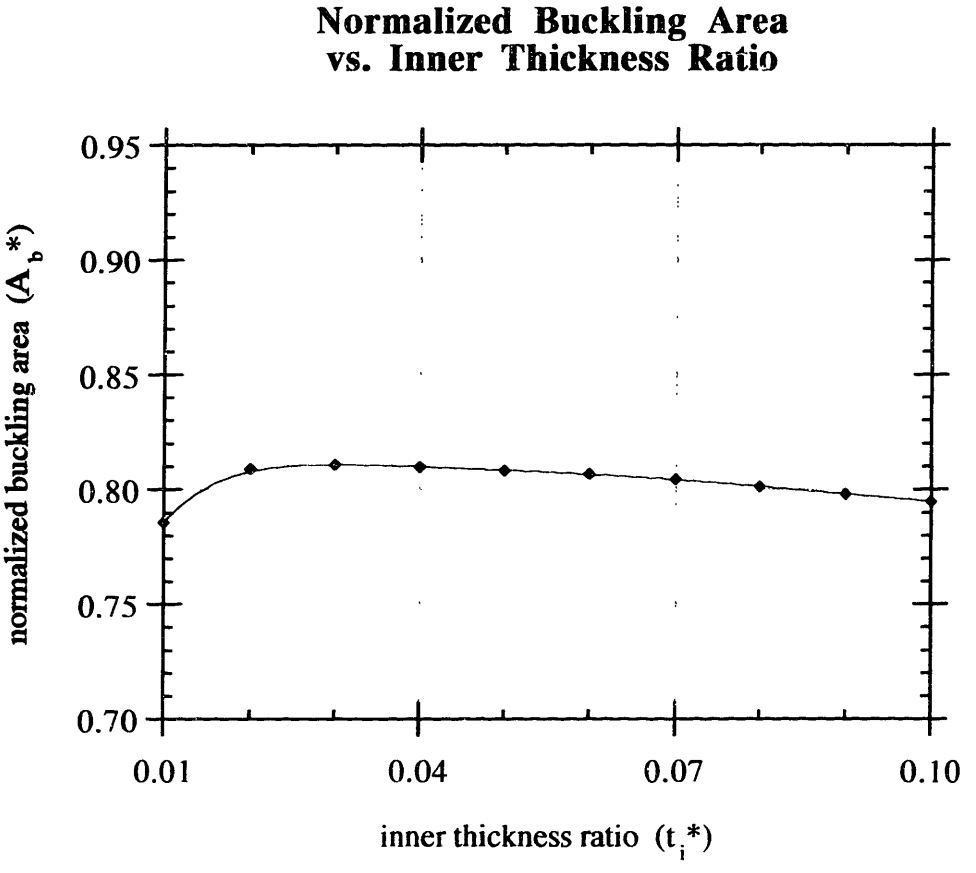

FIGURE 3-6: Linearized buckling analysis results: A_b* vs. t_i* for perturbative cases.

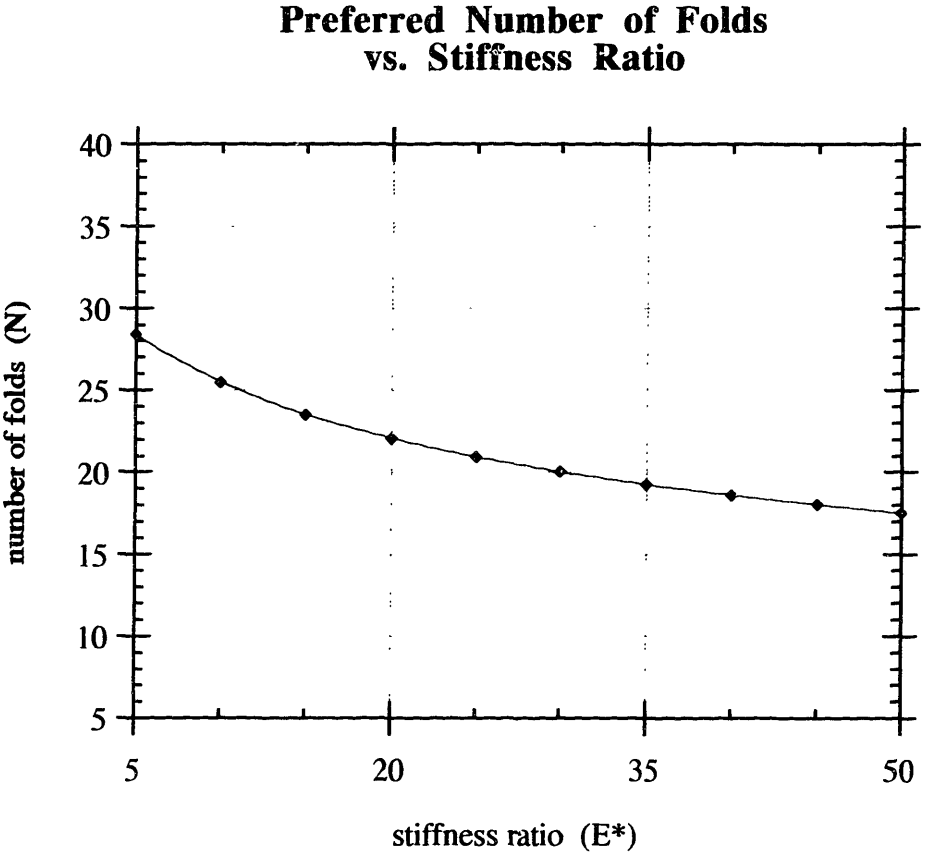

FIGURE 3-7: Linearized buckling analysis results: N vs. E* for perturbative cases.

Effect of Stiffness Ratio (E):*

As with both thickness ratios, an increase in the stiffness ratio tends to hyperbolically decrease the preferred number of folds in the multi-fold buckling pattern. Like inner thickness ratio, the decrease is to a very small number of folds (probably 2) as opposed to a larger number as with the outer thickness ratio. The effect of the stiffness ratio on the buckling pressure is a mild but complex one, with a minimal buckling pressure when the stiffness ratio is around 30, but continuing to be relatively small at larger stiffness ratios. Perhaps counter-intuitively, more energy is required to buckle the inner layer when the stiffness ratio is small. The stiffness ratio has a great impact upon the amount of collapse at buckling though: as the stiffness ratio grows large, buckling appears to occur immediately

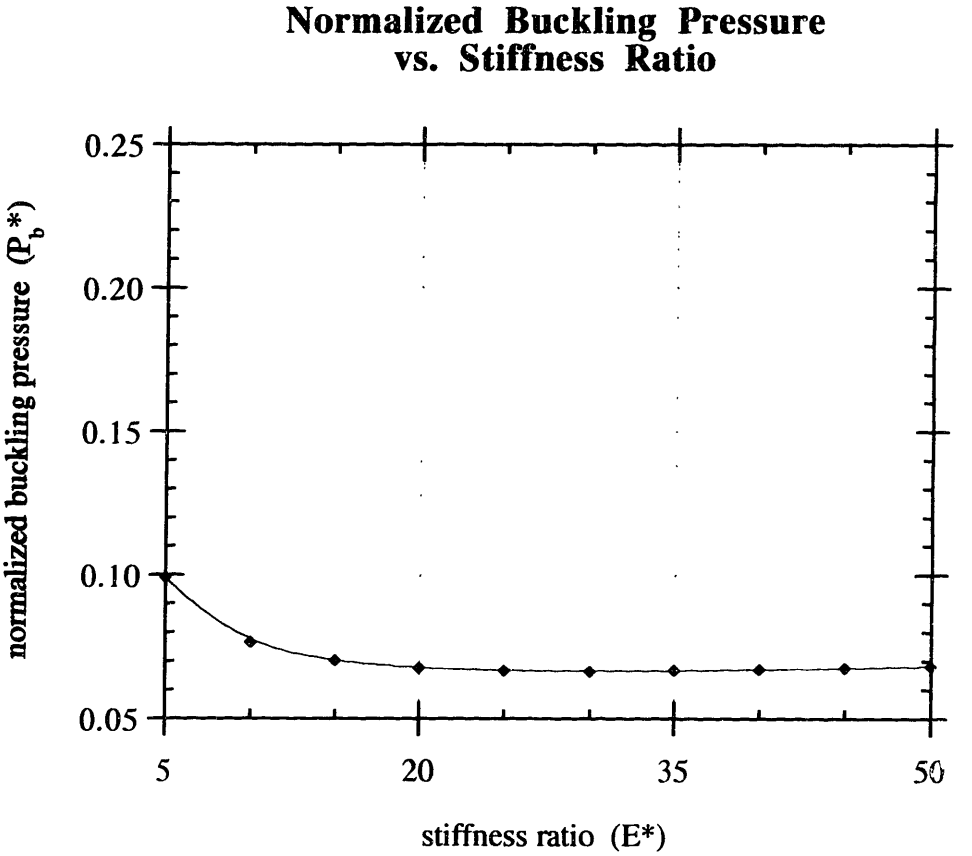

FIGURE 3-8: Linearized buckling analysis results: P_b* vs. E* for perturbative cases.

in the collapse, whereas at small stiffness ratios, axisymmetric contraction persists longer before buckling occurs.

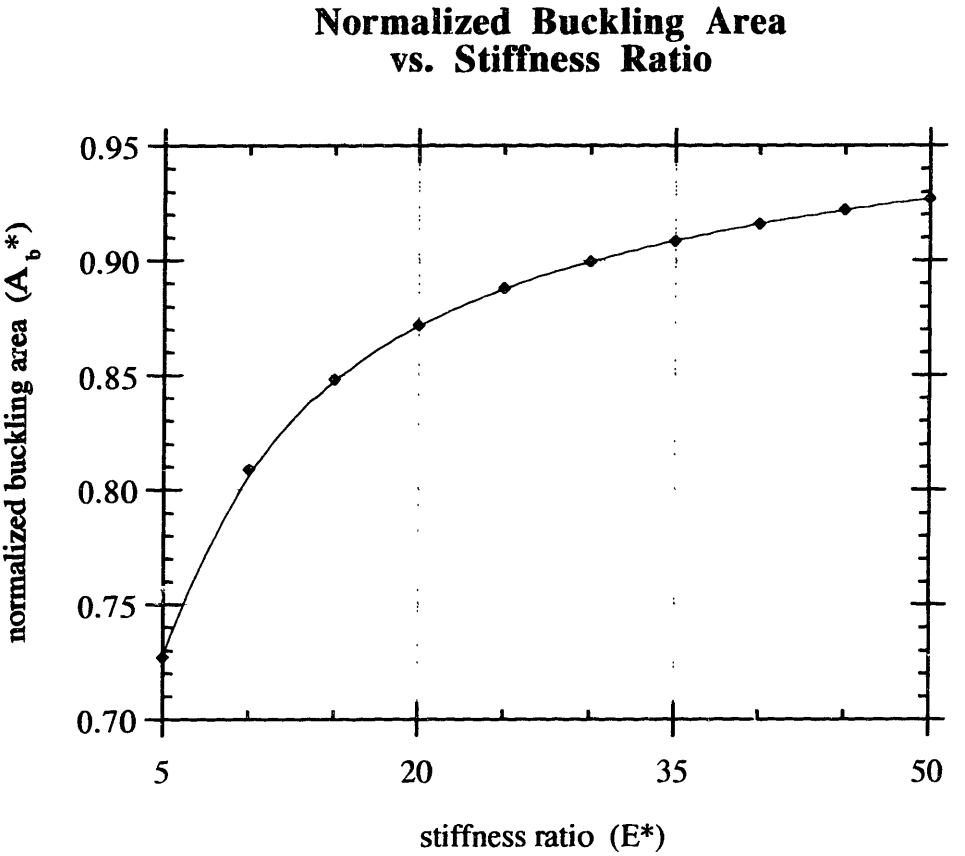

FIGURE 3-9: Linearized buckling analysis results: A_b* vs. E* for perturbative cases.

Summary of Perturbative Results:

Though the ranges over which each input parameter is perturbed may be different (and thus the percentage change in each parameter is different), we can comment on how strong an effect changing each input parameter by an order of magnitude has on each of the output variables. Increasing any of the three input parameters tends to decrease the expected number of folds in multi-fold collapse, although to markedly different degrees. Clearly, the inner thickness ratio is the most important of the three parameters. The outer thickness ratio has almost no effect by comparison. The effect of the stiffness ratio is intermediate, and certainly appreciable. Perturbing t_i* by an order of magnitude changes N by a factor of 6, while perturbing E* changes it by a factor of almost 2, indicating that t_i* has three times the impact on N as E* does. This makes sense physically when you think of the inner

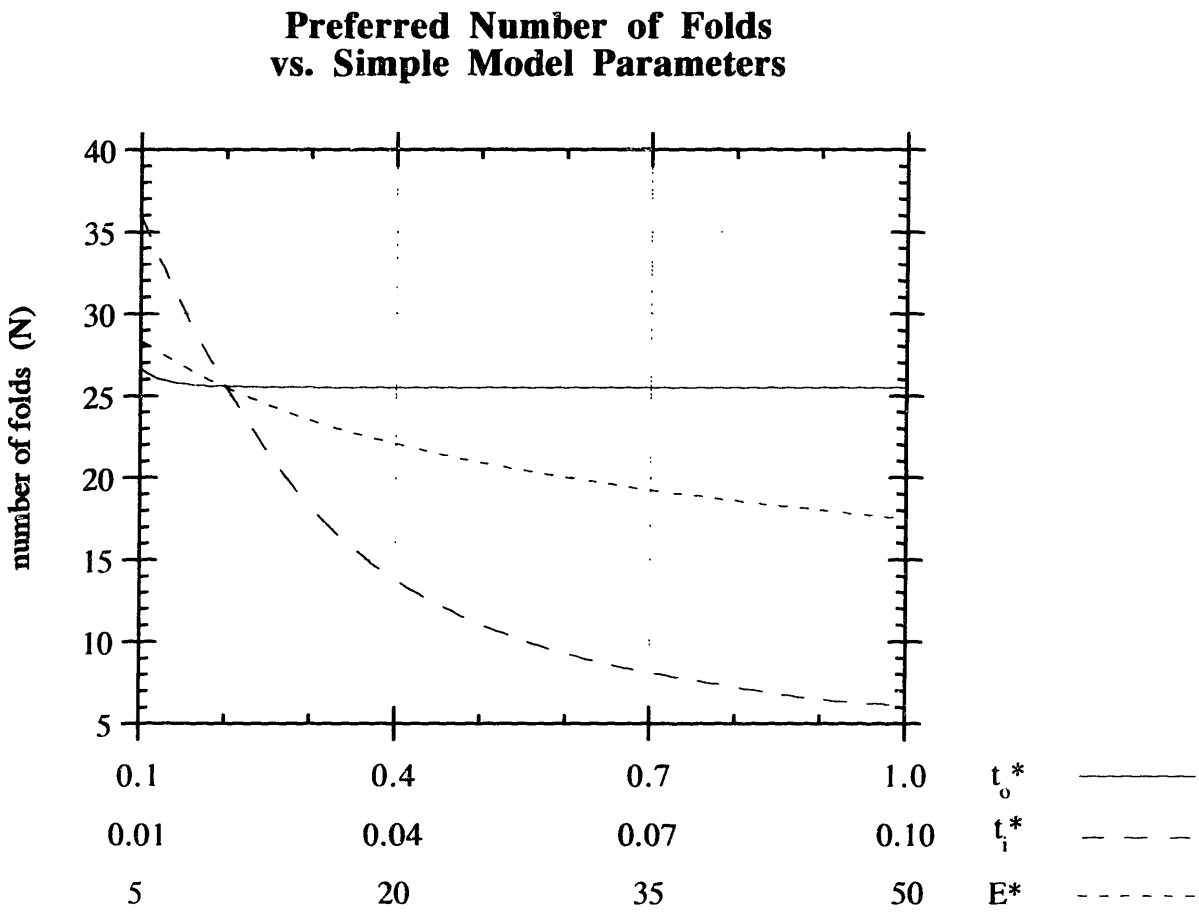

FIGURE 3-10: Linearized buckling analysis results: N vs. t_o*, t_i* and E* (summary) for perturbative cases.

layer as a beam supported by an elastic foundation, the outer layer. Specifically, the moment-curvature relationship of an Euler beam is:

$$M = E I \kappa$$

M is the bending moment at the point of interest in the beam, E is Young's elastic modulus, I is the geometrical moment of inertia, and κ is the curvature at the point of interest in the beam. For a simple rectangular beam the moment of inertia of the inner layer is:

$$I = \frac{1}{12} b t_i^3$$

where b is the width in the axial direction. Therefore, upon substitution:

$$M = \frac{1}{12} E\, b\, t_i^3\, \kappa$$

The number of folds at the bending moment that will buckle the beam would correlate inversely with the curvature of the folds, which is to say:

$$N \propto \frac{1}{\kappa} = \frac{b}{12M} E\, t_i^3$$

$$N \propto E\, t_i^3$$

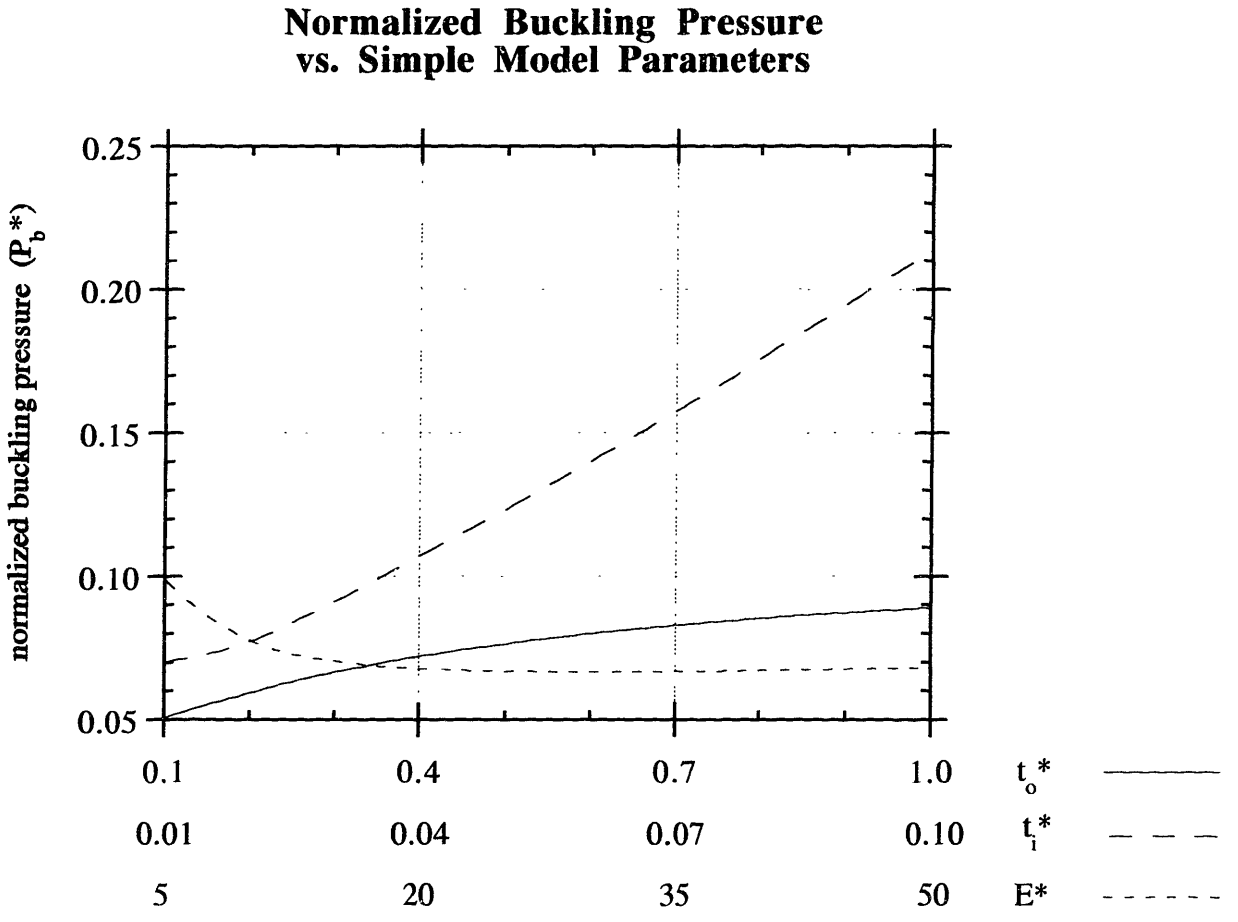

FIGURE 3-11: Linearized buckling analysis results: P_b* vs. t_o*, t_i* and E* (summary) for perturbative cases.

This simple Euler beam argument justifies the idea that the number of folds should be roughly three times more dependent upon the inner thickness ratio than the stiffness ratio.

Like the preferred number of folds, the buckling pressure appears to be most strongly determined by the inner thickness ratio. An order of magnitude change in the other parameters only changes the buckling pressure by a factor of 1.3 to 2, while the inner thickness can change it by a factor of 3.

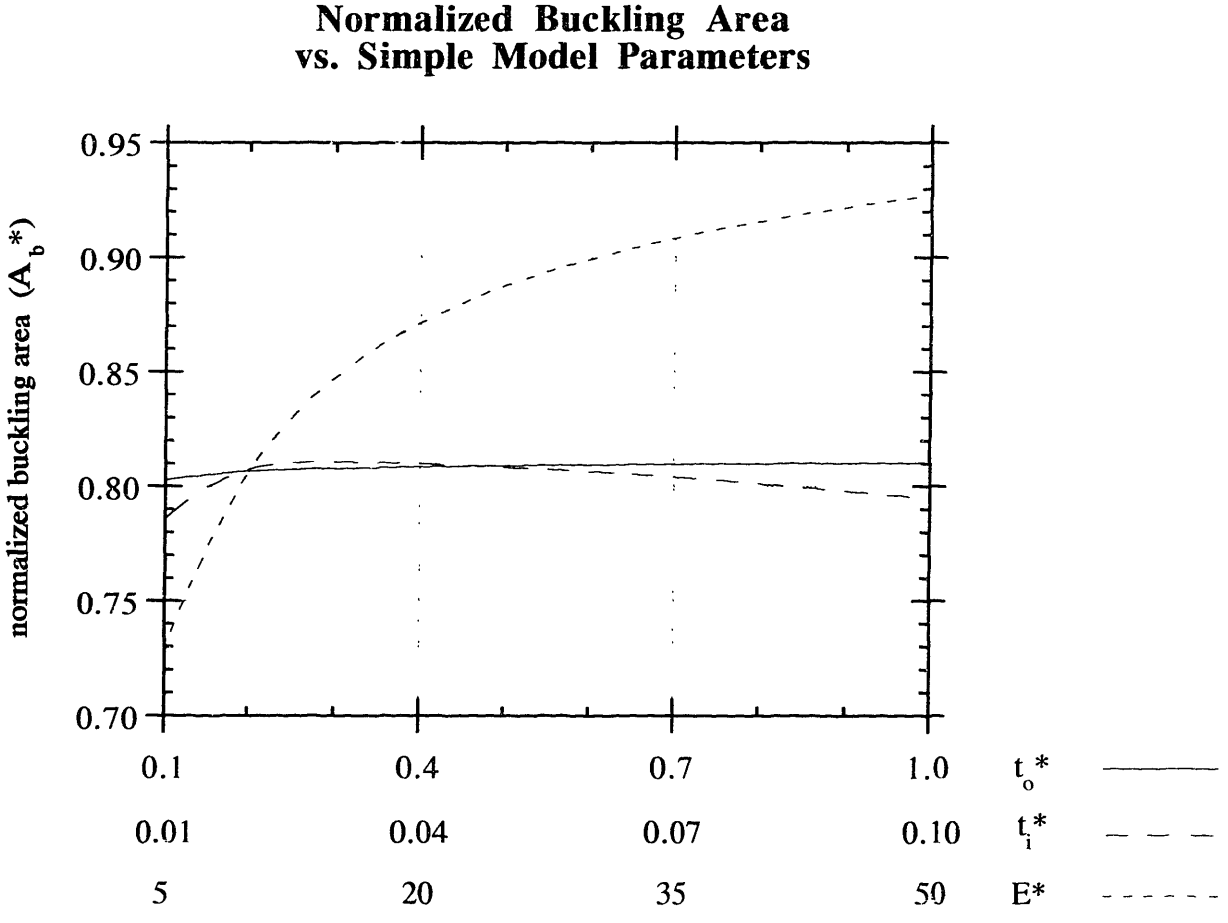

FIGURE 3-12: Linearized buckling analysis results: A_b* vs. t_o*, t_i* and E* (summary) for perturbative cases.

Curiously, it is the stiffness ratio which has the greatest effect on how much collapse there is at the buckling point. In comparison, both of the thickness ratios have unappreciable effects. A very rough idea of the amount of energy required to buckle may be obtained by multiplying P_b* by A_b*. Note that increasing either t_i* or E* increases the beam stiffness

and thus would increase the buckling energy. Increasing t_i* does so by increasing the effort that is necessary to buckle while E* does so by increasing the distance over which that effort is applied.

3.1.2 Results for the Three-Dimensional Domain

The above results outline general trends and identify how each of the input parameters independently affects the output. At this point it is desirable to see how the effects of the parameters might interact as more than one than one of them is perturbed from a base state. For instance, it has been demonstrated that for the base case shown above, increasing the outer thickness ratio lessens the preferred number of folds (N) at smaller values, but has very little effect at larger values. It would be interesting to know if this effect is generally true or only at this particular base state. Similarly, the inner thickness ratio appears to have a profound effect on the number of folds at the given base state, and from that one might (correctly) infer that this is generally true everywhere, but it would be preferable to quantify how much of an effect it has at one base state relative to another.

This section presents results from 500 converged linearized buckling analyses, each of which is performed at a different combination of the tested values of t_o*, t_i* and E* listed below.

t_o*	t_i*	E*
0.1	0.01	2.5
0.2	0.02	5
0.3	0.03	10
0.4	0.04	20
0.5	0.05	40
0.6	0.06	
0.7	0.07	
0.8	0.08	
0.9	0.09	
1.0	0.10	

Since there are 10 values of t_o*, 10 values of t_i* and 5 values of E*, there are $10 \cdot 10 \cdot 5 = 500$ cases total. The next few figures display contour plots of the iso-surfaces of N, P_b*

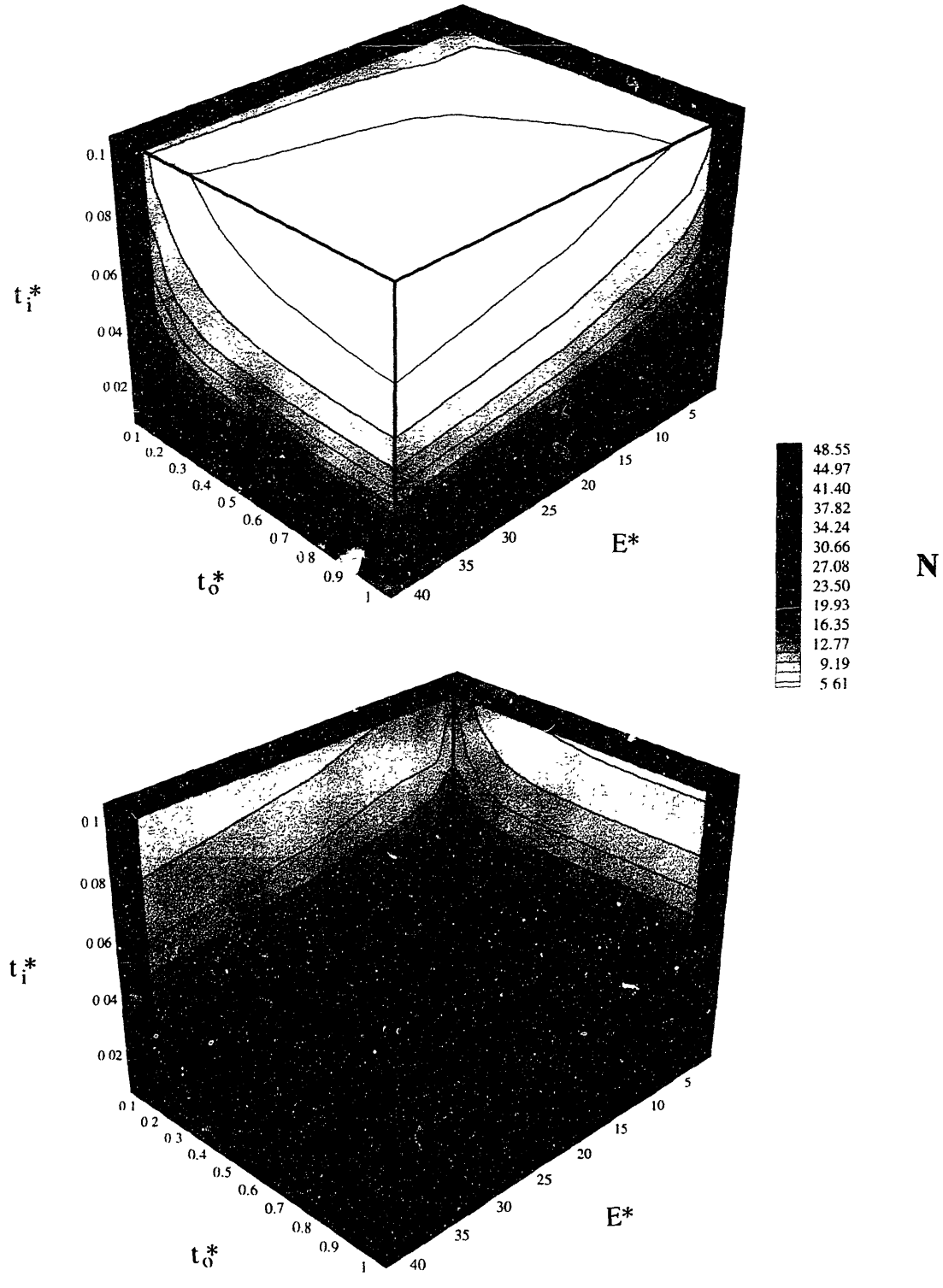

FIGURE 3-13: Linearized buckling analysis results: 3-D plots of N vs. all 3 simple model parameters for 500 analyses. Top view is of the near surfaces of the box-shaped domain; bottom view is of the far surfaces.

and A_b* results over the three-dimensional domain. The domain is essentially box-shaped, and each figure shows first a plot of the contours on the outside of the box, followed by a plot on the inside of the box. The axes are the same for all the 3-D plots.

The nesting sheets in Figure 3-13 show that the expected number of folds (N) decreases with all three of the input parameters. The fact that the iso-surfaces are most perpendicular to the t_i*-axis indicates that N is a relatively strong function of t_i*. It is next most dependent on E*. Particularly for small values of t_i* and large values of t_o*, the iso-surfaces are parallel to the t_o*-axis, indicating that N is a rather weak function of t_o*. N appears to be quite well-behaved over this domain. The smaller the value of any of the input parameters, the faster varying a function N is of that parameter.

Similarly, the buckling pressure (P_b*) is a rather strong function of t_i*. For large t_o*-values, P_b* is mostly a slow-varying function of t_i*. For small t_o*-values, it is a much faster-varying function of t_i* (and to a small extent, E*). It is hard to figure out exactly what is happening around small E* values, although it appears that for large t_i*-values, there is a minimum buckling pressure when $E^* \approx 10$. This function is not quite so well-behaved as N; there may be some type of numerical error at small E* values.

The lumen area at which the two-layer model buckles (A_b*) is clearly most dependent upon E* over most of the domain, with significant dependence on t_i* at small t_o*-values. There is a minimum A_b* when $t_i^* = 0.06$ for small E*, that moves to 0.02 for large E*.

The fact that N is a very well-behaved function of the three input parameters suggests that one could easily find an empirical mathematical model of it. The following expression for the model $\bar{N}$ was found using the simplex method for minimizing the maximum relative error between $\bar{N}$ and N, summed over the 500 data points. The relative error between this model and the LBA results data ranges from –24% to 24% with a median at –1.4%. The standard deviation of the relative error is 10%.

$$\bar{N}(t_o^*,\ t_i^*,\ E^*) \approx \frac{1.54}{(t_o^*)^{0.119}\,(t_i^*)^{0.743}\,(E^*)^{0.159}}$$

At this point it is worthwhile to do some comparison of this computational result with an analytical solution using linearized stability techniques (see Appendix A.3). For both the analytical solution and the FEM results, N is inversely related to all three input parameters

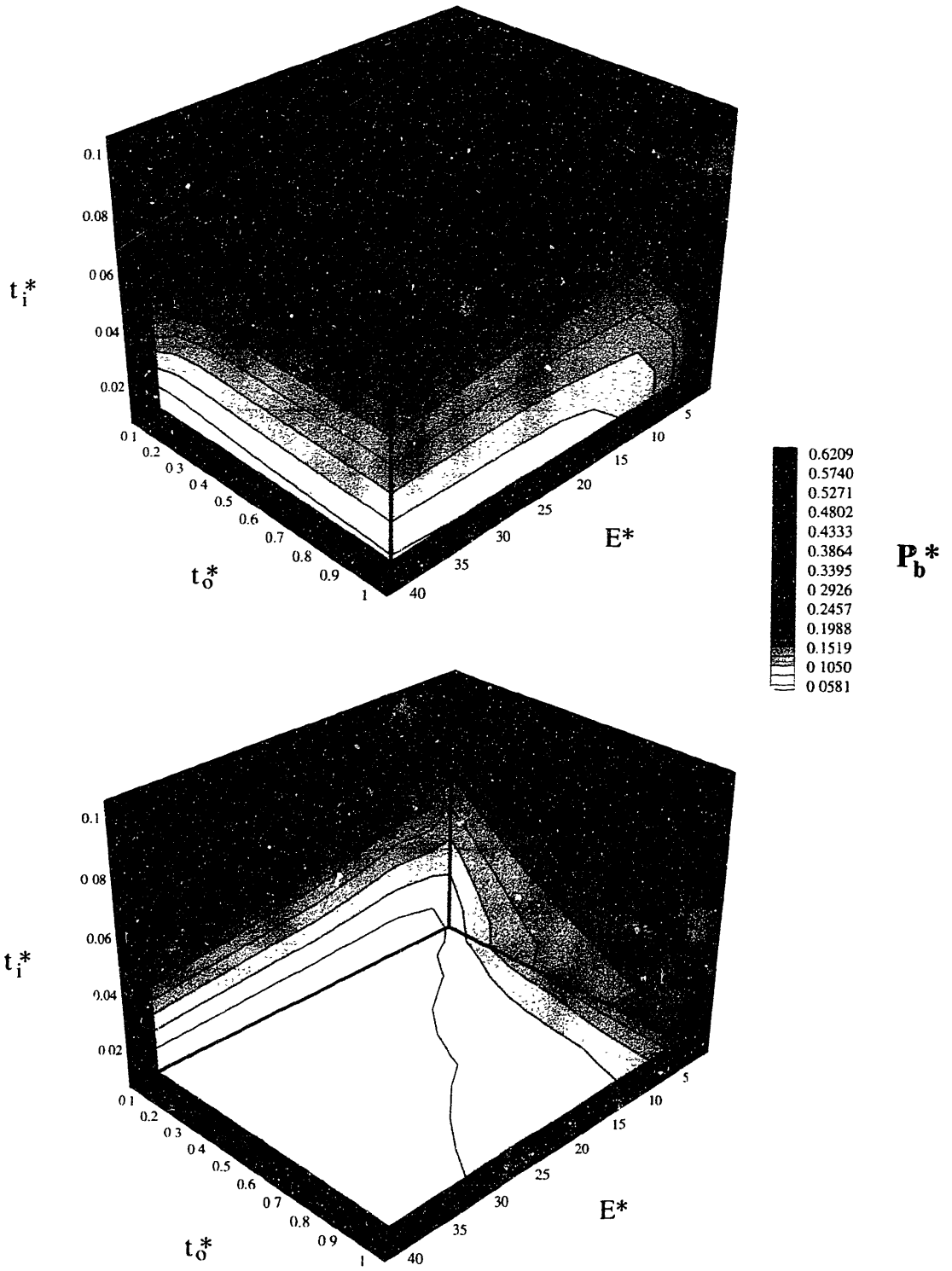

FIGURE 3-14: Linearized buckling analysis results: 3-D plots of P_b^* vs. all 3 simple model parameters for 500 analyses. Top view is of the near surfaces of the box-shaped domain; bottom view is of the far surfaces.

(the outer thickness ratio, the inner thickness ratio and the stiffness ratio). In the analytical solution the exponent on the stiffness ratio turns out to be 0.25 (as opposed to 0.159), but the exponents on the inner thickness ratio are in very good agreement (both about 0.75). Since N is much more dependent on the inner thickness ratio than the other two parameters, it makes sense that the two solutions are in good agreement on this exponent. The dependency on the outer thickness ratio appears more complicated in the analytical solution than the simple inverse power law chosen in the curve fit of simulation results, but over the outer thickness ratios of interest the functional dependence can be made essentially the same by the leading constant. In the analytical solution, that constant is about 1.86, and in the simulations it is about 1.54. The discrepancy between these is due mostly to the difference in the stiffness ratio exponents, and to a much lesser extent, the difference in the dependence on the outer thickness ratio.

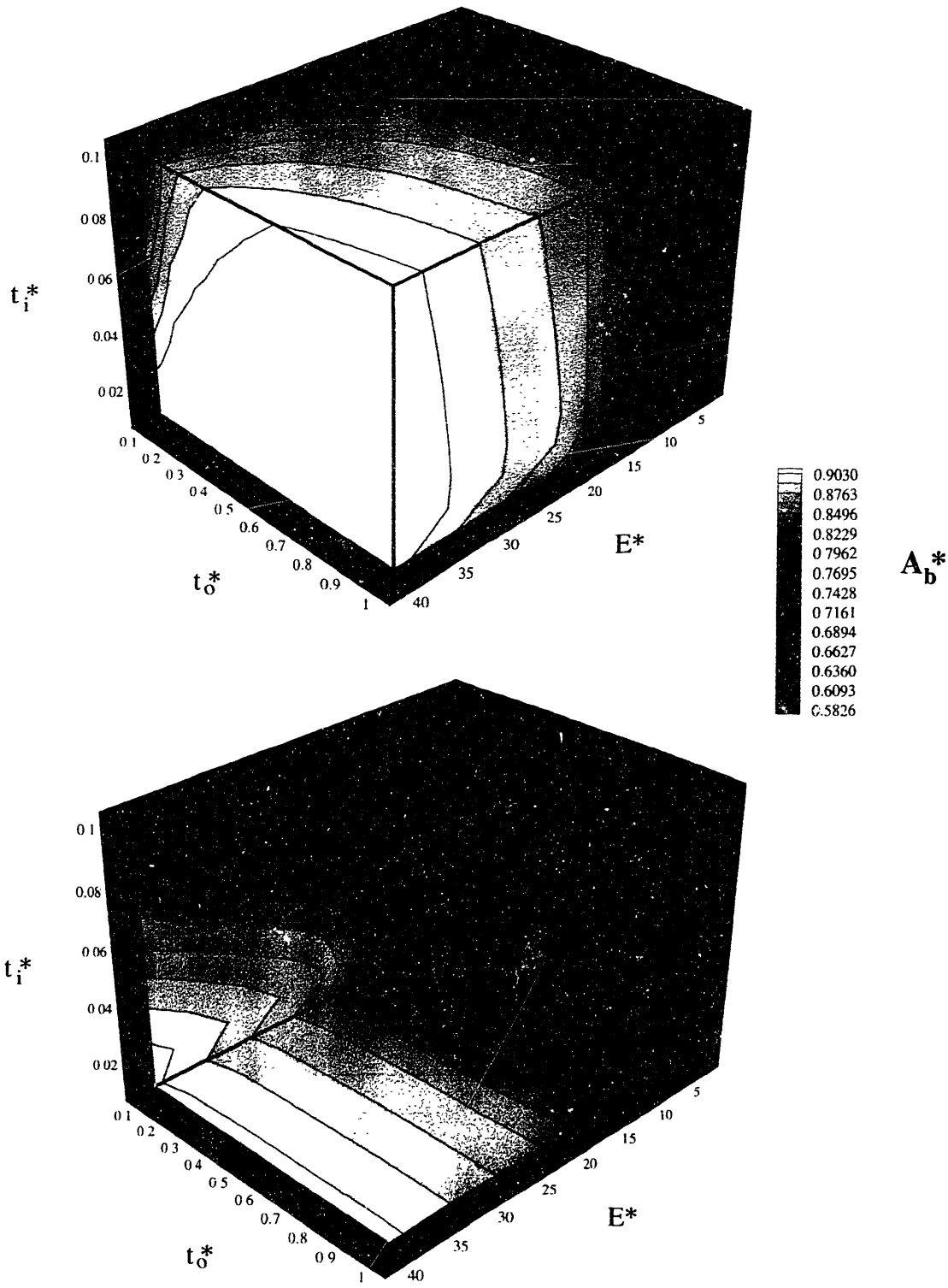

FIGURE 3-15: Linearized buckling analysis results: 3-D plots of A_b* vs. all 3 simple model parameters for 500 analyses. Top view is of the near surfaces of the box-shaped domain; bottom view is of the far surfaces.

3.2 Assumption Verification

Several assumptions were made in order to make the two-layer model remarkably simple. This section provides some inductive verification for those assumptions by loosening them one by one and investigating the effect on the output variables N, P_b*, S_b and A_b* using the converged linearized buckling analysis. Comparisons will be made between the simple model as is (linear-elastic, incompressible, plane-strain) and with one of the assumptions reversed for 7 particular cases whose input parameters are tabulated below. All of the 7 cases are among the 500 analyses whose results were presented in Section 3.1.2. The first (base) case is the familiar arbitrarily chosen one from Section 3.1.1. The remaining cases are similar to the first, but with one of the three parameters either markedly increased or decreased.

case	t_o*	t_i*	E*
1	0.5	0.02	10
2	0.1	0.02	10
3	1.0	0.02	10
4	0.5	0.01	10
5	0.5	0.05	10
6	0.5	0.02	2.5
7	0.5	0.02	40

3.2.1 Compressibility Effects

The first assumption that will be relaxed is the incompressible materials assumption. If there is time for water movement through the airway wall tissues during smooth muscle constriction, there may be a significant effect due to compressibility. There are several ways to investigate such an effect, but the way examined here (which admittedly is not a very rigorous way) is to simply assume that the Poisson ratio is 0 instead of $^1/_2$. When the Poisson ratio is 0, the material can be stretched or compressed in one direction with no force generation of deformation in the other two directions, regardless of what boundary conditions are applied in those directions. This is a somewhat simplistic representation of a "highly compressible" material.

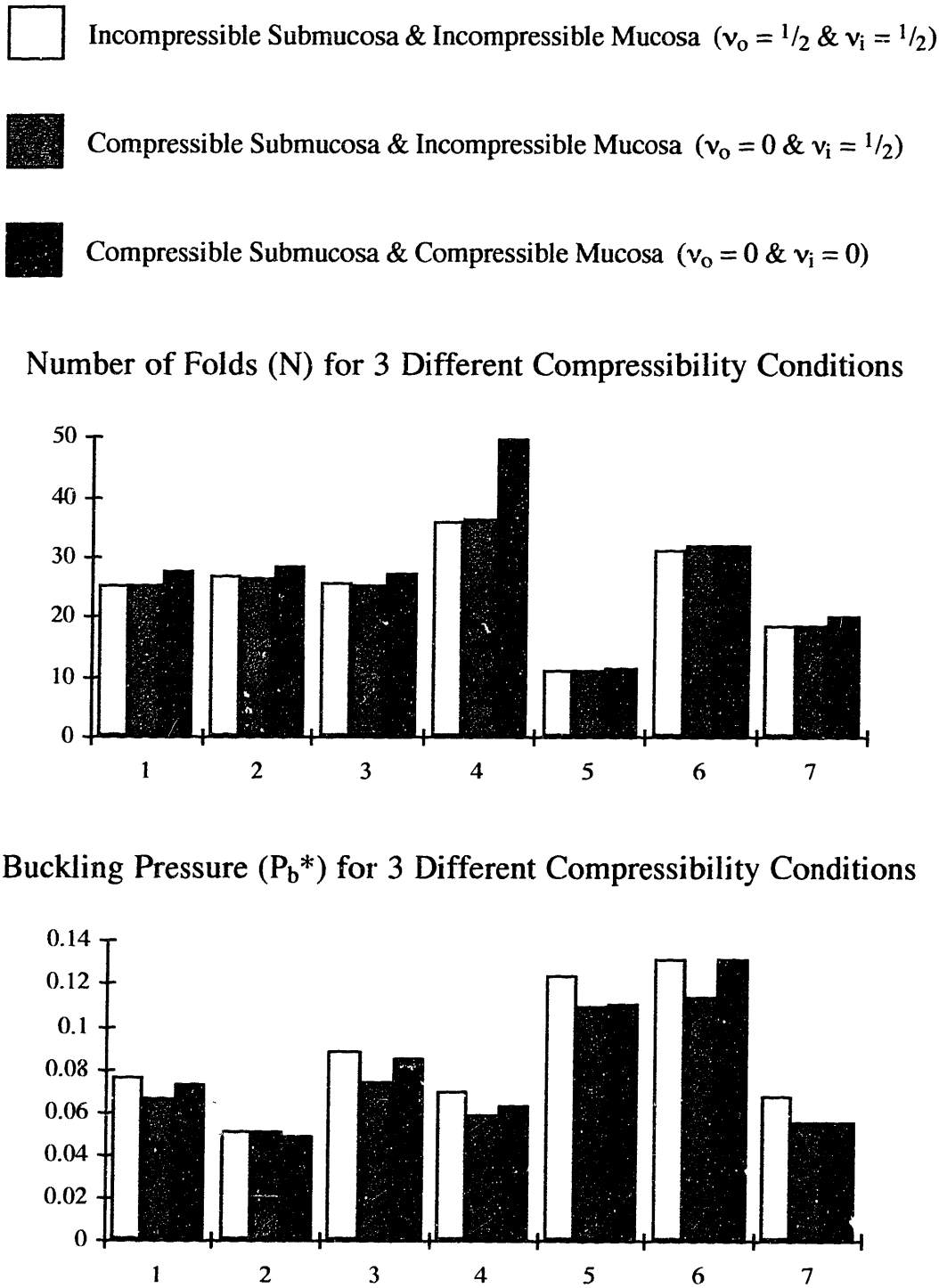

FIGURE 3-16: Assumption verification using LBA: N and P_b* comparison for 7 cases of (t_o*, t_i* and E*) under 3 different compressibility possibilities.

Percent Smooth Muscle Shortening at Buckling (S_b)
for 3 Different Compressibility Conditions

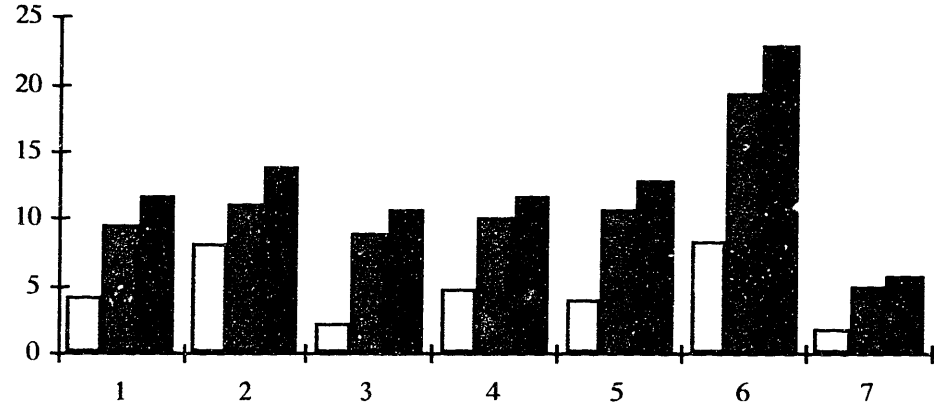

Buckling Lumen Area (A_b*) for 3 Different Compressibility Conditions

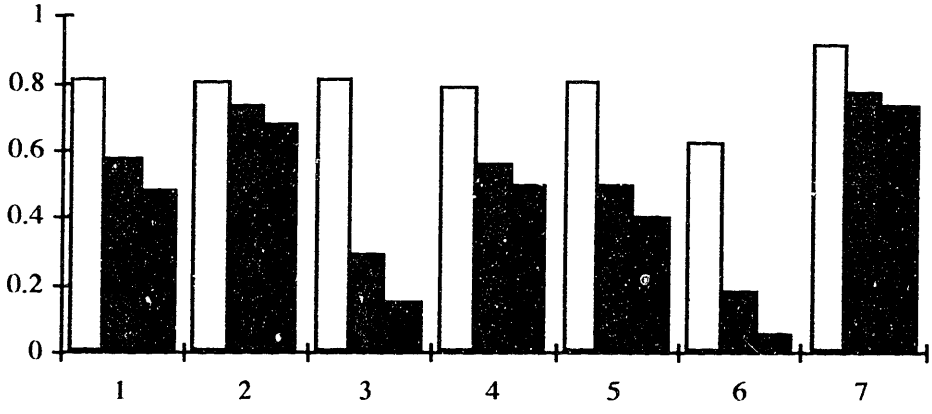

FIGURE 3-17: Assumption verification using LBA: S_b and A_b* comparison for 7 cases of (t_o*, t_i* and E*) under 3 different compressibility possibilities.

Another possibility worth examining is that case where the outer (submucosal) layer is highly compressible, but the inner (mucosal) layer is incompressible. Given the simplistic nature of this model of compressibility this is a better representation of the materials of the airway wall. The submucosa has a large fraction of water in it and is therefore much more likely to be compressible than the layer of densely packed collagen.

Figures 3-16 and 3-17 display N, P_b*, S_b and A_b* values for the 7 base cases assuming (1) both layers incompressible, (2) outer layer highly compressible and inner layer incompressible, and (3) both layers highly compressible.

With the exception of the single case where both layers are highly compressible and the inner layer is thin, there is very good agreement between N-values for all three conditions, particularly when the inner layer is kept incompressible. Increased compressibility seems to always increase the preferred number of folds, but not very much. Thus it would seem that the compressibility assumption is not as important for determining the buckling pattern. The pressure required to buckle (P_b*) is not remarkably different either for any of the compressibility conditions. What is more interesting is the believable result that more smooth muscle shortening is required to buckle (S_b) when the materials are compressible. This is because the radial stress (or applied pressure) on the outer edge is not generating as much hoop stress in the body of the structure as if it were incompressible, and the structure as a whole is more compliant. Another interesting change with compressibility is that the lumen area at buckling is no longer just a function of the stiffness ratio (as it is for the totally incompressible model), but of all three parameters. In general, the buckling lumen area is greatly reduced for compressible tubes compared to incompressible ones, particularly when the outer layer is very thick or compliant.

3.2.2 Axial Deformation Effects

There is good reason to believe that of the two-dimensional possible modeling assumptions, plane-stress and plane-strain, the latter is the better assumption in the case of airway modeling (see Section 2.2.1). However, as an exercise, a similar comparison between converged linearized buckling analyses of the two extreme cases is presented here, just to know better how important the distinction between plane-stress and plane-strain is for this modeling problem. Figures 3-18 and 3-19 report N, P_b*, S_b and A_b* under plane-strain and plane-stress modeling assumptions.

Again, very much like the effect of compressibility, there is relatively good agreement between plane-stress and plane-strain values for N, and a little less so when the inner layer is very thin. The general trend, as with increased compressibility, is a slight increase in the expected number of folds. In some sense, plane-stress is like compressibility in that there are no axial stresses generated since the model is unconfined in that direction. In contrast with compressibility, plane-stress seems to require about half the pressure to buckle the tube than plane-strain does. Plane-strain is a more confined condition in general, thus requiring more force for about the same displacement. The amount of smooth muscle shortening to buckle and the buckling lumen area are also affected a bit, but not in any particularly interesting way. Plane-stress and plane-strain are most different in how much pressure is required to deform them, as if E were uniformly increased or decreased everywhere. Aside from this, the general agreement between the two, particularly in the buckling patterns, suggests that we need not be too worried about axial deformation in our two-layer tube models.

Incidentally, it turns out to be easier to model plane-stress conditions than plane-strain because the problem of singularities occurring in the constitutive relationship is avoided. The following conversion laws are a quick and easy way to convert any two-dimensional analysis from plane-strain to plane-stress and vice versa.

$E_{PE} \equiv$ E in a plane-strain analysis $\qquad \nu_{PE} \equiv \nu$ in a plane-strain analysis

$E_{PS} \equiv$ E in a plane-stress analysis $\qquad \nu_{PS} \equiv \nu$ in a plane-stress analysis

$$\frac{E_{PE}}{1+\nu_{PE}} = \frac{E_{PS}}{1+\nu_{PS}} \qquad \frac{1}{\nu_{PE}} - \frac{1}{\nu_{PS}} = 1$$

$$E_{PS} = \frac{E_{PE}}{1-\nu_{PE}^2} \qquad \nu_{PS} = \frac{\nu_{PE}}{1-\nu_{PE}}$$

$$E_{PE} = E_{PS}\frac{1+2\nu_{PS}}{(1+\nu_{PS})^2} \qquad \nu_{PE} = \frac{\nu_{PS}}{1+\nu_{PS}}$$

In can be seen that making the appropriate substitutions of E_{PS} and ν_{PS} for E_{PE} and ν_{PE} in the linear-elastic relationship of Section 2.2.3 results in a constitutive relationship that is in

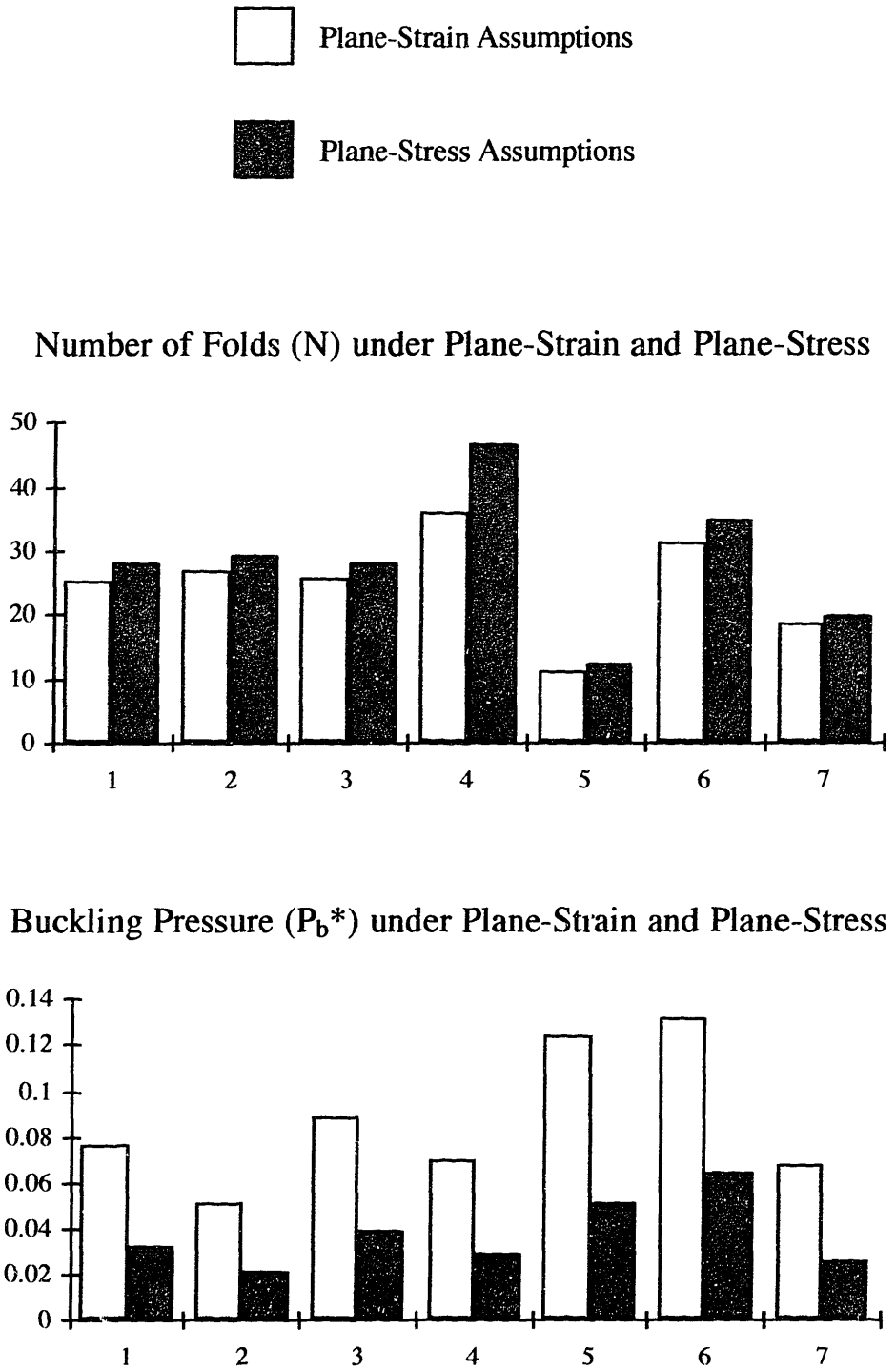

FIGURE 3-18: Assumption verification using LBA: N and P_b* comparison for 7 cases of (t_o*, t_i* and E*) under plane-strain and plane-stress.

Percent Smooth Muscle Shortening at Buckling (S_b)
under Plane-Strain and Plane-Stress

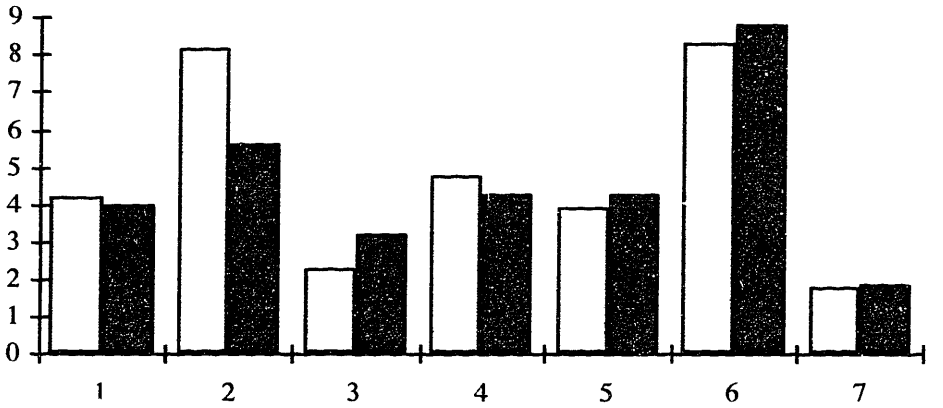

Buckling Lumen Area (A_b*) under Plane-Strain and Plane-Stress

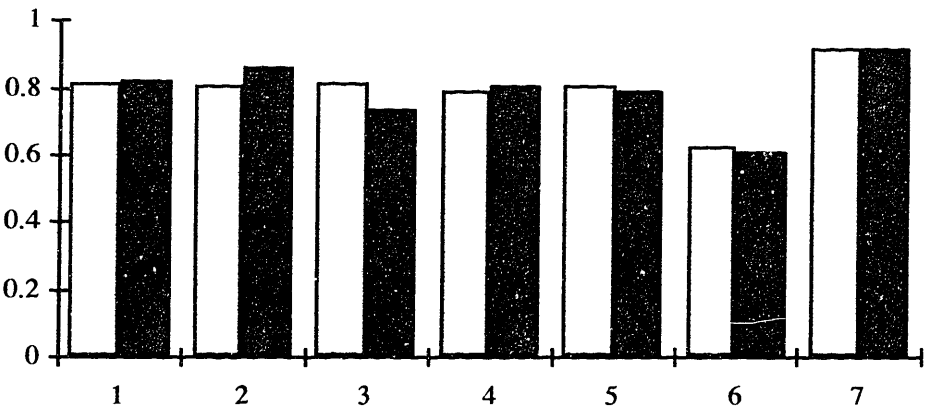

FIGURE 3-19: Assumption verification using LBA: S_b and A_b* comparison for 7 cases of (t_o*, t_i* and E*) under plane-strain and-plane stress.

no danger of approaching any singularities, regardless of what value ν is. That relationship, Hooke's law for plane-stress, is:

$$\begin{Bmatrix} \tau_{11} \\ \tau_{22} \\ \tau_{12} \end{Bmatrix} = \begin{bmatrix} \frac{E}{1-\nu^2} & \frac{E\nu}{1-\nu^2} & 0 \\ \frac{E\nu}{1-\nu^2} & \frac{E}{1-\nu^2} & 0 \\ 0 & 0 & \frac{E}{1+\nu} \end{bmatrix} \begin{Bmatrix} \varepsilon_{11} \\ \varepsilon_{22} \\ \varepsilon_{12} \end{Bmatrix}$$

Note that if $\nu = 0$, the off-diagonal terms vanish, indicating that there is no coupling between perpendicular directions. Since there is no loading in the axial direction, there would be no deformation in that direction. When $\nu = 0$, plane-stress and plane-strain are equivalent, so in a sense, the case of plane-stress with $\nu = 0$ (for both layers) has been examined in the previous section.

3.2.3 Hookean Linear Elasticity vs. Neohookean Rubber Elasticity

The same procedure is now used to evaluate the difference between the Hookean linear-elastic material model (with ν set to $^1/_2$) and the incompressible neohookean rubber elasticity material model (with $D_1 = 0$ and $C_{10} = E/6$) when applied to the 7 base cases. A detailed description of the differences between the two material models is given in Section 2.2.3. Figures 3-20 and 3-21 compare the converged LBA results between (1) the linear-elastic material model and (2) the neohookean material model.

These results are particularly positive. There appears to be very little difference between the two material models when applied to this problem (probably because there is very little rotation anywhere in the simulation, at least not before buckling). This makes it relatively comfortable to use either one at will. Because the linear-elastic model is particularly intuitive (and somewhat easier to implement), aside from this one section, all analyses in this work make use of simple linear-elastic material laws.

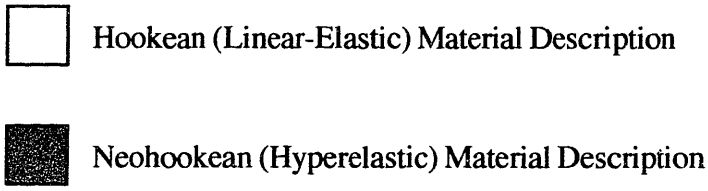

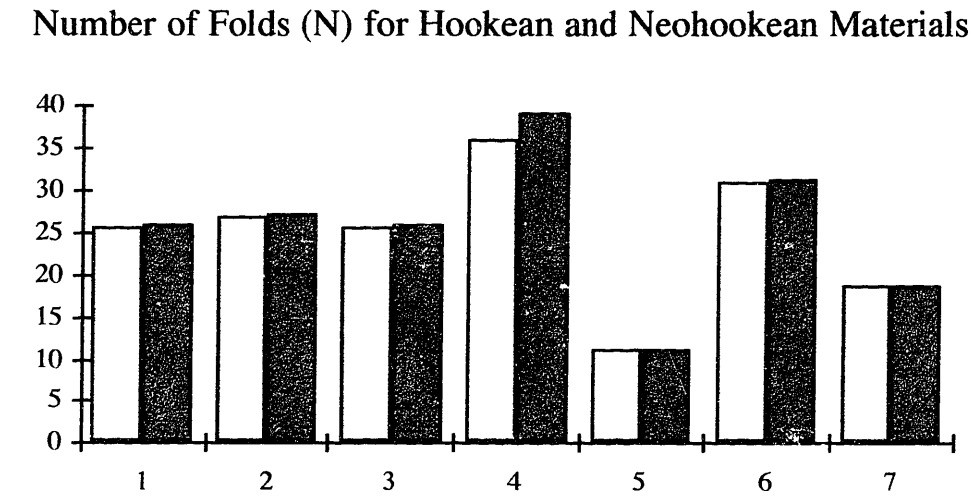

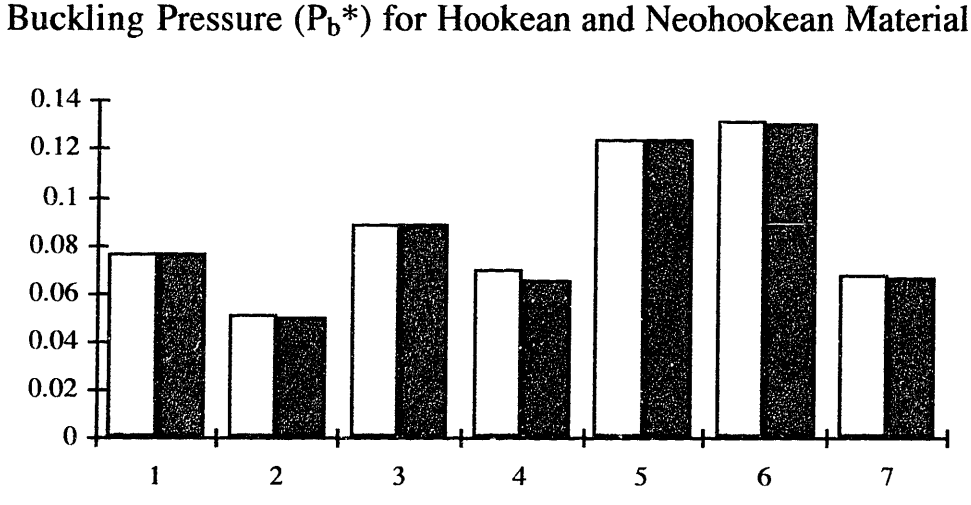

FIGURE 3-20: Assumption verification using LBA: N and P_b* comparison for 7 cases of (t_o*, t_i* and E*) using Hookean (linear-elastic) and neohookean (hyperelastic) material laws.

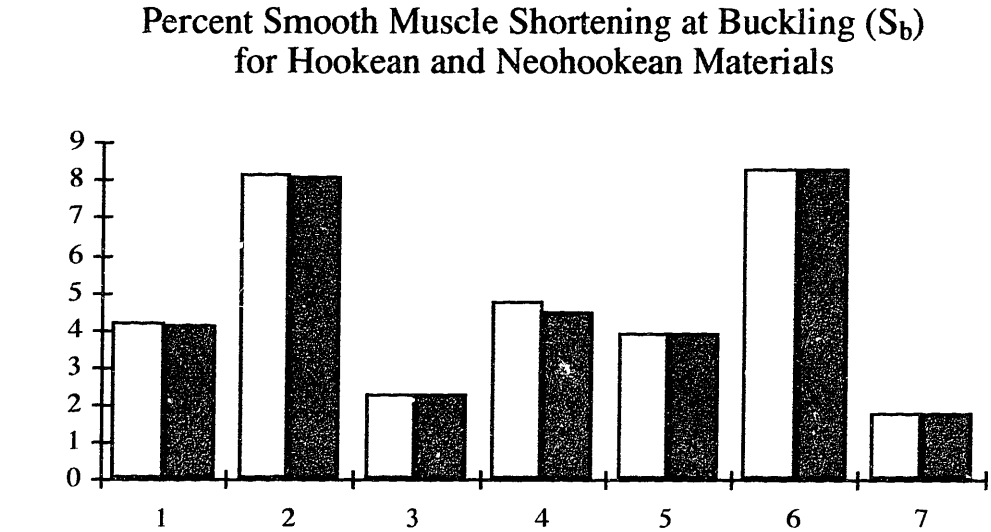

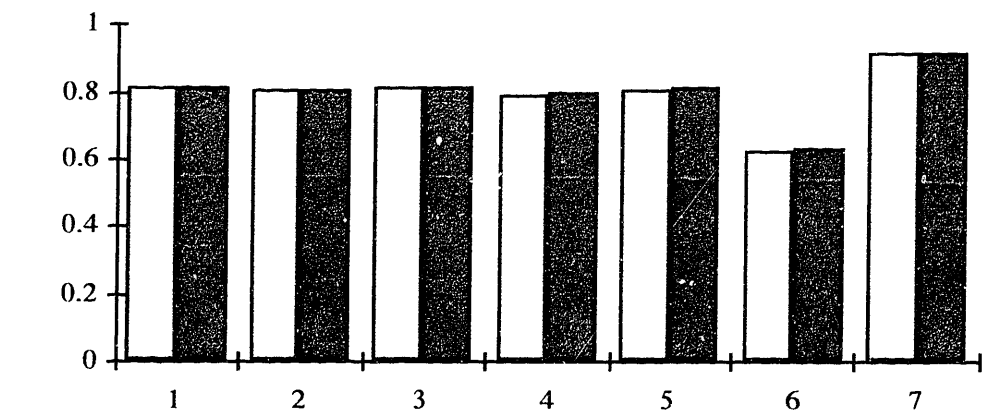

FIGURE 3-21: Assumption verification using LBA: S_b and A_b* comparison for 7 cases of (t_o*, t_i* and E*) using Hookean (linear-elastic) and neohookean (hyperelastic) material laws.

3.3 Static Analysis Results

To test for the late-response post-buckling behavior, the above 7 cases from Section 3.2 were simulated in wedge-model finite element analyses. The values of N from the linearized buckling analyses above were used to model the appropriate fraction of the airway in each case. Remeshing was able to help extend the cases down to A* values from 0.40 to 0.18. Fits to power law curves were used to smooth the remeshed output data and extrapolate when necessary up to P* = 10. Note that the following figures are semi-log plots, so that the full character of the collapse, both before and after buckling, is displayed.

Figure 3-22 shows cases 1, 2 and 3, which have varying outer thickness ratios. Because the pressure coordinate is on the x-axis and lumen area is on the y-axis, curves higher

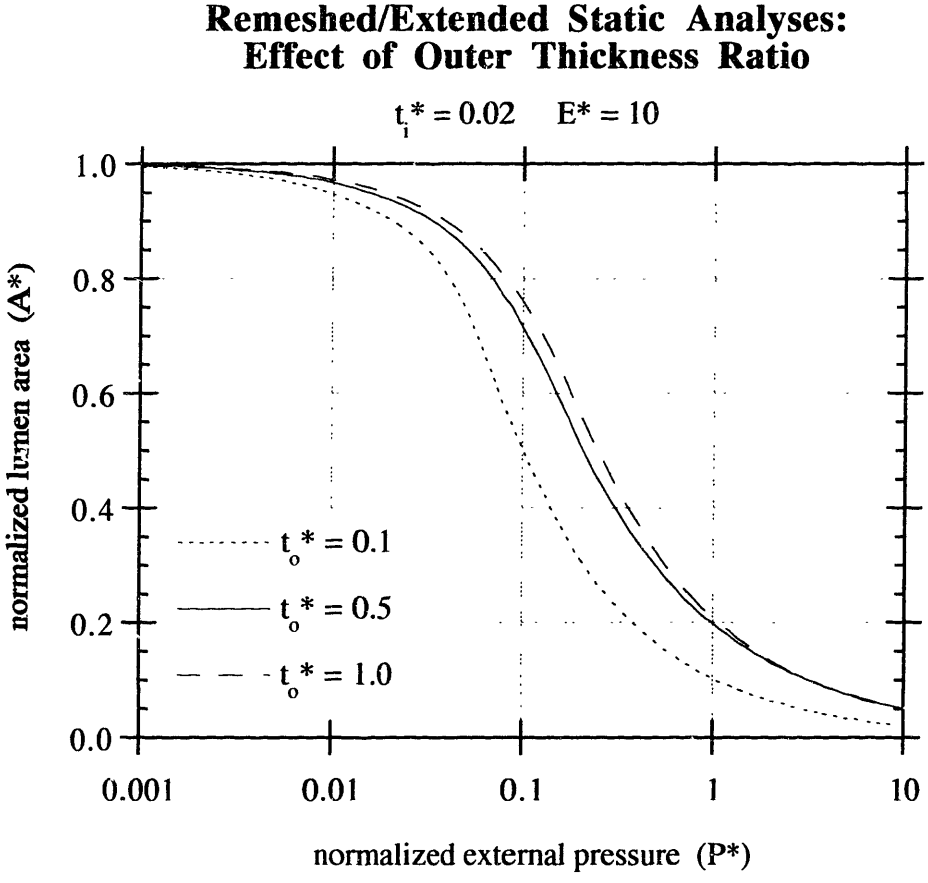

FIGURE 3-22: Remeshed and extended static analyses with varying t_o*.

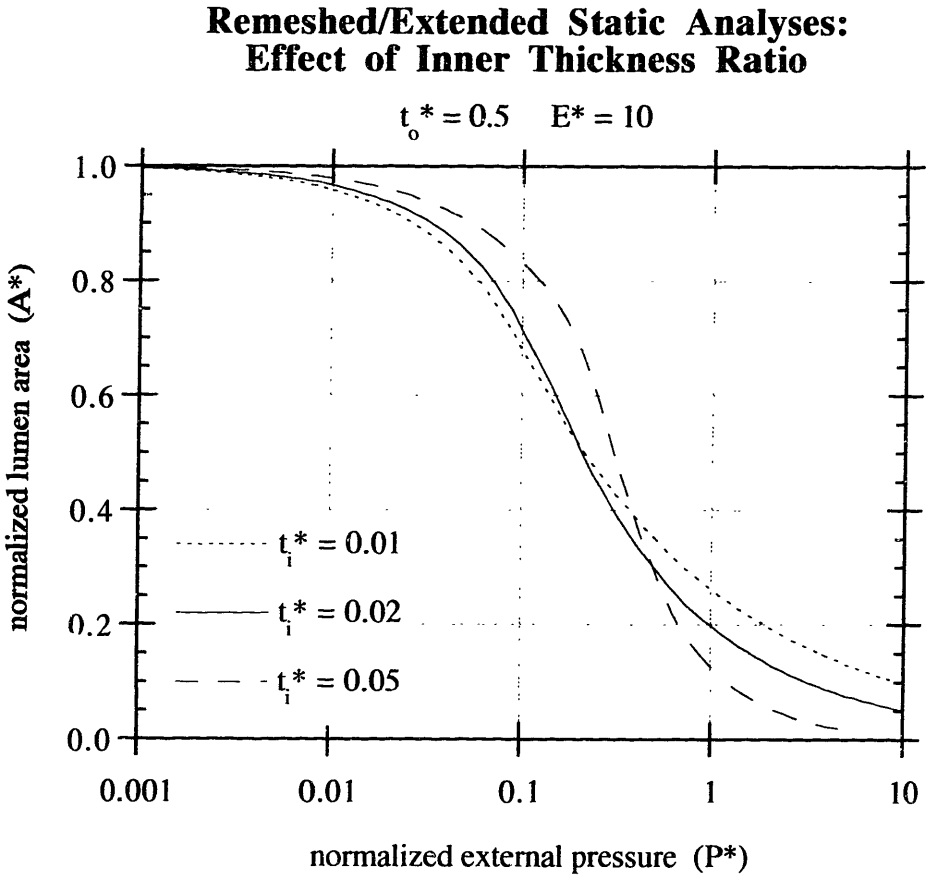

FIGURE 3-23: Remeshed and extended static analyses with varying t_i*.

and/or to the right represent stiffer two-layer tubes. Doubling t_o* from 0.5 to 1.0 produces a marginal increase in airway stiffness, while a factor of 5 reduction down to 0.1 corresponds to a marked decrease in airway stiffness. This result appears to confirm the general hypothesis that thickening of the outer layer tends to increase airway stiffness to occlusion.

Figure 3-23 plots the results from cases 1, 4 and 5, which have varying inner thickness ratios. When t_i* is increased from 0.02 to 0.05 – a 150% increase in t_i* – there is cross-over between the pressure-area curves at about 30% area. Similarly, when t_i* is increased from 0.01 up to 0.02 – a 100% increase in t_i* – there is cross-over again at about 50% area. It is interesting to note that even though from 0.01 to 0.02 there is a smaller percentage change in t_i*, the cross-over occurs earlier. In some sense, though, it is clear

that the $t_i^* = 0.05$ case is the most catastrophic. If the normalized external pressure were to be so great as 3, say, then the $t_i^* = 0.05$ case has about one-quarter the area that the $t_i^* = 0.02$ case has, and therefore has about 16 times the airflow resistance. In general, this comparison does seem to verify the hypothesis that thickening of the inner layer and the corresponding reduction in the number of folds causes delayed buckling, followed by a cross-over in the response such that there is a significant reduction in stiffness to occlusion in the late post-buckling response. For this choice of input parameters, the effect seems to be important only if the external pressure exceeds the value of the elastic modulus of the outer layer (E_o), that is, when $P^* > 1$.

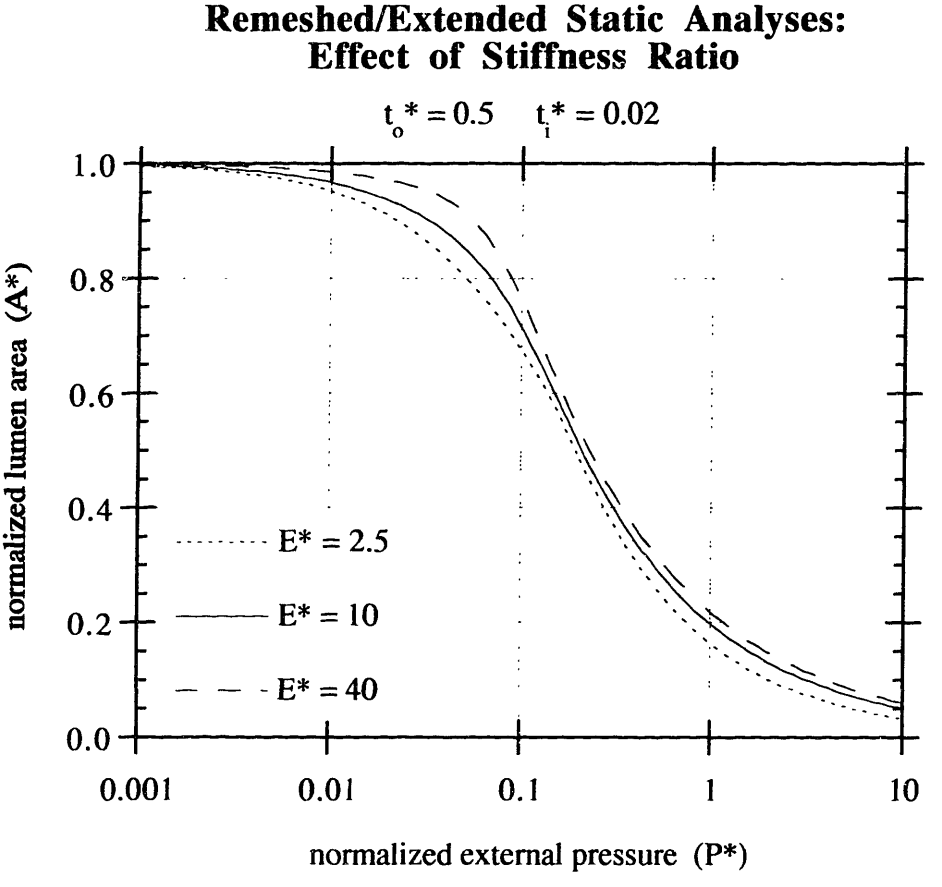

FIGURE 3-24: Remeshed and extended static analyses with varying E*.

Figure 3-24 shows cases 1, 6 and 7 which have varying E*-values. This is perhaps a more interesting result since it seems harder to have intuition about what should happen when the stiffness ratio changes. Perhaps one might guess that because increased stiffness ratio causes fewer folds (like t_i*, but to a lesser extent), there should again be cross-over of the pressure-area curves and more occlusion for the tube with the stiffer inner layer. This however, does not seem to be the case. Like an increase in t_i*, increasing E* tends to require higher buckling pressures, but the late post-buckling response shows no cross-over, as if it is relatively independent of E*. Perhaps the trend of the inner layer becoming stiffer than the outer layer, like thickening of the outer thickness ratio, also has a component that stiffens the airway to occlusion. It is also possible that the two tendencies (two-layer tube stiffening due to intrinsic material stiffening, and weakening due to fewer folds in the buckling pattern) are in balance. It would seem so from this representative case and various similar other ones that the author has examined.

Figure 3-25 shows a typical pressure (negative average normal stress) distribution in a two-layer model simulation at a relatively large amount of constriction (but before remeshing is necessary, $A^* \approx 0.6$). This particular simulation assumes an 11-fold rotationally-symmetric deformation, the closest whole number of folds to the N for this set of input parameters. The pressure map is useful because it indicates sources and sinks for fluid flow from regions of high pressure to regions of low pressure. Most of the modeled domain is in compression (positive pressure), but fluid would tend to collect in the sizable negative pressure pockets forming in the regions of the outer layer which penetrate into the lumen with the folds. The largest compressive stresses in the outer layer are behind the cusps of the folds which protrude into the outer layer. At its points of largest curvature, the inner layer shows a stress distribution much like a bending beam, compressive on the inside and tensile on the outside as shown in the inset of Figure 3-25.

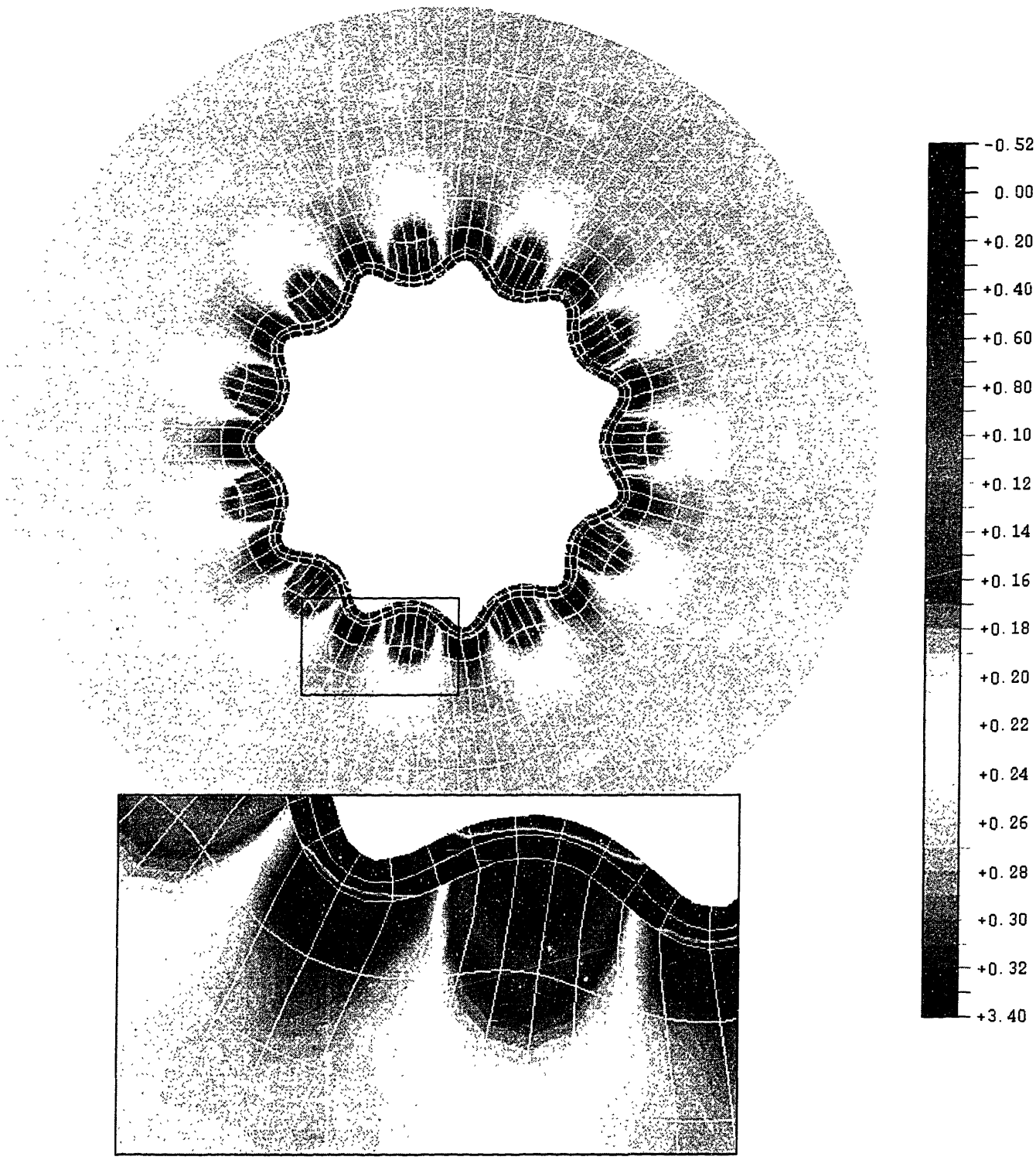

FIGURE 3-25: Contour plot showing a typical distribution of the pressure stress within the model at about A* = 0.6.

4. Large-Scale Physical Model Experiments

4.1 Motivation

Before the remeshing techniques discussed in Section 2.6 were developed, there was as yet not enough support for the hypothesis that a significant change in the number of folds in the buckling pattern of a two-layer tube (or airway) could drastically alter its postbuckling behavior. Simple two-layer physical models were constructed and tested in the hope that the hypothesis could be supported with experimental data. The physical models lend a more intuitive feel for how a two-layer tube buckles, and how the applied boundary conditions are critical in determining the preferred mode. They are a nice hands-on demonstration tool, and serve as a relatively easy way of verifying the computational results obtained from various analytical and computational analyses. Figure 4-1 shows three examples of these physical models (unfortunately, the inner layer is black and hard to see in these images). This set of tubes is small enough to be constricted by hose clamps. They nicely illustrate how as the inner layer increases in thickness, the expected number of folds in the buckling pattern decreases, producing larger folds.

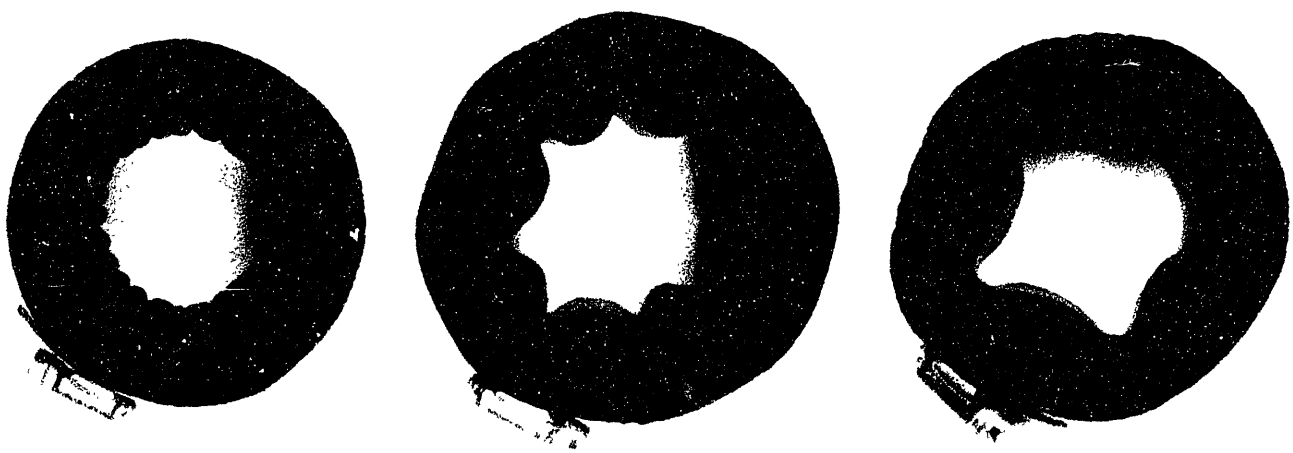

FIGURE 4-1: Examples of large-scale physical two-layer tube models. From left to right, the thickness of the stiff inner layer is increasing, thus the observed number of folds is decreasing.

4.2 Construction of Two-Layer Physical Models

The physical models are perhaps two orders of magnitude larger in size than any possible membranous airways of interest would be, thus the term "large-scale." Fortunately, dimensionless analysis allows us to make our physical models of arbitrary base radius (R). The outer layer of each physical model is a commercially available rubber foam tube (AP Armaflex® by Armstrong World Industries, Inc.), typically used as pipe insulation, which is not ideally linear-elastic, but has been assumed to be so. The inner layer is a commercially available plastic coating (Plasti-Dip® by PDI, Inc., Blaine, MN), which appears to be well-approximated as linear-elastic and incompressible. The coating was applied by keeping the outer surface of the tube covered while dipping in the liquid plastic. After drying, the ends were trimmed, leaving the tubes nearly axisymmetric in their construction. Each tube is 10 cm in length with base radii (R) ranging from 12.6 to 25.0 mm. Their outer thickness ratios (t_o*) range from 1.01 to 1.85, and inner thickness ratios (t_i*) range from 0.0127 to 0.0538. All these dimensions are easily measured directly with calipers. However, the parameter with the most uncertainty is the stiffness ratio (E*) since there is uncertainty in our measurements of Young's elastic modulus of both material layers. Based on the tests for the elastic moduli of the layers (discussed in the coming sections), the range in stiffness ratio (E*) of the physical models is from 210 to 314.

4.2.1 Properties of the Outer Foam Layer

Getting a single reliable value for the elastic modulus of Armaflex® foam turned out to be difficult. Some simple compression tests were performed on a balance by imposing a known displacement from above and measuring the load reading (see Figure 4-2). Specimens were taken from physical models after they were done being tested in other ways. The specimens were approximately 1 cm cubes. In a straightforward simple compression test, the median E-value was measured to be about 30 kPa, although there was a large spread among specimens. Preliminary indentation experiments on the foam (see Section 6.4.1) resulted in a foam modulus of about 35 kPa. More careful inspection of the specimens revealed that there were larger pores in the specimens from tubes with thicker outer layers, and small dense pores in specimens from the thinner tubes. This made it clear that there had to be a difference in the approximate E-value among the 8 different outer layer sizes tested. The foam would probably be better modeled as a poroelastic medium since there was significant decay in load after the displacement had been stepped

up. The tests were performed as slowly as possible, but the results still seemed too approximate and unreliable, thus motivating a different approach.

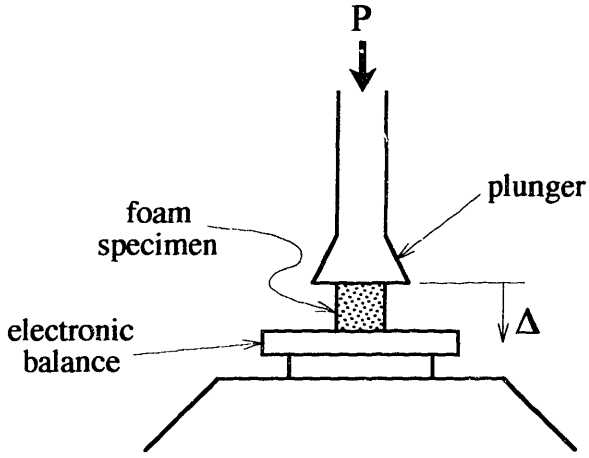

FIGURE 4-2: Diagram of a simple compression test performed on 1-cm foam cube specimens.

Single-layered Armaflex® foam tubes were tested in the sliding cable test fixture (described in Section 4.3 below) to determine their initial stiffness to external pressure. Figures 4-3 and 4-4 show the external pressure (P) recorded as a function of the applied outer edge displacement (Δ) for the 8 different outer layers. An initial P/Δ slope is calculated before the nonlinearity in the response becomes significant. Using the linear model analytical solution for external pressure of a single layer tube (with $\nu = 1/2$), we can compute Young's elastic modulus of the foam to be a function of the measured P/Δ slope.

$$E_o = \frac{3\,(1+t_o^*)}{2\,t_o^*\,(2+t_o^*)}\left(\frac{P_o}{\Delta^*}\right)$$

For a detailed derivation of the linear analytical solution leading up to this result, see Appendix A.2. The measurements and corresponding results for E_o are tabulated as follows.

outer layer designation	R (mm)	t_o (mm)	P/Δ^* (kPa)	E_o (kPa)
A	15.1	19.1	25.4	21.0
B	18.6	19.1	18.9	18.5
C	21.4	19.1	16.0	17.6
D	27.1	19.1	15.1	20.4
E	16.3	25.4	23.3	16.1
F	18.3	25.4	19.5	14.8
G	20.8	25.4	16.6	14.0
H	29.1	25.4	14.0	15.7

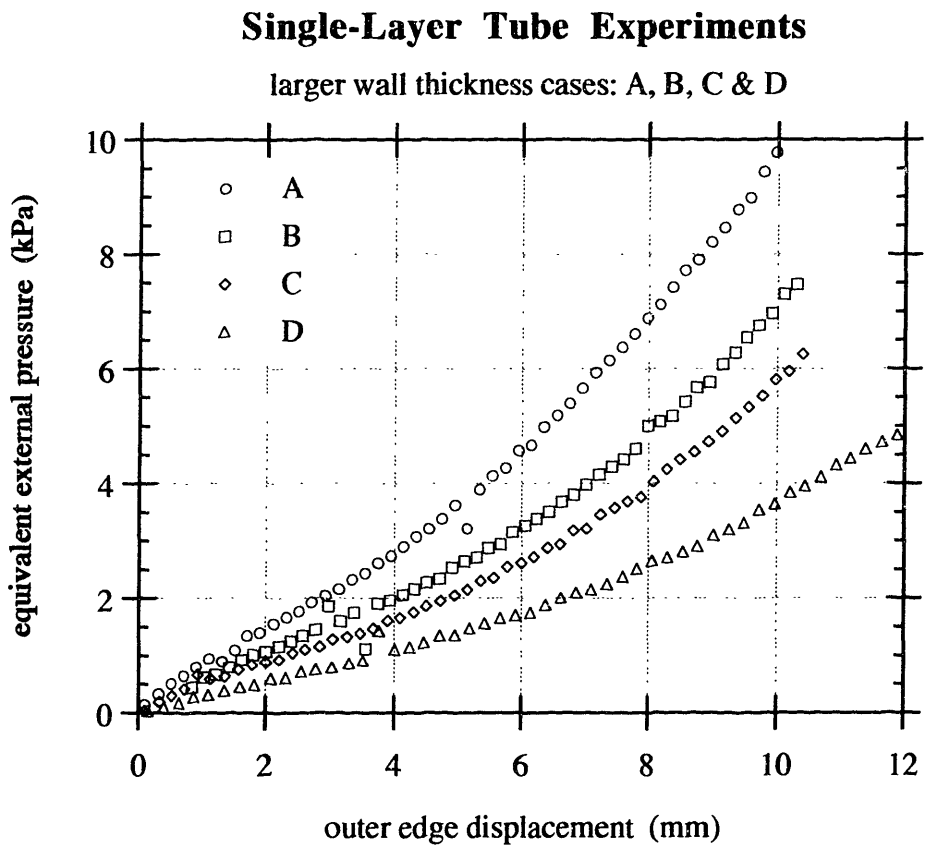

FIGURE 4-3: Outer edge pressure-displacement behavior for single-layered tubes A, B, C & D.

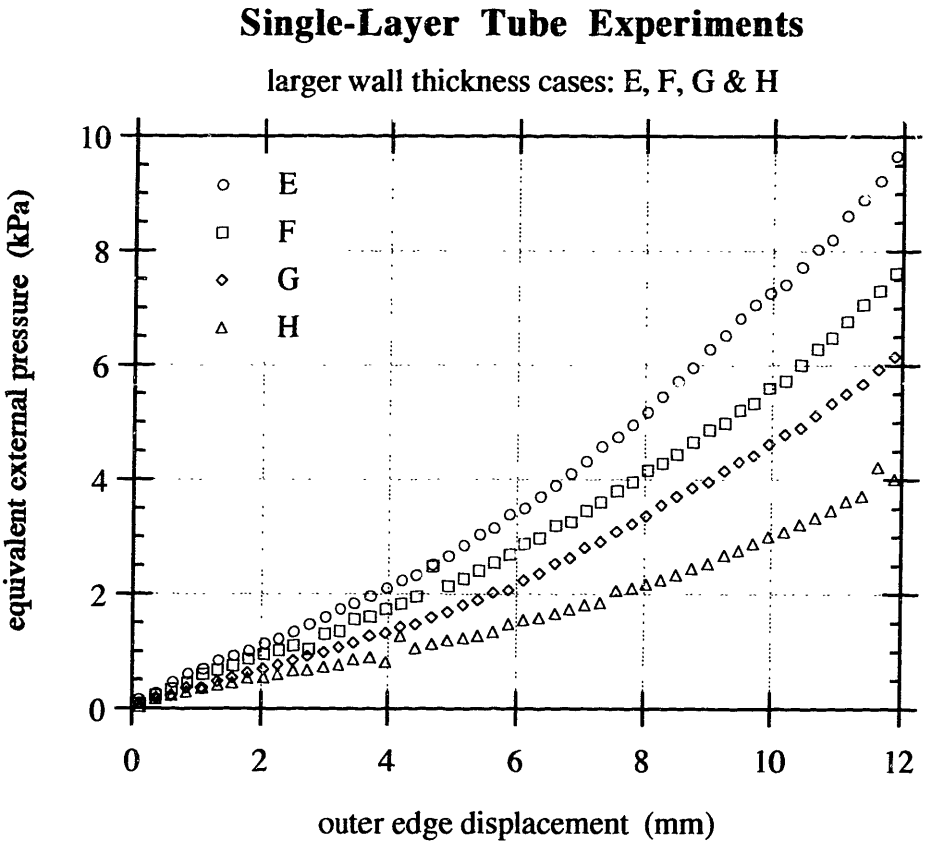

FIGURE 4-4: Outer edge pressure-displacement behavior for single-layered tubes E, F, G & H.

4.2.2 Properties of the Inner Plastic Layer

The inner layer of the large-scale physical models is a coating of a commercially available polymer named "Plasti-Dip," sold by the bucket. A long rope was made out of the Plasti-Dip, and a simple tension test was performed on it. Figure 4-5 displays the stress-strain curve computed from the tension test, showing that Plasti-Dip is not an entirely linear material, but well-approximated as one for relatively small strains.

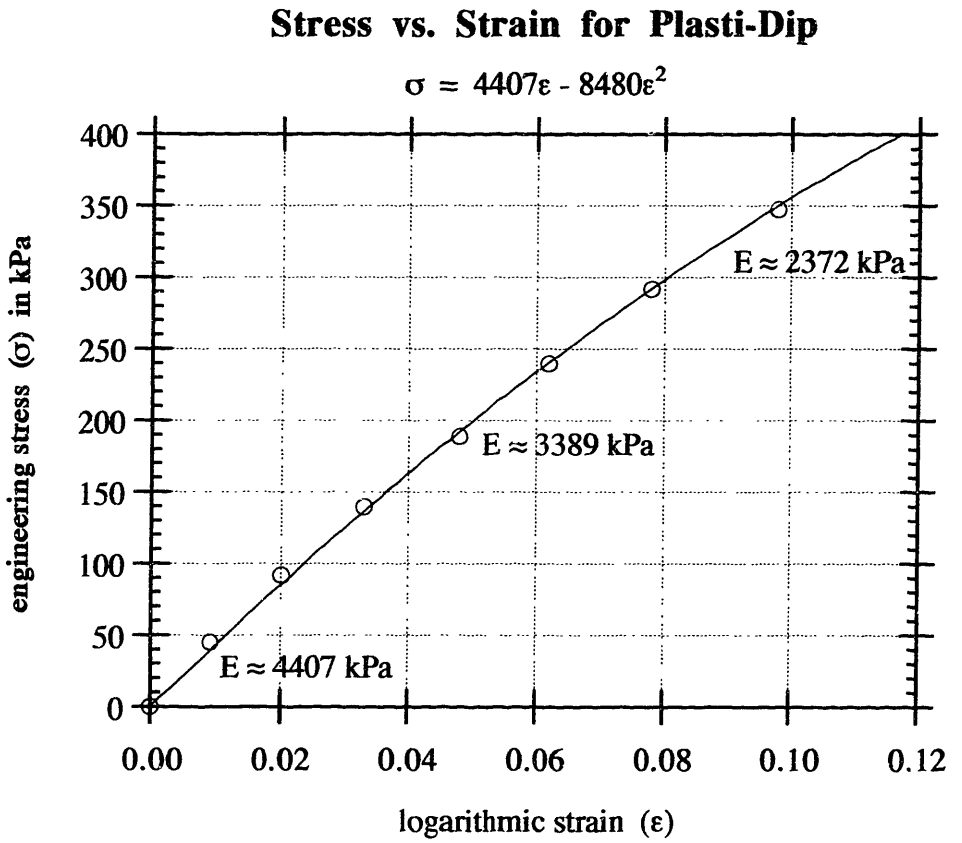

FIGURE 4-5: Results from a simple tension test to determine the elastic modulus of Plasti-Dip.

Given that the two-layer tube physical models buckle almost instantaneously upon loading, the small-strain value of the Plasti-Dip elastic modulus will be used in our buckling calculations, knowing that for larger amounts of deformation, the assumed material model of the Plasti-Dip will be too stiff. Thus for all physical model experiments:

$$E_i \approx 4400 \text{ kPa}$$

This value for E of Plasti-Dip was verified by preliminary indentation experiments on two-layer tubes (see Section 6.4.2).

The outer surfaces of the foam tubes were wrapped with newspaper and dipped in the Plasti-Dip coating. After multiple dips and ample drying time, the newspaper was removed and the ends of the tubes were trimmed and squared off. The inner layer thickness turned out to be thin, medium or thick, depending on whether the tube was dipped 1, 2 or 3 times. Since there are 8 possible outer layers and 3 possible inner layers, there are 24 different test cases total. The following table shows typical inner layer thicknesses for each possible case and calculates corresponding inner thickness ratios. The convention for the case names is the outer layer designation from above, followed by the number of Plasti-Dip coatings that were applied. Because of the shrinkage that accompanies the drying of the Plasti-Dip, these base radii are a bit smaller than for the single-layer tubes that they started out as (thus implying that there is a bit of prestress in the tubes, but this is neglected). The outer and inner thickness ratios are then calculated based on these radii. The stiffness ratio is also calculated for each case as 4400 kPa over the E_o-value that corresponds to the given outer layer (see Section 4.2.1).

case	R (mm)	t_o (mm)	t_i (mm)	t_o*	t_i*	E*
A1	12.9	19.1	0.330	1.48	0.0256	210
A2	12.8	19.1	0.512	1.49	0.0402	210
A3	12.6	19.1	0.677	1.51	0.0538	210
B1	16.2	19.1	0.343	1.18	0.0212	237
B2	16.3	19.1	0.505	1.18	0.0311	237
B3	15.6	19.1	0.702	1.22	0.0451	237
C1	18.8	19.1	0.305	1.02	0.0163	250
C2	19.0	19.1	0.404	1.01	0.0213	250
C3	17.2	19.1	0.673	1.11	0.0392	250
D1	23.3	19.1	0.343	0.82	0.0147	216
D2	21.6	19.1	0.461	0.88	0.0213	216
D3	22.2	19.1	0.728	0.86	0.0328	216
E1	14.3	25.4	0.301	1.77	0.0210	274
E2	13.7	25.4	0.334	1.85	0.0244	274
E3	13.7	25.4	0.648	1.85	0.0473	274
F1	15.8	25.4	0.343	1.61	0.0218	298
F2	14.8	25.4	0.331	1.71	0.0223	298
F3	15.0	25.4	0.670	1.69	0.0447	298
G1	17.5	25.4	0.343	1.45	0.0195	314
G2	16.9	25.4	0.470	1.51	0.0278	314
G3	16.3	25.4	0.799	1.56	0.0489	314
H1	25.0	25.4	0.318	1.02	0.0127	281
H2	23.4	25.4	0.512	1.09	0.0219	281
H3	23.0	25.4	0.817	1.10	0.0355	281

Three identical specimens were created for each case. Often in this chapter, results are reported as averages of the three measurements/observations. While the inner thickness ratios were just about right, the outer thickness ratios turned out to be larger than we would have liked – smaller thicknesses of Armaflex were not available. Thus all of the above cases are such that the number of folds should easily be independent of the outer thickness ratio. Also, Plasti-Dip turns out to be very much stiffer than the Armaflex foam; it would have been preferable to have smaller stiffness ratios. However, these tests should verify the trends observed in the computational models, even if the physiological applicability remains questionable (for a detailed discussion of physiological parameters, see Chapter 6).

4.3 Test Fixture and Imposed Boundary Conditions

The physical models were tested one-by-one in a test fixture, specially designed to create a loading and boundary condition at the outer surface which matches the applied outer-edge circumferential strain of the computational simulations as well as possible. A cuff of thin cables places a pressure on the outer surface while ensuring that the outer perimeter shortens in length. As long as the outer perimeter of the specimen remains circular, the pressure and imposed hoop strain should be constant around the outer edge. At each end the cables are fixed in blocks which are bolted to the crosshead and base of an Instron tensile testing machine, causing the cables to shorten at a fixed rate. The test fixture is very stiff relative to the tubes being tested, thus its deformation causes a negligible increase in the measurement of the tube's outer edge displacement. The fixture's cables apply no moment to the specimen because of their alternating clockwise-counterclockwise-clockwise wrapping pattern. Placing a thin slippery plastic layer between each tube specimen and the fixture's cables reduces friction greatly, encouraging uniform deformation circumferentially around the specimen. A bar is glued to all the cables to keep them nicely aligned and avoid entanglement.

The boundary condition the fixture imposes is not exactly the same as uniform circumferential strain. There is no such guarantee that the outer perimeter shortens by the exact same amount everywhere, only that the sum of the strains around the periphery (that is, the perimeter) shorten in length. Thus the two-lobe peanut-shaped mode of collapse is not inhibited as greatly as it is under uniform circumferential strain. At higher pressures, the buckling of the outer layer into the peanut collapse begins to predominate, but before this point, a large amount of useful data have already been acquired from the test.

D1: P* = 0 A* = 1

D2: P* = 0 A* = 1

D3: P* = 0 A* = 1

D1: P* = .064 A* = .82 N ≈ 18.5

D2: P* = .088 A* = .84 N ≈ 8.5

D3: P* = .11 A* = .81 N ≈ 6

D1: P* = .11 A* = .55 N ≈ 17.5

D2: P* = .14 A* = .44 N ≈ 8

D3: P* = .15 A* = .37 N ≈ 5

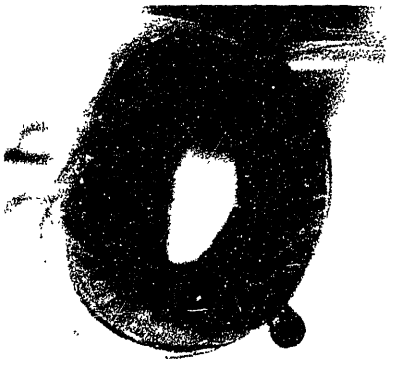

D1: P* = .17 A* = .36 N ≈ 16

D2: P* = .21 A* = .18 N ≈ 6

D3: P* = .21 A* = .10 N ≈ 3.5

FIGURE 4-6: (OPPOSITE) Three two-layer tube specimens (D1, D2 and D3) being tested in the test fixture, before the test has started and at three points during the test.

4.4 Test Setup and Procedure

The crosshead of the Instron moves at a constant rate of 50 mm/min. A load cell monitors the load applied to the fixture, and the measured displacement of the crosshead and fixture cables can be calculated from the time. For many of the various specimens, pictures were taken at known load levels for later processing. Figure 4-6 shows three specimens in the fixture at the beginning of their test and at three points during it along with the measured data for the states shown. The results from these three cases (D1, D2 and D3) will be compared with each other and against simulations in the next section.

The displacement of the crosshead is related to the specimen tube's outer edge inward radial displacement by a constant. The equivalent external pressure is calculated using the load measured by the load cell and the outer edge displacement. Buckling pressure and displacement are estimated by observing features of the resulting pressure-displacement curve. The initial number of folds is measured by observation. This is somewhat subjective, but carried out in a consistent manner. The pictures taken at specific load steps are digitized and processed using an image analysis tool (in this case, NIH Image) which counts pixels in the lumen, resulting in a coarse curve for lumen area as a function of external pressure. Data after any type of secondary buckling event (such as the buckling of the outer layer into the peanut shape) are ignored.

4.5 Results and Comparisons

4.5.1 Folding Pattern

The initial number of folds observed in the tube test experiments is plotted case by case in Figure 4-7 and compared with the linearized buckling analysis results for N. There appears to be general agreement between the experiments and the analyses

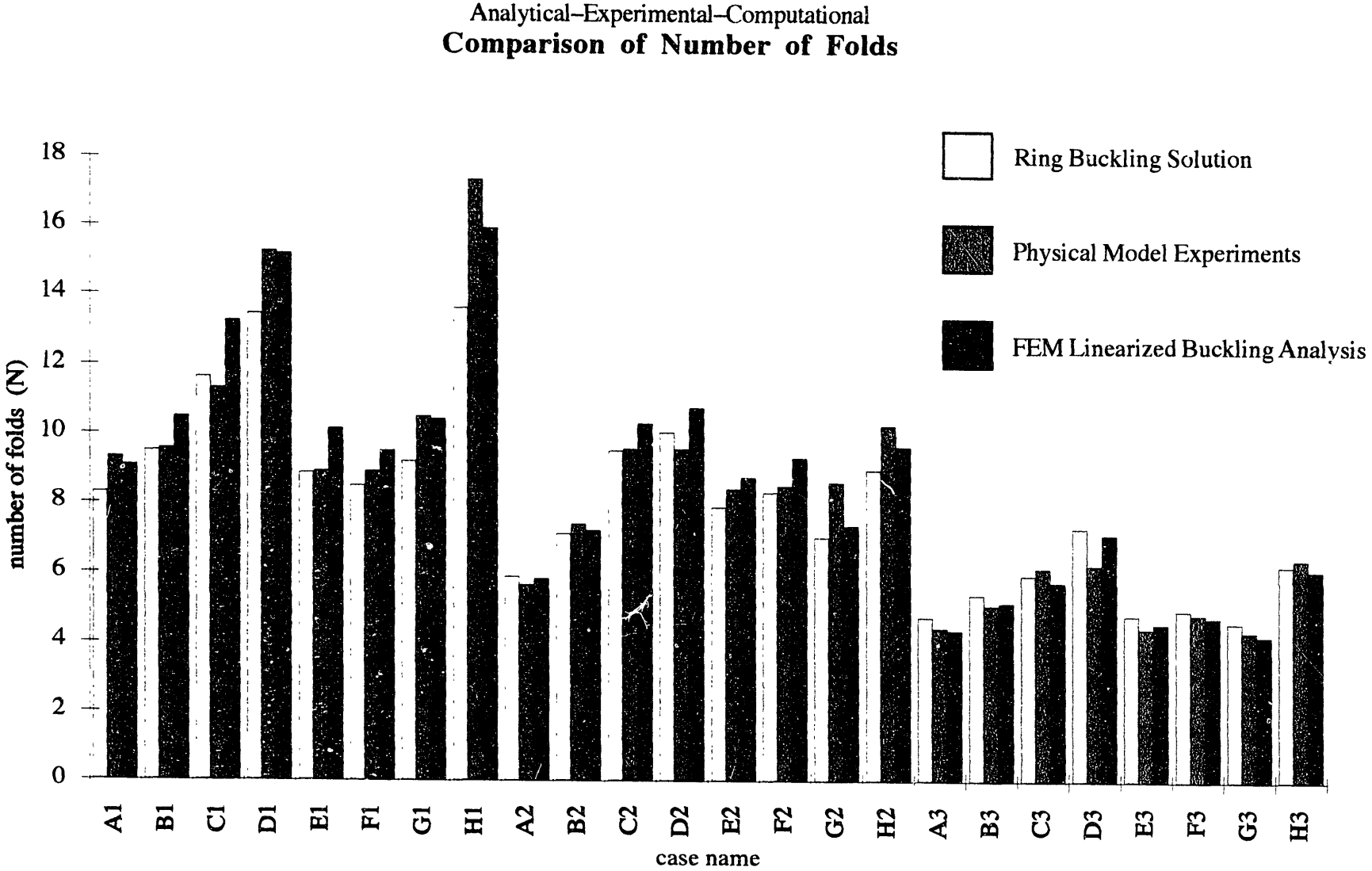

FIGURE 4-7: Two-layer tube physical model experimental results for N compared with LBA finite element solution for N and analytical ring-buckling solution for N (see Appendix A.3).

Figure 4-7 averages the three N-observations for each specimen case and compares with a linearized buckling analysis that was run at the specific average input parameters (t_o*, t_i* and E*). In contrast, Figure 4-8 plots the inner thickness ratio (the strongest of the three parameters) versus the observed number of folds for each individual specimen and the corresponding estimates of the LBA result extrapolated from the curve fit of 500 cases presented in Section 3.1.2. Note that the curve fit was established over a range of E* from 2.5 to 40 while the E* from the tube tests ranges from 210 to 314, so there is slight discrepancy between the extrapolated LBA results and the specific cases run at the appropriate stiffness ratios above.

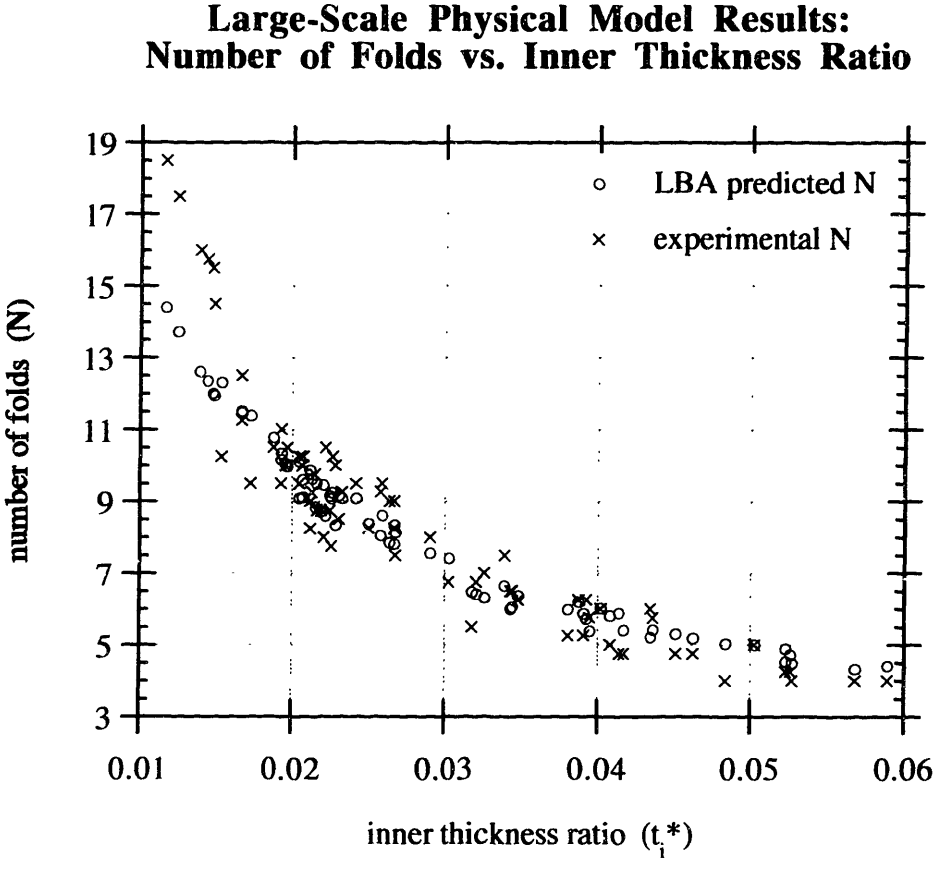

FIGURE 4-8: Two-layer tube experimental N compared with extrapolated LBA solutions for N, plotted against the strongest input parameter, t_i*.

The agreement between N-observations does indeed seem to indicate that despite some of the dubious modeling assumptions made (linear, incompressible materials, etc.), our simulations are good representations of actual two-layer tubes, at least for the leading behavior up to and including the point of buckling. For the sampling of cases shown in Figure 4-7, the ring buckling solution (derived in Appendix A.3) consistently underestimates the number of folds predicted by the FEM linearized buckling analysis. The difference between them, however, is on the order of the error between simulations and experiments. The FEM simulations are usually in better agreement with the experiments than the analytical solution.

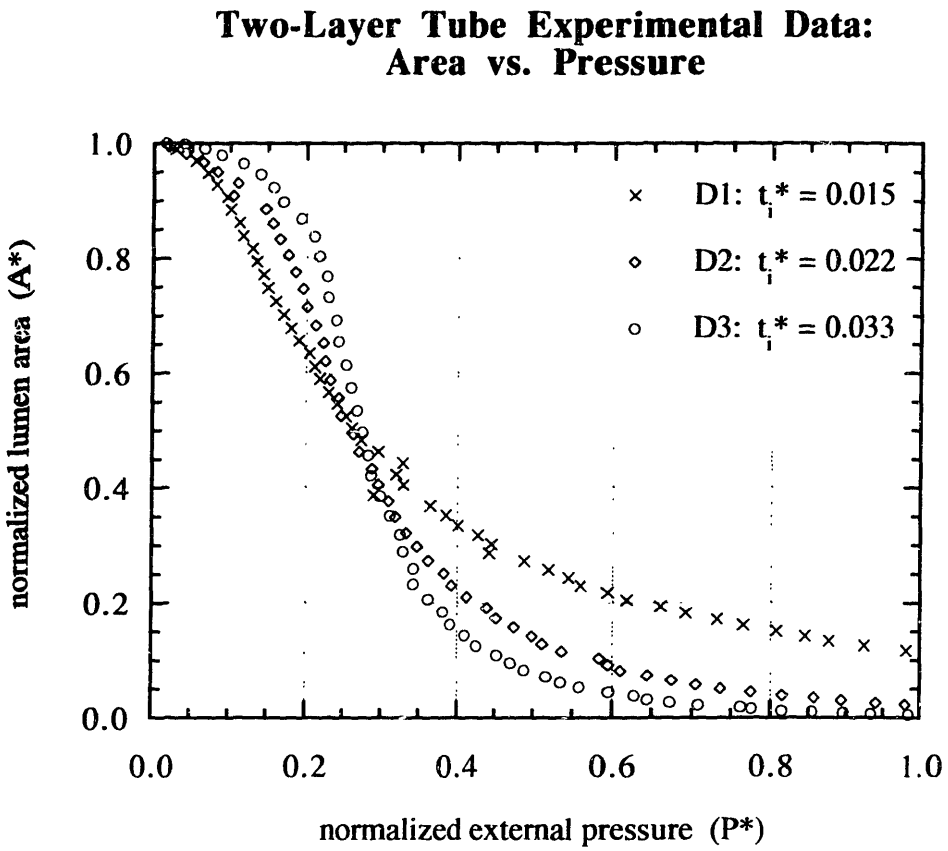

FIGURE 4-9: Two-layer tube experimental results for pressure-area response for three cases (D1, D2 and D3), showing considerable cross-over.

4.5.2 Pressure vs. Area Response

Figure 4-9 compares three experimental pressure-area curves from two-layer tubes with the same outer thickness. These three ("D-series") tubes have the smallest outer thickness ratios, thus the pressure-area response is most likely to be affected by the changing inner thickness ratio. Note that tube D3 has more structure to it than D2, which has more than D1, and yet in the later postbuckling response, tube D1 is the stiffest to occlusion, followed by D2, while D3 with the most mass and structure collapses the easiest. This is the phenomenon of "cross-over" suggested in the hypotheses of Section 1.4.

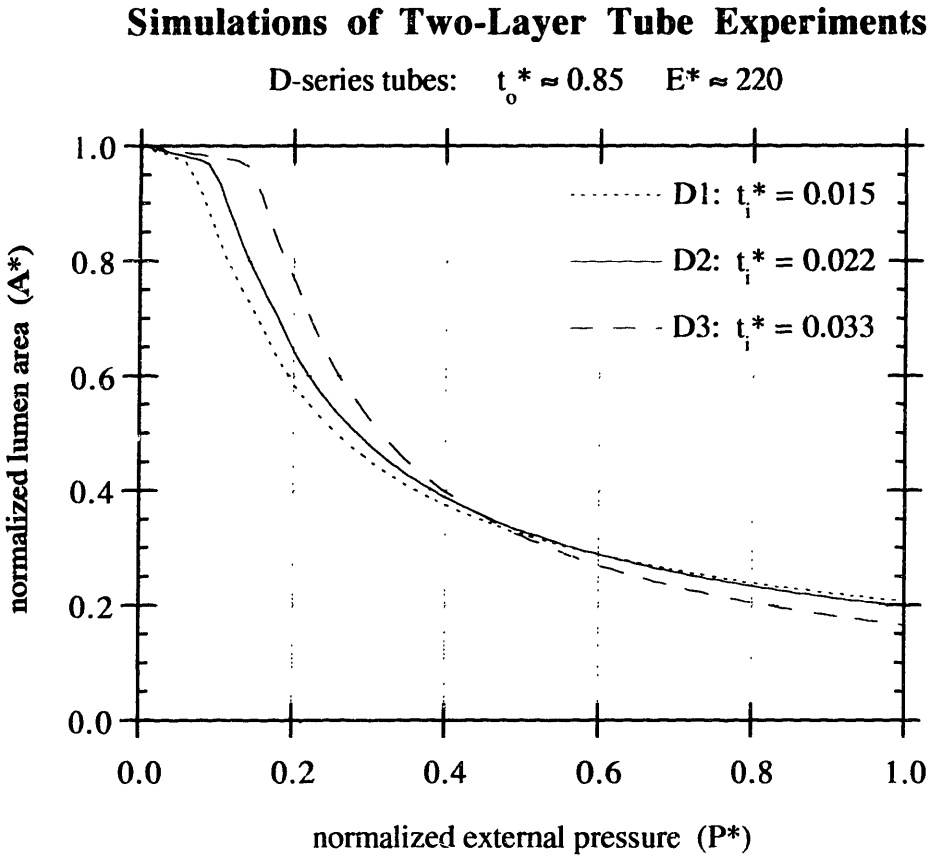

FIGURE 4-10: Finite element simulations of pressure-area response for the three two-layer tubes of Figure 4-8. Curves do cross-over one another, but not to the degree that they do in the experiments. The simulations do not compress as much as experiments in general.

From case D1 to D3, the inner thickness ratio (t_i*) has increased by a factor of about 2. Note that at a P*-value of only about 0.5, tube D1 has about 3 times the lumen area that tube D3 has. That means that at that value of P*, D3 would have at least 9 times as much resistance to airflow than D1 ("at least" because this does not take ovalization into account). At even larger values of P*, this effect is even more pronounced. This phenomenon of cross-over confirms the hypothesis that the consequence of folding in relatively few folds is detrimental to the late-response stiffness to occlusion, (provided that the outer layer is thin enough and/or the inner layer is stiff enough that the outer layer stiffness does not predominate over the inner layer).

Figure 4-10 shows three finite element static analyses (with remeshing, smoothing and extrapolation) at the parameters measured for the three two-layer tubes (D1, D2 and D3).

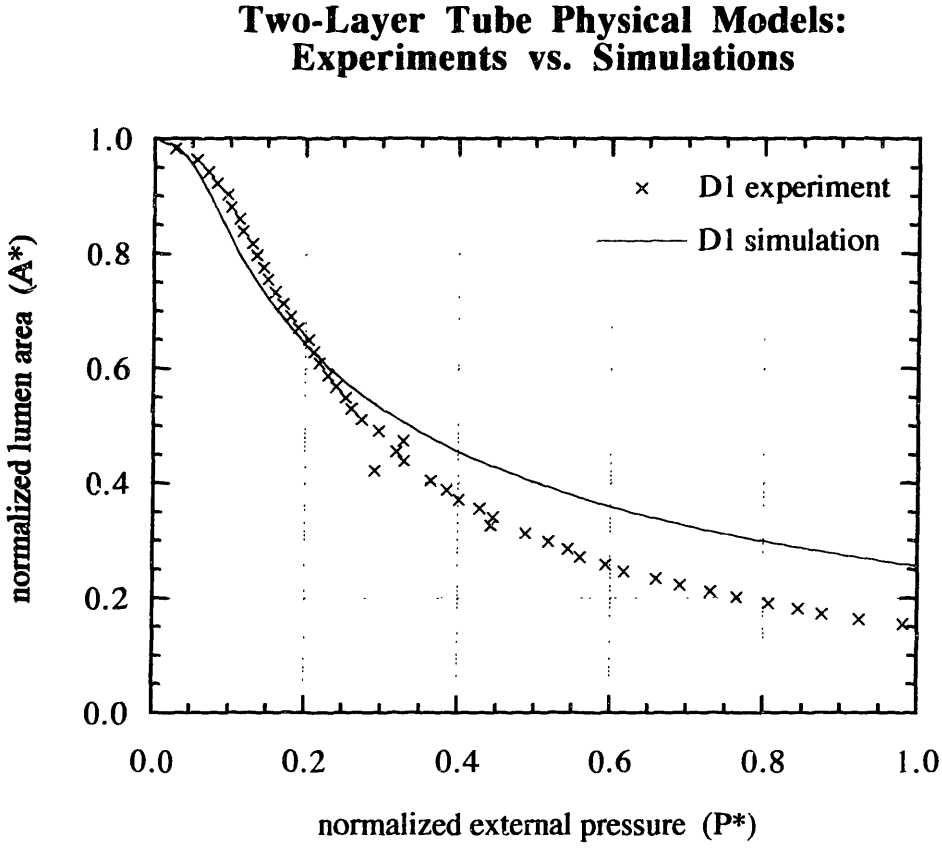

FIGURE 4-11: Comparison between experimental and simulated case D1, showing fair agreement.

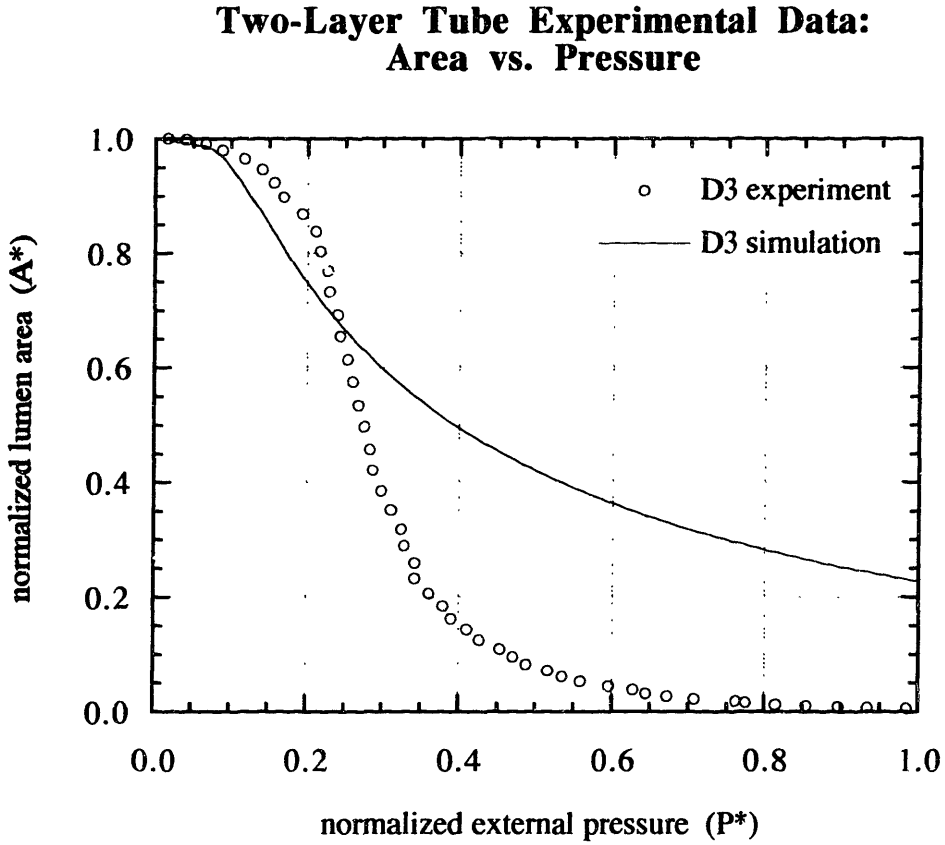

FIGURE 4-12: Comparison between experimental and simulated case D3, showing poor agreement. Constitutive law for foam may not be appropriate.

Figures 4-11 and 4-12 compare data acquired from the D1 and D3 experimental cases against finite element simulations (including remeshing) at the same three input parameters.

The cross-over observed in the experiments is evident in the simulations as well. However, aside from the agreement of trends, the simulations do not match the experiments that well. The experiments and simulations appear to agree on the leading stiffness, and the trend in movement of the buckling point appears to be verified. The experiments do exhibit more crossing-over than the simulations do though. The foam tubes were able to compress significantly more than the simulations predicted, suggesting that some type of strain-softening material law for the outer layer may be more appropriate in the simulations. Other experiments with the Armaflex foam revealed that with time, air

could be compressed from the foam. Maybe a compressible or poroelastic material description would result in better agreement. The tubes did elongate in the axial direction during the test as well, indicating that the real situation was not purely plane-strain, but somewhere in between plane-strain and plane-stress. The number of folds, as shown in Section 3.2, tends not to be strongly correlated to compressibility or the axial deformation assumption, and that is a possible reason why we are able to see such good agreement in the number of folds, but not in the collapse response. As shown in Figure 4-5, the inner layer would also be better modeled as strain-softening, and that would contribute to this type of error as well.

Another very likely possibility is that the test fixture allows too much of the peanut-shaped collapse (see Figure 4-6), resulting in a faster collapse because this lower energy mode is more available than it would be under outer edge hoop strain conditions. Some of the tubes, just because of the way they were constructed, have a slightly oval shape to begin with (too much imperfection in the two-lobe mode), so the resulting collapse is more oval-shaped than it should be.

5. Animal Model Experiments

One goal of our research team is to develop an animal model of asthma which can be used to verify the hypotheses that have been set forth. Ideally one could induce asthma in an animal, then study methods for reversing it. This has proved very difficult because even though different species may have similar materials and components in their airways, it is hard to find an animal that has approximately the same dimensions as humans do. Also, there is no guarantee that an artificial condition which can be induced in an animal would not revert back to a normal state without any counter-action. In short, making the connection between animals and human beings is where the trouble lies. For instance, the fact that no species other than human develops asthma casts doubt on the possibility of even attaining a state that could be considered "asthmatic" in an animal. No less, animal models are our only tool for studying how the asthmatic state is achieved or relieved. This chapter gives a brief overview of some of the experiments that are being done with Brown Norway rats, pointing out successes and shortcomings of the rat models to date.

5.1 Ovalbumin Challenge Experiments

These experiments are being performed by a group of several researchers at the Harvard School of Public Health, including Drs. Drazen, Freidberg, Lai, Rogers and Shore. One particular experiment which is being done is to sensitize a population of Brown Norway rats by frequently giving them inhalations of ovalbumin over the course of 6 weeks or longer along side a control population which is given saline. After the sensitization period, the rats are sacrificed and their lungs are given a large dose of methacholine, an airway smooth muscle agonist. The ovalbumin sensitization does have the desired effect of making the rats' airways hyperresponsive – for the same dose of agonist, the sensitized airways do indeed exhibit greater luminal obstruction and fewer folds than the controls. However, the sensitized airways do not exhibit marked thickening of any sub-epithelial collagen. In fact, it would appear that Brown Norway rats barely have a sub-epithelial collagen layer at all.

Some preliminary results are shown in Figure 5-1. Upon first glance at the data in Figure 5-1, one might be drawn to the conclusion that the number of folds (N) is correlated to the amount of luminal obstruction – that one is merely a function of the other independent of the thicknesses or stiffnesses of the airway layers. Coming to this conclusion is not truly

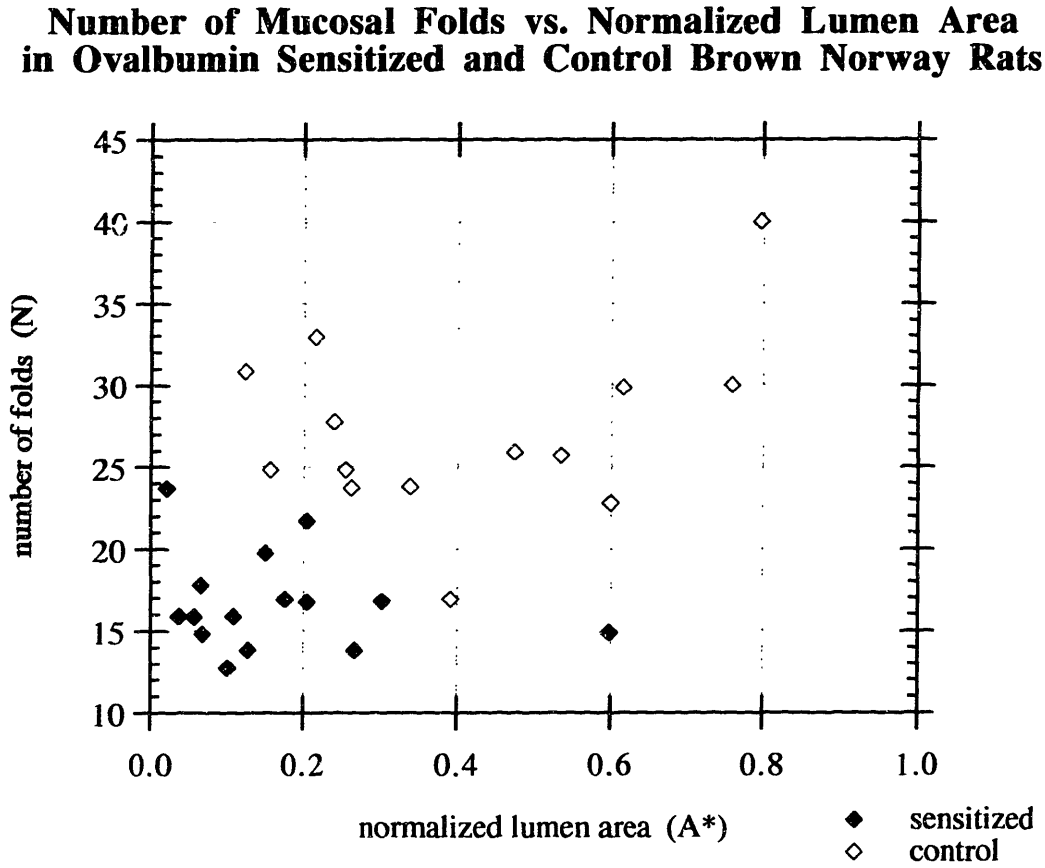

FIGURE 5-1: Preliminary results of number of folds versus normalized lumen area for sensitized and control populations from the ovalbumin challenge experiments.

mechanically sound, since the presence of folds internal to the smooth muscle proves that there must be some zone of higher stiffness at the inner aspect of the airway, otherwise there would be no such folding, and the only way of changing N is by altering the mechanical structure of the folding membrane or the nearby environment. The possibility of making this conclusion is what inspired an experiment to test the validity of the assumption that the number of folds remains constant throughout airway constriction, for if indeed N is independent of the amount of constriction, the decreased N in sensitized animals must be due to changes in the gross geometry and structure of the airway. The linearized buckling analyses presented in Section 3.1 indicate that because of their thinner geometries (small t_o* and t_i*), rat airways may fall into a different mechanical response

regime, one in which the thickness of the outer layer has a much larger effect on N than we would expect for human airway dimensions.

5.2 Split-Lung Experiments

The experiments described in this section were conceived by Dr. Robert Schellenberg of the University of British Columbia Pulmonary Research Laboratory, executed by the author, and analyzed by Dr. Stephanie Shore of the Harvard School of Public Health and Dr. Barry Wiggs (also of UBC PRL). The basic goal is to verify that the number of folds exhibited by an airway as it constricts is roughly constant.

The way that this is accomplished is described pictorially in Figure 5-2. Normal Brown Norway rats are given a lethal dose of the anesthetic sodium pentobarbital. Soon after the animal expires, the lungs are excised, and their lobes are separated from each other. Each lobe is carefully sliced with a sharp scalpel and the sides which were originally facing each other are placed face-down in a bath of methacholine. One side is placed in a low dose (10^{-7} M) bath, just enough to induce some constriction and folding; the other is placed in a high dose (10^{-4} M) bath, enough to induce almost maximal constriction and deeper folding. The baths are kept at physiological temperatures over an interval of 20 minutes to allow thorough penetration of the methacholine and smooth muscle contraction. Afterward, the specimens are fixed in formalin and histology samples are taken from as close as possible to the faces that were originally in contact with one another.

The histology now reveals a high-dose/low-dose pair of folding patterns (see Figure 5-3). Using the commonly accepted techniques for measuring the amount of smooth muscle constriction (based on the assumption that inner perimeter remains constant and that the airway wall materials are incompressible), the degree of airway constriction (A*) is plotted against the number of folds (N) for the high-dose/low-dose pair as shown in Figure 5-4. An arrow is drawn to pair up corresponding data points and to accentuate the slope of the relationship between A* and N. Note that the axes of Figure 5-4 are identical to those of Figure 5-1, allowing direct comparison. The mostly horizontal relationships between A* and N indicate that it is indeed a good assumption that N remains constant as A* decreases. The median reduction in N per 0.1 reduction in A* is about 0.15 folds.

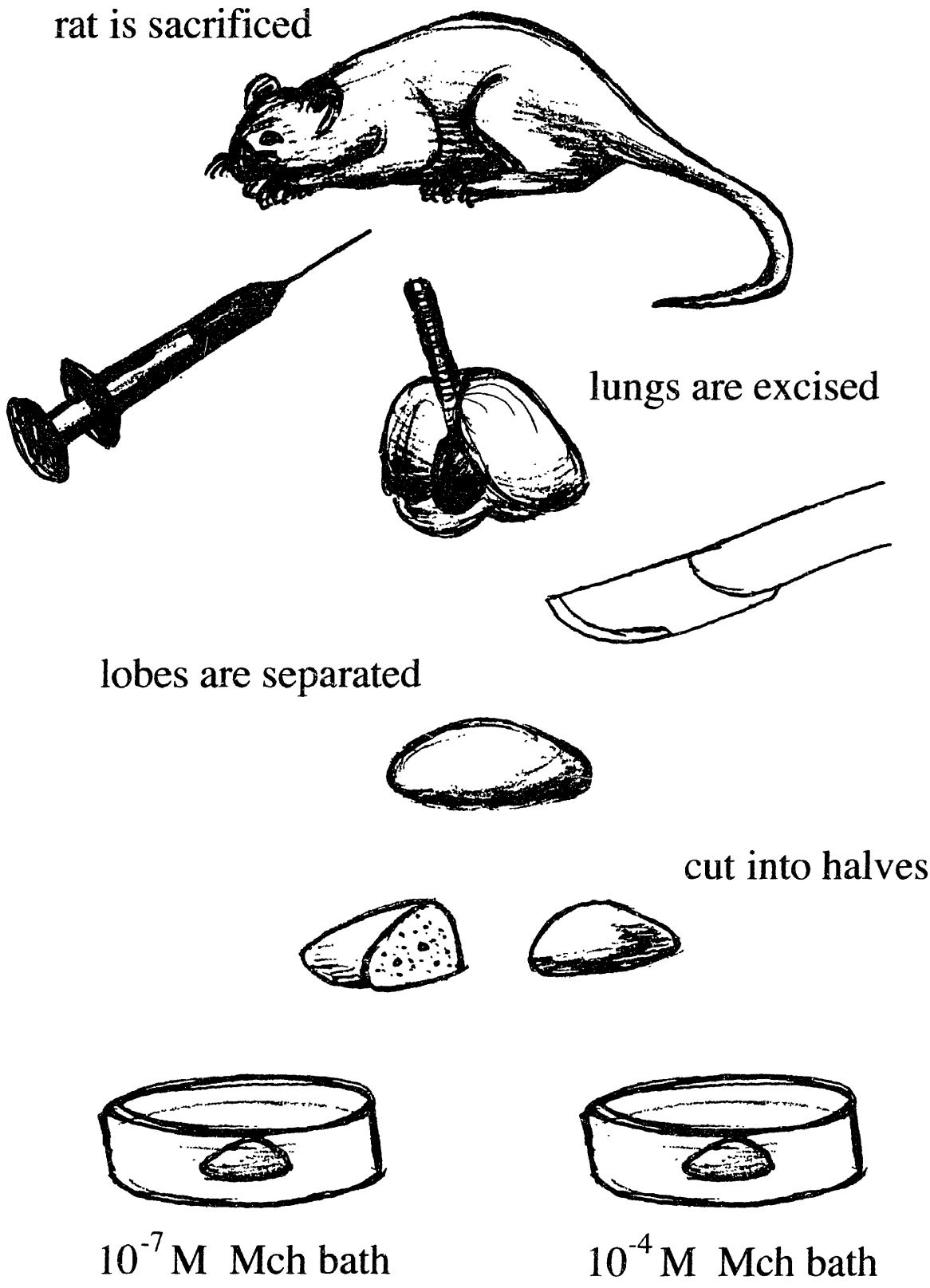

FIGURE 5-2: Sketch showing the general procedure of the split-lung experiments.

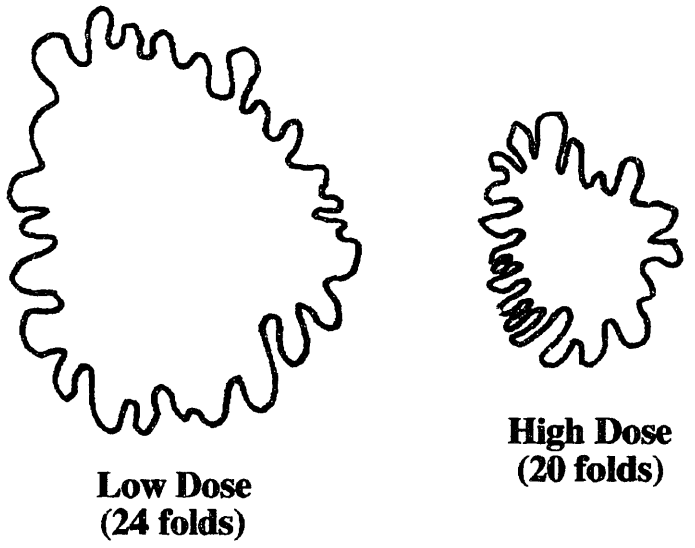

FIGURE 5-3: Two example tracings of high-dose/low-dose buckling pattern pairs.

The results of the 11 high-dose/low-dose pairs have been subjected to t-tests to establish the merit of the hypothesis that the number of folds is approximately constant. P-values for various hypotheses are summarized in the table below. In this case, the P-value is the smallest level of significance at which the hypothesis would be rejected when the t-test is applied to the split-lung experimental data.

define x as the % decrease in N from A* = 1 to A* = 0	
Hypothesis	P-value
$\bar{x} < 0\%$	0.13
$\bar{x} < 10\%$	0.08
$\bar{x} < 20\%$	0.05

The results of this experiment make us more confident that some significant structural change is indeed occurring between normal and sensitized animals in the ovalbumin challenge experiments. Also, it verifies that the constant N assumption is an appropriate one, supporting the use of constant-N wedge-models of airway collapse (see Section 2.4.4).

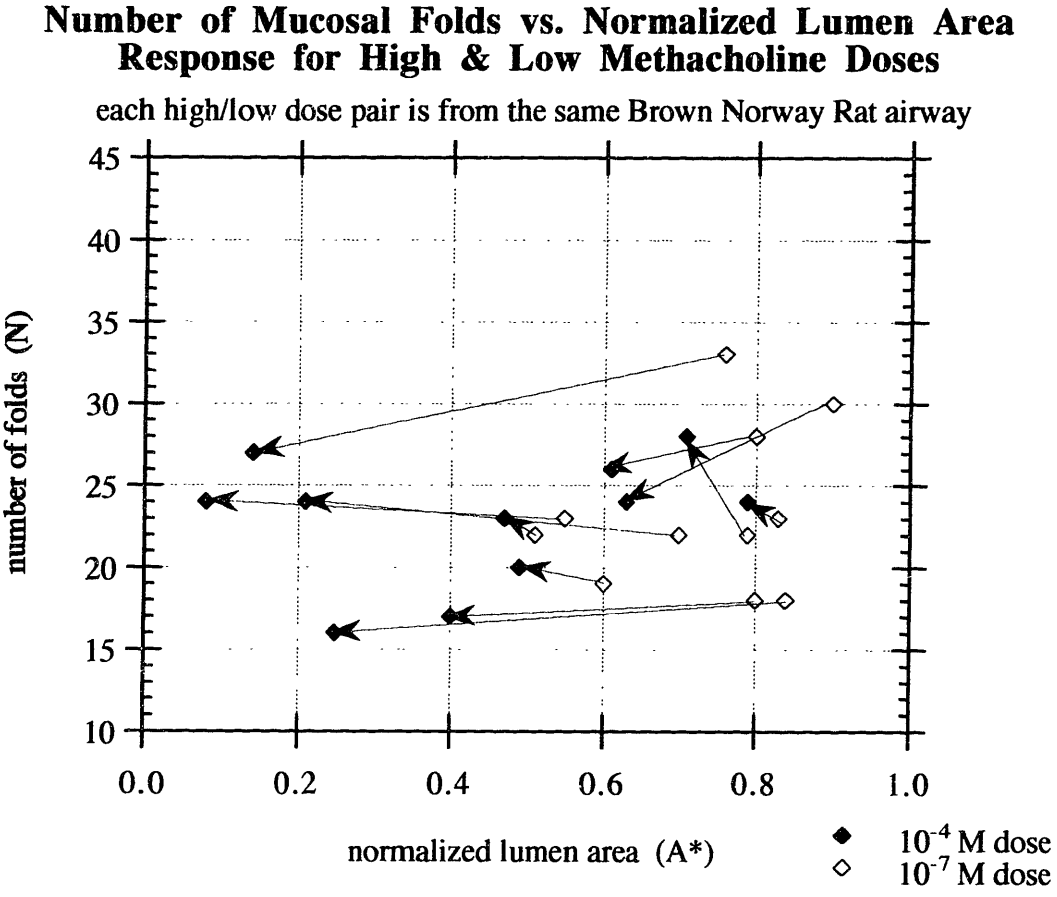

FIGURE 5-4: Number of folds versus normalized lumen area results from the split-lung experiments (with same scale as Figure 5-1). Arrows point from each low-dose state to its corresponding high-dose state.

CHAPTER 5 REFERENCES

1. Bellofiore S, Martin JG. Antigen challenge of sensitized rats increases airway responsiveness to methacholine. *J. Appl. Physiol.* 65(4): 1642-1646, 1988.

2. Blyth DI, Pedrick MS, Savage TJ, Hessel EM, Fattah D. Lung inflammation and epithelial changes in a murine model of atopic asthma. *Am. J. Respir. Cell Mol. Biol.* 14: 425-438, 1996.

3. Dandurand D, Lenahan T, Fayvilevich Y, Kosinski R, Eidelman D. In vitro allergic bronchoconstriction in the brown Norway rat. *Amer. Rev. Resp. Dis.* 149: 1499-1505, 1994.

4. Du T, Xu JL, Lei M, Wang NS, Eidelman DH, Ghezzo H, Martin JG. Morphometric changes during the early airway responses to allergen challenge in sensitized inbred rats. *Am. Rev. Resp. Dis.* 146: 1037-1041, 1992.

5. James AL, Paré PD, Hogg JC. Effects of lung volume, bronchoconstriction and cigarette smoking on morphometric airway dimensions. *J. Appl. Physiol.* 64(3): 913-919, 1988.

6. Lutchen KR, Hantos Z, Peták F, Adamicza Á, Suki B. Airway inhomogeneities contribute to apparent lung tissue mechanics during constriction. *J. Appl. Physiol.* 80(5): 1841-1849, 1996.

7. Lutchen KR, Suki B, Zhang Q, Peták F, Daróczy B, Hantos Z. Airway and tissue mechanics during physiological breathing and bronchoconstriction in dogs. *J. Appl. Physiol.* 77(1): 373-385, 1994.

8. Sapienza S, Du T, Eidelman H, Wang NS, Martin JG. Structural changes in the airways of sensitized brown Norway rats after antigen challenge. *Am. Rev. Respir. Dis.* 144: 423-427, 1991.

9. Sasaki F, English D, Paré PD, Okazawa M. Airway wall dimensions during carbachol induced bronchoconstriction. *Amer. Rev. Resp. Dis.* 149(4): A586, 1994.

10. Shore S, Kobzik L, Long NC, Skornik W, Van Staden CJ, Boulet L, Rodger IW, Pon DJ. Increased airway responsiveness to inhaled methacholine in a rat model of chronic bronchitis. *Am. J. Respir. Crit. Care Med.* 151: 1931-1938, 1995.

6. Appropriate Model Parameters

Critical to the applicability of the airway collapse models presented in this work to the study of asthmatic airways in humans is the use of appropriate model input parameters. In the case of the "simple" two-layer model, the only parameters necessary to fully describe the structure are those that define the geometry (the radius to the interface between layers, R, and layer thicknesses, t_o and t_i) and each material's intrinsic stiffness (the elastic moduli, E_o and E_i). While knowing the geometry does not appear to be much of a problem based on previously published studies, the elastic moduli are a different matter. Measuring the linear-elastic modulus E appears to be a hard enough task (much less the Poisson ratio, ν, or any other parameters which might specify a more complicated and possibly nonlinear material). This in essence is why simplicity is desired in our models, because the appropriate material parameters are at best known to an order of magnitude, and thus finely tuned adjustments such as slight nonlinearities are overly precise and superfluous.

6.1 Geometry Parameters

6.1.1 Outer Thickness Ratio (t_o*)

In order to obtain appropriate values for the two geometrical input parameters (t_o* and t_i*), one need only refer to any of several human airway morphometry studies. For the outer thickness ratio, the ones which will be used here are those of Wiggs et al.[34,35,36] The following tables show how the outer thickness ratio is calculated as a function of the generation number and corresponding airway size (characterized by R) for both normal and asthmatic airways. James et al. have shown that regardless of how much a particular airway has collapsed, its internal perimeter remains roughly constant.[17] This is because the stiffer mucosal layer would prefer to buckle and bend into folds rather than shorten under axisymmetric deformation.

The top of each column indicates, along with the variable name, whether or not the data in that column are "given" from a paper by Wiggs et al. or if the data were "calculated" from preceding data. The first column is the airway generation number (Z). The second column is the volume-corrected internal diameter of the airways of that generation. The third column is simply the second divided by two to make a radius, then multiplied by ten to convert to mm, and this column is the familiar base radius (R) in mm. The fourth column is the lumen area as calculated by R, assuming circular geometry. The fifth is the cross-

sectional area of airway wall ("wall area"), as given by the Wiggs studies. It will be assumed here that the given wall area measured is completely submucosa, although there may be a small fraction that is mucosa. Thus the following calculations may be using overestimates of t_o*. This error will increase with increasing generation number since a larger proportion of the airway wall is mucosa in smaller airways. The sixth column is the total area, simply the sum of lumen area and wall area. The seventh is the airway outer radius (R_o), as calculated from the total area, assuming circular geometry. The eighth column is the outer layer thickness ($t_o = R_o - R$). Finally, the last column tabulates the outer thickness ratio ($t_o^* = t_o/R$).

NORMAL AIRWAY DIMENSIONS[36]

Z	given D_v (cm)	calc. R (mm)	calc. LA (mm^2)	given WA (mm^2)	calc. TA (mm^2)	calc. R_o (mm)	calc. t_o (mm)	calc. t_o*
0	1.783	8.915	249.69	32.20	281.89	9.472	0.5574	0.063
1	1.210	6.050	114.99	15.01	130.00	6.433	0.3828	0.063
2	0.805	4.025	50.90	7.34	58.24	4.305	0.2805	0.070
3	0.538	2.690	22.73	3.58	26.31	2.894	0.2041	0.076
4	0.421	2.105	13.92	2.35	16.27	2.276	0.1708	0.081
5	0.330	1.650	8.55	1.51	10.06	1.790	0.1397	0.085
6	0.262	1.310	5.39	1.00	6.39	1.426	0.1163	0.089
7	0.211	1.055	3.50	0.68	4.18	1.153	0.0980	0.093
8	0.172	0.860	2.32	0.48	2.80	0.945	0.0847	0.098
9	0.142	0.710	1.58	0.34	1.92	0.783	0.0725	0.102
10	0.119	0.595	1.11	0.26	1.37	0.661	0.0659	0.111
11	0.101	0.505	0.80	0.19	0.99	0.562	0.0567	0.112
12	0.087	0.435	0.59	0.15	0.74	0.487	0.0518	0.119
13	0.076	0.380	0.45	0.12	0.57	0.427	0.0473	0.125
14	0.067	0.335	0.35	0.10	0.45	0.380	0.0445	0.133
15	0.060	0.300	0.28	0.09	0.37	0.344	0.0445	0.148
16	0.054	0.270	0.23	0.07	0.30	0.309	0.0385	0.143
17	0.050	0.250	0.20	0.07	0.27	0.291	0.0412	0.165
18	0.046	0.230	0.17	0.06	0.23	0.268	0.0383	0.167
19	0.043	0.215	0.15	0.05	0.20	0.249	0.0343	0.159
20	0.041	0.205	0.13	0.05	0.18	0.241	0.0357	0.174
21	0.040	0.200	0.13	0.05	0.18	0.236	0.0365	0.182
22	0.039	0.195	0.12	0.05	0.17	0.232	0.0373	0.191
23	0.038	0.190	0.11	0.05	0.16	0.228	0.0381	0.200

ASTHMATIC AIRWAY DIMENSIONS[35]

Z	given D_v (cm)	calc. R (mm)	calc. LA (mm^2)	given WA (mm^2)	calc. TA (mm^2)	calc. R_o (mm)	calc. t_o (mm)	calc. t_o*
0	1.572	7.860	194.09	86.17	280.25	9.445	1.5850	0.202
1	1.067	5.335	89.42	39.91	129.33	6.416	1.0810	0.203
2	0.724	3.620	41.17	18.54	59.71	4.360	0.7395	0.204
3	0.491	2.455	18.93	8.65	27.58	2.963	0.5081	0.207
4	0.389	1.945	11.88	5.49	17.37	2.351	0.4064	0.209
5	0.307	1.535	7.40	3.47	10.87	1.860	0.3249	0.212
6	0.245	1.225	4.71	2.25	6.96	1.489	0.2639	0.215
7	0.198	0.990	3.08	1.50	4.58	1.208	0.2176	0.220
8	0.163	0.815	2.09	1.03	3.12	0.996	0.1812	0.222
9	0.135	0.675	1.43	0.73	2.16	0.829	0.1539	0.228
10	0.113	0.565	1.00	0.53	1.53	0.698	0.1328	0.235
11	0.096	0.480	0.72	0.39	1.12	0.596	0.1162	0.242
12	0.083	0.415	0.54	0.30	0.84	0.518	0.1027	0.248
13	0.072	0.360	0.41	0.24	0.64	0.452	0.0925	0.257
14	0.064	0.320	0.32	0.19	0.51	0.404	0.0840	0.262
15	0.057	0.285	0.26	0.16	0.41	0.363	0.0777	0.272
16	0.052	0.260	0.21	0.13	0.35	0.332	0.0716	0.275

Note that there are only 16 generations listed for asthmatic airways because data are not reported for smaller airways in the studies by Wiggs et al.[35] Approximate data for smaller asthmatic generations are extrapolated using curve fitting procedures. The above data are summarized graphically in Figure 6-1.

Figure 6-1 is a log-log plot of the outer thickness ratio (t_o*) as a function of the characteristic airway radius (R). Adequate fitting relationships are graphed along with the data in Figure 6-1. These relationships are:

$$\text{NORMAL:} \quad t_o^* = 0.0583 \exp\left[0.450 \left(\frac{R}{mm}\right)^{-0.577}\right]$$

$$\text{ASTHMATIC:} \quad t_o^* = 0.198 \exp\left[0.104 \left(\frac{R}{mm}\right)^{-0.876}\right]$$

(The notation $^{R}/_{mm}$ implies that R must be substituted in with units of mm.) It is interesting to note that for smaller and smaller airway sizes, the factor of outer layer growth from normal to asthmatic is decreasing, suggesting that smaller asthmatic airways exhibit less submucosal thickening than larger ones. Wiggs et al. have pointed out with their calculations of airflow resistance that the outer layer remodeling changes due to asthma

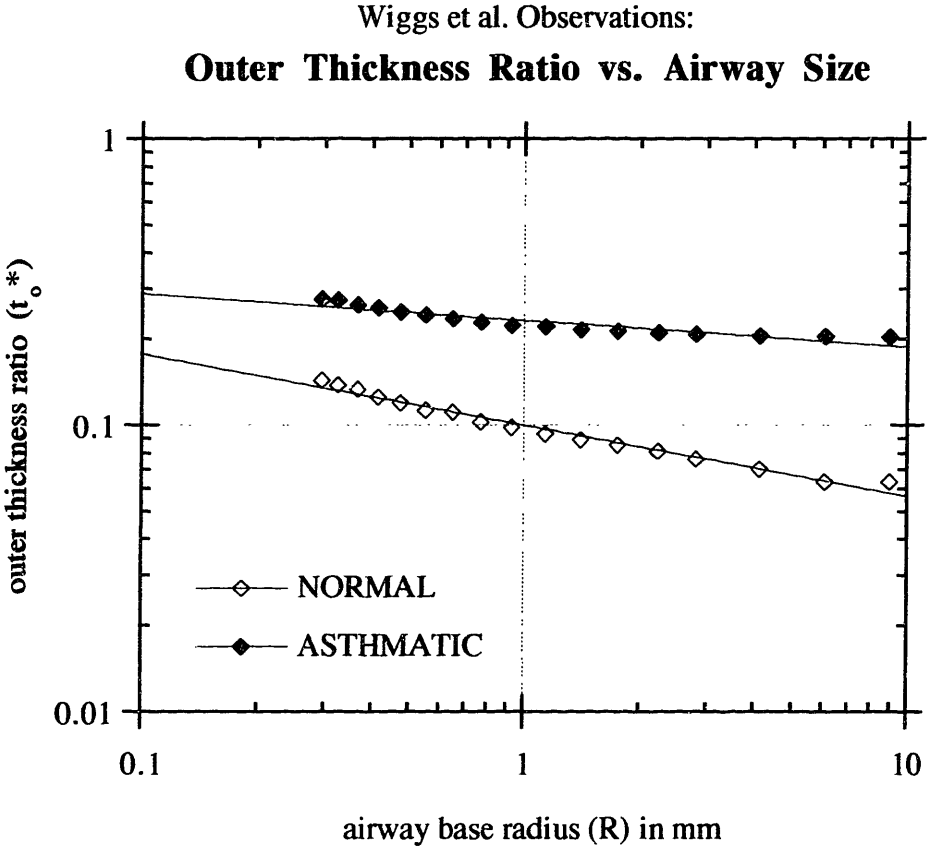

FIGURE 6-1: Log-log plot of outer thickness ratio versus asthmatic and normal airway size as calculated from Wiggs papers. Data points are fit to a power law.

appear to cause the greatest increase in resistance in the smaller airways, around generations 10 through 16. The fact that the smaller airways show a lesser percentage of outer layer thickening than the larger ones yet still are responsible for the majority of the total increase in airflow resistance suggests that there is no correlation between outer layer thickening and the local increase in resistance to airflow.

6.1.2 Inner Thickness Ratio (t_i*)

Many studies have reported that there is an increase in sub-epithelial collagen deposition in asthma.[3,5,10,28,29] In particular, an earlier one by Roche et al. reports an average growth from 4.17 μm in normal human bronchi (generation 1) to 7.95 μm in asthmatic bronchi.

Roberts claims that this layer ranges from 5 to 8 μm in normals to 10 to 15 μm in asthmatics (although which airway generations this applies to is unclear). The following table compares results from 5 studies in order from earliest to latest, left to right.

MEASUREMENTS OF THE SUB-EPITHELIAL COLLAGEN LAYER THICKNESS (in μm)

STUDY	Roche	Brewster	Roberts	Boulet	Foresi
REF. #	29	5	28	3	10
YEAR	1989	1990	1995	1997	1998
Norm. (lo)	4	3	5	4	9
Norm. (hi)		6	8	9	10
Asth. (lo)	8	4	10	6	12
Asth. (hi)		11	15	28	14

It appears safe to say that the sub-epithelial collagen layer roughly doubles in thickness between normal and asthmatic states. One perhaps naive approach is to assume that this thickness is constant through the entirety of the tracheobronchial tree. Another study by Codd et al. recapitulates some measurements of only asthmatic airways made by Huber and Koessler in 1920, expressing the sub-epithelial collagen thickness as a function of the airway radius (R). Those measurements are presented again in Figure 6-2, but in a logarithmic format. The way the data line up suggests a power-law relationship.

The best power-law fit of the Huber-Koessler data is the function:

$$\text{ASTHMATIC:} \quad t_i^* = 0.0122 \left(\frac{R}{mm}\right)^{-0.954}$$

Note that the exponent on R is very close to –1, suggesting that the naive approach of assuming the sub-epithelial collagen thickness to be constant throughout the tree would not be bad at all. In the absence of detailed data for the inner thickness in normal airways as a function of R, here it will be assumed that from normal to asthmatic, the inner thickness everywhere grows by a factor of 2 in every airway generation. The resulting normal inner thickness is divided by the normal base radius (R) to yield the normal inner thickness ratio in every generation. Similarly, these data fit a power law relationship nicely:

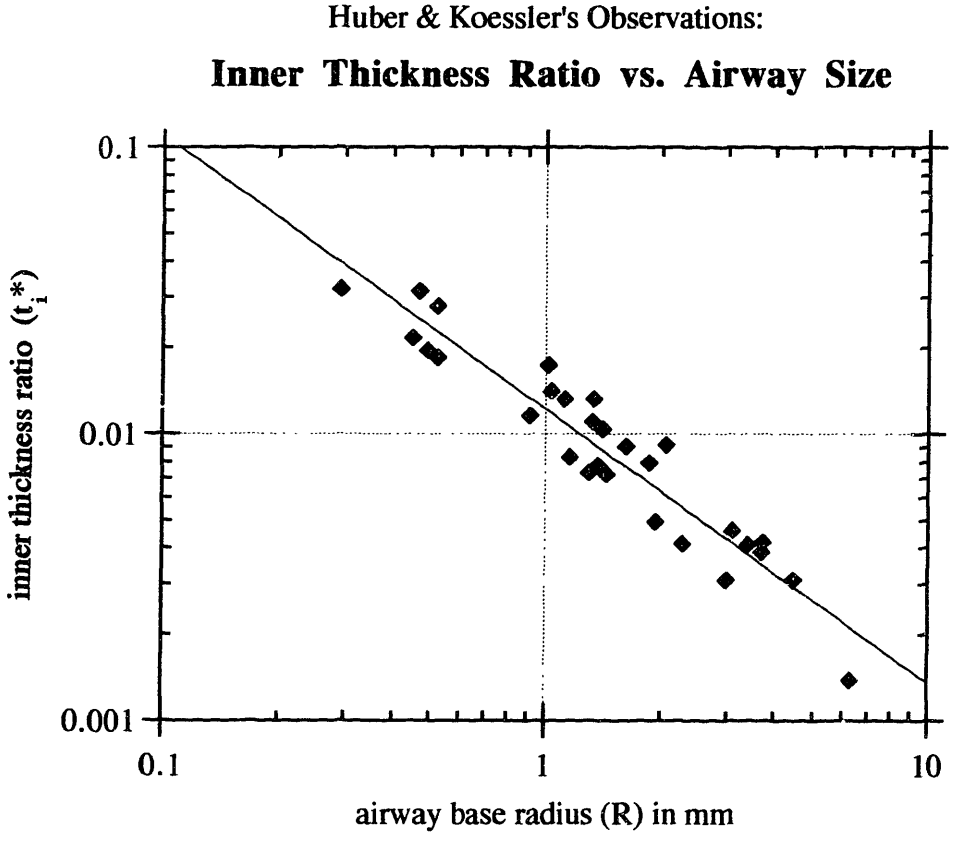

FIGURE 6-2: Log-log plot of inner thickness ratio versus airway size for asthmatics from Huber & Koessler data. Data points are fit to a power law.

$$\text{NORMAL:} \quad t_i^* = 0.00611 \left(\frac{R}{mm}\right)^{-0.946}$$

To summarize, the following table shows what geometric parameters will be assumed under normal and asthmatic conditions in this work, extrapolating to smaller airways as necessary. The extrapolation rule for the size (R) of asthmatic airways of generations 17 through 23 is based on a curve fit of the values for the previous several generations. Again, Z is the airway generation number.

$$R_{ASTH} = R_{NORM} - 0.166 \exp(-0.169\, Z) \text{ mm}$$

When other extrapolations are necessary, they are based on the curve fits for t_o* and t_i* of normal and asthmatic airways that have been presented in this and the previous sections.

SUMMARY OF AIRWAY GEOMETRY:

Z	R (mm) NORM	R (mm) ASTH	t_o* NORM	t_o* ASTH	t_i* NORM	t_i* ASTH	$\frac{t_o}{t_i}$ NORM	$\frac{t_o}{t_i}$ ASTH	$\frac{t_o^*{}_{ASTH}}{t_o^*{}_{NORM}}$	$\frac{t_i^*{}_{ASTH}}{t_i^*{}_{NORM}}$
0	8.915	7.860	0.063	0.202	0.0008	0.0015	81.07	133.25	3.23	1.96
1	6.050	5.335	0.063	0.203	0.0011	0.0022	56.84	92.50	3.20	1.97
2	4.025	3.620	0.070	0.204	0.0016	0.0032	42.58	63.22	2.93	1.97
3	2.690	2.455	0.076	0.207	0.0024	0.0047	31.66	43.61	2.73	1.98
4	2.105	1.945	0.081	0.209	0.0030	0.0060	26.85	34.84	2.58	1.98
5	1.650	1.535	0.085	0.212	0.0038	0.0076	22.26	27.97	2.50	1.99
6	1.310	1.225	0.089	0.215	0.0047	0.0094	18.76	22.85	2.43	1.99
7	1.055	0.990	0.093	0.220	0.0058	0.0116	16.00	18.96	2.37	2.00
8	0.860	0.815	0.098	0.222	0.0070	0.0141	13.97	15.78	2.26	2.00
9	0.710	0.675	0.102	0.228	0.0084	0.0169	12.09	13.48	2.23	2.00
10	0.595	0.565	0.111	0.235	0.0100	0.0200	11.09	11.74	2.12	2.01
11	0.505	0.480	0.112	0.242	0.0117	0.0234	9.63	10.34	2.16	2.01
12	0.435	0.415	0.119	0.248	0.0134	0.0270	8.87	9.17	2.08	2.01
13	0.380	0.360	0.125	0.257	0.0153	0.0307	8.16	8.36	2.06	2.01
14	0.335	0.320	0.133	0.262	0.0172	0.0346	7.73	7.58	1.97	2.01
15	0.300	0.285	0.148	0.272	0.0191	0.0385	7.76	7.08	1.84	2.02
16	0.270	0.260	0.143	0.275	0.0211	0.0425	6.77	6.47	1.93	2.02
17	0.250	0.241	0.165	0.284	0.0227	0.0458	7.26	6.21	1.73	2.02
18	0.230	0.222	0.167	0.292	0.0245	0.0496	6.79	5.89	1.75	2.02
19	0.215	0.208	0.159	0.299	0.0262	0.0529	6.10	5.65	1.87	2.02
20	0.205	0.199	0.174	0.304	0.0274	0.0553	6.37	5.49	1.74	2.02
21	0.200	0.195	0.182	0.306	0.0280	0.0566	6.51	5.40	1.68	2.02
22	0.195	0.191	0.191	0.309	0.0287	0.0580	6.66	5.32	1.62	2.02
23	0.190	0.187	0.200	0.311	0.0294	0.0595	6.82	5.23	1.55	2.02

The second and third columns give airway size as quantified by R in mm as a function of airway generation (first column) for both normal and asthmatic airways. The fourth and fifth columns give outer thickness ratios. The sixth and seventh give inner thickness ratios. The remaining columns are presented only for discussion. The eighth and ninth columns give an idea of aspect ratio between outer and inner thicknesses. It is interesting to note that despite which condition is present ("normal" or "asthmatic"), the ratio of thicknesses is about the same for a particular smaller airway generation. The final two columns give an idea of the factor of growth between normal and asthmatic conditions for each layer. The inner thickness grows uniformly by a factor of two (mostly because we dictated that, although there is slight variation because of the volume correction on the base radius – see studies by Wiggs et al.). The outer thickness, however, grows by a greater percentage for

the larger airways than the smaller ones. As mentioned earlier, however, the smaller airways are responsible for the greater percentage increase in airflow resistance. This observation casts some doubt on the idea that outer layer remodeling is solely responsible for increased airflow resistance.

6.2 Compression Experiments for E_o

As was mentioned earlier, knowing the quantitative stress-strain behavior of the inner and outer layer materials is another matter entirely. It is a common approach to assume that these materials are described well by a single parameter (E), that the behavior is approximately linear-elastic and relatively incompressible under quick deformations. The fact that measurements for this single parameter tend to be imprecise suggests that this is an overly simplistic model of the material behavior. It is, however, a starting point. Young's uniaxial elastic modulus (E) is a very concrete and intuitive parameter which gives a quick and simple impression of the material's intrinsic stiffness.

Here it is not advisable to rely on the previously published data for E of either layer because no previous studies attempt to separate the effect of the thick and relatively compliant submucosal layer from that of the thinner and stiffer mucosal elements (or sometimes even the cartilage in the upper airways). They all tend to report some type of effective combined E-value, or perhaps not even go that far and merely report load vs. displacement behavior for an entire airway segment. For instance, Habib et al. have used impedance modeling to find an airway modulus of 58 ± 32 kPa,[14] a value which is both imprecise and may include cartilage. This is why our research group found it necessary to perform new experiments to approximate the E-values of either layer separately.

The rest of this section concerns itself with compression experiments for the modulus of the submucosal layer (E_o) that were not performed by the author, but by a group headed by Prof. Barry R. Wiggs of the University of British Columbia Pulmonary Research Laboratory at St. Paul's Hospital in Vancouver, British Columbia. The following sections (6.3 and 6.4) describe the author's attempts to experimentally determine the stiffness ratio (E^*) assuming that the modulus of the outer layer (E_o) has been determined a priori.

It is assumed that the material moduli are neither functions of the generation number (distance down the tracheobronchial tree), nor airway size (R). Also note that no

distinction is made between normal and asthmatic conditions as none of these experiments were performed on human airways. The assumption is that the general microstructure of the airway components is similar between species, and that there may merely be more or less of a particular component in different species. Roberts has suggested that the sub-epithelial collagen of asthmatic airways appears more organized than that of normal airways, perhaps indicating that the value of E* increases from normal to asthmatic conditions.[28] However, since no one has been quantitative about such observations nor speculated about the direct effect on E_i, no such effect is considered in this work. When "normal" and "asthmatic" models are compared, the only differences between them are in the models' geometries as dictated by t_o* and t_i*.

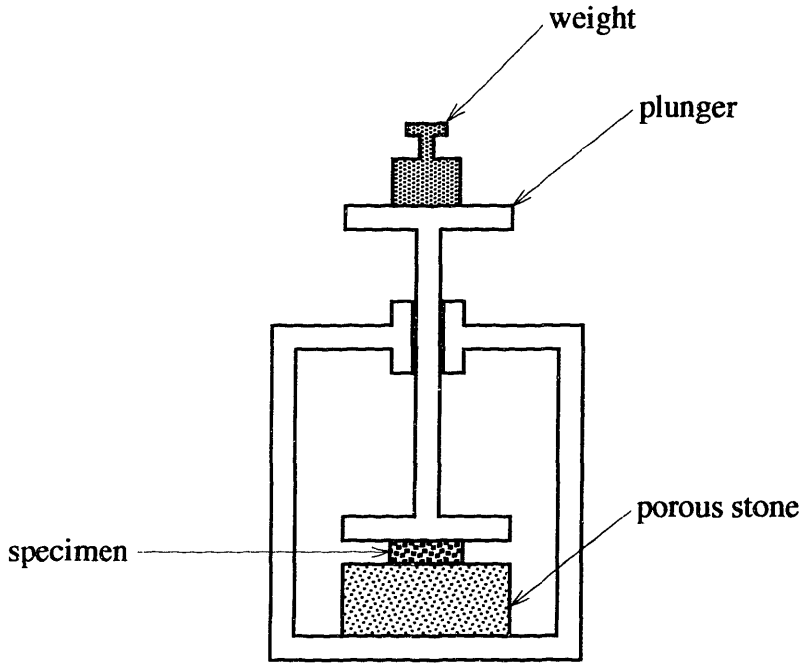

FIGURE 6-3: Sketch of Wiggs' submucosal compression experiment setup.

In the airway compression experiments, performed by Prof. Wiggs et al. in Vancouver, circular cores of porcine airways were cut and placed in an unconfined compression testing apparatus as shown in Figure 6-3. A porous stone allows fluid flow through the bottom. As weights are placed on a plunger from above, a constant load is transmitted through the specimen core, and the displacement of the plunger is monitored. Before the test actually begins, there is the option to precondition with repeated loadings of 20 gf on the plunger.

After multiple preconditioning cycles, the response of the specimen becomes more repeatable. As the official test begins, weights of 1, 2.5, 5, 10 and 15 gf are placed on the plunger and the displacement is read after equilibration, as in a static test. The radius of the core for every experiment is 6.95 mm and is observed to remain about the same size during the compression experiment, thus indicating that under such slow loading, the material behaves as if it is completely compressible (and its Poisson ratio, $\nu = 0$). Under these loading and boundary conditions, the uniaxial elastic modulus (E) is simply the slope of the stress-strain curve.

$$E = \frac{d\sigma}{d\varepsilon}$$

$$\text{where} \quad \sigma = \frac{\text{load}}{\text{area}} \quad \text{and} \quad \varepsilon = \frac{\text{displacement}}{\text{original thickness}}$$

Each test is a different combination of the following three choices:

1) with and without preconditioning (as described above)

2) with both smooth muscle and submucosal layers intact, or just the submucosal layer dissected away from the smooth muscle

3) in a saline solution, or in a 0.2 mM calcium ion concentration solution (the increased calcium concentration keeps the actin-myosin complex locked, inducing a condition of tetanus in the smooth muscle layer)

Thus there are 8 different combinations of these choices to try in different tests. The following two tables display the stress and strain data points for the 8 tests. The relationship between stress and strain does indeed appear quite linear, thus the modulus E_o is approximately constant. The last row of each table displays for each test the slope of the measured stress-strain function, which is the modulus of interest, E_o. Figure 6-4 summarizes the results for E_o graphically.

COMPRESSION TESTS IN SALINE SOLUTION

stress, σ (kPa)	strain, ε			
	submucosa & smooth muscle		submucosa alone	
	preconditioned	no preconditioning	preconditioned	no preconditioning
0.06465	0.00743	0.00694	0.00662	
0.16162	0.01505	0.01800	0.00885	0.00882
0.32324	0.03152	0.03197	0.01634	0.01594
0.64647	0.05377	0.05350	0.03291	0.02890
0.96971	0.07081	0.07001	0.05086	0.04453
E (kPa)	**13.980**	**14.360**	**19.949**	**22.803**

COMPRESSION TESTS IN 2.5 mM Ca SOLUTION

stress, σ (kPa)	strain, ε			
	submucosa & smooth muscle		submucosa alone	
	preconditioned	no preconditioning	preconditioned	no preconditioning
0.06465	0.00764	0.01045		
0.16162	0.01899	0.02293	0.01006	0.01618
0.32324	0.03763	0.04055	0.01857	0.03372
0.64647	0.06456	0.07971	0.03119	0.06007
0.96971	0.08305	0.10611	0.05432	0.10631
E (kPa)	**11.785**	**9.2849**	**18.438**	**9.0654**

It would appear that the smooth muscle is somewhat less stiff than the smooth muscle. This surprising result is contrary to some of the modeling assumptions that were made in order to de-couple the inner airway from the outer airway. It is also possible that too much of the submucosa was dissected off with the smooth muscle, thus biasing the measured stiffness toward that of the mucosa, which normally would be negligible in such a test because of its small thickness (most of the deformation occurs in the submucosa). Therefore, the author is reluctant to draw conclusions about the stiffness of submucosal material relative to the smooth muscle. The effect of the calcium bath is to make non-preconditioned airway material significantly less stiff, whereas it has little effect on the preconditioned material (which makes sense since the goal of the preconditioning is to break links which are due to rigor mortis and make the response repeatable).

Compression Experiments For E_o

values reported in kPa

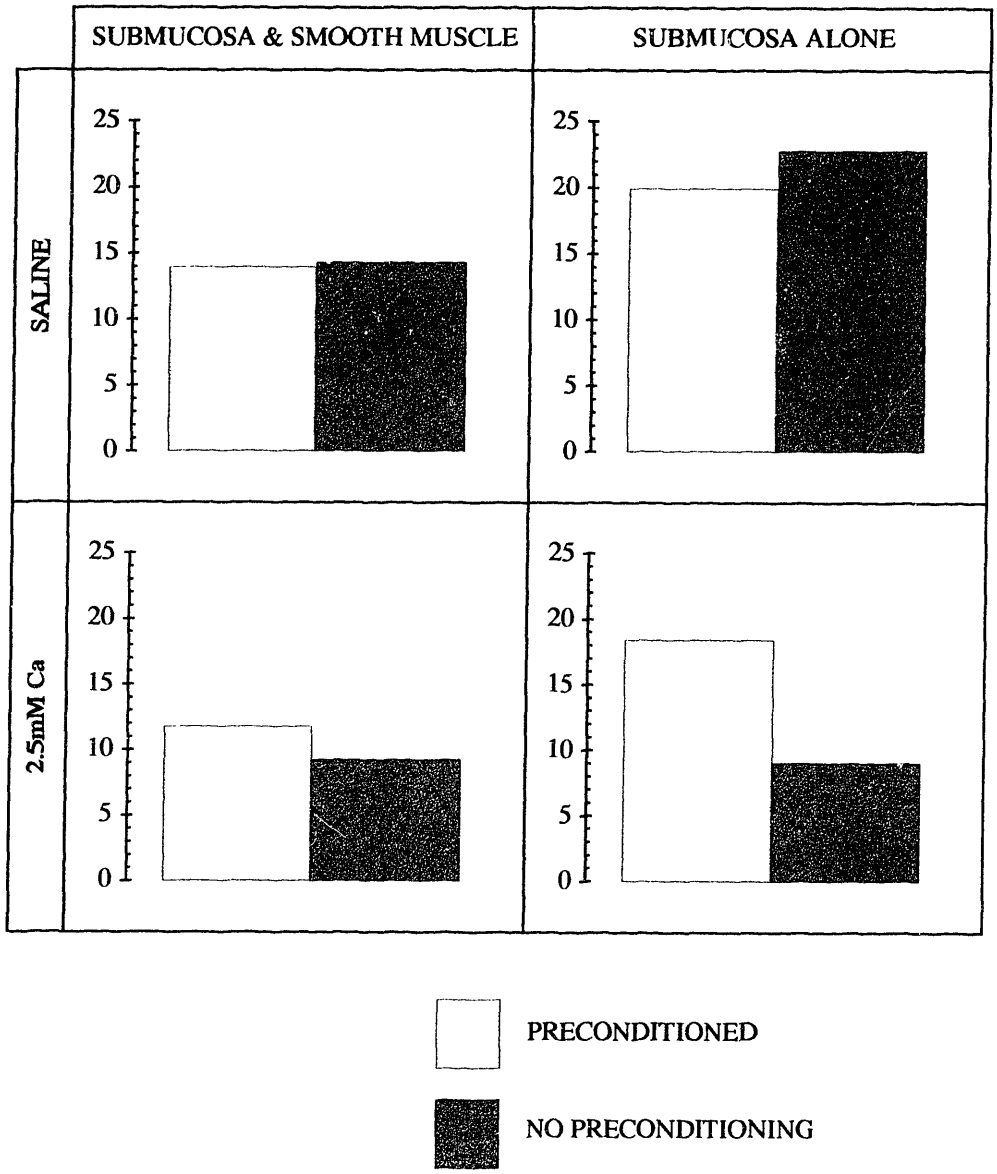

FIGURE 6-4: Summary of the results from Wiggs' submucosal compression experiments.

Given that it is hard to draw conclusions about the submucosa versus the smooth muscle, in order to obtain a ball-park figure for the outer layer stiffness, a median value of all the preconditioned tests will be used in future calculations.

$$E_o \approx 17 \text{ kPa}$$

There has been some speculation that the value of E_o would be somewhat smaller in asthmatic airways than normal ones,[4] but in the absence of hard numbers these analyses assume that the value of E_o is the same in normal and asthmatic airways.

6.3 Two-Pin Bending Experiments for E*

Measuring E_i independently of E_o is very tricky because the mucosal layer is so thin and susceptible to damage upon dissection. Instead, it is preferable to perform a test which will keep an airway intact (or at least intact near the mucosa-submucosa boundary). Our first attempt at such a test used a simple ring of membranous airway as a sample. Two thin wires are threaded through the interior of the ring and monitored as they are slowly pulled apart from one another. As in several procedures developed by Fung et al., the bending deflection in the wires provide an accurate measurement of the applied load. The next step is to produce a finite-element model of the ring specimen and iteratively update guesses of the outer and inner elastic moduli (E_o and E_i) until the computed behavior matches that observed in the experiment. A finite element simulation of the experiment (which exploits symmetry in each of the three directions, thus modeling only one octant of the specimen) is depicted in Figure 6-5.

This experiment unfortunately turned out to be unsuccessful because it is extremely difficult to find a specimen that is well-modeled by the perfect geometry of the finite element simulation. Even a surgeon of five years experience was unable to dissect an airway small enough that lacked enough cartilage to yield viable experimental data. The presence of cartilage completely throws off the calculation because the stiffness of cartilage is so much larger than our expected E_o or E_i. Figure 6-6 shows our best specimen being tested in the two-pin bending apparatus. The sample is a segment of a fibrotic fifth-generation human airway. Its dimensions are highly asymmetric and there are patches of cartilage on the thicker side. Performing a simulation of so complex a structure is sophisticated enough that there is little hope of backing out E* reliably.

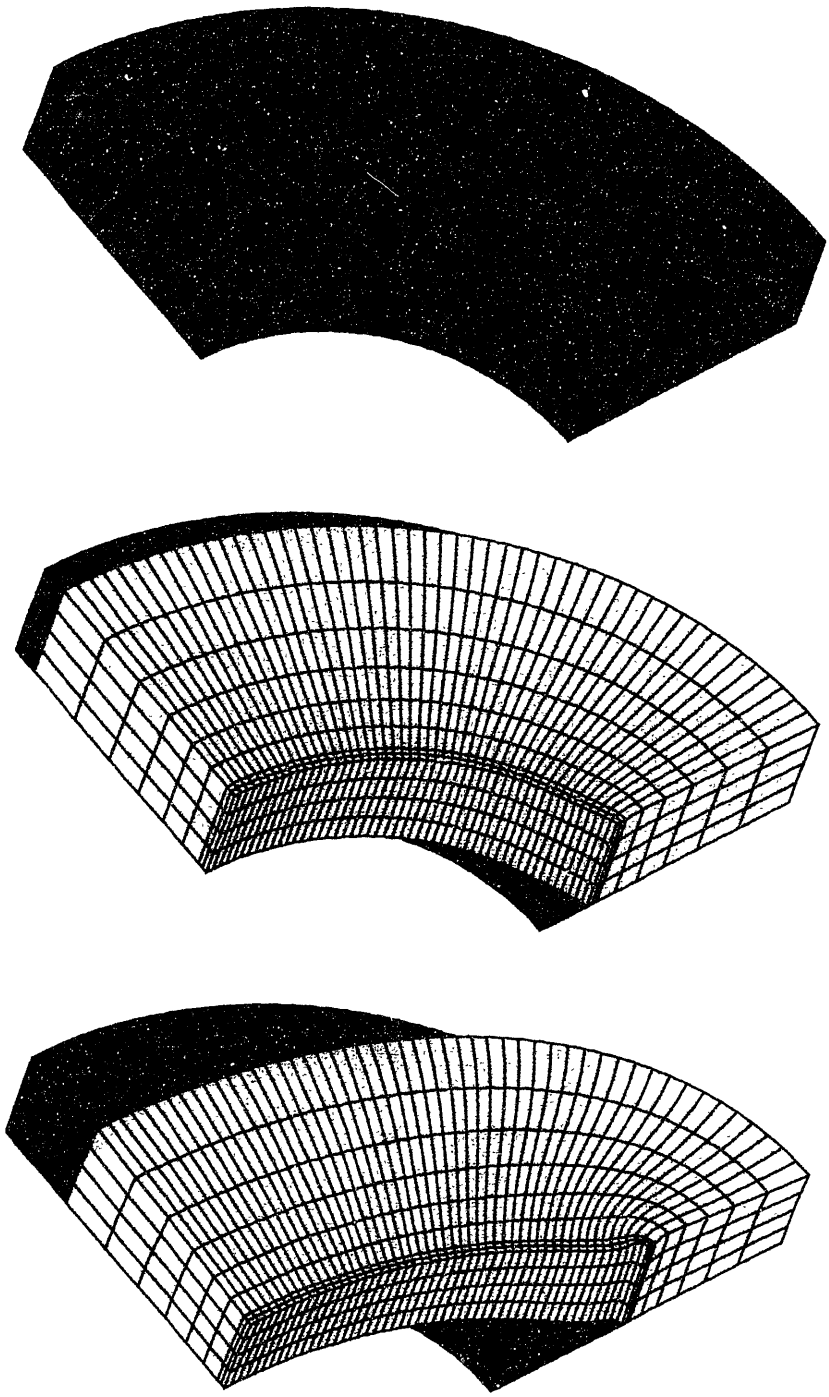

FIGURE 6-5: A 3-D finite element simulation of the two-pin bending experiment.

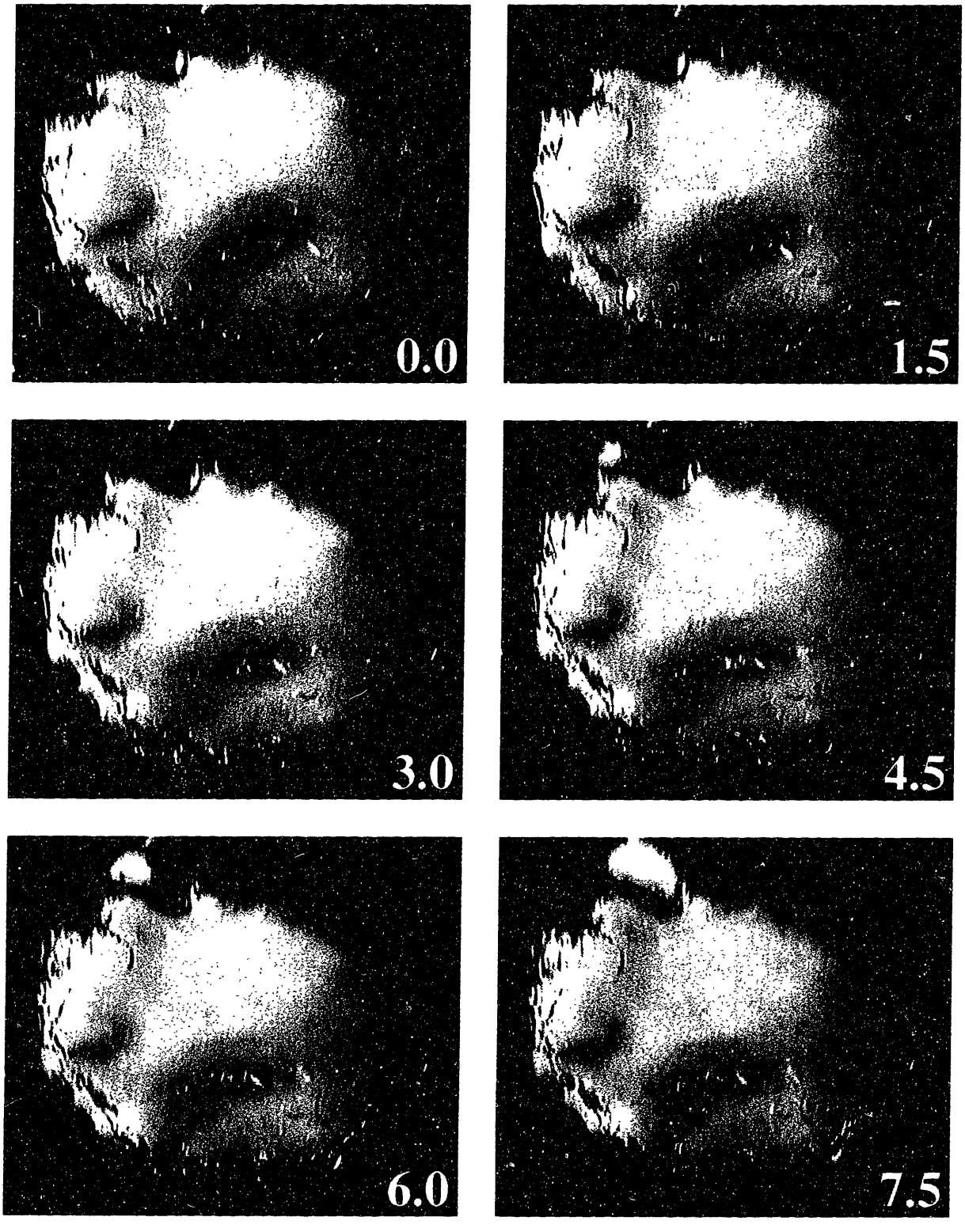

FIGURE 6-6: A fibrotic human airway specimen being stretched in the two-pin bending apparatus. Number in the lower right is the right pin's displacement from its initial position in mils (thousandths of an inch).

These experiments were indeed helpful because they pointed us in a better direction with our airway modulus experiments. The new approach became to avoid procedures that rely on finely specified gross geometries with measurements of gross displacements. Instead it is preferable to focus on a small region which accentuates the behavior of the inner layer. The size of the testing apparatus and expected displacements must be on the order of the thickness of the inner layer. This is how indentation experiments with a very fine indenter were inspired.

6.4 Indentation Experiments for E*

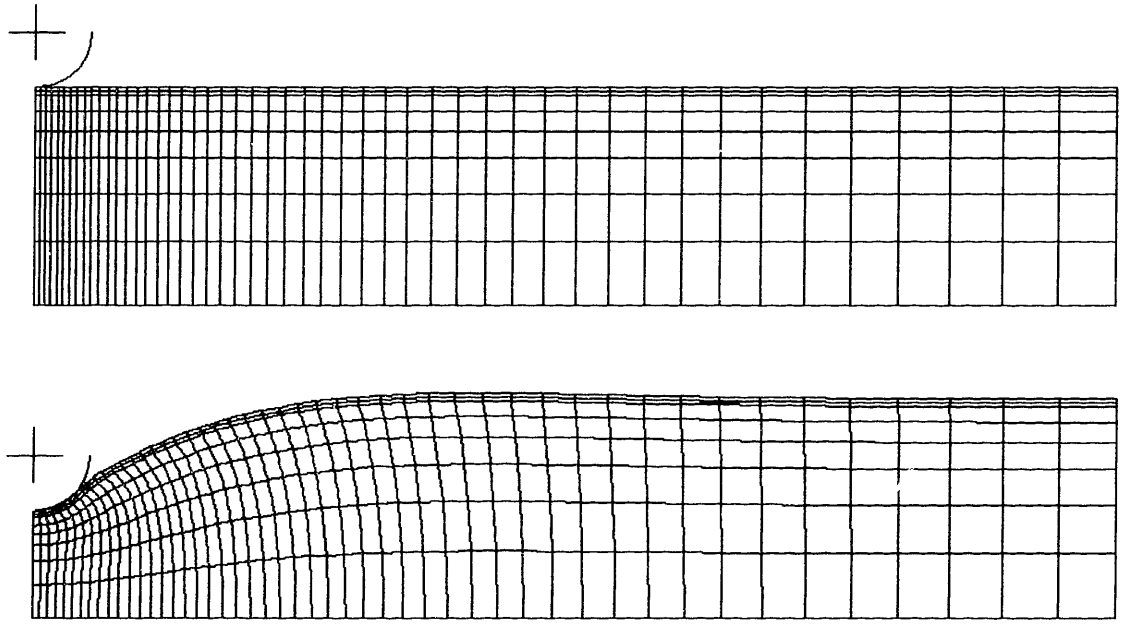

FIGURE 6-7: Undeformed and deformed meshes from an ABAQUS simulation of a typical (two-layer) indentation test. The simulation is axisymmetric about the left edge of this mesh.

The purpose of the following preliminary experiments is to perfect a technique which could be performed at smaller scales on airways. The basic strategy of the technique presented here is to force a blunt probe into the structure from the inside (or what was the inside after the airway is opened up and allowed to lie flat), monitoring the load required as the probe displaces into the material. The entire experiment is performed on a digital electronic

balance that gives the reading of the applied probe load. The experimental load-displacement curve is compared to numerical finite element solutions, allowing back-calculation of the stiffness ratio (E*) between the two materials (or better yet, the magnitudes of the two elastic moduli, E_o and E_i, separately). Figure 6-7 shows two mesh plots from two-layer indentation ABAQUS simulations, before and after a displacement is imposed. The simulation assumes axisymmetry about the left-hand edge of the modeled region. The right-hand edge is free to move, but since the displacements are small there, it is reasonable to assume that the results of this simulation are not very different from those for a semi-infinite domain. All of the indentation experiments rely on ABAQUS simulations like this one.

6.4.1 Preliminary Single-Layer Indentation Experiments on Foam

During March of 1997, the author was assisted by Shizuka Sugawara, an undergraduate of Tohoku University, Japan, in the preliminary indentation experiments discussed in Sections 6.4.1 and 6.4.2, and is very grateful for her help.

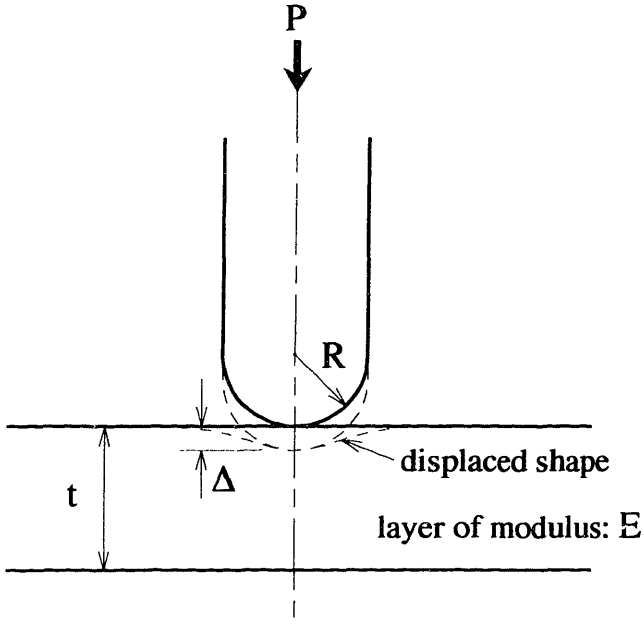

FIGURE 6-8: Sketch of an idealized single-layer indentation test, defining nomenclature.

Since we expect (at worst) an estimate of the stiffness ratio (E*) between the two layers from an indentation test of the bilayered structure, we should have a good estimate of the modulus of the more compliant base material (E_o) so that we can also quantify that of the stiffer material (E_i). That will be accomplished through an indentation test of a single thick layer. The test setup is as pictured in Figure 6-8. Note that the test setup assumes an infinite flat layer beneath the indenter. The large-scale foam samples tested, though originating from closed tubes of the material, have the least curvature possible and are relatively large compared to the other candidates.

For this single-layer test, the test output load (P) is a function of the input displacement (Δ) and three parameters: the indenter radius (R), the layer thickness (t) and modulus (E). After normalization, the dependence $P(\Delta; R, t, E)$ reduces to $P^*(\Delta^*; t^*)$, where:

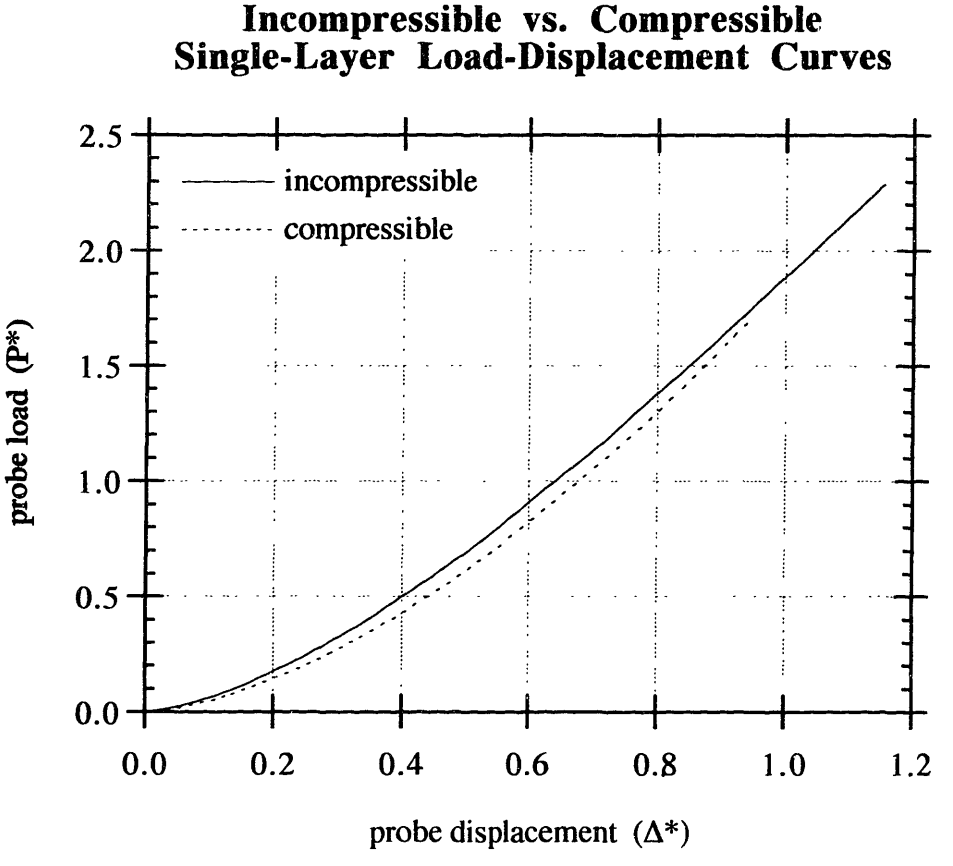

FIGURE 6-9: A comparison of indenter load-displacement results from $\nu = 0$ and $\nu = {}^1/_2$ indentation simulations. The fact that the results are so similar suggests that this test will be unable to measure ν of either layer.

$$P^* = \frac{P}{E\,R^2} \qquad \Delta^* = \frac{\Delta}{R} \qquad t^* = \frac{t}{R}$$

So far the issue of compressibility and Poisson ratio (ν) has not been addressed. Figure 6-9 shows load-displacement curves from two ABAQUS simulations of the single-layer indentation test, one for an incompressible material (assuming $\nu = 1/2$) and the other for a highly compressible one (assuming $\nu = 0$).

From these ABAQUS simulations, it appears that the indentation test load-displacement behavior is fairly independent of the material's compressibility. This essentially proves that there is very little Poisson effect in this experiment, and that the Poisson ratio cannot be

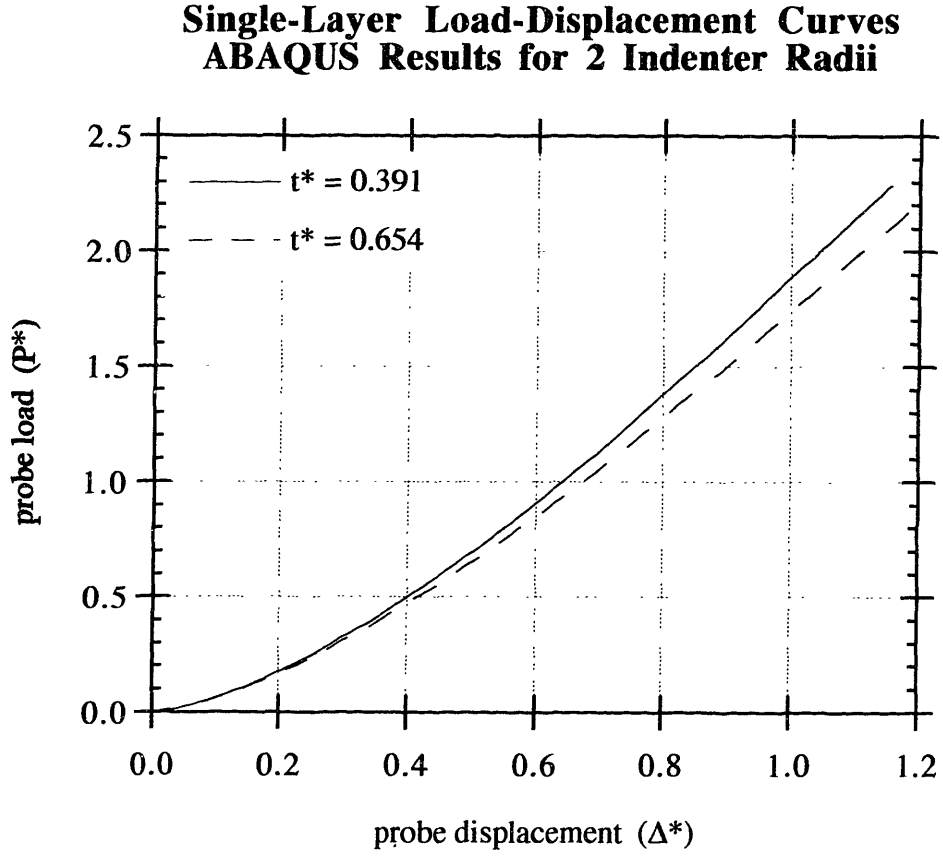

FIGURE 6-10: Two typical indenter load-displacement plots from single-layer indentation simulations. Beyond a certain threshold value of t*, the results are pretty much independent of t*.

measured in this experiment. For convenience and consistency with past analyses, all related indentation simulations will assume that $\nu = 1/2$.

After making that simplification there remains only one varying parameter of interest, the thickness ratio (t*). Two different indenters were used on the same foam specimen in the single-layer experiments, one of radius 5.12 mm and the other of radius 3.06 mm. The foam specimen had a thickness of 20.0 mm, yielding thickness ratios (t*) of 0.391 and 0.654 for the two tests, respectively. Figure 6-10 shows the results of ABAQUS simulations for the two thickness ratios, to which the experimental data will be compared. Note that since the layer is relatively thick, it may as well be infinitely thick since there is little effect of t* on the indenter load-displacement behavior.

The two curves of Figure 6-10 were subjected to a power-law curve fit (of the form $P^* = \alpha \Delta^{*\beta}$). Those results are included in the summary table at the end of this section and are used in fitting the experimental data to curves also.

Below are the data from the first of four single-layer experiments performed (case "tip1-exp1"). The first column contains displacement data obtained from the transducer by subtracting the length reading of the last step which caused no load reading on the balance. Note that there is some uncertainty as to what the exact zero-displacement reading should be. This difficulty is circumvented during the fitting of the experimental data to curves with forms suggested by the ABAQUS simulation results (explained below). The displacement is normalized by the indenter radius (R) and recorded in column 2. The balance reading (in Newtons) is in column 3. It is not possible to have a column for P* since E is unknown. Instead P from column 3 is divided by the indenter radius squared (R^2) to give EP* (multiplied by various conversion constants for appropriate units).

disp. (mm)	Δ*	P (N)	EP* (kPa)
0.000	0.000	0.000	0.00
0.635	0.124	0.018	0.69
1.270	0.248	0.077	2.92
1.905	0.372	0.161	6.14
2.540	0.496	0.266	10.15
3.175	0.620	0.402	15.35
3.810	0.744	0.567	21.63
4.445	0.868	0.791	30.17
5.080	0.992	1.049	40.02
5.715	1.116	1.359	51.84

Column 4 (EP*) is plotted as a function of column 2 (Δ^*) for the four single-layer experiments (two for each indenter size) in Figures 6-11 and 6-12. Each experiment's data are subjected to a curve fit which is based on that of the results from the simulation for that tip radius. For instance, for the first experiment (data listed above) the ABAQUS simulation load-displacement data were shown to fit well to the curve $P^* = 1.86\,\Delta^{*1.50}$. The data from case tip1-exp1 are then fit to $EP^* = 1.86\,\gamma\,(\Delta^* - \delta)^{1.50}$. The offset δ is a degree of freedom which simultaneously allows for uncertainty in the zero-displacement reading for the experiment while forcing the data to fit a relationship with the 1.50 exponent expected from the ABAQUS simulation. This procedure reveals a plausible toe-region for the smaller displacements where the foam layer might not yet be in total contact with the balance or the indenter may not be evenly touching the layer. The other fitting parameter γ allows EP* to be a simple amplification of the displacement-shifted P*, and thus is the experiment's best estimate for the layer's elastic modulus (E).

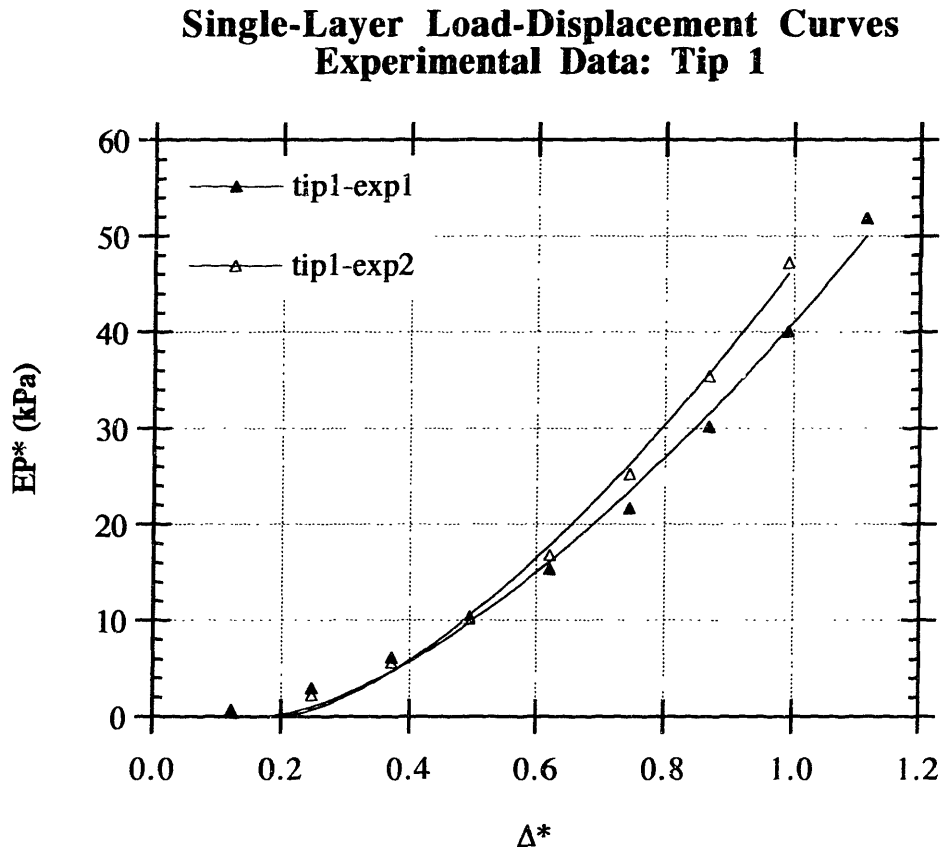

FIGURE 6-11: Results from two single-layer indentation experiments with a relatively broad tip.

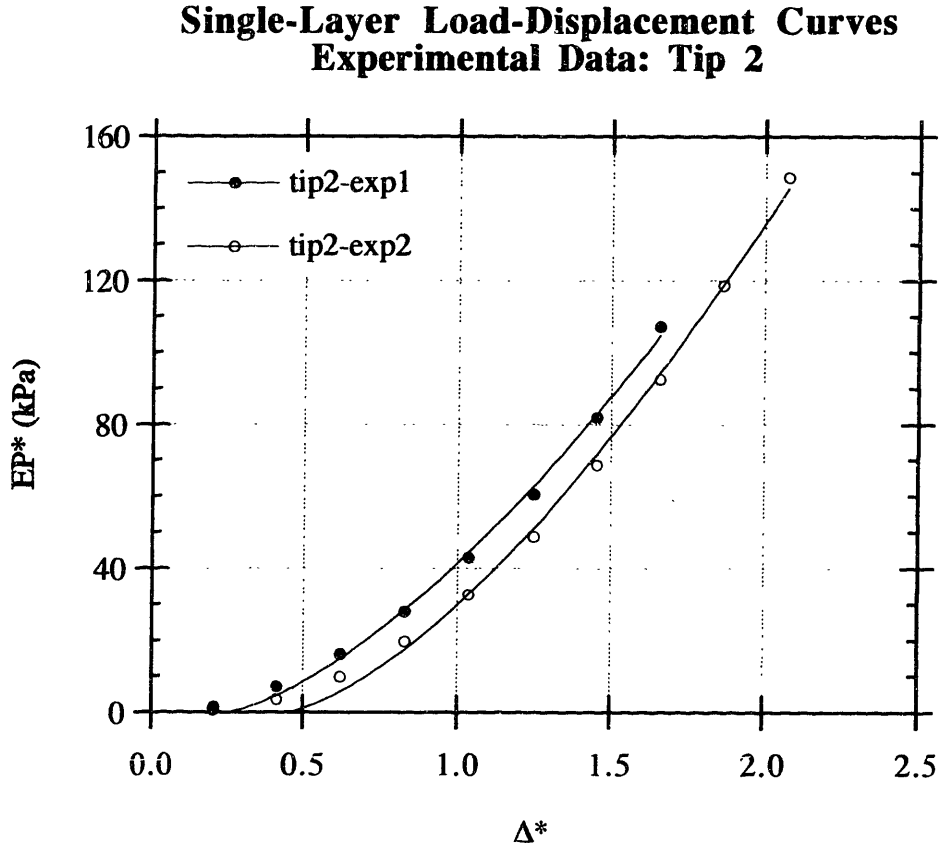

FIGURE 6-12: Results from two single-layer indentation experiments with a relatively fine tip.

The table which follows summarizes the single-layer indentation theoretical simulations and experiments. The mean estimated Young's elastic modulus of the foam for the four trials is about 35 kPa, which is just a bit larger than the range of what has been previously measured for this foam (from 9-30 kPa). The indentation test is more local; that is, less material is actively deforming than in the previous measurements (which have involved either deformation of an entire tube of the material or a smaller plug of the material cut from the tube). There appears to be, however, less variability in the indentation test E-estimates, which lends some more confidence to this method as opposed to the previous ones.

CASE #	R (mm)	t (mm)	t*	curve fit of data points	Δ* offset	E (kPa)
tip1-theory	5.12	20.0	3.91	$P^* = 1.86\ \Delta^{*1.50}$		
tip1-exp1	5.12	20.0	3.91	EP^* (kPa) = 29.6*1.86 $(\Delta^*-0.179)^{1.50}$	0.179	29.6
tip1-exp2	5.12	20.0	3.91	EP^* (kPa) = 35.1*1.86 $(\Delta^*-0.201)^{1.50}$	0.201	35.1
tip2-theory	3.06	20.0	6.54	$P^* = 1.74\ \Delta^{*1.48}$		
tip2-exp1	3.06	20.0	6.54	EP^* (kPa) = 35.9*1.74 $(\Delta^*-0\ 244)^{1.48}$	0.244	35.9
tip2-exp2	3.06	20.0	6.54	EP^* (kPa) = 40.4*1.74 $(\Delta^*-0.442)^{1.48}$	0.442	40.4

6.4.2 Preliminary Indentation Experiments on Large-Scale Two-Layer Physical Models

The next step is to take as given from the above single-layer tests the 35 kPa E-value for the foam and try to calculate that of the thinner, stiffer layer laminated to it. This test, very similar to the single-layer test, is depicted in Figure 6-13.

The input-output dependency for this two-layer test, $P(\Delta; R, t_o, t_i, E_o, E_i)$, can be nondimensionalized, as was done for the single-layer test. The resulting nondimensional statement is $P^*(\Delta^*; t_o^*, t_i^*, E^*)$ where:

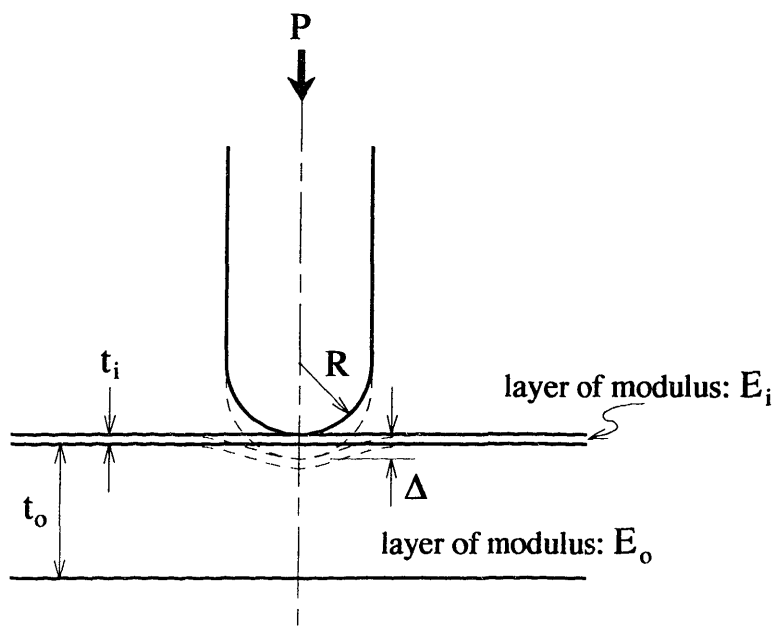

FIGURE 6-13: Sketch of idealized two-layer indentation test, defining nomenclature.

$$P^* = \frac{P}{E_o R^2} \qquad \Delta^* = \frac{\Delta}{R} \qquad t_o^* = \frac{t_o}{R} \qquad t_i^* = \frac{t_i}{R} \qquad E^* = \frac{E_i}{E_o}$$

Two of the parameters (t_o^* and t_i^*) are geometric and thus can be directly measured, but the stiffness ratio (E^*) is the unknown we are looking for.

Six experiments of slightly different geometry were performed. Three different thin-layer thicknesses and two indenter tip radii were available, thus there are six different thin-layer thickness to tip radius ratios (t_i^*). Since only one foam thickness was available, three of these tests (with the larger indenter) had a smaller thick-layer ratio (t_o^*) and the other three had a larger one. These geometric parameters for the two-layer tests are summarized in the table below.

TEST #	COLOR	R (mm)	t_o (mm)	t_i (mm)	t_o^*	t_i^*
1	blue	5.12	20	0.343	3.91	0.067
2	red	5.12	20	0.470	3.91	0.092
3	both	5.12	20	0.711	3.91	0.139
4	blue	3.06	20	0.343	6.54	0.112
5	red	3.06	20	0.470	6.54	0.154
6	both	3.06	20	0.711	6.54	0.232

These six indentation tests are performed as for the single-layer tests, recording the indenter displacement and the balance reading as raw data. For example, the table below shows the raw and calculated data from the first of these tests. The first column shows the indenter displacement (Δ) in mm, which is normalized by the indenter radius (R) to give the dimensionless displacement (Δ^*) in column 2. The balance reading of the applied force (P) in Newtons is in column 3. Dividing this load by the indenter radius squared (R^2) and converting to kPa yields column 4. An assumption of the foam elastic modulus (E_o) has to be used to finally obtain the dimensionless load (P^*). For all the tests here, the foam modulus is assumed to be 35 kPa (the mean result from the single-layer tests), thus column 4 is divided by 35 kPa to obtain column 5.

Δ (mm)	Δ^*	P (N)	$E_o P^*$ (kPa)	P^*
0.635	0.124	0.0134	0.5135	0.0146
1.270	0.248	0.0495	1.888	0.0539
1.905	0.372	0.0946	3.611	0.1031
2.540	0.496	0.1602	6.111	0.1746

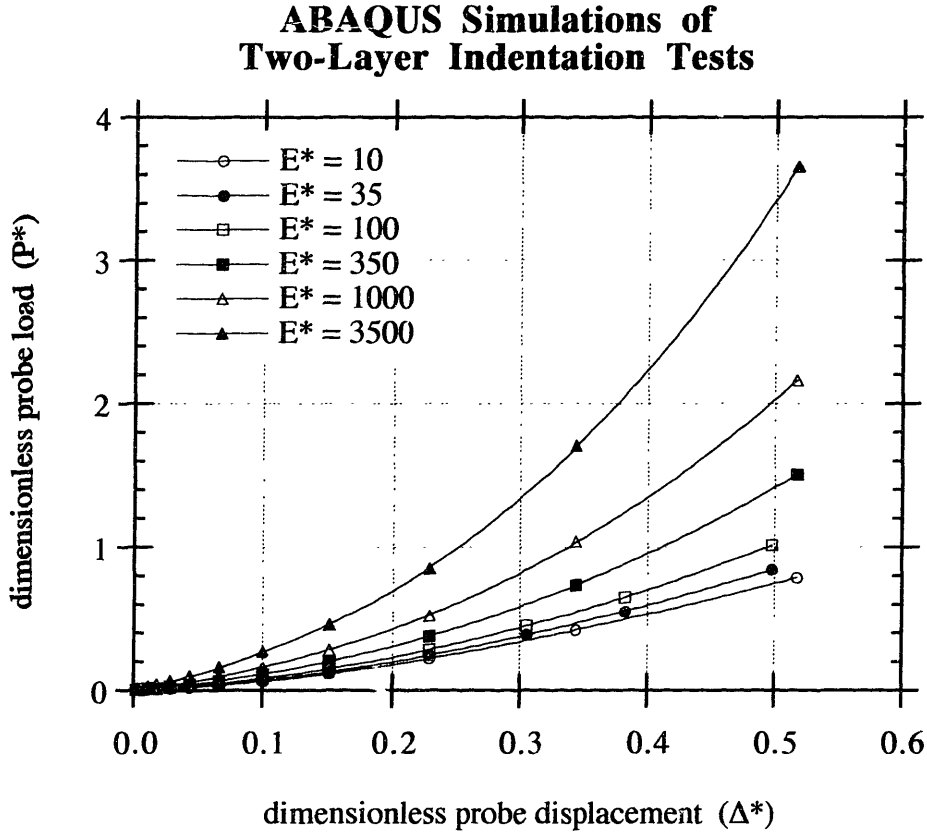

FIGURE 6-14: ABAQUS simulations of the two-layer indentation test at the known t_o* and t_i*-values over a range of values for the unknown E*.

Having obtained P*(Δ*) curves from the experiments, we now need data from finite element simulations for comparison. However, since the stiffness ratio (E*) is unknown, several simulations for each particular geometry are performed at varying stiffness ratios, logarithmically spaced. Below is the dimensionless load-displacement output from 6 ABAQUS simulations for the example geometry of test #1. The simulation is performed at stiffness ratios (E*) of 10, 35, 100, 350, 1000 and 3500.

The goal at this point is to condense all of the 6 simulation results into a single continuous function of the form P*(Δ*; E*) to which the experimental data can be fit, thus backing out the optimal E*. The approach used here is to subject the simulation data to two successive curve fits as follows. First each of the 6 load-displacement curves of Figure 6-14 are fit to

a third-order polynomial, without the constant term though since we want the y-intercept to be zero anyway (the power law curve fit used in the single-layer experiments does not work as well for this data). The optimal fitting parameters for the six simulations are tabulated below. Also note that the experimental data indicate that the Δ^* domain of interest is from 0.0 to about 0.5. Simulation points outside this range are masked from the curve-fitting procedure so that the fit is as close as possible over this domain of interest.

$$P^* = \alpha_1 \Delta^* + \alpha_2 \Delta^{*2} + \alpha_3 \Delta^{*3}$$

E^*	α_1	α_2	α_3
10	0.0344	0.3073	-0.1548
35	0.0397	0.3188	-0.1183
100	0.0503	0.3317	-0.0490
350	0.0753	0.3701	0.0910
1000	0.1135	0.4445	0.2799
3500	0.1934	0.6322	0.6976

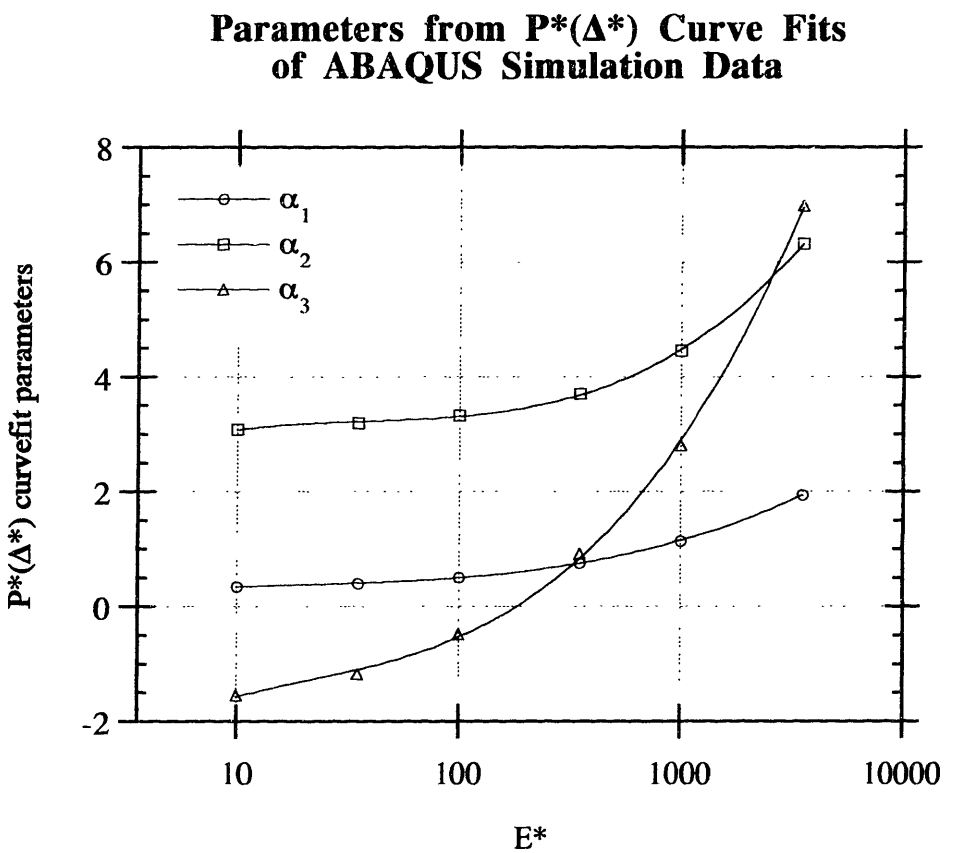

FIGURE 6-15: Parameters resulting from curve fits of the ABAQUS simulations.

The next step is to approximate an analytical function for each of the α-fitting parameters. The values from the table above are plotted in Figure 6-15. Note that the stiffness ratio (E*) axis is logarithmic.

Now the α-curves are subjected to a curve fit based on E*. The fit here will also be a cubic polynomial one, but with the constant left in. Note that because of the logarithmic spacing of the E*-values, "x" has been transformed to "log(x)".

$$\alpha_i = \beta_{i0} + \beta_{i1} \log(E^*) + \beta_{i2} \log(E^*)^2 + \beta_{i3} \log(E^*)^3$$

	β_{i0}	β_{i1}	β_{i2}	β_{i3}
α_1	0.0025	0.0613	–0.0406	0.01084
α_2	0.1500	0.2985	–0.1799	0.03779
α_3	–0.3525	0.3509	–0.2108	0.05507

Thus this procedure requires 12 parameters to fully specify the P*(Δ*; E*) dependency for this particular geometry. That may seem like a lot at first, but considering that 6 full load-displacement curves' behavior has been captured with 12 numbers, that is really not that bad after all. The final general expression for P*(Δ*; E*) is as follows:

$$P^* = [\beta_{10} + \beta_{11} \log(E^*) + \beta_{12} \log(E^*)^2 + \beta_{13} \log(E^*)^3]\Delta^* +$$
$$[\beta_{20} + \beta_{21} \log(E^*) + \beta_{22} \log(E^*)^2 + \beta_{23} \log(E^*)^3]\Delta^{*2} +$$
$$[\beta_{30} + \beta_{31} \log(E^*) + \beta_{32} \log(E^*)^2 + \beta_{33} \log(E^*)^3]\Delta^{*3}$$

All the β-coefficients are subject to the geometry of the experiment. In the example case (test #1) that has been followed, the specific P*(Δ*; E*) expression is:

$$P^* = [0.0025 + 0.0613 \log(E^*) - 0.0406 \log(E^*)^2 + 0.01084 \log(E^*)^3]\Delta^* +$$
$$[0.1500 + 0.2985 \log(E^*) - 0.1799 \log(E^*)^2 + 0.03779 \log(E^*)^3]\Delta^{*2} +$$
$$[-0.3525 + 0.3509 \log(E^*) - 0.2108 \log(E^*)^2 + 0.05507 \log(E^*)^3]\Delta^{*3}$$

To illustrate how well this expression captures the behavior of the ABAQUS simulations, the Figure 6-16 shows the simulation data in bullet points on top of lines showing the above curve fit expression evaluated for E* = 35 and 1000. At the resolution of this plot, there appears to be very good agreement, suggesting that the error in our final results is due mostly to experimental error as opposed to error caused by the curve-fitting procedure.

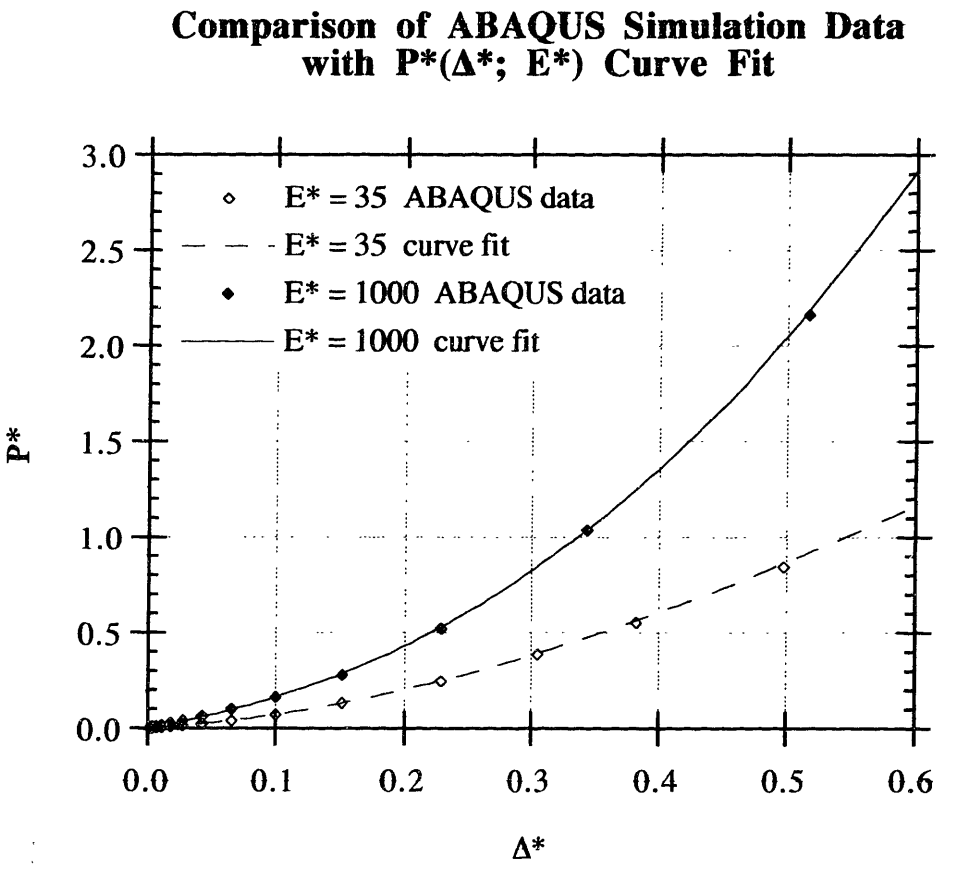

FIGURE 6-16: Comparison of simulation data points with interpolated continuous solutions.

All that remains is to compare the numerical solutions to the experimental measurements. The primary procedure is to fit the experimental P*(Δ*) data points to curves of the above form with E* being the sole fitting parameter. Thus the least-squares (chi-squared minimization) technique calculates the optimal E* for the data set, tabulated for each of the 6 experiments in the first column of the tables to follow. As in the single-layer foam indentation experiments there is some uncertainty as to the exact zero-displacement reading (due mostly to slop in the experimental system, causing a larger load reading at small displacements because of incomplete engagement between the indenter and the specimen). Thus a second fitting parameter (a Δ*-offset), will be introduced here, adding a degree of freedom which would lessen concern for that uncertainty. The numerically-derived P*(Δ*; E*) curves above are simply transformed to P*(Δ*–δ; E*) where δ is the offset in Δ*. The

optimal E*-values and corresponding offsets for this procedure are in the second column of the tables to follow.

An additional possibility worth investigating is whether both elastic moduli of interest (E_0 and E_i) can be obtained independently from the two-layer indentation test experiment. This may be possible because of the inherent curvature in the indentation test's $P^*(\Delta^*)$ behavior. It would be preferable to have 3 to 4 times as many data points as in these large scale experiments to better define that curvature. In this case, the fitting parameter E* is left as is, but E_0 is also introduced by fitting the experimental $E_0P^*(\Delta^*)$ data points to a numerically-derived $E_0P^*(\Delta^*; E_0, E^*)$ curve, simply equal to E_0 times $P^*(\Delta^*; E^*)$ from above. Finally, a curve-fit with all three fitting parameters (E*, E_0 and the offset δ) is also performed. The results for the curve-fits with E_0 unknown both without and with the Δ^*-offset (δ) are listed in columns 3 and 4 of the tables below, respectively. Each fitting parameter is listed with its percent uncertainty due to the curve fitting procedure, as reported by the curve fitting program (Kaleidagraph).

TEST #1	E_0 known		E_0 unknown	
	no offset	w/offset	no offset	w/offset
E*	68.4	74.1	74.9	17.6
E* unc.	3%	11%	120%	164%
E_0 (kPa)			33.8	57.7
E_0 unc.			45%	44%
offset		0.0071		0.0176
offset unc.		135%		80%

TEST #2	E_0 known		E_0 unknown	
	no offset	w/offset	no offset	w/offset
E*	139.1	161.4	1.5	0.5
E* unc.	5%	18%	339%	111%
E_0 (kPa)			109.0	154.0
E_0 unc.			48%	53%
offset		0.0123		0.0173
offset unc.		117%		95%

TEST #3	E_0 known		E_0 unknown	
	no offset	w/offset	no offset	w/offset
E*	113.4	111.8	24.9	22.3
E* unc.	8%	29%	855%	1337%
E_0 (kPa)			68.2	70.6
E_0 unc.			324%	473%
offset		–0.0014		–0.0016
offset unc.		1864%		3070%

TEST #4	E_0 known		E_0 unknown	
	no offset	w/offset	no offset	w/offset
E*	83.7	93.9	large	12.3
E* unc.	3%	12%		157%
E_0 (kPa)			small	74.6
E_0 unc.				43%
offset		0.0184		0.0382
offset unc.		98%		60%

TEST #5	E_0 known		E_0 unknown	
	no offset	w/offset	no offset	w/offset
E*	210.0	171.0	30.9	0.4
E* unc.	6%	18%	1163%	46%
E_0 (kPa)			78.7	248.8
E_0 unc.			436%	42%
offset		–0.0308		–0.0180
offset unc.		87%		163%

TEST #6	E_0 known		E_0 unknown	
	no offset	w/offset	no offset	w/offset
E*	123.6	141.2	large	large
E* unc.	6%	16%		
E_0 (kPa)			small	small
E_0 unc.				
offset		0.0227		0.0119
offset unc.		106%		

The notation of "large" or "small" indicates that the curve-fitting procedure did not converge, iteratively modifying the fitting parameters until they were well out of the expected range for those parameters (and out of the range of E* over which the P*(Δ*; E*) expression was derived). It is clear that there is more uncertainty in the computed parameters as the number of them increases and the function they are fit to becomes more sophisticated (column-wise left to right). For the tests shown here, only the curve fits which assume E_0 = 35 kPa (first two columns) should be trusted. It is also possible that if more data points were available, the E_0-unknown curve fits might produce better results, and since there is no difference in the test procedure, one need not discount that method completely at this stage. Below is a table with average values of the fitted parameters (of those that did converge) and their standard deviations as a percentage of the mean value. It is interesting to note that for the more reliable E_0-known cases there is better repeatability in the estimation of E* (and therefore of E_i) when the Δ*-offset is used, suggesting that for these preliminary experiments the Δ*-offset is a worthwhile complication.

AVERAGES	E_0 known		E_0 unknown	
	no offset	w/offset	no offset	w/offset
E*	123	126	33.1	10.6
% standard deviation	41%	31%	93%	93%
E_0 (kPa)	35	35	72.4	121.1
% standard deviation			43%	67%
E_i (kPa)	4310	4390	2390	1280

6.4.3 Indentation of Bovine Tracheal Specimens

The experiments presented in this section were performed by Ashish Verma, an undergraduate at M.I.T., and the author. Much of the information present here is also in Ashish's bachelor's thesis.[33] The author is very grateful to Ashish for his part in this very successful collaboration.

The same technique is now applied to actual airway specimens, specifically, sections of calf trachea. The indenter used is of a size on the order of the inner thickness with a radius (R) of 10 μm. Any epithelial cells which might come in contact with the indenter before the sub-epithelial collagen layer are assumed to have a modulus so small that the loads they would generate are less than the resolution of the electronic balance which monitors the indenter load. The same exact experimental procedure that was used in the large scale

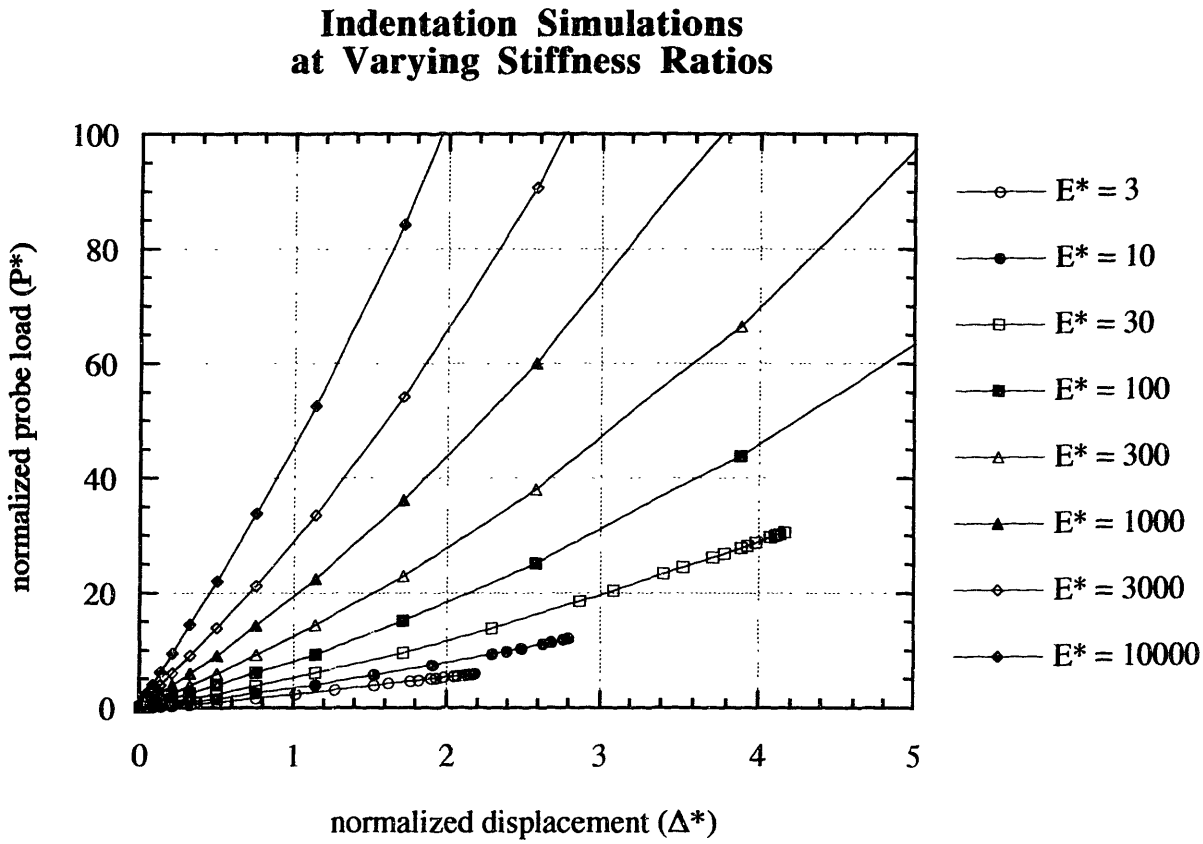

FIGURE 6-17: Indentation simulations for bovine specimens at varying stiffness ratios (linear scales).

preliminary experiments is performed with an extremely fine indenter, but the computational procedure has a few modifications. Based on some of the data in Section 6.1, it would appear that the outer thickness (t_o) should be about 5 or 6 times the size of the inner thickness (t_i). Simulations have proven this to be comfortably close to the limit of infinite outer thickness. This simplifies the nondimensional dependency to $P^*(\Delta^*; t_i^*, E^*)$. Correspondingly, the ABAQUS simulation domain has extensive depth below the indenter as well as far from the axis of symmetry (much more than shown in Figure 6-7).

The electronic balance used has an accuracy of 0.1 mg (~1%) and has a negligible response time (< 0.1 s). The uncertainty in the measurement of the displacement is about 0.5 μm (~8%), somewhat larger because of the resolution of the camera that was used.

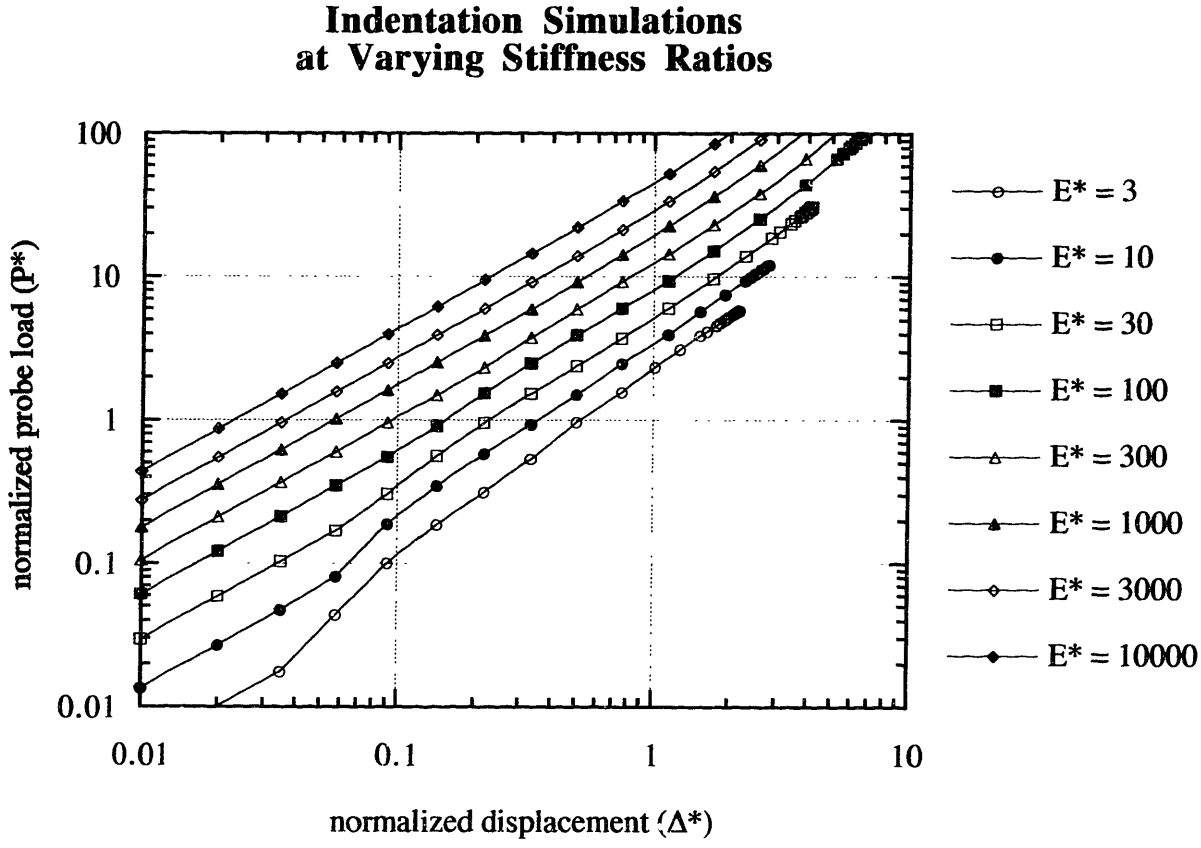

FIGURE 6-18: Indentation simulations for bovine specimens at varying stiffness ratios (logarithmic scales).

In the preliminary tests presented here, the thickness of the inner layer is not known precisely a priori, but will be assumed to be 10 μm, making the inner thickness ratio, $t_i^* \approx 1$. Simulations were performed at this t_i^* over a range of possible E* values, producing the load-displacement data shown in Figures 6-17 and 6-18. Figure 6-17 shows the data on a linear scale. The fact that the simulation data line up on a log-log plot, as in Figure 6-18, suggests that each curve can be fit to a power law relationship.

Note from Figure 6-18, that particularly for $0.1 < \Delta^* < 10$ and $1 < P^* < 100$ the simulation data fit a power law relationship well (and none of the experimental data fall outside of this regime). The table blow summarizes the curve fits performed over the simulation data in this regime. Since all of the lines in Figure 6-18 have roughly the same slope, the power

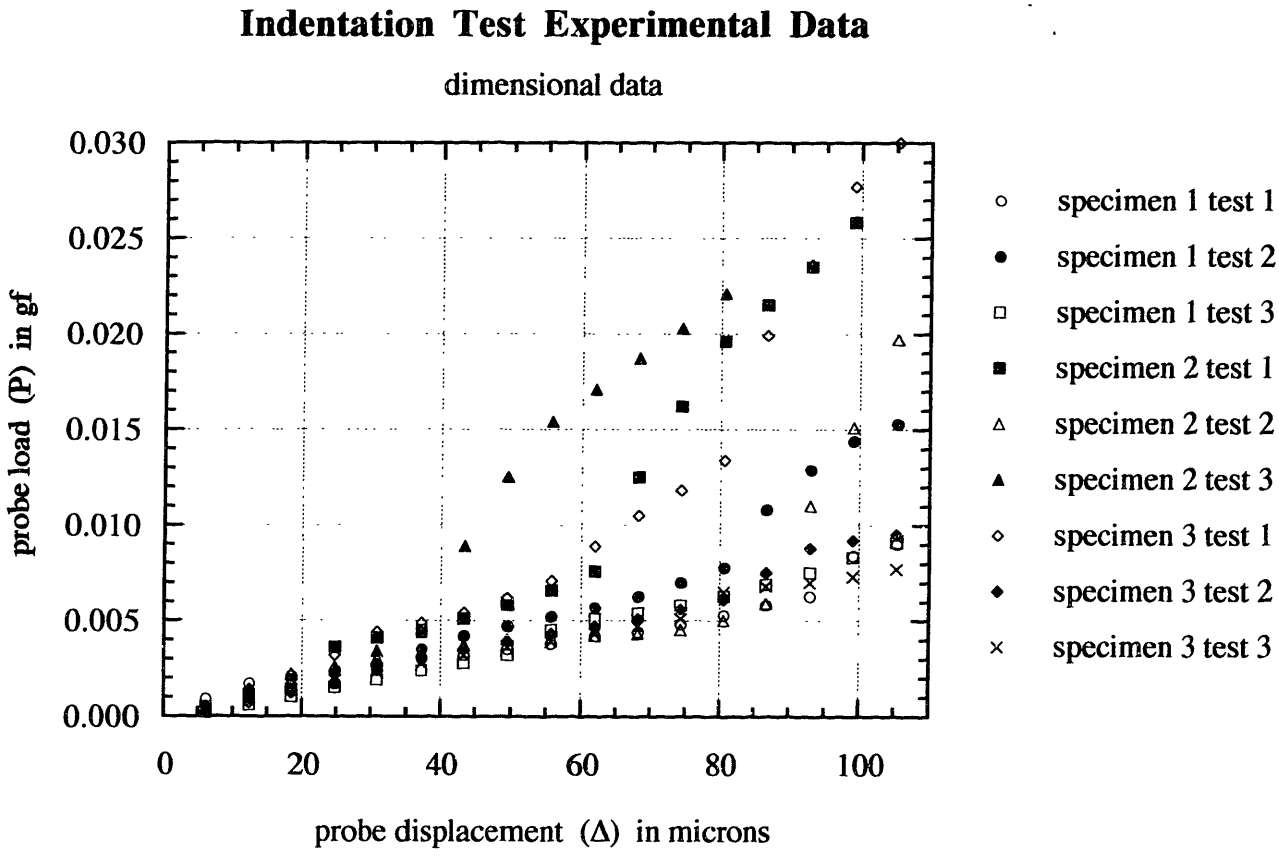

FIGURE 6-19: Dimensional bovine specimen indenter load-displacement experimental data.

laws that describe them all have approximately the same exponent, and an average value of 1.15 is taken for all of them. These 8 simulations fit the form $P^* = c\,(\Delta^*)^{1.15}$ where the sole fitting parameter c is directly related to E^* by the function $E^* = 0.334\,c^{2.68}$.

The raw experimental data shown in Figure 6-19 are nondimensionalized using the definitions of P^* and Δ^* previously defined. The value of $E_o \approx 17$ kPa, found in Section 6.2, is used for nondimensionalizing the load. The non-dimensional data are shown in Figure 6-20.

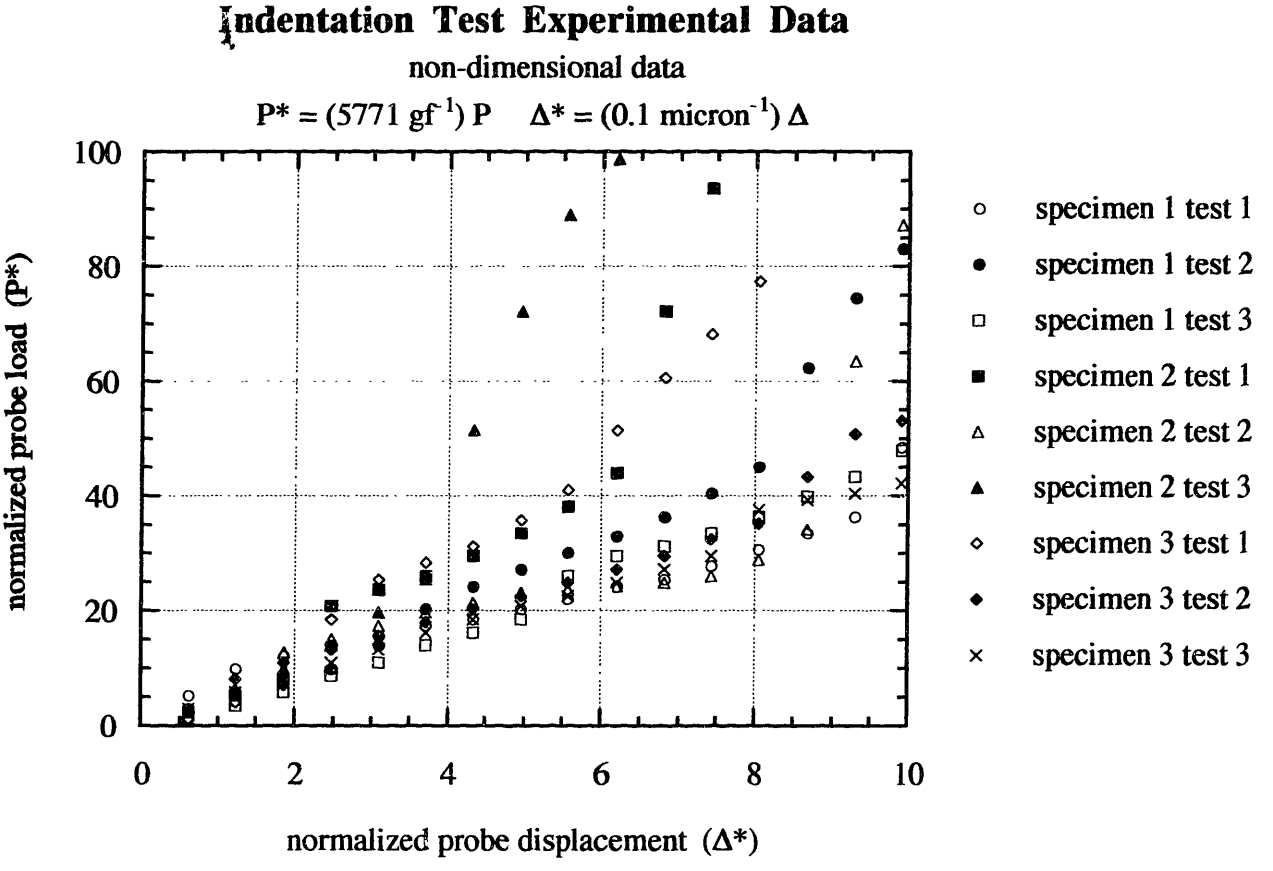

FIGURE 6-20: Nondimensionalized bovine specimen experimental data (linear scales).

The same experimental data are shown in log-log format in Figure 6-21 to show the same power law behavior with roughly the same slope as in the simulations. The mean elevation of the data on this plot determines the best estimate of E*.

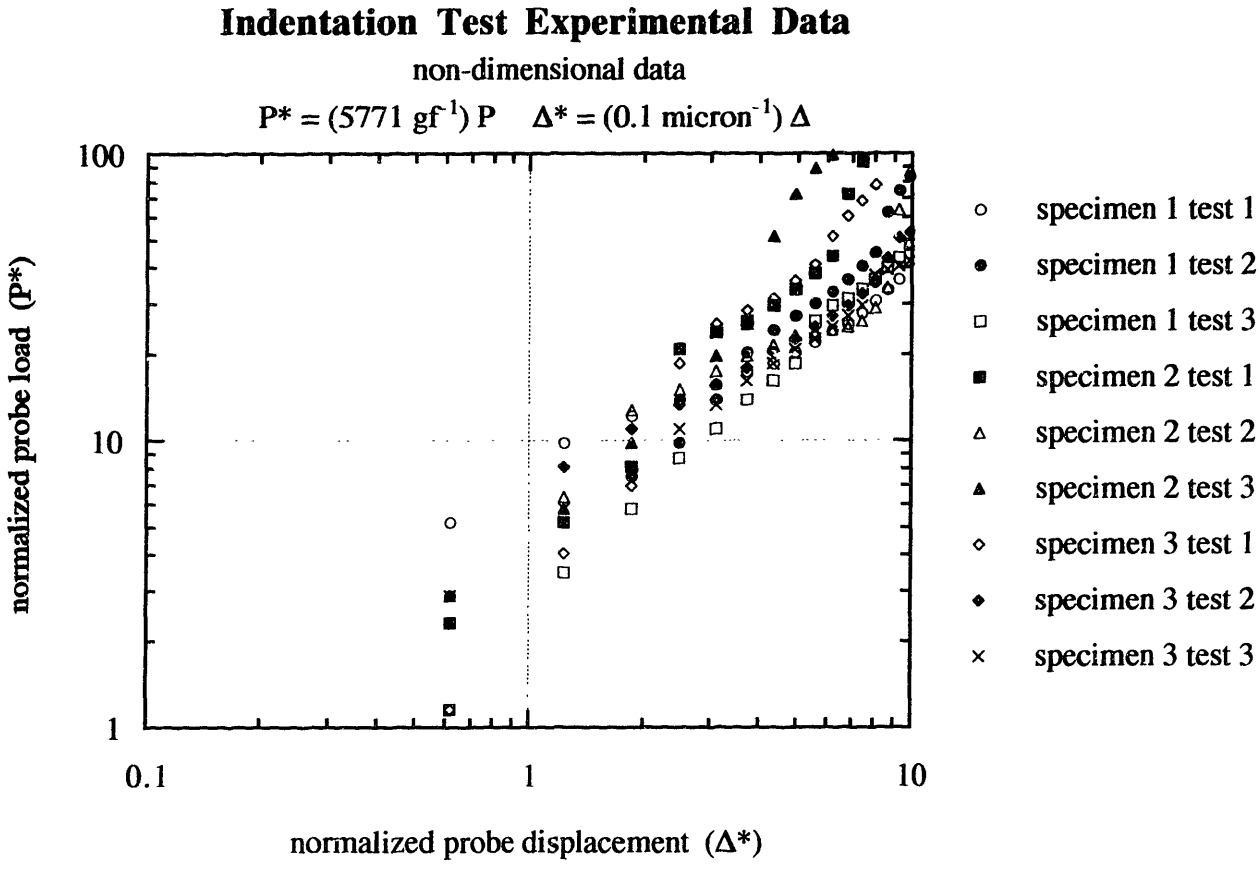

FIGURE 6-21: Nondimensionalized bovine specimen experimental data (log scales).

Next, the load-displacement curves from each experiment are fit to the power law curve $P^* = c\,(\Delta^*)^{1.15}$. The data are plotted along with the curves of this form that best fit them in Figure 6-22.

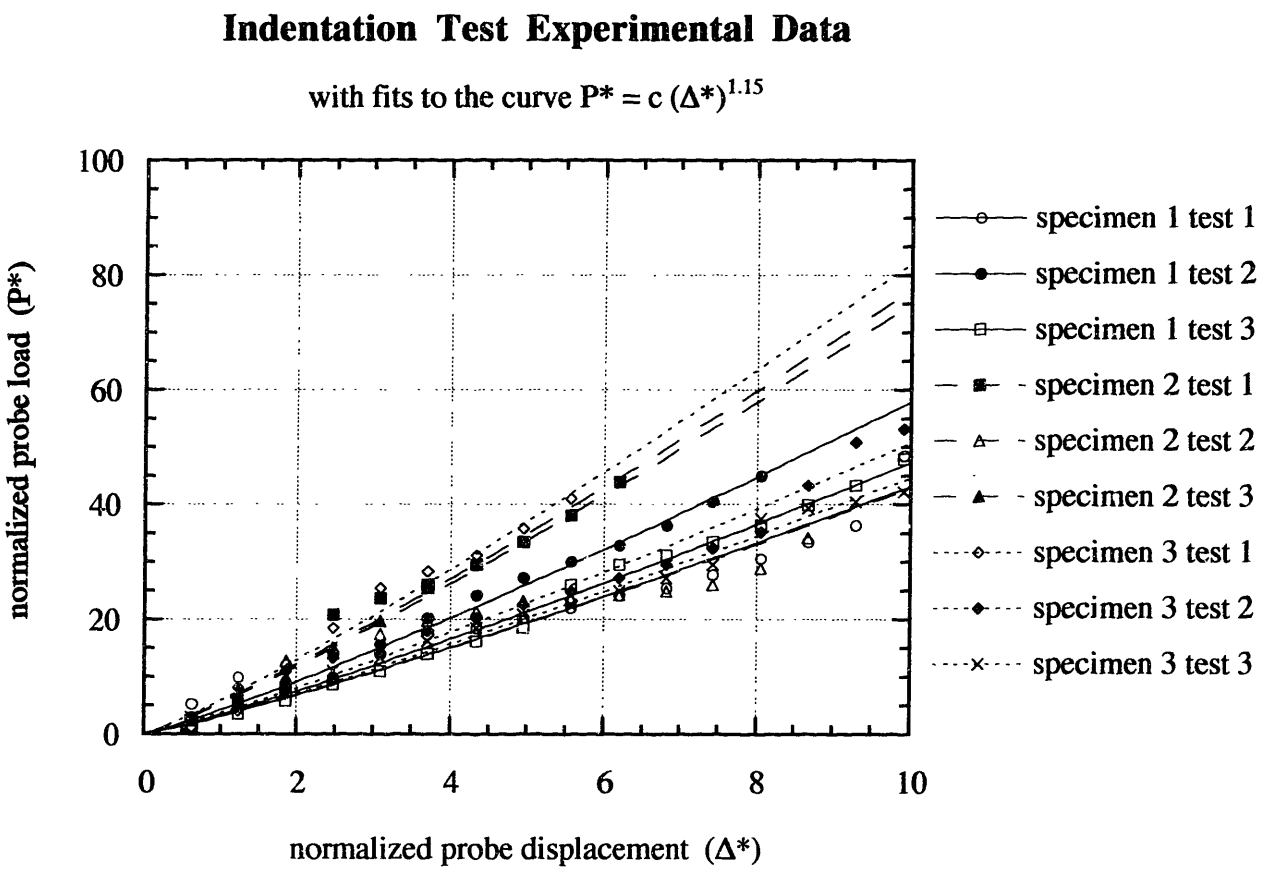

FIGURE 6-22: Indentation test experimental data with fits to curves.

The following table summarizes the results for the 9 tests (3 on each of 3 specimens). The mean value of E* found is 17, which with the assumption of E_o = 17 kPa indicates that the modulus of the sub-epithelial collagen layer, $E_i \approx 290$ kPa. Figure 6-23 summarizes the results graphically, showing where the results fall in the range of simulated E* values.

SIMULATIONS

E*	corresponding c
3	2.336
10	3.660
30	5.125
100	8.125
300	12.49
1000	19.87
3000	30.03
10000	47.68

EXPERIMENTS

specimen	test	best fitting c	corresponding E*
1	1	3.05	6.6
	2	4.09	14.6
	3	3.34	8.5
2	1	5.47	31.7
	2	3.03	6.5
	3	5.30	29.2
3	1	5.81	37.3
	2	3.59	10.3
	3	3.16	7.3

AVERAGE E* : 17

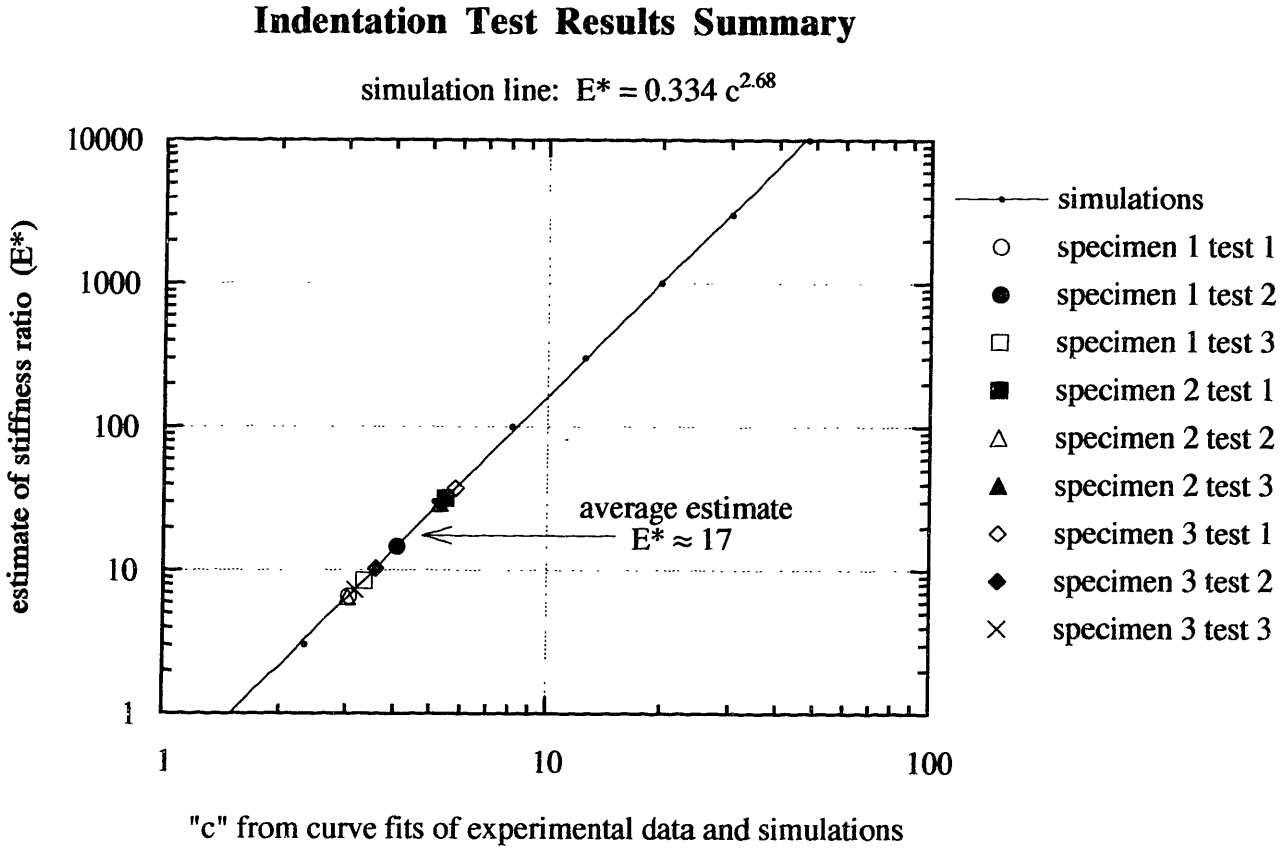

FIGURE 6-23: Bovine tracheal indentation test result summary. The line displays E* versus the curve-fit parameter c predicted by ABAQUS simulations. The larger symbols display where the experimental data fall in the simulated range. The mean value of E* from these 9 indentation tests is 17.

Probably the greatest contributor to error in this measurement for E* is inaccuracy in measurement of the input parameters E_o and t_i. If either of the two input parameters is actually smaller than the measurement used in these calculations, but the experimental probe load-displacement curve is correct, then the actual value of E* is higher than that reported. This makes sense intuitively because decreasing either E_o or t_i would tend to produce a more compliant composite structure, and if the measured load-displacement curve is correct, then only an increase in E* would compensate for the decreased E_o or t_i and give the same load-displacement curve.

Ashish Verma has quantified how much a hypothetical inaccuracy in each of the input parameters would affect the true value of E*. His findings are summarized below:

IF THE ACTUAL VALUE OF...	THEN THE ACTUAL VALUE OF...
E_o is 10% less than 17 kPa (15 kPa)	E* is 15% greater than 17 (20)
t_i is 50% less than 10 μm (5 μm)	E* is 40% greater than 17 (24)

6.5 Smooth Muscle Constriction Limit

Gunst and Stropp have reported that typical canine airways are capable of generating more than 30 cm H_20 (3 kPa) transmural pressures.[13] Using our dimensional analysis:

$$P_{max}^* \equiv \frac{P_{max}}{E_o} \approx \frac{3\ kPa}{17\ kPa} \approx 0.18$$

Opazo-Saez and Paré have measured a maximum stress of 140 kPa in rabbit trachealis, and then gone so far as to quantify the amount of stress generated in the muscle as a function of dose of the agonist acetylcholine.[26] Rearranging the Laplace law for stress in thin-walled pressure vessels as applied to the simple model geometry yields:

$$P_{max} = \frac{\sigma_{max}\ t_m}{R_o} = \frac{\sigma_{max}\ t_m}{R + t_o}$$

where t_m is the thickness of the smooth muscle layer. Previous airway geometry data have suggested approximate geometric similarity throughout the tracheobronchial tree. From the

scaled image and the given dimensions from Opazo-Saez and Paré's work, the muscle thickness to radius ratio is calculated:

$$\frac{t_m}{r_o} \approx \frac{0.120 \text{ mm}}{7.05 \text{ mm}} \approx 0.017$$

Now, using their σ_{max} measurement, P_{max} is calculated, then normalized by the modulus of the outer layer to get P_{max}*.

$$P_{max} \approx (140 \text{ kPa})(0.017) \approx 2.4 \text{ kPa}$$

$$P_{max}^* = \frac{P_{max}}{E_o} \approx \frac{2.4 \text{ kPa}}{17 \text{ kPa}} \approx 0.14$$

Jiang and Stephens have measured maximal smooth muscle stresses (σ_{max}) of 71 ± 2 kPa in membranous airways.[18] Performing the same calculations with this measurement results in $P_{max}^* = 0.07$. It is possible that this measurement is half of that previously calculated because these investigators claim to have found σ_{max} for smaller airways. In summary, it is probably safe to say that the correct order of magnitude for P_{max}^* is 0.1, but it is hard to be more precise.

CHAPTER 6 REFERENCES

1. Amirav I, Kramer SS, Grunstein MM, Hoffman EA. Assessment of methacholine-induced airway constriction by ultrafast high-resolution computed tomography. *J. Appl. Physiol.* 75(5): 2239-2250, 1993.

2. Battaglioli JL, Kamm RD. Measurements of the compressive properties of scleral tissue. *Invest. Opthalmol. Vis. Sci.* 25: 59-65, 1984.

3. Boulet L-P, Laviolette M, Turcotte H, Cartier A, Dugas M, Malo J-L, Boutet M. Bronchial subepithelial fibrosis correlates with airway responsiveness to methacholine. *Chest.* 112(1): 45-52, 1997.

4. Bramley AM, Thomson RJ, Roberts CR, Schellenberg RR. Hypothesis: excessive bronchoconstriction in asthma is due to decreased airway elastance. *Eur. Respir. J.* 7: 337-341, 1994.

5. Brewster CEP, Howarth PH, Ratko D, Wilson J, Holgate ST, Roche WR. Myofibroblasts and subepithelial fibrosis in bronchial asthma. *Am. J. Respir. Cell Mol. Biol.* 3: 507-511, 1990.

6. Brown RH, Mitzner W. Effect of lung inflation and airway muscle tone on airway diameter in vivo. *J. Appl. Physiol.* 80(5): 1581-1588, 1996.

7. Chitano P, Sigurdsson SB, Halayko AJ, Stephens NL. Relevance of classification by size to topographical differences in bronchial smooth muscle response. *J. Appl. Physiol.* 75(5): 2013-2021, 1993.

8. Codd SL, Lambert RK, Alley MR, Pack RJ. Tensile stiffness of ovine tracheal wall. *J. Appl. Physiol.* 76(6): 2627-2635, 1994.

9. Croteau JR, Cook CD. Volume-pressure and length-tension measurements in human tracheal and bronchial segments. *J. Appl. Physiol.* 16(1): 170-172, 1961.

10. Foresi A, Chetta A, Bertorelli G, Olivieri D. Remodelling of the bronchi influences maximal airway narrowing to methacholine in asthma. *Am. J. Respir. Crit. Care Med.* 157(3): A503, 1998.

11. Fung Y-C. *Biomechanics: Motion, Flow, Stress and Growth.* Springer-Verlag, New York, 1990.

12. Gao Y, Vanhoutte PM. Responsiveness of the guinea pig trachea to stretch: role of the epithelium and cyclooxygenase products. *J. Appl. Physiol.* 75(5): 2112-2116, 1993.

13. Gunst SJ, Stropp JQ. Pressure-volume and length-stress relationships in canine bronchi in vitro. *J. Appl. Physiol.* 64(6): 2522-2531, 1988.

14. Habib RH, Chalker RB, Suki B, Jackson AC. Airway geometry and wall mechanical properties estimated from subglottal input impedance in humans. *J. Appl. Physiol.* 77(1): 441-451, 1994.

15. Heard BE, Hossain S. Hyperplasia of bronchial muscle in asthma. *J. Pathol.* 110: 319-331, 1973.

16. Huber HL, Koessler KK. The pathology of bronchial asthma. *Arch. Int. Med.* 30(6): 689-760, 1922.

17. James AL, Hogg JC, Dunn L, Paré PD. The use of internal perimeter to compare airway size and to calculate smooth muscle shortening. *Amer. Rev. Resp. Dis.* 138: 136-139, 1988.

18. Jiang H, Stephens NL. Contractile properties of bronchial smooth muscle with and without cartilage. *J. Appl. Physiol.* 69(1): 120-126, 1990.

19. Love AEH. The stress produced in a semi-infinite solid by pressure on part of the boundary. *Philisophical Transactions of the Royal Society of London,* Series A1, vol. 228, 1929. pp. 377-420.

20. Ma X, Li W, Stephens NL. Detection of two clusters of mechanical properties of smooth muscle along the airway tree. *J. Appl. Physiol.* 80(3): 857-861, 1996.

21. Mitchell RW, Ruhlmann E, Leff AR, Rade KF. Passive sensitization of human bronchi augments smooth muscle shortening velocity and shortening capacity. *Am. J. Physiol.* 267: L218-L222, 1994.

22. Okazawa M, Bai TR, Wiggs BR, Paré PD. Airway smooth muscle shortening in excised canine lung lobes. *J. Appl. Physiol.* 74(4): 1613-1621, 1993.

23. Okazawa M, Vedal S, Verburgt L, Lambert RK, Paré PD. Determinants of airway smooth muscle shortening in excised canine lobes. *J. Appl. Physiol.* 78(2): 608-614, 1995.

24. Okazawa M, Wang L, Bert J, Paré PD. The elastic properties of airway mucosal membrane in rabbits. *Amer. Rev. Resp. Dis.* 147(4): A856, 1993.

25. Opazo-Saez A, Du T, Wang NS, Martin JG. Methacholine-induced bronchoconstriction and airway smooth muscle in the guinea pig. *J. Appl. Physiol.* 80(2): 437-444, 1996.

26. Opazo-Saez A, Paré PD. Stimulus-response relationships for isotonic shortening and isometric tension generation in rabbit trachealis. *J. Appl. Physiol.* 77(4): 1638-1643, 1994.

27. Ophir J, Céspedes I, Ponnekanti H, Yazdi Y, Li X. Elastography: a quantitative method for imaging the elasticity of biological tissue. *Ultrasonic Imaging.* 13: 111-134, 1991.

28. Roberts CR. Is asthma a fibrotic disease? *Chest.* 107(3): 111S-117S, 1995.

29. Roche WR, Beasley R, Williams JH, Holgate ST. Subepithelial fibrosis in the bronchi of asthmatics. *Lancet.* 1: 520-524, 1989.

30. Sato J, Suki B, Davey BLK, Bates JHT. Effect of methacholine on low-frequency mechanics of canine airways and lung tissue. *J. Appl. Physiol.* 75(1): 55-62, 1993.

31. Stephens NL, Van Niekerk W. Isometric and isotonic contractions in airway smooth muscle. *J. Physiol. Pharmacol.* 55: 833-838, 1970.

32. Tepper RS, Shen X, Bakan E, Gunst SJ. Maximal airway response in mature and immature rabbits during tidal ventilation. *J. Appl. Physiol.* 79(4): 1190-1198, 1995.

33. Verma AK. *A Method for Determining the Elastic Moduli of an Airway Model.* S.B. Thesis, Massachusetts Institute of Technology, 1998.

34. Wiggs BR, Moreno R, James A, Hogg JC, Paré PD. A model of the mechanics of airway narrowing in asthma, in *Asthma: Its Pathology and Treatment.* eds. Kaliner MA, Barnes PJ, Persson CGA. Marcel Dekker, New York, 1991. ch. 3.

35. Wiggs BR, Bosken C, Paré PD, James A, Hogg JC. A model of airway narrowing in asthma and in chronic obstructive pulmonary disease. *Am. Rev. Respir. Dis.* 145: 1251-1258, 1992.

36. Wiggs BR, Moreno R, Hogg JC, Hilliam C, Paré PD. A model of the mechanics of airway narrowing. *J. Appl. Physiol.* 69(3): 849-860, 1990.

37. Xie J, Zhou J, Fung YC. Bending of blood vessel wall: stress-strain laws of the intima-media and adventitial layers. *J. Biomech. Eng.* 117: 136-145, 1995.

7. Application of Simulations to Normal and Asthmatic Airway Response

Now that a two-layer model of an airway has been developed, and appropriate airway parameters have been gathered, it is appropriate to apply these parameters to our model and use it to speculate on how the mechanical behavior of asthmatic airways is different from that of normal airways. This is the point at which we examine the credence of the hypotheses put forth in Section 1.4. Much of the information contained in this chapter can also be found in a recent paper by our research group.[7]

7.1 General Conclusions (based on trends)

Based on our simple two-layer model results in general, the following conclusions can be drawn regarding the behavior of airways:

- Thickening of the so-called "outer layer" of submucosal proteoglycans (and sparse collagen, elastin, etc.) always tends to increase an airway's stiffness to occlusion. The pressure-area curve of an airway with a thicker submucosa (and all moduli and other dimensions constant) will always lie to the right (at a higher pressure) of that of a reference airway. Therefore, if thickening of the submucosa were the only aspect of asthmatic airway remodeling, we would expect the airways to be stiffer to occlusion, yet we know that they are not. Asthmatic airways are "hyperresponsive," and though there may be some evidence to indicate that the amount of pressure generated by the smooth muscle has increased in asthma,[2] growth of the submucosal layer alone would serve to make airways more "hyporesponsive" to smooth muscle pressure. Therefore, other aspects of asthmatic airway wall remodeling (found in combination with submucosal thickening) must be more important in altering the mechanical behavior of the airways.

- Many thickened asthmatic airways appear to collapse such that their mucosa folds with fewer lobes than normal airways of the same location in the tracheobronchial tree would. Our model indicates that thickening of the submucosal layer alone hardly reduces the number of folds at all, whereas thickening of the inner sub-epithelial collagen layer indeed does tend to greatly reduce the number of mucosal folds. A stiffening of the sub-epithelial collagen layer (which although not quantified, is probable[5]) or increased compliance of the submucosal layer (which also has not been

rigorously quantified, but is probable[1]) would increase the inner layer to outer layer stiffness ratio, which our model predicts would also tend to reduce the number of mucosal folds. The dependency is not nearly as strong as for the collagen layer thickness but nonetheless is probably not negligible.

- If the inner sub-mucosal collagen layer has sufficient thickness and stiffness, buckling into fewer mucosal folds leads to lessened airway stiffness to occlusion in the late post-buckling airway collapse response. Though the smooth muscle pressure required to buckle may be slightly higher, the smooth muscle is always able to exceed that pressure. It is later when the folds press up against one another that the airway is able to greatly resist further collapse (thus the plateau in dose-response and pressure-area curves). An airway that buckles with many smaller folds will still have a relatively open, unobstructed lumen by the time the folds close and begin resisting further collapse.

To summarize the previous two points, the simple model lends credence to the following mechanism of asthma pathogenesis.

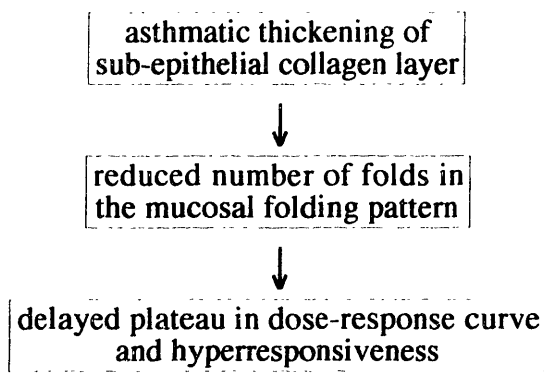

More conclusions that we can draw from the simple two-layer model and our knowledge of normal and asthmatic airways include the following:

- Normal airways, once constricted, have a generally open and circular lumen because the folds have pressed closed against one another at a relatively early stage in the airway collapse. Constricted asthmatic airways, by contrast, have much larger folds which usually are filled with mucus and other airway fluids (see below). This tends to further reduce the amount of lumen area available for airflow during the collapse. Even in the

absence of such fluids, the shape of the lumen is more irregular, causing a greater wetted perimeter to cross-sectional area ratio and driving up the airflow resistance.

- In asthmatic airways, the reduced number of folds results in a greater range of motion for the material in each of the folds, involving more of the submucosa in the deformation. The amount of submucosa being sheared and thus active in the deformation is greater. There are larger shear stresses over greater areas, as well as larger pressure gradients and therefore, more fluid motion through the submucosa and into the lumen. Inter-airway fluids flow from the high-pressure creases to the low-pressure bulges of the folds. Blood vessels which would be located just inside a crease would be squeezed shut, whereas those in the bulges would be open and engorged. This pattern of open and closed vessels is consistent with the observations of Wagner and Mitzner, who claim that the mucosal folding pattern is a result of the blood vessel pattern without accounting for why the blood vessels would be engorged or occluded in the first place.[6] Our explanation – that the blood vessel pattern is due to the mucosal folding pattern, which in turn is due to structural instability and a function of the gross structural geometry and material moduli – is a self-consistent and closed argument.

7.2 Simulations with Best Airway Parameter Estimates

This section presents comparisons of simulations performed at the specific parameters appropriate for normal and asthmatic airways as discussed in Chapter 6. Six different cases are examined, representing "normal" and "asthmatic" states of airways from generations 10, 15 and 20. The input parameters for each case are summarized in the chart below:

NORMAL			ASTHMATIC		
case	t_o*	t_i*	case	t_o*	t_i*
N10	0.111	0.0100	A10	0.235	0.0200
N15	0.148	0.0191	A15	0.272	0.0385
N20	0.174	0.0274	A20	0.304	0.0553

It is worth noting that a "generation 20 airway" is probably not of the same general structure as membranous conducting airways, but more an assemblage of adjoining alveoli. The computations for generation 20 airways are included here more to show the trends in

OUTER THICKNESS RATIO (t_o*):

Z	NORM	ASTH	CHANGE
10	0.111	0.235	+112%
15	0.148	0.272	+84%
20	0.174	0.304	+75%

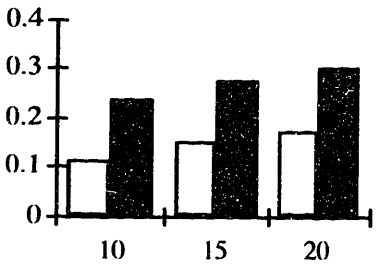

INNER THICKNESS RATIO (t_i*):

Z	NORM	ASTH	CHANGE
10	0.0100	0.0200	+100%
15	0.0191	0.0385	+102%
20	0.0274	0.0553	+102%

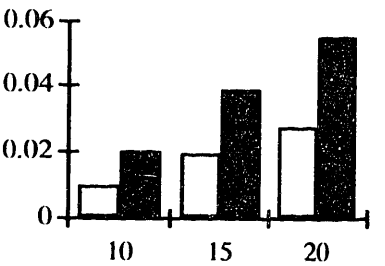

STIFFNESS RATIO (E*):

Z	NORM	ASTH	CHANGE
10	17	17	0%
15	17	17	0%
20	17	17	0%

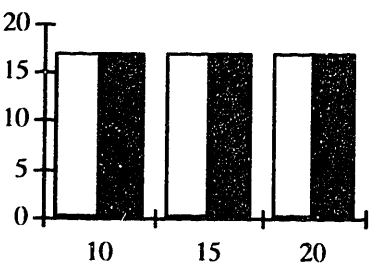

FIGURE 7-1: Tabular and graphical summaries of parameters used as input in 6 simulations of human airways.

NUMBER OF FOLDS (N):

Z	NORM	ASTH	CHANGE
10	34.4	22.9	-33%
15	24.1	12.9	-46%
20	18.1	9.5	-47%

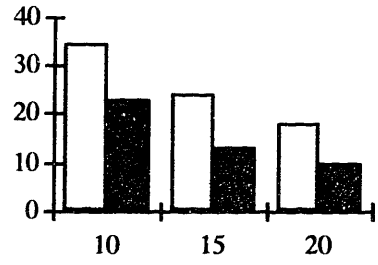

BUCKLING PRESSURE (P_b*):

Z	NORM	ASTH	CHANGE
10	0.0359	0.0587	+63%
15	0.0522	0.0959	+84%
20	0.0696	0.1334	+92%

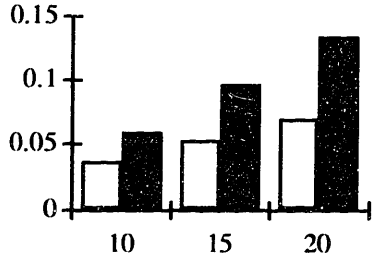

PERCENT SMOOTH MUSCLE SHORTENING AT BUCKLING (S_b):

Z	NORM	ASTH	CHANGE
10	0.0732	0.0566	-23%
15	0.0619	0.0529	-15%
20	0.0591	0.0513	-13%

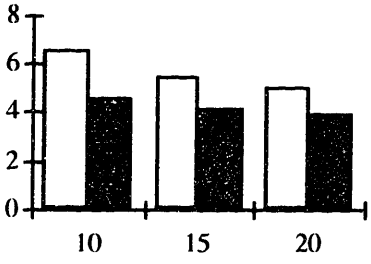

BUCKLING LUMEN AREA (A_b*):

Z	NORM	ASTH	CHANGE
10	0.840	0.858	+2%
15	0.856	0.857	0%
20	0.857	0.853	0%

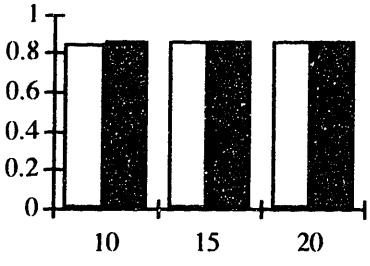

FIGURE 7-2: Tabular and graphical summaries of linearized buckling analysis results from 6 simulations of human airways.

airway behavior as the airways grow smaller, given the airway parameters collected in Chapter 6.

7.2.1 Linearized Buckling Analysis Results

Figure 7-1 reiterates graphically the input parameters for the six above cases. Converged linearized buckling analyses were performed on each of them, and their results are summarized in Figure 7-2.

As we might expect from our previous analyses, from normal to asthmatic airways, the number of folds decreases by about a third for 10th generation airways and by about half for 20th generation airways. The buckling pressure has increased markedly, which is

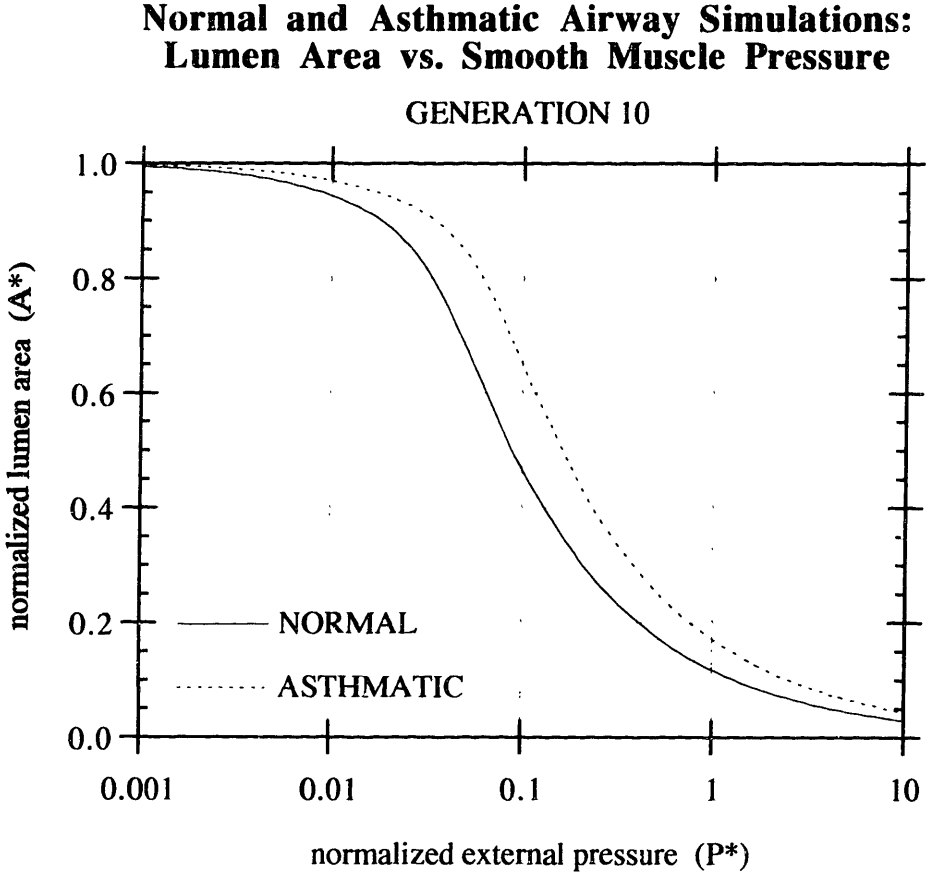

FIGURE 7-3: Area-pressure curves resulting from nonlinear static analyses (with remeshing and extrapolation) of simulated normal and asthmatic generation 10 airways. (Pressure axis has logarithmic scale.)

expected given the great increase in submucosal thickness. Interestingly, it requires a little less smooth muscle shortening to buckle the asthmatic airways. Because the stiffness ratio is assumed to not change between normal and asthmatic states, the buckling event occurs at about 85% luminal area in all cases.

7.2.2 Results of Nonlinear Static Analysis with Remeshing

The six cases are also analyzed using constant-N wedge models with remeshing. The results from remeshed analyses need some smoothing so that they can be interpreted correctly. Figures 7-3, 7-4 and 7-5 display the six analyses that describe asthmatic remodeling in airways (at generations 10, 15 and 20) given the model parameters collected in Chapter 6. Note that at generation 10, the simulated asthmatic airway is always stiffer

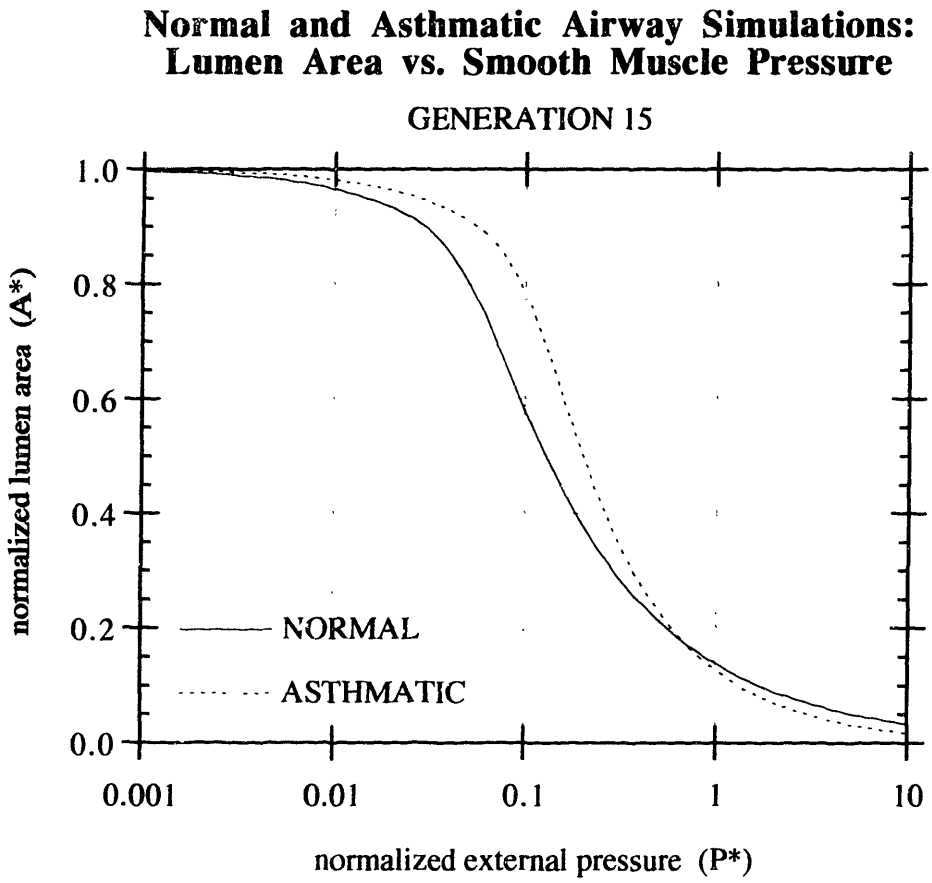

FIGURE 7-4: Area-pressure curves resulting from nonlinear static analyses (with remeshing and extrapolation) of simulated normal and asthmatic generation 15 airways. (Pressure axis has logarithmic scale.)

than the normal airway. The pressure-area curve for the asthmatic airway lies entirely to the right of the normal, indicating that for any amount of occlusion, the asthmatic airway will need to generate more smooth muscle pressure than the normal one. At the depth of generation 15 airways, the story is somewhat different. If the smooth muscle produces a pressure greater than the elastic modulus of the outer layer ($\approx$ 17 kPa), it begins becoming easier to collapse an asthmatic airway than a normal one. At the depth of generation 20 airways (close to the end of the tree), this effect would be even greater, such that if the smooth muscle pressure is on the order of 2 E_0, the normal airway is still about 10-15% open while the asthmatic airway is down to 2-3%.

Unfortunately, using the measurements of maximal smooth muscle stress and pressure obtained from previous studies (see Section 6.5) the order of magnitude of the maximal

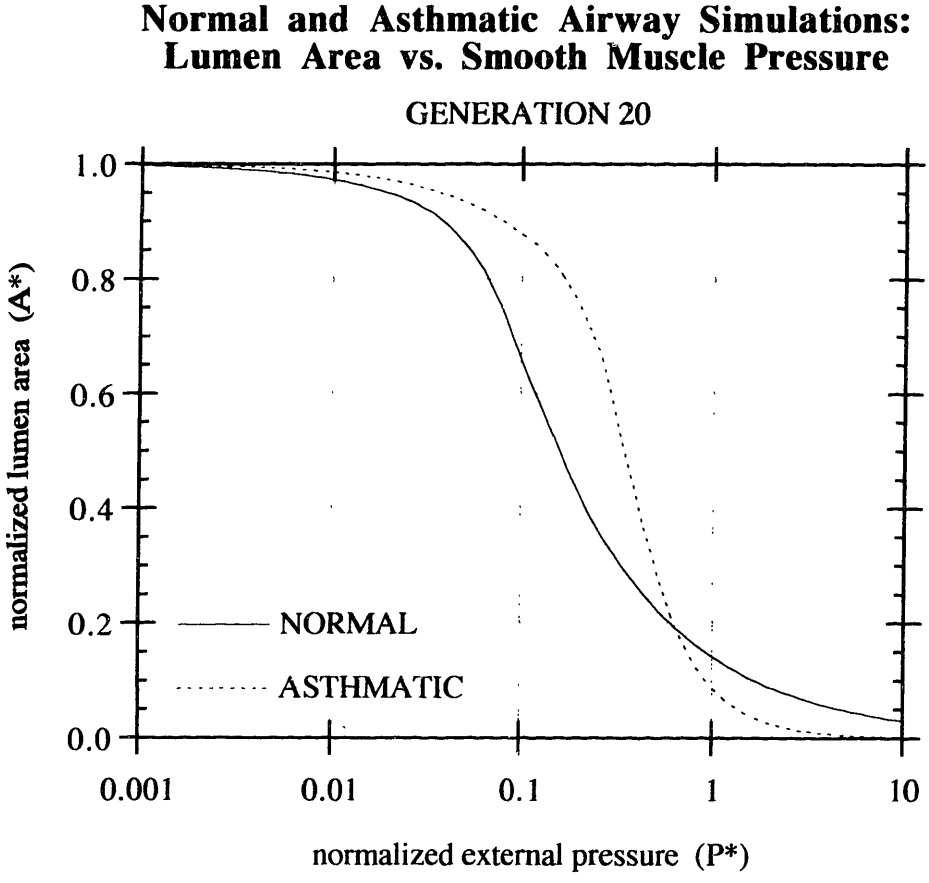

FIGURE 7-5: Area-pressure curves resulting from nonlinear static analyses (with remeshing and extrapolation) of simulated normal and asthmatic "generation 20 airways." (Pressure axis has logarithmic scale.)

smooth muscle pressure (P_{max}) is merely 0.1. It would appear the airways do not reach the cross-over point at all. The author would of course prefer to be more sure of all the airway parameters before coming to that conclusion. Some supplemental (albeit arbitrary) analyses have verified that cross-over tends to occur earlier at higher stiffness ratios. If the E* value measured in the preliminary indentation tests is found to be an order of magnitude too low, the true airway behavior would begin to "plateau" (become markedly stiffer to airway occlusion) at smaller P* values.

CHAPTER 7 REFERENCES

1. Bramley AM, Thomson RJ, Roberts CR, Schellenberg RR. Hypothesis: excessive bronchoconstriction in asthma is due to decreased airway elastance. *Eur. Respir. J.* 7: 337-341, 1994.

2. Gunst SJ, Stropp JQ. Pressure-volume and length-stress relationships in canine bronchi in vitro. *J. Appl. Physiol.* 64(6): 2522-2531, 1988.

3. Okazawa M, Paré PD, Hogg JC, Lambert RK. Mechanical consequences of remodelling of the airway wall, in *Airways and Vascular Remodelling*. eds. Page C, Black J. Academic Press, Toronto, 1994. ch. 8.

4. Opazo-Saez A, Paré PD. Stimulus-response relationships for isotonic shortening and isometric tension generation in rabbit trachealis. *J. Appl. Physiol.* 77(4): 1638-1643, 1994.

5. Roberts CR. Is asthma a fibrotic disease? *Chest.* 107(3): 111S-117S, 1995.

6. Wagner EM, Mitzner W. Bronchial vascular engorgement and airway narrowing. *Amer. Rev. Resp. Dis.* 149(4): A585, 1994.

7. Wiggs BR, Hrousis CA, Drazen JR, Kamm RD. On the mechanism of mucosal folding in normal and asthmatic airways. *J. Appl. Physiol.* 83(6): 1814-1821, 1997.

8. Poroelastic Numerical Modeling

Of the many assumptions that are made in the development of what has been termed the "simple" two-layer model, the one which is the most doubtful is that the airway materials are best described as linear incompressible single-phase continua. The airway wall, like most tissues, is comprised mainly of water, either bound in proteoglycans or able to flow subject to friction resistance as is passes through the matrix of various collagens and cellular materials. In essence, most tissue materials are like a sponge: very slow compression results in free release of water from the intersticies and flow out of the material boundaries, but very fast compression is more greatly resisted because the velocity of the water against the solid sponge matrix generates local friction forces which slow down the water, effectively binding it in place as if it were intrinsic to the material. The assumption of the "simple" two-layer model is the latter: that the compression of the smooth muscle is fast enough that there is little fluid movement, and the material is effectively of a single phase. But what if we relax this assumption and allow the smooth muscle to compress more slowly? Would this effect change the expected number of folds in the airway buckling pattern? Would there be an appreciable effect on the load-displacement character of the airway? This chapter is devoted to approaching these concerns, albeit in a rather simplified and intuitive way by incorporating a simple poroelastic material model.

8.1 Finite Element Implementation in ABAQUS

In addition to the usual parameters describing a linear-elastic material, equations are incorporated for keeping track of the local ratio of fluid to solid in the material (through the void ratio, solid fraction or porosity), the estimated resistance to fluid flow (through the permeability or hydraulic conductivity), and the rate of smooth muscle contraction. These parameters are defined as below. One of the following three quantities must be specified in order to quantify how much fluid is present versus how much solid is present for every material point in the original configuration.

$$\text{void ratio:} \quad e \equiv \frac{\text{volume of voids}}{\text{volume of solid matrix}} = \frac{n}{1-n} = \frac{1-\varphi}{\varphi}$$

$$\text{porosity:} \quad n \equiv \frac{\text{volume of voids}}{\text{total volume}} = \frac{e}{1+e} = 1-\varphi$$

$$\text{solid fraction:} \quad \varphi \equiv \frac{\text{volume of solid matrix}}{\text{total volume}} = \frac{1}{1+e} = 1-n$$

In the poroelastic models presented here, the voids are always completely full of the wetting fluid, water (as opposed to any type of non-wetting fluid such as air, which would fill voids but not generate resistance to flow). It is reasonable to assume that the airway tissue starts out fully saturated and is compressed, reducing the void volume and squeezing out water as opposed to drawing in air.

The poroelastic implementation used in ABAQUS is called the "effective stress principle" where the stresses and strains are modified (to "effective stresses" and "effective strains") such that the fluid pressure is transmitted through the first invariant of the stress tensor. For a fully saturated porous medium, the effective stress tensor (σ) is related to the Cauchy stress (τ) and the fluid (or pore) pressure (p_f) as follows:

$$\sigma \equiv \tau + p_f \mathbf{1}$$

For incompressible constituents in the absence of moisture swelling or thermal strains, the effective strain (conjugate to the effective stress) is equal to the typical small strain (from Chapter 2), so no new notation is introduced here regarding the strain. The jacobian, however, defined as the determinant of the deformation gradient, also happens to be equal to the ratio of volume in the current configuration to the volume in the reference configuration.

$$J \equiv \det \mathbf{F} = \left| \frac{dV}{dV^0} \right|$$

Assuming that both the solid and fluid constituents are individually incompressible, the continuity relationship between fluid and solid motions, defined in terms of the jacobian (J), the average velocity of the wetting liquid relative to the solid phase ($\mathbf{v}_f$) and the porosity (n) is:

$$\frac{1}{J}\frac{d}{dt}(J\,n) + \text{div}\,(n\,\mathbf{v}_f) = 0$$

The general constitutive relationship between fluid flow and the driving pore pressure in the fluid is Darcy's law:

$$n\,\mathbf{v}_f = -\frac{1}{g\rho_f}\,\mathbf{k}\,\nabla p_f$$

In the above expression of Darcy's law, ρ_f is the density of the wetting fluid, g is the acceleration due to gravity, and $\mathbf{k}$ is a second-order tensor describing the hydraulic conductivity (or permeability – different authors use different semantics). All of the analyses here will assume isotropically permeable materials, where the hydraulic conductivity tensor is completely described by one scalar quantity (k) as follows.

$$\mathbf{k} = k\,\mathbf{1}$$

Therefore, Darcy's law is simply:

$$n\,\mathbf{v}_f = -\frac{k}{g\rho_f}\,\nabla p_f$$

For convenience, this work uses a generalized isotropic "permeability parameter" (κ) which incorporates the effect of changing either the material permeability or the wetting fluid specific weight ($g\rho_f$). In this notation, Darcy's law is written:

$$n\,\mathbf{v}_f = -\kappa\,\nabla p_f$$

Substituting Darcy's law into the solid-fluid continuity relationship yields:

$$\frac{1}{J}\frac{d}{dt}(J\,n) - \operatorname{div}(\kappa\,\nabla p_f) = 0$$

Upon simplification:

$$\frac{\dot{J}}{J}n + \dot{n} - \kappa\,\nabla^2 p_f = 0$$

This equation, evaluated multiple times over every element provides the extra equations (the constraint, or Lagrange multiplier equations) that allow solution of the pressures at the corner nodes as well as the displacements.

As for boundary conditions on the flow imposed in the poroelastic two-layer model, free flow is allowed from both the inner aspect of the inner layer (bordering the lumen) and the outer aspect of the outer layer (bordering smooth muscle). It will be assumed that the only resistance to flow is the Darcy friction that occurs when the wetting fluid flows through the solid matrix.

8.2 Poroelastic Parameters

The "simple" two-layer tube model of an airway was so entitled because a mere three dimensionless parameters (t_o^*, t_i^* and E^*) determined its behavior. This complication of poroelasticity introduces several new parameters. However, with various well-substantiated assumptions, the number of dimensionless parameters only increases by two. This section explains the rationale behind this development, then quantifies the two poroelastic parameters.

The simple two-layer model, before assumptions about the material compressibility are made, is completely described by seven dimensional parameters, namely:

$$R \quad t_o \quad t_i \quad E_o \quad E_i \quad \nu_o \quad \nu_i$$

To simplify the model, the materials were assumed incompressible (that is, $\nu_o = \nu_i = {}^1/_2$). The verification in Section 3.2.1 shows that compressibility effects tend not to change the buckling pattern in the simple model, but to change the amount of force to collapse the simulated airway to a relatively small extent (i.e., the "airway stiffness"). After the Poisson ratio assumptions, dimensional analysis then demonstrates that the number of independent parameters in the simple model is three, and those parameters are:

$$t_o^* \equiv \frac{t_o}{R} \qquad t_i^* \equiv \frac{t_i}{R} \qquad E^* \equiv \frac{E_i}{E_o}$$

The poroelastic formulation used in ABAQUS assumes that the materials of each of the two phases (solid network and wetting fluid) are individually incompressible. That is, the water is incompressible, and if one could isolate a completely solid chunk of the tissue matrix materials without voids, it would be incompressible as well. What is still free to be

assigned is the Poisson ratio of the drained solid network (with voids built into it). The notation for this parameter will be $\bar{\nu}_o$ and $\bar{\nu}_i$ for the outer and inner layers, respectively.

In addition, the poroelastic formulation introduces parameters previously discussed in Section 8.1, namely, the generalized permeability parameters for the outer and inner layers, κ_o and κ_i, and the porosity of the outer and inner layers, n_o and n_i.

Furthermore, because this is now a transient problem (no longer static), parameters are necessary for quantifying how the model is loaded through the course of time. The full-circle model with spectral imperfections (discussed in Section 2.5.2) is used, assuming that the smooth muscle band shortens at a constant rate. Because no remeshing is used, this technique simulates only until just past buckling and there is no need to incorporate consideration of P_{max} (or σ_{max}); the smooth muscle shortening parameter (S) just ramps up with time at a constant rate. The parameter used here for quantifying this rate is τ_{10}, the period of time necessary for 10% smooth muscle shortening at this constant rate, $\dot{S}$. The relationship between τ_{10} and $\dot{S}$ is:

$$\tau_{10} = \frac{10}{\dot{S}}$$

So in summary, ABAQUS allows a total of 12 adjustable parameters for this problem.

$$R \quad t_o \quad t_i \quad E_o \quad E_i \quad \bar{\nu}_o \quad \bar{\nu}_i \quad \kappa_o \quad \kappa_i \quad n_o \quad n_i \quad \tau_{10}$$

Some "numerical experimentation" has shown that for this configuration, the results are completely independent of n_o and n_i. As in the simple model, knowing values of the Poisson ratio is very difficult, and some arbitrary decisions must be made. Setting both $\bar{\nu}_o$ and $\bar{\nu}_i$ to $^1/_2$ makes the model completely incompressible again, as if the poroelastic formulation were "shut off". When modeling poroelastic effects in tissues, small values of $\bar{\nu}$ are usually assumed (and there is little difference between cases with $\bar{\nu} < 0.2$). However, setting both $\bar{\nu}_o$ and $\bar{\nu}_i$ to 0 results in the non-physiologic result of *no folding*. (Note, however, that in the "simple" two-layer computational model, setting ν_o and ν_i to 0 *did* result in folding; there is a definite alteration in the material constitutive law introduced with the poroelastic formulation.) Therefore, the most interesting combination is to set $\bar{\nu}_o$ to 0 and $\bar{\nu}_i$ to $^1/_2$, which is probably the most realistic choice, given the high density of the inner

layer. The following results are based on models which make this compressible submucosa and incompressible mucosa assumption.

Taking into account these assumptions and observations, the simulated airway behavior is a function of only eight dimensional parameters, namely:

$$R \quad t_o \quad t_i \quad E_o \quad E_i \quad \kappa_o \quad \kappa_i \quad \tau_{10}$$

Now that the problem is unsteady and time is involved, the number of independent parameters can be reduced by three. The chosen normalizing parameters are R, E_o and κ_o. The final set of non-dimensional parameters relevant to the poroelastic two-layer tube model is:

$$t_o^* \quad t_i^* \quad E^* \quad \kappa^* \quad \tau_{10}^*$$

where the two new non-dimensional parameters are defined:

$$\kappa^* \equiv \frac{\kappa_i}{\kappa_o} \qquad \tau_{10}^* \equiv \frac{\tau_{10}\ \kappa_o\ E_o}{R^2}$$

Based on a measurement reported by Tsai et al.,[8] the shortening parameter appropriate for modeling airways is calculated as follows. This calculation assumes the "hydraulic diffusivity" (κ_o) reported by Tsai et al., a submucosal modulus (E_o) of 17 kPa, a 1-mm diameter airway ($R \approx 0.5$ mm), and that the smooth muscle shortens 10% in about 1 second. Some of these choices are fairly arbitrary, but should result in the appropriate order of magnitude for τ_{10}^*.

$$\tau_{10}^* \equiv \frac{\tau_{10}\ \kappa_o\ E_o}{R^2} = \frac{(1\ s)(6\times10^{-14}\ m^4/Ns)(1.7\times10^4\ N/m^2)}{(5\times10^{-4}\ m)^2} = 0.005$$

As will be shown momentarily, this places our airways comfortably in the "incompressible behavior" regime. An acceptable value for κ^* (the ratio in layer permeabilities) might be about 0.01, but definitely less than or equal to 1.

8.3 Results of Perturbative Studies

Several tests were performed on the most often used base case of geometry and material parameters (t_o*=0.5, t_i*=0.02, E*= 10), while individually varying the poroelastic parameters, τ_{10}* and κ*. The most interesting results of these studies are summarized below.

8.3.1 Effect of τ_{10}*

Figure 8-1 shows how the familiar pressure-area curve varies as τ_{10}* is changed. Note that the value of τ_{10}* spans 5 orders of magnitude, and though the plot does not indicate this, it spans the entire range of possible pressure-area curves as well. When τ_{10}* is less

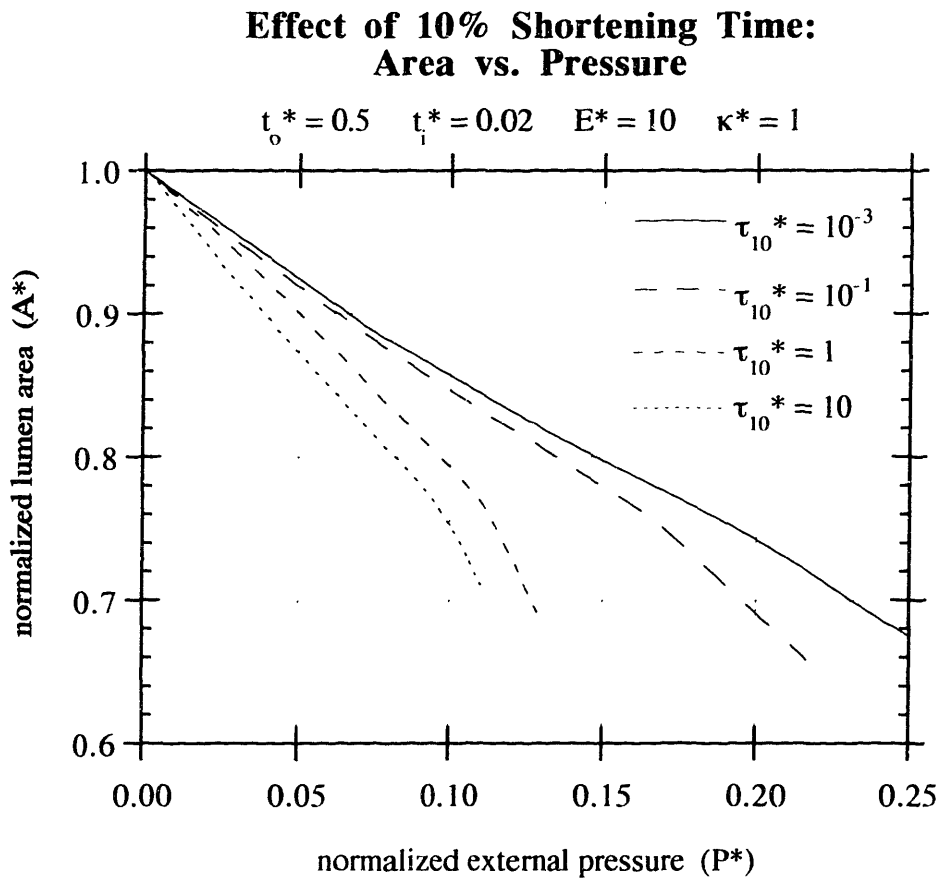

FIGURE 8-1: Area versus pressure results from transient poroelastic analysis with spectral imperfections. Plot shows full range of possible responses from τ_{10}* = 10^{-3} and smaller to τ_{10}* = 10 and larger.

than 10^{-3}, it is hardly right of the plot shown (here the behavior is identical to that of an incompressible single-phase model). When it is greater than 10, it is pretty close to the curve for $\tau_{10}^* = 10$ (where the behavior is very much like a simple model with $\nu_o = 0$ and $\nu_i = {}^1/_2$). It would appear that the greatest effect poroelasticity could have is to reduce the airway stiffness by about one-half. If the base case we are perturbing is close to appropriate, we can conclude at this point that airway tissues are mostly incompressible. The interesting result, however, is that if asthmatic airway remodeling causes the submucosal permeability to increase by several orders of magnitude, the airway stiffness may be reduced by as much as a factor of two, but within the limits of the assumptions made, *this is the greatest possible extent of the effect of compressibility.* Figure 8-2 merely shows that τ_{10}^* has a rather inconsequential effect on the number of mucosal folds, as might have been predicted from experience with the simple model.

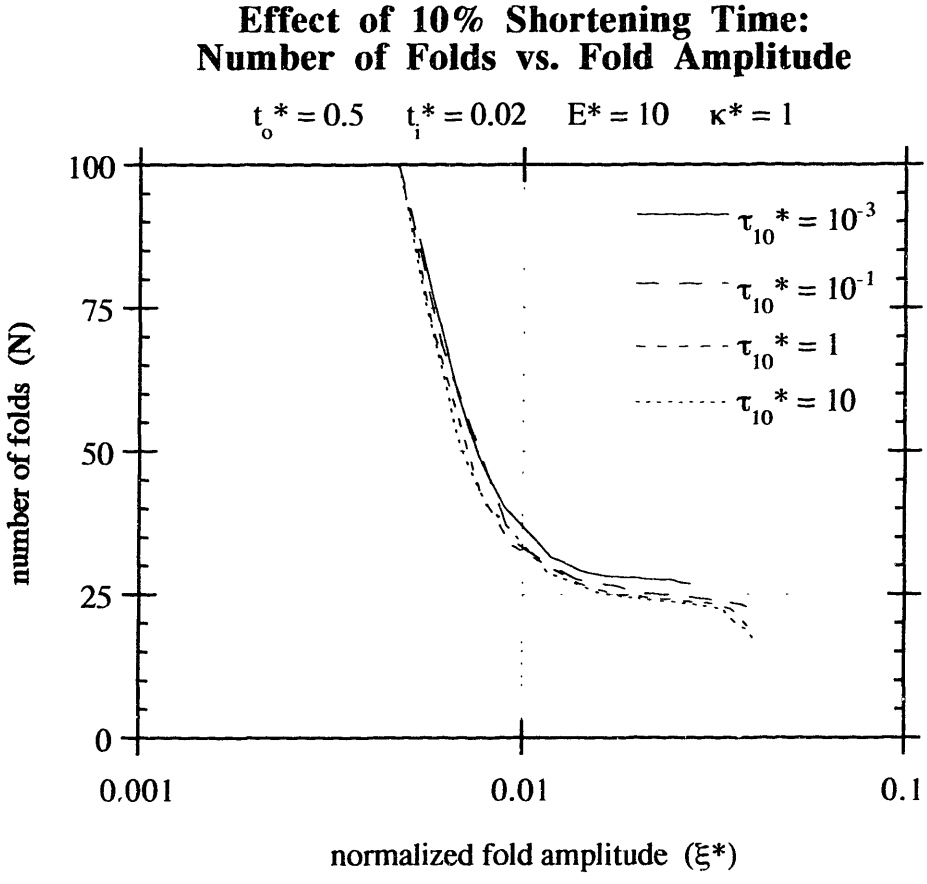

FIGURE 8-2: Number of folds versus fold amplitude results from transient poroelastic analysis with spectral imperfections. Plot shows full range of possible responses from $\tau_{10}^* = 10^{-3}$ and smaller to $\tau_{10}^* = 10$ and larger.

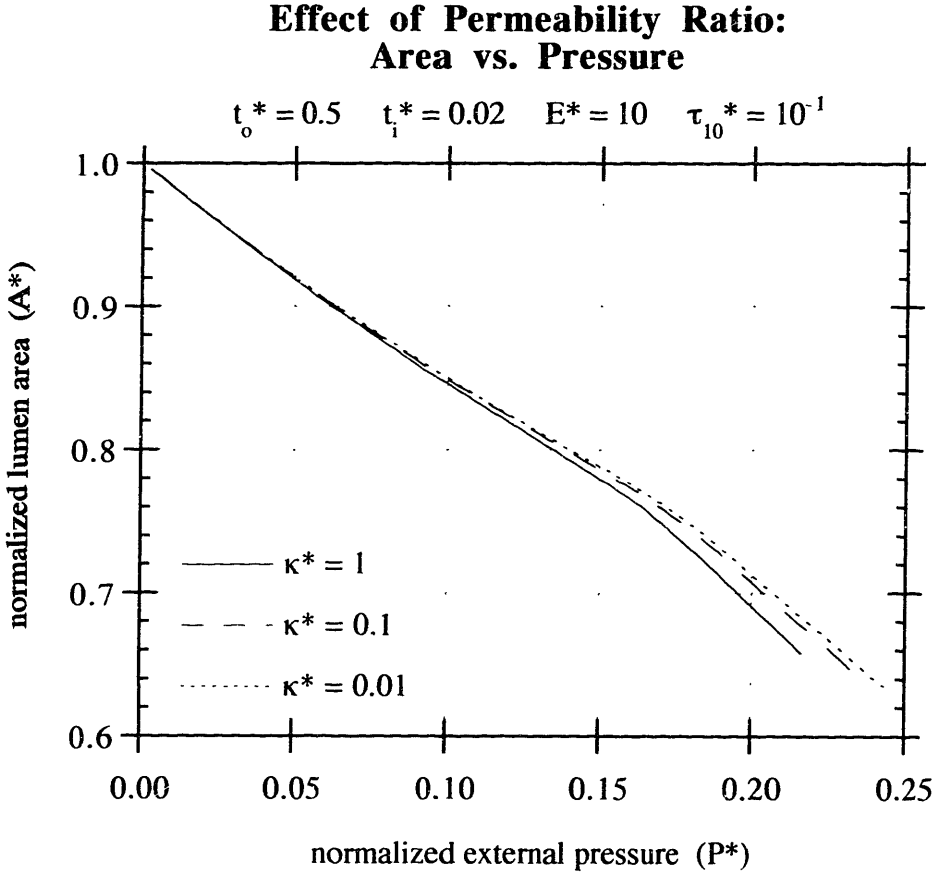

FIGURE 8-3: Area versus pressure results from transient poroelastic analysis with spectral imperfections. Plot shows a range of possible responses from $\kappa^* = 0.01$ and smaller to $\kappa^* = 1$.

8.3.2 Effect of κ^*

As evidenced by Figures 8-3 and 8-4, κ^* appears to have even less of an effect than τ_{10}^*. The number of folds is independent of κ^*, and the pressure-area curve is hardly affected.

In conclusion, it appears that the poroelastic parameters of an airway are in such a regime that the behavior is well-approximated by a completely incompressible model. Disregarding this, the model is not remarkably affected by compressibility anyway, although a possible increase in permeability and the resulting reduction in airway stiffness could be significant (but the great change necessary for this seems improbable).

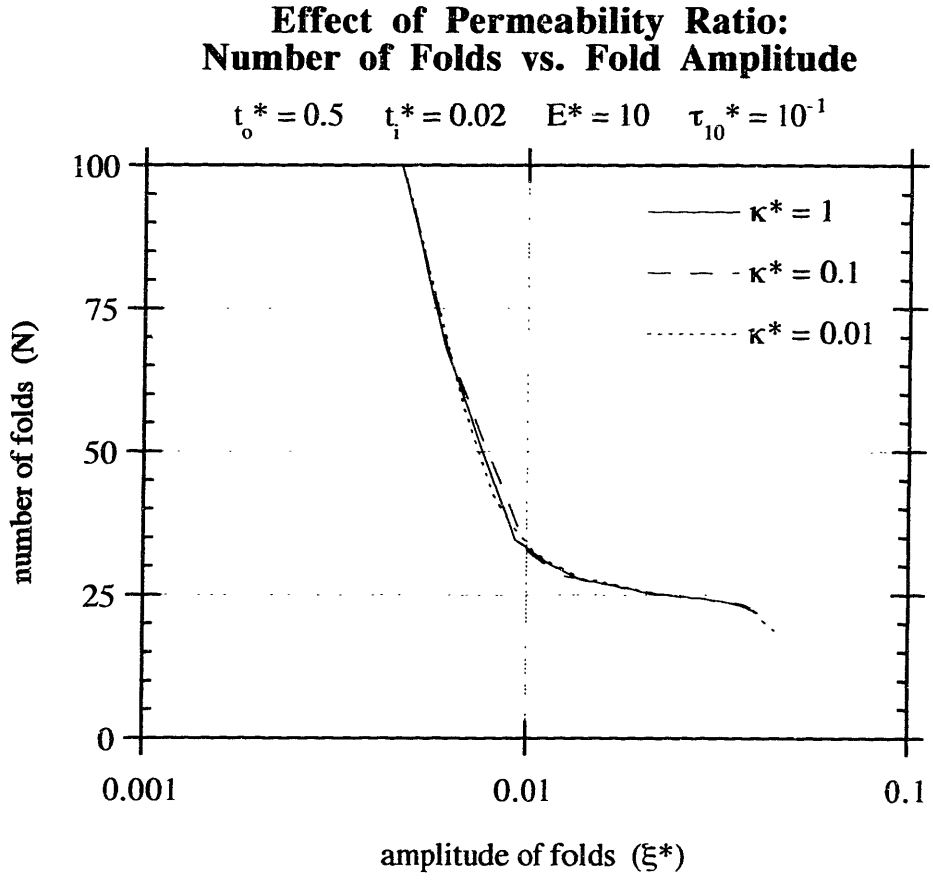

FIGURE 8-4: Number of folds versus fold amplitude results from transient poroelastic analysis with spectral imperfections. Plot shows a range of possible responses from $\kappa^* = 0.01$ to $\kappa^* = 1$.

CHAPTER 8 REFERENCES

1. Abeyaratne R. Lecture notes from M.I.T. course 2.072, Mechanics of Continuous Media. Spring 1995.

2. Anand L. Lecture notes from M.I.T. course 2.072, Mechanics of Continuous Media. Spring 1994.

3. Bathe K-J. *Finite Element Procedures in Engineering Analysis.* Prentice-Hall, Toronto, 1982.

4. Bathe K-J. Lecture notes from M.I.T. course 2.093, Computer Methods in Dynamics. Spring 1993.

5. Bathe K-J. Lecture notes from M.I.T. course 2.094, Theory and Practice of Continuum Mechanics. Fall 1993.

6. Grodzinsky AJ. Course notes from M.I.T. course 2.795, Fields, Forces and Flows: Rheology of Hydrated Biological Tissues and Polymeric Materials, ch. 8. Fall 1995.

7. Hibbitt, Karlsson & Sorensen, Inc. *ABAQUS Theory Manual*, ver. 5.5. Pawtucket RI, 1995.

8. Tsai C-L, Saidel GM, McFadden ER Jr., Fouke JM. Radial heat and water transport across the airway wall. *J. Appl. Physiol.* 69(1): 222-231, 1990.

9. Ying X, Qiao R, Ishikawa S, Bhattacharya J. Removal of albumin microinjected in rat lung perimicrovascular space. *J. Appl. Physiol.* 77(3): 12994-1302, 1994.

9. Conclusion

9.1 Summary of Progress

Asthmatic airways are known to be markedly thickened in comparison to normal airways, and yet they exhibit hyperresponsiveness upon smooth muscle contraction. Why an airway which has remodeled in such a way that would seem to reinforce and stiffen it against luminal occlusion, and yet be more susceptible to collapse under roughly the same amount of pressure has eluded researchers for quite some time.

A very simple two-layer tube model has been developed for the purpose of better understanding the mechanics of the airway, before and after asthmatic remodeling. The mathematical model has been solved numerically with finite element software (via the ABAQUS package), using linearized buckling analyses and nonlinear static analyses with remeshing techniques. Large-scale physical models made of foam and plastic were tested in a fixture which applied a loading and boundary condition similar to smooth muscle shortening for the purpose of further developing intuition regarding the collapse of tubes, verifying the results of the computational model, and helping to extend to the late post-buckling regime.

Simple experiments on Brown Norway rat lungs were performed to examine the effect of degree of constriction (induced by a smooth muscle agonist) on the observed number of folds in an airway's mucosal folding pattern, verifying that the number of folds is approximately constant throughout the collapse of the airway. Appropriate airway modeling parameters were determined from compression experiments on porcine airways (by Prof. Wiggs at the UBC PRL) and from indentation experiments on calf trachea specimens. Based on these moduli data and previously studied morphometric data on normal and asthmatic airway geometry, simulations of normal and asthmatic airways were performed, resulting in the general prediction that asthmatic airways do tend to buckle with fewer mucosal folds, and because of this altered buckling pattern become more hyperresponsive in their late post-buckling collapse.

Simulations with poroelastic material laws predict that the number of mucosal folds is not a function of the rate of smooth muscle shortening. Nor is it a function of the degree of disparity between layer permeabilities, nor the porosity of the materials. The number of folds appears to be governed strictly by the geometry and elastic constants of the airway

layers and is a statically-determined feature of airway collapse. If asthmatic airways are markedly more permeable than normal ones, there may be an increase in hyperresponsiveness due to the resulting increased compressibility.

9.2 Future Directions

This work, like many other bodies of research, has helped to answer a set of questions, while leaving a new set in its place. It is probably safe to say that much of the necessary airway modeling is complete, but that there are lingering concerns about the applicability of the research. The author leaves to the asthma modeling community the following suggestions for future work related to the airway modeling approach presented in this thesis.

- It must be verified more rigorously that the number of mucosal folds in asthmatic *human* airways is less than that of normal airways of comparable size. Knowing this quantitatively is preferable.

- It is desirable to have *better* estimates of the airway wall dimensions and material parameters, particularly for normal and asthmatic *human* airways. In particular, it would be helpful to better quantify by how much the E-values of the submucosa and the sub-epithelial collagen layers change from normal to asthmatic conditions. It would be helpful to know where within the airway wall the muscle is located and how much of the airway is submucosa, how much is smooth muscle, etc. The experimental results should be examined by someone well-versed in statistics who can assess their reliability.

- The issue of how much stress the asthmatic airway smooth muscle can generate (relative to normal) must be resolved somehow. Is asthmatic airway smooth muscle stronger or not? If it is markedly stronger, models such as this one may be moot.

- If animal model experiments are to be perfected which accurately simulate asthmatic airway remodeling, some type of thickening inner layer must be present. This thesis is testament to that importance. Existing rat models may be operating in a regime where the inner and outer thickness ratios are so small that perturbing the outer layer thickness may be what is responsible for the observed change in the number of folds. The

parameters in Chapter 6 and analyses in Chapter 7 indicate a different regime for *human* airways, and therefore different mechanics.

A. Appendix

A.1 Nomenclature and Defining Relationships

The list below defines variables of interest when evaluating the results of the two-layer computational models presented in this work. The dimensions of all dimensional variables are stated after the variable's description. If no dimensions are stated, the variable is dimensionless. If the variable has been nondimensionalized, an asterisk (*) is usually used in the variable symbol. The only dimensions of interest here are length (L), force (F) and time (T).

Simple Two-Layer Model Parameters:

R	base radius to the interface between inner and outer layers [L]
t_o	thickness of the outer (submucosal) layer [L]
t_i	thickness of the inner (mucosal) layer [L]
$t_o^* \equiv \frac{t_o}{R}$	outer thickness ratio
$t_i^* \equiv \frac{t_i}{R}$	inner thickness ratio
E_o	Young's uniaxial elastic modulus of the outer (submucosal) layer $\left[\frac{F}{L^2}\right]$
E_i	Young's uniaxial elastic modulus of the inner (mucosal) layer $\left[\frac{F}{L^2}\right]$
$E^* \equiv \frac{E_i}{E_o}$	elastic modulus ratio or "stiffness ratio"
ν_o	Poisson ratio of the outer (submucosal) layer
ν_i	Poisson ratio of the inner (mucosal) layer

Additional Poroelastic Two-Layer Model Parameters:

k hydraulic conductivity as defined in ABAQUS literature $\left[\frac{L}{T}\right]$

γ specific weight of wetting fluid (water) $\left[\frac{F}{L^3}\right]$

$\kappa \equiv \frac{k}{\gamma}$ generalized "permeability" parameter $\left[\frac{L^4}{FT}\right]$

κ_o permeability of the outer (submucosal) layer $\left[\frac{L^4}{FT}\right]$

κ_i permeability of the inner (mucosal) layer $\left[\frac{L^4}{FT}\right]$

$\kappa^* \equiv \frac{\kappa_i}{\kappa_o}$ permeability ratio

τ_{10} time required for 10% smooth muscle contraction [T]

$\tau_{10}^* \equiv \frac{\tau_{10}\, \kappa_o\, E_o}{R^2}$ shortening period parameter

Effort and Flow (Input-Output) Variables:

σ_m smooth muscle stress $\left[\frac{F}{L^2}\right]$

σ_{max} maximal smooth muscle stress $\left[\frac{F}{L^2}\right]$

t_m thickness of smooth muscle [L]

$P \equiv \frac{\sigma_m\, t_m}{R + t_o}$ equivalent smooth muscle pressure on outer aspect of outer layer $\left[\frac{F}{L^2}\right]$

$P_{max} \equiv \frac{\sigma_{max}\ t_m}{R + t_o}$	maximal equivalent smooth muscle pressure $\left[\frac{F}{L^2}\right]$
$P^* \equiv \frac{P}{E_o}$	normalized equivalent external pressure
$P_{max}^* \equiv \frac{P_{max}}{E_o}$	maximum normalized equivalent external pressure
P_b^*	normalized buckling pressure
Δ	inward radial displacement of outer edge of outer layer [L]
$\Delta^* \equiv \frac{\Delta}{R}$	normalized outer edge displacement
$S \equiv \frac{\Delta^*}{1+t_o^*} \cdot 100$	percent of smooth muscle shortening
S_b	percent of smooth muscle shortening at buckling
A	current cross-sectional lumen area [L^2]
$\pi(R-t_i)^2$	original cross-sectional lumen area [L^2]
$A^* \equiv \frac{A}{\pi(R-t_i)^2}$	normalized lumen area
A_b^*	normalized buckling lumen area
N	number of folds in the mucosal buckling pattern
ξ	imperfection/fold amplitude [L]
$\xi^* \equiv \frac{\xi}{R}$	normalized imperfection/fold amplitude

A.2 Simple Linear Analytical Solutions of a Single-Layer Tube

The simplest analysis of a thick-walled tube structure that can be performed is to assume that the displacements and strains are very small so that we can perform a simple linear

analysis. The analysis presented here is somewhat similar to the plane-strain solution for a thick-walled tube as presented in Section 5.2 of *Elasticity: Theory and Applications* by Reisman and Pawlik, pp. 155-158.[14] The three main ingredients, as usual, are (1) the force balance or stress equilibrium law, (2) the compatibility of strains relationship and (3) the constitutive law for the material under consideration, which in this case will be a simple linear-elastic one.

The general linear stress equilibrium equations written in polar (r,θ,z) coordinates are:

$$\frac{\partial \tau_{rr}}{\partial r} + \frac{\tau_{rr} - \tau_{\theta\theta}}{r} + \frac{1}{r}\frac{\partial \tau_{r\theta}}{\partial \theta} + \frac{\partial \tau_{rz}}{\partial z} + F_r = 0$$

$$\frac{\partial \tau_{r\theta}}{\partial r} + \frac{2\,\tau_{r\theta}}{r} + \frac{1}{r}\frac{\partial \tau_{\theta\theta}}{\partial \theta} + \frac{\partial \tau_{\theta z}}{\partial z} + F_\theta = 0$$

$$\frac{\partial \tau_{rz}}{\partial r} + \frac{\tau_{rz}}{r} + \frac{1}{r}\frac{\partial \tau_{\theta z}}{\partial \theta} + \frac{\partial \tau_{\theta\theta}}{\partial z} + F_z = 0$$

It is assumed that the deformation is completely axisymmetric, and thus the problem is one-dimensional in r. Also, there are no relevant body forces. Therefore $F_r = F_\theta = F_z = 0$. Applying these assumptions, the r-direction equilibrium equation becomes:

$$\frac{\partial \tau_{rr}}{\partial r} + \frac{\tau_{rr} - \tau_{\theta\theta}}{r} = 0$$

The assumption of axisymmetric deformation implies $u_r = u = u(r)$, $u_\theta = 0$ and $u_z = 0$. Because of this the θ and z-direction equilibrium equations become trivial, leaving this single equilibrium equation. In polar coordinates, the (two-dimensional) strains of interest are:

$$\varepsilon_{rr} \equiv \frac{\partial u_r}{\partial r} = \frac{\partial u}{\partial r}$$

$$\varepsilon_{\theta\theta} \equiv \frac{1}{r}\frac{\partial u_\theta}{\partial \theta} + \frac{u_r}{r} = \frac{u}{r}$$

$$\varepsilon_{r\theta} \equiv \frac{1}{2}\left(\frac{1}{r}\frac{\partial u_r}{\partial \theta} - \frac{u_\theta}{r} + \frac{\partial u_\theta}{\partial r}\right) = 0$$

The general form of Hooke's constitutive law for small deformations, appropriate for plane-strain in cartesian or cylindrical systems, is:

$$\tau_{ij} = \lambda\, e\, \delta_{ij} + 2\, G\, \varepsilon_{ij}$$

$$\text{where} \quad e = \varepsilon_{11} + \varepsilon_{22} + \varepsilon_{33}$$

Applied to this cylindrical geometry, Hooke's law is:

$$\tau_{rr} = (\lambda + 2G)\, \varepsilon_{rr} + \lambda\, \varepsilon_{\theta\theta}$$

$$\tau_{\theta\theta} = (\lambda + 2G)\, \varepsilon_{\theta\theta} + \lambda\, \varepsilon_{rr}$$

$$\tau_{zz} = \lambda\, (\varepsilon_{rr} + \varepsilon_{\theta\theta})$$

Substituting this into the equilibrium statement yields:

$$\frac{\partial}{\partial r}\left[(\lambda+2G)\varepsilon_{rr} + \lambda\varepsilon_{\theta\theta}\right] + \frac{(\lambda+2G)\varepsilon_{rr} + \lambda\varepsilon_{\theta\theta} - (\lambda+2G)\varepsilon_{\theta\theta} - \lambda\varepsilon_{rr}}{r} = 0$$

$$(\lambda+2G)\frac{\partial \varepsilon_{rr}}{\partial r} + \lambda\frac{\partial \varepsilon_{\theta\theta}}{\partial r} + 2G\frac{\varepsilon_{rr} + \varepsilon_{\theta\theta}}{r} = 0$$

$$(\lambda+2G)\frac{\partial^2 u}{\partial r^2} + \lambda\frac{\partial}{\partial r}\left(\frac{u}{r}\right) + \frac{2G}{r}\frac{\partial u}{\partial r} - \frac{2G\, u}{r^2} = 0$$

$$(\lambda+2G)\frac{\partial^2 u}{\partial r^2} + \frac{\lambda}{r}\frac{\partial u}{\partial r} - \frac{\lambda\, u}{r^2} + \frac{2G}{r}\frac{\partial u}{\partial r} - \frac{2G\, u}{r^2} = 0$$

$$(\lambda+2G)\frac{\partial^2 u}{\partial r^2} + \frac{\lambda+2G}{r}\frac{\partial u}{\partial r} - \frac{\lambda+2G}{r^2}u = 0$$

$$\frac{\partial^2 u}{\partial r^2} + \frac{1}{r}\frac{\partial u}{\partial r} - \frac{1}{r^2}u = 0$$

The above equidimensional equation can be solved for the solution:

$$\boxed{u(r) = C_1 r + C_2 \frac{1}{r}}$$

This happens to be the general linear solution for the displacement of all homogeneous single-layer tubes, regardless of whether plane-stress or plane-strain assumptions have been made. Following is the general solution for the radial stress, starting with Hooke's law for the radial stress under plane-strain.

$$\tau_{rr} = (\lambda + 2G)\,\varepsilon_{rr} + \lambda\,\varepsilon_{\theta\theta}$$

$$\tau_{rr} = (\lambda + 2G)\frac{\partial u}{\partial r} + \lambda\frac{u}{r}$$

$$\tau_{rr} = (\lambda + 2G)\left[C_1 - \frac{C_2}{r^2}\right] + \lambda\frac{1}{r}\left[C_1 r + \frac{C_2}{r}\right]$$

$$\tau_{rr} = (\lambda + 2G)\left[C_1 - \frac{C_2}{r^2}\right] + \lambda\left[C_1 + \frac{C_2}{r^2}\right]$$

$$\boxed{\tau_{rr} = 2\,(\lambda+G)\,C_1 - 2\,G\,\frac{C_2}{r^2}}$$

Single-Layer Tube with Pressure-Pressure Boundary Conditions:

Here, the pressure P is defined positive when it is directed onto the surface. The pressure-pressure boundary conditions are:

$$\tau_{rr}(R_o) = -P_o \qquad \tau_{rr}(R) = -P_m$$

Substituting these in for the radial stress yields:

$$-P_o = 2\,(\lambda+G)\,C_1 - 2\,G\,\frac{C_2}{R_o^2} \qquad -P_m = 2\,(\lambda+G)\,C_1 - 2\,G\,\frac{C_2}{R^2}$$

Next this pair of equations is solved simultaneously for the constants C_1 and C_2.

$$R_o^2\,P_o + 2\,(\lambda+G)\,R_o^2\,C_1 = R^2\,P_m + 2\,(\lambda+G)\,R^2\,C_1$$

$$C_1 = -\frac{R_o^2\ P_o - R^2\ P_m}{2\ (\lambda+G)\ (R_o^2 - R^2)}$$

$$2\,G\,\frac{C_2}{R_o^2} = P_o + 2\,(\lambda+G)\,C_1 = P_o - \frac{R_o^2\ P_o - R^2\ P_m}{R_o^2 - R^2}$$

$$2\,G\,\frac{C_2}{R_o^2} = \frac{R_o^2\ P_o - R^2\ P_o - R_o^2\ P_o + R^2\ P_m}{R_o^2 - R^2}$$

$$C_2 = -\frac{R_o^2\ R^2\ (P_o - P_m)}{2\ G\ (R_o^2 - R^2)}$$

The constants are substituted back into the general displacement solution to yield:

$$-u(r) = \frac{R_o^2\ P_o - R^2\ P_m}{2\ (\lambda+G)\ (R_o^2 - R^2)}\,r + \frac{R_o^2\ R^2\ (P_o - P_m)}{2\ G\ (R_o^2 - R^2)}\,\frac{1}{r}$$

In terms of the more familiar elastic constants, E_o (since ultimately, this single-layer analysis models the material of the outer layer) and ν, this becomes:

$$-u(r) = \frac{(1+\nu)(1-2\nu)}{E_o}\left(\frac{R_o^2\ P_o - R^2\ P_m}{R_o^2 - R^2}\right)r + \frac{1+\nu}{E}\left(\frac{R_o^2\ R^2\ (P_o - P_m)}{R_o^2 - R^2}\right)\frac{1}{r}$$

$$\boxed{-u(r) = \frac{1+\nu}{E_o\ (R_o^2 - R^2)}\left[(1-2\nu)(R_o^2 P_o - R^2 P_m)\ r + R_o^2 R^2 (P_o - P_m)\ \frac{1}{r}\right]}$$

Stiffness of an Externally-Pressured Incompressible Single-Layer Tube:

This solution is used in Chapter 4 for computing the elastic modulus (E_o) of single-layer foam specimens. Set $P_m = 0$ to get:

$$-u(r) = \frac{(1+\nu)\ R_o^2\ P_o}{E_o\ (R_o^2 - R^2)}\left[(1-2\nu)\ r + \frac{R^2}{r}\right]$$

Evaluate at outer edge, defining $\Delta = -u(R_o)$:

$$\Delta = \frac{(1+\nu)\ R_o\ P_o}{E_o\ (R_o^2 - R^2)} \left[(1-2\nu)\ R_o^2 + R^2\right]$$

Rearrange to get elastic modulus as a function of linear stiffness:

$$E_o = \frac{(1+\nu)\ R_o}{R_o^2 - R^2} \left[(1-2\nu)\ R_o^2 + R^2\right] \left(\frac{P_o}{\Delta}\right)$$

If material is incompressible ($\nu = {}^1/_2$):

$$E_o = \frac{3\ R_o\ R^2}{2\ (R_o^2 - R^2)} \left(\frac{P_o}{\Delta}\right)$$

In terms of dimensionless parameters:

$$\boxed{E_o = \frac{3\ (1+t_o^*)}{2\ t_o^*\ (2+t_o^*)} \left(\frac{P_o}{\Delta^*}\right)}$$

Internal Pressurization of a Compressible Single-Layer Tube (with Outer Edge Fixed):

The result derived here is used in calculating the foundation stiffness of Section A.3. At this point, we have to take a step backward in our analysis because the boundary conditions are different. Starting with our general solution for the deformation of a single-layer tube:

$$u(r) = C_1\, r + C_2 \frac{1}{r}$$

Assume that the displacement is known at both boundaries:

$$u_m = u(R) = C_1\, R + C_2 \frac{1}{R} \qquad u_o = u(R_o) = C_1\, R_o + C_2 \frac{1}{R_o}$$

$$R\, u_m = C_1\, R^2 + C_2 \qquad R_o\, u_o = C_1\, R_o^2 + C_2$$

$$C_1 = \frac{R_o u_o - R\, u_m}{R_o^2 - R^2}$$

$$C_2 = R\,u_m - C_1\,R^2$$

$$C_2 = \frac{R_o^2\,R\,u_m - R^3\,u_m - R_o\,R^2\,u_o + R^3\,u_m}{R_o^2 - R^2}$$

$$C_2 = \frac{R_o\,R\,(R_o u_m - R u_o)}{R_o^2 - R^2}$$

So the linear displacement solution for a (plane-strain or plane-stress) single-layer tube with both edge displacements known is:

$$\boxed{u(r) = \frac{(R_o u_o - R u_m)\,r + (R_o u_m - R u_o)\,\frac{R_o\,R}{r}}{R_o^2 - R^2}}$$

If the outer edge is known to be fixed ($u_o = 0$), this simplifies to:

$$u(r) = \left(-\,r + \frac{R_o^2}{r}\right)\frac{R\,u_m}{R_o^2 - R^2}$$

Also:

$$\frac{du}{dr} = -\left(1 + \frac{R_o^2}{r^2}\right)\frac{R\,u_m}{R_o^2 - R^2}$$

From the plane-strain constitutive law:

$$P = -\tau_{rr} = -(\lambda + 2G)\frac{du}{dr} - \lambda\frac{u}{r}$$

Or in terms of E_o and ν:

$$P = -\frac{E_o}{(1+\nu)(1-2\nu)}\left[(1-\nu)\frac{du}{dr} - \nu\frac{u}{r}\right]$$

$$P = \frac{E_o}{(1+\nu)(1-2\nu)}\frac{R\,u_m}{R_o^2 - R^2}\left[(1-\nu)\left(1 + \frac{R_o^2}{r^2}\right) + \nu\left(-1 + \frac{R_o^2}{r^2}\right)\right]$$

$$P = \frac{E_o}{(1+\nu)(1-2\nu)} \frac{R\ u_m}{R_o^2 - R^2} \left[(1-2\nu) + \frac{R_o^2}{r^2}\right]$$

Notice that due to the prescribed displacement on the outer edge, axisymmetric deformation of an incompressible tube would be impossible. Instead we'll assume a highly compressible tube ($\nu = 0$), and evaluate the stiffness at the inner surface ($r = R$).

$$\frac{P_m}{u_m} = E_o \frac{R}{R_o^2 - R^2} \left(1 + \frac{R_o^2}{R^2}\right)$$

Using our dimensionless parameters:

$$\frac{P_m}{u_m} = \frac{E_o}{R} \frac{2 + 2t_o^* + t_o^{*2}}{t_o^* (2 + t_o^*)}$$

Alternatively:

$$\boxed{\frac{P_m}{u_m} = \frac{E_o}{R} \frac{(1+t_o^*)^2 + 1}{(1+t_o^*)^2 - 1}}$$

A.3 Two-Layer Ring-Buckling Analytical Solution

An analytical solution for the simple two-layer model is desirable to help develop an intuition regarding its behavior. It is also valuable to have approximate results for the expected number of folds and the buckling pressure as functions of the three dimensionless input parameters as opposed to curve fits from isolated data points.

The solution presented here is inspired by Prof. David M. Parks of M.I.T.[12] It is based on a ring buckling formulation with a radial elastic foundation from Brush and Almroth's *Buckling of Bars, Plates and Shells,* Chapter 4.[7]

Equation 4.35 from Brush and Almroth for the buckling pressure (at the interface between layers) reads as follows in our notation:

$$P_{m_b}(N) = \frac{1}{b}\left[\alpha(N^2-1) + \frac{\beta}{N^2-1}\right]$$

$$\text{where } \alpha \equiv \frac{\text{beam bending stiffness}}{R^3} = \frac{E_i\ I_{beam}}{R^3}$$

$$\text{and } \beta \equiv k_f R$$

This is a good approximation for $N \geq 2$. In these equations b is the length of the structure under consideration in the axial direction, and k_f is the beam's foundation stiffness with units of pressure. Brush and Almroth's solution often calls for the mean radius of the beam, which is commonly approximated here as simply R since $R >> t_i$.

I_{beam} is the geometrical moment of inertia of the inner layer when it is considered to be a beam. Since it has a simple rectangular cross section,

$$I_{beam} = \frac{1}{12} b\, t_i^3$$

$$\text{therefore } \alpha = \frac{1}{12} E_i\, b \frac{t_i^3}{R^3} = \frac{1}{12} E_i\, b\, t_i{}^{*3}$$

The foundation stiffness is derived using the simple linear homogeneous tube model of Section A.2. For this beam it is defined as the amount of increase of internal force per unit arc length per unit radial deformation at the interface between beam and foundation.

$$k_f \equiv b \frac{P_m}{u_m}$$

Using the solution from Section A.2:

$$k_f = b \frac{E_o}{R} \frac{(1+t_o{}^*)^2 + 1}{(1+t_o{}^*)^2 - 1}$$

$$\text{and } \beta = k_f R = b\, E_o \frac{(1+t_o{}^*)^2 + 1}{(1+t_o{}^*)^2 - 1}$$

Though several neighboring buckling modes may appear in a buckled two–layer tube, here the optimal number of folds will be considered to be that which occurs with the lowest

buckling pressure (and thus the least strain energy). If we treat N as a continuous variable (which is a good assumption particularly for large N), this becomes a simple minimization problem:

$$\frac{d(P_{m_b})}{dN} = \frac{2N}{b}\left[\alpha - \frac{\beta}{(N^2-1)^2}\right] = 0$$

Solving for N yields:

$$N = \sqrt{1 + \sqrt{\beta/\alpha}}$$

If N is sufficiently large, then $\sqrt{\beta/\alpha} >> 1$ and we can approximate:

$$N \approx (\beta/\alpha)^{1/4}$$

Substituting in the expressions for α and β, we get:

$$N \approx \left[\frac{b\ E_o\ \frac{(1+t_o^*)^2 + 1}{(1+t_o^*)^2 - 1}}{\frac{1}{12}\ E_i\ b\ t_i^{*3}}\right]^{1/4}$$

With some simplification, the ring-buckling solution for the number of folds is:

$$\boxed{N \approx \left(12\ \frac{(1+t_o^*)^2 + 1}{(1+t_o^*)^2 - 1}\ \frac{1}{t_i^{*3}}\ \frac{1}{E^*}\right)^{1/4}}$$

This analytical solution tends to overestimate the number of folds, which actually makes sense since earlier studies have shown that added compressibility tends to increase the number of folds a bit (see Section 3.2.1). Over the three-dimensional space of 500 linearized buckling analyses, the relative error ranges from –15% to +83%, with a median at 15%. The standard deviation of the relative error is 16%.

APPENDIX REFERENCES

1. Abeyaratne R. Lecture notes from M.I.T. course 2.072, Mechanics of Continuous Media. Spring 1995.

2. Allen HG. *Analysis and Design of Structural Sandwich Panels.* Pergamon Press, London, 1969. pp. 156-163.

3. Anand L. Lecture notes from M.I.T. course 2.072, Mechanics of Continuous Media. Spring 1994.

4. Bathe K-J. *Finite Element Procedures in Engineering Analysis.* Prentice-Hall, Toronto, 1982.

5. Bathe K-J. Lecture notes from M.I.T. course 2.093, Computer Methods in Dynamics. Spring 1993.

6. Bathe K-J. Lecture notes from M.I.T. course 2.094, Theory and Practice of Continuum Mechanics. Fall 1993.

7. Brush DO, Almroth BO. *Buckling of Bars, Plates, and Shells.* McGraw-Hill, New York, 1975. ch. 4.

8. Chaskalovic J, Naili S. Bifurcation theory applied to buckling states of a cylindrical shell. *Z. agnew. Math. Phys.* 46: 149-155, 1995.

9. Dion B, Naili S, Renaudeaux JP, Ribreau C. Buckling of elastic tubes: study of highly compliant device. *Med. & Biol. Eng. & Comput.* 33: 196-201, 1995.

10. Etter DM. *Structured FORTRAN 77 for Engineers and Scientists,* 2nd Ed. Benjamin-Cummings, Menlo Park CA, 1987.

11. Hibbitt, Karlsson & Sorensen, Inc. *ABAQUS Theory Manual,* ver. 5.5. Pawtucket RI, 1995.

12. Parks DM. Written communication and conversations regarding a closed-form solution for N. 1996.

13. Press WH, Teukolsky SA, Vetterling WT, Flannery BP. *Numerical Recipes in FORTRAN: The Art of Scientific Computing,* 2nd Ed. Cambridge University Press, New York, 1986.

14. Reismann H, Pawlik PS. *Elasticity: Theory and Applications.* Krieger, Malabar FL, 1991.

15. Timoshenko SF, Goodier JN. *Theory of Elasticity,* 3rd Ed. McGraw-Hill, New York, 1970.

16. Timoshenko SF, Gere JM. *Theory of Elastic Stability,* 2nd Ed. McGraw-Hill, Toronto, 1961. Ch. 11, pp. 457-520.

17. Ugural AC, Fenster SK. *Advanced Strength and Applied Elasticity,* 2nd Ed. Elsevier, New York, 1987.

18. Young WC. *Roark's Formulas for Stress and Strain,* 6th Ed. McGraw-Hill, New York, 1989.

THESIS PROCESSING SLIP

FIXED FIELD: ill. _____ name _____

index _____ biblio _____

▸ COPIES: (Archives) Aero Dewey (Eng) Hum

Lindgren Music Rotch Science

TITLE VARIES: ▸☐ _____

NAME VARIES: ▸☐ _____

IMPRINT: (COPYRIGHT) _____

▸ COLLATION: 220 l.

▸ ADD: DEGREE: _____ ▸ DEPT.: _____

SUPERVISORS: _____

NOTES:

cat'r: date:

page: ▸ 3172

▸ DEPT: M.E.

▸ YEAR: 1998 ▸ DEGREE: Ph.D.

▸ NAME: HROUSIS, Constantine Athanasios